Politecnico di Torino

ScuDo
Scuola di Dottorato ~ Doctoral School
WHAT YOU ARE, TAKES YOU FAR

Doctoral Dissertation

Doctoral Program in Mechanical Engineering (36^{th} cycle)

On ocean wave dynamics and their importance on assessing wave energy converters performance

By

Giulia Cervelli

Supervisor:
Prof. Giuliana Mattiazzo
Co-supervisor:
Gianmaria Sannino

Doctoral Examination Committee:
Prof. Claudia Cecioni, Università degli Studi Roma 3
Prof. Diego Vicinanza, Università degli Studi della Campania "Luigi Vanvitelli"

You're not a wave
you are a part of the ocean.

Mitch Albom

CONTENTS

ABSTRACT

The thesis explores ocean wave dynamics and their impact on the performance evaluation of Wave Energy Converters (WECs). The analysis focuses on Pantelleria, an Italian island in the Strait of Sicily, a strategic area for renewable energy, evaluating seasonal and interannual variations in sea conditions and their influence on energy convertion.
The research uses a combination of in-situ and remote sensing techniques to collect wave data, integrating advanced numerical models to more accurately predict the performance of WECs. In particular, the performance of the Pendulum Wave Energy Converter (PeWEC) is analyzed, studying the correlations between wave data and energy conversion estimates.
The results show that the correct interpretation of wave characteristics, including directionality as well as frequency, is crucial for improving the effectiveness of WECs. The thesis highlights the importance of considering multidirectional spectra for accurate evaluation, highlighting how monodirectional assumptions overestimate performance results.
The conclusions suggest that different sources of wave data can lead to significant differences in annual estimates of converted energy, and a correction method to reduce the error induced by the monodirectional assumption is provided.
This study provides a significant contribution to understanding ocean wave dynamics and improving analytical methodologies for estimating WEC performance.

List of Figures

LIST OF TABLES

1

INTRODUCTION

1.1. BACKGROUND

GLOBAL energy demand is projected to increase by 20-30% alongside population and economic growth by 2040 [1]. To meet this demand and hinder climate change, it is necessary to reduce greenhouse gas emissions and provide sustainable energy. The Energy Roadmap 2050 sets the objective to reduce greenhouse gas emissions by 80% and to have renewable energy represent at least 40% of energy consumption by 2050 [2]. Achieving these goals requires gradually replacing fossil fuels with renewable energy sources.

Ocean renewable energy, with its vast availability, is receiving significant attention and development. Among the various renewable energies, wave energy has many significant advantages over others, such as high availability, low environmental impact, greater predictability, and high energy density [3, 4]. In particular, wave energy is more predictable than wind energy, and its nighttime availability provides an additional advantage over solar energy [5]. For these reasons, ocean energy is one of the renewable energy resources that has the potential to accelerate the energy transition and support the adoption of sustainable policies. However, currently, technologies capable of harnessing wave energy are relatively immature compared to other renewables, and this source is currently underutilized. Nevertheless, it has the potential to play a significant role in diversifying the renewable energy portfolio and achieving sustainable growth. Specifically, the achievable capacity from the exploitation of waves and tides in the EU is expected to reach 100 GW by 2050 [6].

Given the crucial importance of wave energy, the portfolio of developed converters is very broad; indeed, more than 200 devices were under development worldwide in 2017 [7]. However, very few devices are operational and commercially used [8]. Reasons include the high Levelized Cost Of Energy (LCOE), much higher than other energy sources, adverse environmental conditions, the need for special installation permits, and high equipment costs such as ships [9]. Reducing Operation and Maintenance (O&M) costs is one of the challenges to overcome to make wave energy a commercially viable innova-

tive energy source. Maintenance can account for up to 57% of total operating expenses [10]. Implementing monitoring and control systems represents a valid solution to reduce these costs. Similarly, detailed knowledge of the average and extreme environmental conditions of the installation site is crucial. The fundamental approach to capturing energy from waves involves identifying high-energy sites and optimizing Wave Energy Converters (WECs) based on the characteristics of the sea states.

Carlos et al. [11] proposed a methodology for identifying site selection for wind and wave farms. The five-step approach presented is based on identifying zones with significant energy resources near urban areas. These sites must be characterized by suitable weather conditions for device survivability and appropriate environmental conditions for construction and maintenance operations, in addition to having satisfactory extractable power. The energy assessment is the first step of the methodology and can be carried out through the calculation of wave energy [12, 13, 14]. Unfortunately, the extractable wave energy is only a fraction of the wave power and depends on the performance of the WECs. Moreover, both the potential wave power and the extractable power by means of WECs are challenging to evaluate because they depend on the interaction between wind and sea surface and between waves and device, respectively, and can be subject to computational errors. Therefore, proper sea characterization and detailed WEC design are critical to reducing uncertainty levels.

The main parameters describing wave conditions are the significant wave height and the wave energy period, which allow for the estimation of the average wave power, and the peak direction, which indicates the primary incoming wave direction. However, these parameters provide limited information as they do not account for the directional distribution of different wave components. Detailed analysis should include directional spreading, which measures the distribution of wave energy over the directions. Considering the spreading parameter is particularly significant for directional-sensitive WEC devices. Specifically, there are many types of WECs capable of harnessing wave energy, classified based on operational principle, sensitivity with the wave direction, location, and power take-off system [15, 16]. Often, a basic categorization using the terms terminator, attenuator, and point absorber is used [17]. Terminators are devices characterized by large extensions, parallel to the wave direction, while attenuators have a large orthogonal size relative to the wave direction. Both terminators and attenuators are also called directional sensitive WECs because they are activated by a narrow range of wave directions. In contrast, point absorbers are smaller than the predominant wavelength and can generate power from waves of any direction. Consequently, directional characterization of sea states is crucial, especially when designing direction-sensitive devices.

Each ocean wave can be considered as a superposition of harmonic waves with different amplitudes, frequencies, phases, and directions [18, 19]. Typically, the assessment of sea characteristics is based on wave spectrum analysis, which shows how wave energy is distributed over frequencies and directions and allows the calculation of synthetic wave parameters. Specifically, it is possible to identify the directional variability of individual wave components by calculating the directional spreading of waves [14]. This parameter represents the width of the spectrum in the directional domain and describes the variability of direction according to individual harmonic waves that compose the irregular water surface.

In general, the waves of interest for the energy conversion are produced by the friction between wind and sea surface water, and their characteristics vary based on the wind duration and the area size over which it blows. Thus, wave energy increases with the increase of time duration and area size [20]. Moreover, the wind location relative to the analyzed waves is crucial. Specifically, two main types of wind-generated waves are of interest: wind waves and swells. Wind waves form at sea when wind speed exceeds a critical value. Under the continuous action of the wind, the waves gradually increase in height, length, and period to a maximum value that mainly depends on wind speed, the extent of the sea over which the wind blows, wind duration, and depth. During the initial stage of the wave generation process, the irregularity of wind action on the sea surface creates waves of various sizes with different propagation directions. On the other hand, swell waves originate from wind action that has occurred in regions even very distant from the observation area. When the waves leave the generation area or the wind stops blowing, the waves continue to propagate as swell waves. These waves are more regular than wind waves because there is a natural dispersion of waves component in space, determined by the different propagation speeds of each spectral component. For these reasons, the spectrum of swell waves is narrow in direction, leading to higher WEC performance.

The primary purpose of this thesis is to provide valid support in describing sea waves and using the best methodology to investigate the interaction between WECs and waves. Additionally, a high focus is placed on evaluating the performance of the PeWEC under different wave assumptions. The PeWEC is a floating device based on a pendulum and begins its motion when waves rock the hull [21, 22]. Moreover, it is a directional-sensitive WEC, and the more the wave direction is parallel to the device's principal axis, the higher the harvesting wave energy. To evaluate the PeWEC performance, wave excitation forces are calculated by combining excitation coefficients with wave component coefficients based on frequency spectra and frequency-directional spectra. In this way the results that come from the monodirectional assumption is compared with the multidirectional one.

1.2. MAIN OBJECTIVES AND CONTRIBUTIONS

THE primary goals and unique contributions of this thesis are outlined below.

Chapter 2 focuses on describing the characteristics of ocean waves using statistical methods, providing a detailed classification of waves based on their periods. The main contributions include the detailed description of the spectral analysis, as well as the spectral reconstruction and spectrum partitioning models. Such mathematical tools are of fundamental importance in the characterization and analysis of sea states. The chapter is composed as follows:
Section 2.1 provides a comprehensive analysis of ocean waves, focusing on their types, generation mechanisms, and statistical analysis methods relevant for wave energy conversion. The classification of different types of ocean waves based on their periods is pro-

vided, highlighting tides, storm surges, tsunamis, seiches, surf beats, and wind-generated waves. Among these, wind-generated waves are the primary focus, as they directly interact with WECs.
Section 2.2 describes the importance of understanding wave characteristics for designing and optimizing WECs and provides methodologies for statistical wave analysis. Furthermore, synthetic wave parameters are introduced, and equations useful for their calculation are provided. These parameters are defined as synthetic since they synthetically describe the characteristics of sea states. These parameters are derived from statistical analysis of wave information, typically obtained through in-situ instruments such as buoys and Acoustic Doppler Current Profilers (ADCP).
The zero-crossing method is introduced as a fundamental technique for analyzing apparent waves, where waves are identified by consecutive crossings of the mean sea level. This method allows the determination of wave height and period parameters, essential for evaluating sea states. However, it lacks directional information, necessitating spectral analysis for a more comprehensive understanding of the sea states. Spectral analysis is presented as a more advanced method, describing ocean waves as a stochastic process. This approach involves Fourier analysis to decompose waves into sinusoidal components, each characterized by its frequency, amplitude, and direction. Specifically, the frequency spectrum and frequency-directional spectrum, i.e., the distribution of wave energy over different frequencies and the distribution of wave energy over different frequencies and directions, respectively, are introduced.
Section 2.3 provides the main spectral models for reconstructing the frequency spectrum, directional spectrum, and frequency-directional spectrum based on synthetic parameters.
Section 2.4 explores spectrum partitioning techniques, both one-dimensional (1D) and two-dimensional (2D), to differentiate between wind waves and swell. These techniques are essential for accurately modeling wave components and improving the design and management of maritime structures. In fact, by partitioning the overall spectrum and obtaining the wind wave and the swell spectrumit is possible to analyze the characteristics of the individual sea states that coexist in the same site at the same time. This method is particularly valuable in regions where multi-modal sea states occur concurrently, offering a comprehensive view of the wave dynamics and contributing to more efficient and resilient maritime engineering solutions.

Chapter 3 examines different wave measurement techniques, including in-situ and remote sensing, and provides information on global numerical models as well as local numerical model for wave downscaling. Key contributions include comparisons of wave measurement techniques in terms of precision, ease of access, reliability, and accuracy. In particular, by knowing the strengths and weaknesses of the different data sources it is possible to choose which of these is the most suitable for specific needs. The chapter is composed as follows:
Section 3.1 focuses on various methodologies and techniques used to obtain and evaluate wave data, which are fundamental for assessing wave energy resources and designing efficient and safe WECs. The section describes the requirements that wave data should have to be considered reliable and complete, emphasizing the need for high informa-

tional content, accuracy, and good temporal and geographical coverage to support various stakeholders, including planners, scientists, and marine safety experts.
Section 3.2 describes in-situ measurement techniques, such as wave buoys, wave probes, and Acoustic Doppler Current Profilers (ADCP). These methods provide accurate and direct measurements of wave characteristics but involve high costs and logistical challenges, especially in harsh marine environments. Despite their reliability, the sparse distribution of in-situ instruments limits their long-term applicability for large-scale wave energy assessments.
Section 3.3 presents alternative measurement techniques to the in-situ methods, such as remote sensing techniques, including stereophotography, high-frequency radar, and satellite altimetry. These methods offer broader spatial coverage and have the potential to complement in-situ measurements. For example, satellite altimetry provides significant wave height data with good global coverage, although its accuracy may be compromised near coastal areas due to signal contamination and are characterized by a low temporal resolution.
Section 3.4 discusses numerical model techniques, with a focus on the SWAN model. These models simulate waves propagation over vast areas and long time periods, providing valuable data for wave energy assessments. The SWAN model, in particular, stands out for its ability to incorporate various physical processes and interactions with the seabed, being particularly useful in nearshore regions.
Section 3.5 introduces various freely available wave data products, distinguishing their source, processing and validation methodology. These products are of particular interest when seeking wave information for a specific site and are classified into in-situ data products, satellite data products, and numerical model data products. Each category is evaluated based on its utility in wave energy resource assessments, emphasizing that combining multiple data sources often yields the most comprehensive understanding of wave conditions.
Section 3.6 provides an overview of wave analysis standards, such as IEC/TS 62600-101:2015 and SeaDataNet, outlined to ensure consistency and reliability in wave data analysis. The IEC Technical Specification provide guidelines for the spatial and temporal resolution of wave data, acceptable types of wave boundary conditions, and the minimum duration of time series data required for reliable assessments. Furthermore, the procedure to validate wave data through a quality process is provided by SeaDataNet.

Chapter 4 aims to evaluate the energy potential of the waves around the island of Pantelleria and analyze the seasonal and interannual variability of the waves. Contributions include the calibration and validation of the SWAN model with in-situ and satellite data. In particular, the applicability of satellite data for the validation of numerical models is investigated showing its advantages even in unfavorable geographical situations. Indeed, unlike common applications, the satellite measurements utilized in this study are recorded near the coastline, which may reduce their accuracy.
Regarding the calibration of the SWAN model, an innovative methodology is presented, drastically reducing the number of configurations to be analyzed for identify the best set-up. In this analysis, both the model performance in terms of accuracy of H_s and T_e and the computational times are considered. The chapter is composed as follows:

Section 4.1 describes the case study, which involves the evaluation of the wave energy potential at the island of Pantelleria. The island's advantageous location in the Mediterranean Sea experiences strong and consistent wave patterns, making Pantelleria an ideal site for testing and developing WECs.
Section 4.2 provides information on the available wave datasets for the area of interest, including in-situ measurements, satellite data, and numerical model data. The MOREnergy Lab has installed two in-situ instruments near the northwestern coast of Pantelleria, providing valuable local wave data. Additionally, Level-3 satellite datasets and data from the ERA5 reanalysis project are utilized. Satellite data is used to validate the SWAN downscaling model, while ERA5 data is used to drive this model. The meticulous calibration and validation process of the SWAN model is also described, providing performance indicators to indicate the accuracy of the numerical results.
Section 4.3 reveals insights into the wave conditions around Pantelleria. The in-situ dataset offers accurate measurements of wave characteristics, while satellite datasets complement these information by providing broader long-term data records. The SWAN model, calibrated with these datasets, enhances the understanding of wave dynamics and energy potential and is used to conduct evaluation on seasonal variability, interannual variability, the prevalence of multimodal wave systems, directional variability of the resource, and the occurrence of sea states.

Chapter 5 provides an overview of the different types of WECs and discusses the evolution of WEC modeling. The main contribution is the introduction of the Wave RES platform for the analysis of wave energy resources. In particular, this tool has the aim of supporting marine stakeholders to make informed decisions and to estimate, in the first analysis, the producibility of a given site based on different WECs. The chapter is composed as follows:
Section 5.1 introduces various aspects of WECs, highlighting their importance in harnessing ocean wave energy for electricity production. This contributes to global sustainability goals and diversifies the renewable energy mix.
Section 5.2 focuses on the classification of WECs, which can be categorized based on operational principles, directional-sensitivity, location, and power take-off mechanisms. Common classifications include terminators, attenuators, and point absorbers. Terminators are aligned parallel to the wave direction, attenuators are positioned orthogonally, and point absorbers can operate independently of the wave direction.
Section 5.3 describes the evolution of WEC modeling, highlighting advancements in hydrodynamic models. These models use potential flow theory to describe the interaction between waves and the device's body. The section explains how these models have become increasingly sophisticated, incorporating various physical processes to improve accuracy.
Section 5.4 delves deeper into hydrodynamic models, describing how potential flow theory is used to simulate wave-body interactions. It explains the concepts of incident, diffracted, and radiated wave fields, and how these are utilized in Boundary Element Methods (BEM) to calculate the response of Wave Energy Converters (WECs) based on wave forces.
Section 5.5 introduces the Wave RES platform, developed to support the analysis of wave

energy resources and evaluate the productivity of a portfolio of WECs. The platform provides various tools and visualizations to help users evaluates the energy potential and productivity of different WECs at specific sites.

Chapter 6 describes the operating principles and geometric characteristics of the PeWEC, analyzing the performance of the device under various wave scenarios. The main contributions include evaluating the efficiency of the WEC by considering the multidirectional interaction of the waves and analyzing the response of the device as a function of the wave incidence direction with reference to the hull orientation. The chapter is composed as follows:
Section 6.1 describes the case study, emphasizing the need to analyze the complexity of sea waves, especially for multimodal sea states, through a multidirectional analysis of wave-device interaction.
Section 6.2 introduces the PeWEC and its operational principles. The PeWEC is a floating device that harnesses wave energy through the movement of a pendulum inside its hull. This section details the geometric and dynamic characteristics of the device, highlighting its innovative design tailored for efficient wave energy conversion in the Mediterranean Sea.
Section 6.3 discusses the dynamic equations governing the PeWEC's motion. It explains how these equations are derived and used to model the device's response to wave excitation forces. Additionally, wave excitation forces and Response Amplitude Operators (RAOs) for PeWEC are presented. Finally, the performance of PeWEC under various wave scenarios is investigated. The analysis compares monodirectional and multidirectional wave assumptions, highlighting the impact of directional spreading on energy capture efficiency as well as the angle of incidence of the waves with respect to the orientation of the device.

Chapter 7 aims to evaluate the performance of PeWEC in Pantelleria using different data sources and spectral approximations, analyzing the errors based on monodirectional and multidirectional data. Contributions include comparing the performance of PeWEC based on different data sources (in-situ, global and local models) and demonstrating the importance of considering spectral complexity for precise energy conversion estimates. Furthermore, the inherent error in evaluating the performance of the WEC through the power matrix is addressed and quantified for the case study. The chapter is composed as follows:
Section 7.1 introduces the overall objective of the chapter, which is to systematically analyze the performance of the PeWEC using various data sources and different wave approximations and assumptions.
Section 7.2 delves into specific investigations aimed at understanding the errors in performance estimation based on different assumptions. This includes examining discrepancies in PeWEC's performance based on the wave data sources used, investigating differences between in-situ measurements, a global numerical model (i.e. ERA5), and a local numerical model (i.e. SWAN).
Further analysis is carried out to assess performance estimation errors based on monodirectional and multidirectional spectra reconstructed from discretized synthetic param-

eters. This involves evaluating the implications of using simplified representations and how these influence the accuracy of energy conversion estimates.
The correlation between performance estimates based on 1D (monodirectional) and 2D (multidirectional) assumptions is investigated. This study highlights the need to consider multidirectional wave interactions to obtain a more realistic assessment of PeWEC's performance.
Finally, the errors in performance estimation arising from the use of multi-peak versus single-peak spectra are addressed. This analysis explores how the complexity of wave spectra occurring in Pantelleria, characterized by multi-modal sea state, influences the accuracy of performance predictions. The results suggest that incorporating the full spectral complexity is crucial for precise energy conversion estimates.
Section 7.3 shifts the focus to the practical application of these findings by evaluating the energy conversion potential of PeWEC in Pantelleria. This section integrates the insights from previous analyses on the error related to the monodirectional assumption to provide a holistic view of how PeWEC performs under real conditions, considering the unique wave climate of the Mediterranean region.

I

LITERATURE REVIEW: OCEAN WAVES

2

OCEAN WAVES ANALYSIS

2.1. INTRODUCTION

THE types of waves that occur in the oceans and along the coasts are numerous and diverse. All these waves can be categorized by referencing their period, as proposed in [23] and described in Fig. 2.1. Later in this chapter, we will explore the meaning of this parameter in more detail, for now, a general classification can be made considering the wave period as the time wave takes to complete one full cycle, from trough to trough or from crest to crest.

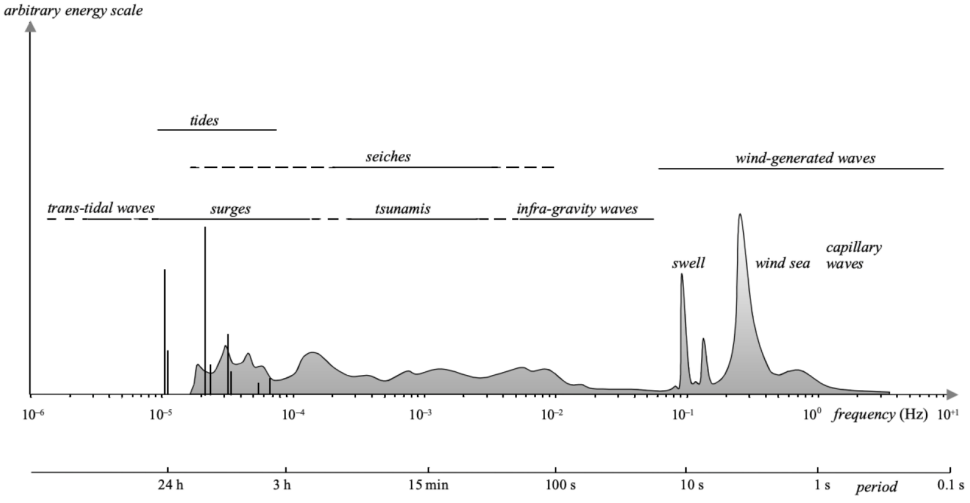

Figure 2.1: Normalized energy and wave period for the main ocean waves categories [24]

Among the different types of waves, *tides* are notably significant. They are generated by the interaction between the ocean's water mass and the sun and moon and their periods

generally range between 12 and 24 hours. *Storm surge* is another type of wave having a period of one or two days. The term storm surge describes a large-scale rise in sea level caused by a combination of high wind speeds and low atmospheric pressure. When a storm surge occurs near the coast, the risk of flooding is high. Another type of wave that can cause significant damage is the *tsunami*. These waves are generated by earthquakes or submarine landslides that displace large masses of water. Their periods can range from a few minutes to an hour. A further potentially dangerous type of wave is the *seiche*, which is a standing wave that develops in enclosed or semi-enclosed bodies of water, such as harbours, lakes, or partially enclosed seas, due to resonance in the disturbed water body. In the case of an harbour, the wave can be high enough to flood the docks and break mooring lines. These waves are usually generated by waves from the open sea and have periods of less than an hour. *Surf beat*, instead, typically occurs in the surf zone near beaches, caused by the overlapping of groups of wind-generated waves and having periods of a few minutes. Finally, there is the category of *wind-generated waves*, which generally have periods of less than 30 seconds. This last category is the focus of this thesis since it is the primary wave that interactes with WECs, enabling the conversion of its energy into electrical one. When these waves are generated by local wind, they are called *wind waves* and are characterized by high irregularity and short crests [25]. When wind waves leave their area of generation, they exhibit a more regular behaviour and are called called *swell*, characterized by a long crest[26].
In the following sections, an in-depth description of the statistical methodologies used to derive necessary synthetic parameters for WECs and coastal design is presented, with a particular focus on the analysis of wind-generated waves.

2.2. WAVE ANALYSIS

THE *short-term statistical analysis* of ocean waves is a crucial step for understanding and analyzing the temporal evolution of sea states occurred at a site of interest [27]. Through this analysis, it is possible to determine synthetic parameters that represent and describe each sea state.
In the field of renewable wave energy, knowing the characteristics of the waves is fundamental for designing and optimizing WECs. In particular, both the device geometric and operational attributes can be set-up to maximize energy production based on the waves occurring at the installation site [28]. However, the analysis of waves cannot be limited to short-term statistical analysis alone. Through *long-term statistical analysis*, environmental conditions that may be considered dangerous in terms of the survival of the device and its mooring system must be identified [29]. This statistical analysis enables the identification of the design wave associated with the expected lifetime of the device itself [30].
In this thesis, the focus is on short-term statistical analysis, as the emphasis is placed on the device's performance under operational conditions, achievable by short-term analysis, rather than in extreme wave conditions, object of the long-term analysis. In particular, the WEC's energy conversion efficiency is evaluated considering different wave data sources and wave analysis techniques.

The starting point for short-term statistics is the measurements of the sea surface elevation. These measurements, commonly conducted with in-situ instruments, must consider two fundamental aspects: the *sampling interval* and the *duration of the recording*. Specifically, the measuring instruments provide discrete measurements, and the sampling interval corresponds to the time between two consecutive measurements. This interval must be sufficiently small to capture the wave behavior [31]. The typical interval for in-situ instruments is 2 Hz, corresponding to 0.5 seconds [32]. Regarding the duration of each single measurement, it must be short enough to consider the waves as a stationary phenomenon and long enough to obtain a robust statistical sample. A compromise between these two temporal requirements is to use a recording duration of 15 to 30 minutes. Finally, each measurement window should be conducted at most every three hours to capture the temporal evolution of the diffetent sea states.
Once in-situ measurements are recorded, the evolution of sea states and their analysis can be determined using the zero-crossing or spectral analysis.

2.2.1. ZERO-CROSSING ANALYSIS

The zero-crossing method is based on the identification and analysis of apparent waves, i.e. the waves identified by two consecutive crossings of the mean sea level which occur strictly in the same direction [33, 34]. To apply the method it is necessary to define a reference level equivalent to the average level of the free surface elevation. The method involves identifying all (upward or downward) crossings of the sea elevation with respect to the average level. Using upward crossings, the analysis is called *upward-zero crossing*, using downward crossings, it is called *downward-zero crossing*. The downward-zero crossing analysis is the most used one, however, the basic methodology is similar in the case of the downward-zero crossing one. Then, the apparent waves are identified within two successive crossings of the mean level downwards. The Fig. 2.2 provides a representation of the of the two versions of the method.

For each wave, the *wave height* (H), which is the vertical distance between the highest and lowest surface elevation in a wave, can be determined. The *wave period* (T), on the other hand, is defined as the time interval between two successive crossings. The statistical sample of the apparent waves therefore becomes the set of N pairs of H and T values. To statistically evaluate the sea state, it is necessary to sort the sample of waves by height in decreasing order, keeping each corresponding period associated. Then the *significant wave height* ($H_{1/3}$) is defined as the arithmetic mean of the heights of the highest waves, representing 33% of the record. Its formulation is:

$$H_{1/3} = \frac{1}{N/3} \sum_{j=1}^{N/3} H_j \tag{2.1}$$

where $N/3$ corresponds to the total share of 33% of highest waves and j is the index of these waves.
The value of $H_{1/3}$ does not represent the height of any wave observed, but represents a statistical measure that reflects the severity of the sea state. Consequently, WECs are designed not to operate with respect to individual waves but to address a sea state defined by such statistical analysis.
The *significant wave period* ($T_{1/3}$) is defined as the average period of the highest one-third of waves, emphasizing the direct relationship with the significant height, and it

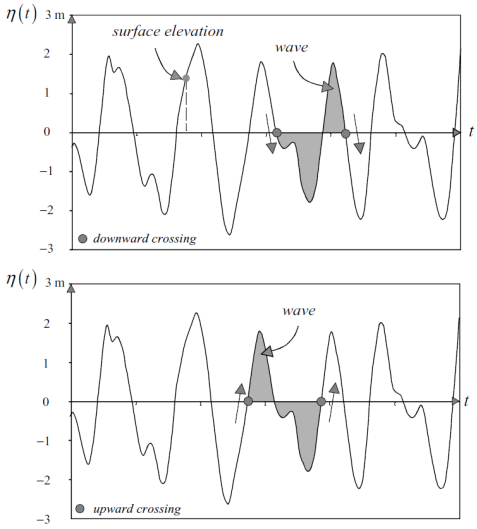

Figure 2.2: The "wave" definition based on a time record of surface elevation using the downward (top panel) or upward (bottom panel) zero crossing method [24]

reads:

$$T_{1/3} = \frac{1}{N/3} \sum_{j=1}^{N/3} T_j \tag{2.2}$$

These two parameters, $H_{1/3}$ and $T_{1/3}$, are among the most important ones for describing ocean conditions. Additional parameters, but less important, are H_{max} and T_{max}, i.e. the maximum wave height and the maximum wave period among the recorded waves, respectively. H_m and T_m are the mean wave height and the mean wave period over the recorded waves, respectively. Further parameters describing the directional information of the sea are not obtainable from this method and the spectral analysis is required. These directional parameters are especially important for WECs having a preferred axis for energy capture. Specifically, two aspects are crucial in the conversion of energy from waves. Firstly, some devices have a preferred operational direction and capture maximum energy when the wave direction aligns with this operational orientation [35]. Secondly, although waves have a dominant direction of propagation, not all wave energy follows this direction [36]; this characteristic is the basis of the directional spreading concept. These two aspects will be explored and discussed in detail throughout the thesis.

2.2.2. SPECTRUM ANALYSIS

Describing ocean waves using a spectrum analysis allows the sea surface to be represented as a stochastic process [37]. The elevation of the free surface of the sea can appear extremely irregular, however, this can be analyzed through a *random-phase/amplitude model*, considering the surface elevation as resulting from the combination of an infinite number of monochromatic sine waves, each with its own frequency, amplitude and

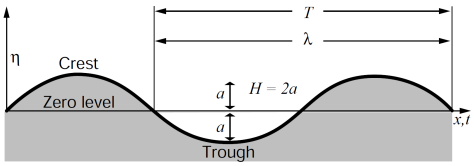

Figure 2.3: An example of a sine wave [38]

direction [38].

In particular, each sine wave can be described by its *frequency* (f), expressed in hertz, which represents the number of crests that pass through a fixed point in one second and corresponds to the inverse of the wave's period (T), stated in seconds. The *amplitude* (a), measured in metres, indicates the maximum displacement from mean sea level, equivalent to half of the wave height. Fig. 2.3 graphically illustrates the parameters described above.

Each frequency and direction that characterizes a sinusoidal component is associated with an amplitude and a phase. The *phase* of a wave (φ), measured in degrees or radians, specifies the position of the wave in its oscillation cycle at a given time, identifying the wave's progress through its complete cycle. Using *Fourier harmonic analysis* [39], it is possible to approximate a real wave with the sum of sine waves. For surface elevations that vary over time and with components moving in the same direction, the model reads:

$$\eta(t) = \sum_{j=1}^{N} a_j \sin(2\pi f_j t + \varphi_j) \tag{2.3}$$

Fig. 2.4 describes the concept of irregular wave generated by the linear superposition of regular waves.

From Fourier analysis, the energy distribution associated at each sea state is obtained. In particular, two distributions can be deduced, depending on whether directional information is considered or not. The distribution of energy over the frequency is known as *frequency spectrum*, denoted as $S(f)$, while the distribution that combines frequency and directional information is called *frequency-directional spectrum*, indicated by $S(f,\theta)$. Depending on the circumstances, it may be advantageous to express the spectrum as a function of the angular frequency ω according to the following relations

$$S(\omega) = \frac{S(f)}{2\pi} \tag{2.4}$$

$$S(\omega,\theta) = \frac{S(f,\theta)}{2\pi} \tag{2.5}$$

where

$$\omega = 2\pi f \tag{2.6}$$

The effect of high-frequency components is typically negligible, and establishing a threshold of N sine wave is a feasible compromise that does not sacrifice reliability. Phases and

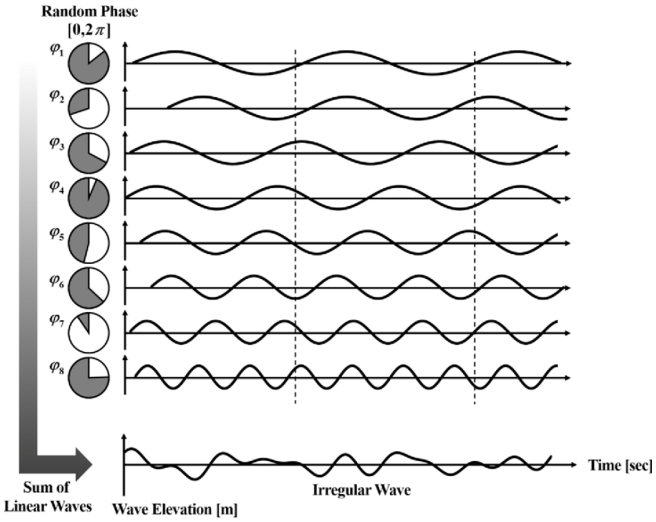

Figure 2.4: An example of an irregular wave generated by the linear superposition of sine waves [40]

amplitudes, being random variables, are completely characterized by their respective probability density functions. In this model, the phase distribution is assumed uniform over [0, 2π], while the amplitude for each frequency follows the Rayleigh distribution and can be computed following:

$$a_{jl} = \sqrt{2S(\omega_j, \theta_l)\Delta\omega\Delta\theta} \tag{2.7}$$

where $\Delta\omega$ and $\Delta\theta$ are the frequency spectrum and directional resolution, respectively. The indices j and l correspond to the $j-th$ and $l-th$ frequency and direction of the wave, respectively.

Despite the irregularity of the waves, both the frequency spectrum and the frequency-directional spectrum present a relative uniformity, evolving slowly in space and time. This coherence, in contrast to the apparent chaotic movement of the sea surface, allows precise and reliable analysis of sea states.

FREQUENCY SPECTRUM

The frequency spectrum describes the distribution of total energy in a sea state over the frequencies. Since a WEC typically is a resonant oscillator device, tailoring a WEC to the frequency spectrum is critical for efficient energy capture.
Wave spectra are typically represented as continuous curves joining discrete points obtained from Fourier analysis. These curves tend to have a general shape, like the one illustrated in Fig 2.5. However, the curve is not always smooth. Irregular seas can generate broad spectra that show multiple peaks, which may be clearly separated from each other or merged into a very broad curve with different reliefs [41] (Fig. 2.6). This occurs when different sea states, such as wind waves and one or more swells, propagate simultaneously in the same marine area. These sea states are called multi-modal. On the contrary,

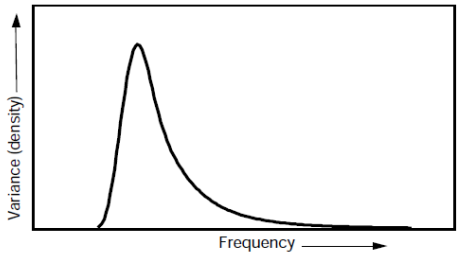

Figure 2.5: Typical frequency spectrum shape for a single system of wind-generated waves [38]

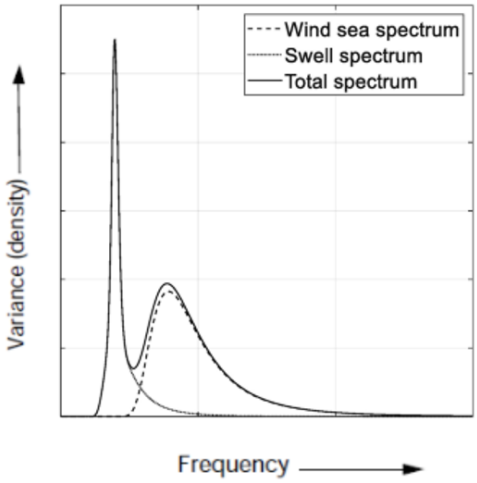

Figure 2.6: Typical frequency spectrum shape for a double system of wind wave and swell

the wave motion resulting from the only swell produces a very narrow spectrum, concentrating the energy in a narrow range of frequencies around a peak value [24].

Through frequency spectral analysis it is possible to obtain a series of synthetic parameters useful to describe the sea states. Indeed, the wave spectrum is a statistical distribution and many of the parameters derived from it are expressed in terms of the moments of the distribution. The n-th moment of order n of the frequency spectrum is defined by the following equation:

$$m_n = \int_0^\infty f^n S(f) df \tag{2.8}$$

The *spectral wave height parameter*, H_{m0}, derived from the spectrum, closely approximates the significant wave height $H_{1/3}$ derived directly from the wave record [42]. It reads:

$$H_{m0} = 4\sqrt{(m_0)} \tag{2.9}$$

The *energy period* (T_{m-10} or T_e), so-called for its role in computing wave power, describes the energy in the irregular wave train and gives an indication of how a WEC might perform in sea conditions. It reads:

$$T_{m-10} = \frac{m_{-1}}{m_0} \tag{2.10}$$

The *peak period* (T_p) describes the dominant wave system in a given sea state corresponding to the value of the period at the peak of the spectrum. Accordingly, the following condition must be verified:

$$S(f_p) = max(S(f)) \tag{2.11}$$

where the parameter f_p corresponds to the peak frequency and, consequently, is equivalent to the inverse of T_p.

The parameter T_{m01} is the wave period theoretically equivalent with mean period computed through the zero-crossing analysis.

$$T_{m01} = \frac{m_0}{m_1} \tag{2.12}$$

The relative spreading of the energy over the frequency, ϵ_0, often called the *spectral width*, can be defined as the standard deviation of the frequency spectrum, as suggested in [43]. This measure is normalized by the energy period, which provides a relative measure of the spread of energy across the frequency. It reads:

$$\epsilon_0 = \sqrt{\frac{m_0 m_{-2}}{m_{-1}^2} - 1} \tag{2.13}$$

It is important to understand that, under the principle of linear superposition, the power of each individual wave can be assessed independently and then aggregated to determine the total average wave power density. Therefore, when analyzing a single sine wave component, the wave power can be calculated by:

$$P(f) = \rho g S(f) c_g(f) \tag{2.14}$$

where c_g is group velocity, that is the velocity at which the energy is propagating [44] and is given by:

$$c_g(f) = \frac{\pi f}{k}\left(1 + \frac{2kh}{\sinh(2kh)}\right) \tag{2.15}$$

where h is water depth and k is the wavenumeber, providing a cyclic measure of the number of crests per unit distance.
Under linearity assumption, the mean wave power can be determined by integrating of the wave power of each individual sine component:

$$P = \int_0^\infty \rho g S(f) \frac{\pi f}{k} \left(1 + \frac{2kh}{\sinh(2kh)}\right) df \tag{2.16}$$

Corresponding to

$$P = \frac{\rho g^2}{64\pi} H_{m0}^2 T_{m-10} \tag{2.17}$$

This formulation is generally approximated [38] with

$$P = 0.49 H_{m0}^2 T_{m-10} \tag{2.18}$$

Typically, a wave field consists of various wave systems, and its spectrum features several peaks. These formulations are only valuable in uni-modal sea state conditions, when only one wave train occur. When sea states are bi-modal or multi-modal, it would be essential to pre-process the spectral information partitioning the spectrum in order to isolate the different sea state components. This spectrum partitioning is addressed in the 2.4 section.

FREQUENCY-DIRECTIONAL SPECTRUM

To describe the three-dimensional moving waves, the frequency-direction spectrum S(f, θ), also known as the multidirectional wave spectrum, must be used. It describes how the wave energy is distributed over the frequency (f) and the propagation direction (θ) (Fig. 2.7).

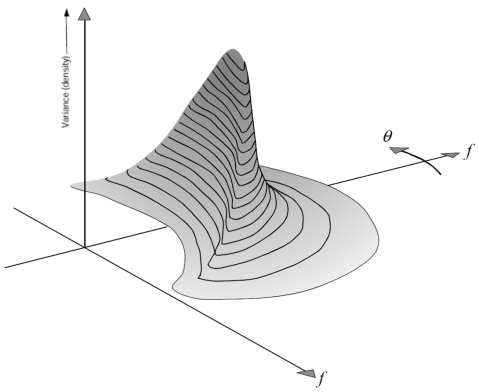

Figure 2.7: Typical frequency-directioanl spectrum shape for a single system of wind-generated waves

When the wind begins to blow, at first short waves are generated. These quickly grow and the wave system formed consists of waves of various heights, periods and directions. As the wind diminishes, or as waves move into regions with significantly lower wind speeds, they transform into swell. The shorter waves dissipate, while the swell waves persist and travel until they reach a coastline. If the wind direction changes significantly, again the existing wave system becomes swell, and a new wave system forming over it. Only the frequency-directional spectrum provides a complete statistical description of the uni-modal and multi-modal sea states.
The frequency and frequency-directional spectra are linked by a simple relation:

$$S(f,\theta) = S(f)D(f;\theta) \tag{2.19}$$

where $D(f;\theta)$ is the *directional distribution*, that is a frequency-dependence and normalized function such that its integral over the direction is unity. This establishes that:

$$\int_0^{2\pi} D(f,\theta)d\theta = 1 \tag{2.20}$$

The condition of Eq. 2.20 is easily verified:

$$\int_0^{2\pi} D(f,\theta)d\theta = \int_0^{2\pi} \frac{E(f,\theta)}{E(f)}d\theta = \frac{\int_0^{2\pi} E(f,\theta)}{E(f)} = \frac{E(f)}{E(f)} = 1 \tag{2.21}$$

It should be emphasized that each frequency can have a different directional distribution. This variability highlights the complex dynamics of wave behavior.

Through the frequency-directional spectrum it is possible to obtain synthetic parameters that completely describe the sea state. Unlike the frequency spectrum, in fact, in addition to the spectral significant wave height and different period variables, directional information can also be deduced. This feature is very important since, for most oceanographic applications, it is inconvenient to describe a sea state by only two variables. In the case of frequency-directional spectrum, the formulation for the n-th moment spectral becomes:

$$m_n = \int_0^{\infty}\int_0^{2\pi} f^n S(f,\theta)df d\theta \tag{2.22}$$

Consequently, H_{m0}, T_{m-10}, T_{m01}, and ϵ_0 can be calculated on the basis of Eq. 2.9, 2.10, 2.12, and 2.13, respectively, and considering n-th moment provided be Eq. 2.22
The *peak period*, similarly to the case of frequency spectrum, can be deduced as the period corresponding to the peak of the spectrum $S(f,\theta)$. Then the following condition must be verified:

$$S(f_p,\theta) = max(S(f,\theta)) \tag{2.23}$$

Among the main directional parameters there are the mean wave direction, the directional spreading and the peak direction. The *mean wave direction* (θ_m), as proposed by Kuik in [45], may be obtained from the frequency-directional spectrum by:

$$\theta_m(f) = \arctan\left(\frac{\int_0^{2\pi}\sin(\theta)S(f,\theta)d\theta}{\int_0^{2\pi}\cos(\theta)S(f,\theta)d\theta}\right) \tag{2.24}$$

The *directional spreading*, as defined in [45], corresponds to the standard deviation of the spectral width and it reads:

$$\sigma_\theta(f) = \sqrt{2\left[1-\sqrt{\left(\int_0^{2\pi}\cos\theta S(f,\theta)d\theta\right)^2+\left(\int_0^{2\pi}\sin\theta S(f,\theta)d\theta\right)^2}\right]} \tag{2.25}$$

Moreover, the frequency-directional spectrum can be used to calculate *directionally resolved wave power density* P_θ, whitch is a key parameter defining the wave power propagation in a particular direction. It has the form:

$$P_\theta = \rho g \int_{-\pi}^{+\pi}\int_0^{\infty} S(f,\theta)c_g(f)\cos(\theta_{inv}-\theta)\delta\, d\theta\, df \tag{2.26}$$

where θ_{inv} is the direction investigated, object of analysis, and δ is a parameters to state that only wave power with a positive contribution to the directionally resolved wave power, according to [46]. It is reads:

$$\delta = \begin{cases} 1 & \text{for } \cos(\theta_{inv}-\theta) \geq 0 \\ 0 & \text{for } \cos(\theta_{inv}-\theta) < 0 \end{cases} \tag{2.27}$$

The direction θ_{inv} for which the maximum value of P_θ ($P_{\theta_{J_{\max}}}$) is obtained should be considered as the *direction of the maximum directionally resolved wave power* ($\theta_{P_{max}}$). This value can therefore be calculated by varying the parameter θ_{inv} within $[0, 2\pi]$ and identifying its maximum value.

It is important to restate that these formulations, as in the case of the frequency spectrum, are only valid for uni-modal sea states. In situations where there is an overlap of different sea states it is necessary to pre-process the spectral information to obtain, through the partitioning process, the spectra corresponding to each single coexisting sea state. The treatise of the partition of spectra is discussed in the 2.4 section.

2.3. SPECTRUM MODELS FOR UNI-MODAL AND MULTI-MODAL SEA STATES

MULTI-MODAL sea states describe intricate oceanographic scenarios in which various wave systems coexist and interact within the same maritime region. In fact, wave formations often derive from the interaction of locally generated wind waves with swell originating from one or more distant locations.
According to [47, 48], a bi-modal maritime state could synthesize the most challenging marine conditions encountered by sea defenses, beaches, offshore structures, small vessel operations, and naval passages near port entrances.

Several studies [49, 50, 51] have indicated that the probability of encountering bi-modal spectra varies between 10% and 30%. However, this frequency may increase depending on specific sea conditions and measurement locations.
In this context, data combining wind wave and swell characteristics are represented through a frequency-directional spectrum, showing double-peaked waves. This phenomenon is described by the following equation:

$$S(f,\theta) = S_{windwave}(f,\theta) + S_{swell}(f,\theta) \tag{2.28}$$

By analyzing exclusively the frequency spectrum the situation is simplified and the one-dimensional spectrum can be expressed as:

$$S(f) = S_{windwave}(f) + S_{swell}(f) \tag{2.29}$$

In this scenario the spectrum includes the sum of the frequency components of the wind waves and swell, without considering their respective directional information. This approach is useful in analyzes where wave directionality is of lesser relevance or difficult to determine.
Numerous studies have focused on determining typical shapes of frequency and frequency-directional spectrum. The objective was to estimate of the entire wave spectrum from known values of a limited number of parameters such as the significant wave height and wave period.

If the sea state is bi-modal, it is possible to reproduce its frequency spectrum directly through mathematical formulations. Alternatively, in the case of bi-modal or multi-modal spectra, it is possible to deduce the frequency-directional spectrum by summing the frequency-directional spectra relating to the different sea states. This technique allows us to obtain an accurate representation of the distribution of sea wave energy as a function of direction and frequency. Combining the directional spectra of various sea states allows complex marine conditions to be precisely modeled, providing a detailed view of the wave characteristics present in a given area. Furthermore, analysis of bi-modal or multi-modal spectra can help identify and distinguish the influences of different wave systems, such as waves generated by local wind and swell waves from distant storms, improving the understanding of ocean dynamics.

2.3.1. FREQUENCY SPECTRUM MODEL FOR UNI-MODAL SEA STATES

Numerous models have been proposed to reconstruct the frequency spectrum for uni-modal maritime states. These models aim to capture the distribution of wave energy over different frequencies in scenarios where the sea state is predominantly characterized by a single wave mode. Uni-modal maritime states are those in which a dominant wave system prevails, while the other wave components are relatively minor in comparison. Such models can be applied to determine fully developed sea states or waves in a growing phase.

The *Pierson and Moskowitz* [52] proposed an empirical form for the entire spectrum, based on fully developed sea states. The empirical formulation reads:

$$S_{Pierson-Moskowitz}(f) = \alpha_{PM} g^2 (2\pi)^{-4} f^{-5} exp\left[-\frac{5}{4}\left(\frac{f}{f_p}\right)^{-4}\right] \tag{2.30}$$

where α_{PM} is the energy scale parameter.

The *Bretschneider* spectrum [53], also know as ISSC or Modified Pierson-Moskowits (MPM) spectrum, is used for open seas without limits of fetch, i.g. the portion of the sea over which the wind is blowing, or wind blow duration [54], as the Pierson-Moskowitz one.

$$S_{Bretschneider}(f) = \frac{5}{16} H_S^2 f_p^4 f^{-5} exp\left[-\frac{5}{4}\left(\frac{f}{f_p}\right)^{-4}\right] \tag{2.31}$$

It was soon realized that at in fetch-limited conditions, i.e. where wave growth under a steady offshore wind was limited by the distance from the shore, the spectral shapes can differ significantly [55].
The *JONSWAP* (Joint North Sea Wave Project) [56] spectrum is often used to describe waves in a growing phase. Data were collected during a meteorologial experiment in the North Sea and from these observations gave a bit of different description of the wave spectra shape. A peak enhancement paramter was added to the Pierson-Moskowitz formulation, obtaining:

$$S_{JONSWAP}(f) = \alpha_{PM} g^2 (2\pi)^{-4} f^{-5} exp\left[-\frac{5}{4}\left(\frac{f}{f_p}\right)^{-4}\right] \gamma^{exp[-\frac{1}{2}(\frac{f/f_p-1}{\epsilon_0})^2]} \tag{2.32}$$

The parameter ϵ_0 corresponds with the spectral width over the frequency, γ is the peak enhancement parameter which regulates the degree of energy concentration around the peak frequency and A_γ is a normalizing factor. The γ formulation follows:

$$\gamma = \begin{cases} 5 & \text{for} \quad \frac{T_p}{\sqrt{H_s}} \leq 3.6 \\ \exp\left(5.75 - 1.15\frac{T_p}{\sqrt{H_s}}\right) & \text{for} \quad 3.6 < \frac{T_p}{\sqrt{H_s}} < 5 \\ 1 & \text{for} \quad 5 \leq \frac{T_p}{\sqrt{H_s}} \end{cases} \tag{2.33}$$

and

$$A_\gamma = 1 - 0.287 \ln(\gamma) \tag{2.34}$$

If γ is equal to 1, then the spectrum is a Pierson-Moskowitz spectrum, otherwise, for high values of γ (> 3.3) indicate very narrow spectra, in which most of the wave energy is concentrated around the peak frequency. On the contrary, lower values of γ (< than 3.3) represent sea states with greater variability in wave frequency.

2.3.2. FREQUENCY SPECTRUM MODEL FOR BI-MODAL SEA STATES

Because oceans and seas are characterized by a wide range of dynamic and changing conditions, it is common to encounter sea states that are not limited to a single wave mode, but can be bi-modal or even multi-modal.
Given the complexity of such situations, several formulations and methodologies have been proposed to model and analyze wave spectra more accurately and in detail.

Ochi and Hubble [57] provide the most probable spectrum with a 95% confidence limit for a given significant wave height [58]. They formulated a double-peak spectral model where the resulting spectrum is represented as the sum of two distributions, each corresponding to a sea state:

$$S_{Ochi-Hubble}(f) = \sum_{j=1}^{2} \frac{H_{s_j}^2 T_{p_j} (\lambda_j + 0.25)^{\lambda_j}}{4\Gamma(\lambda_j) T_{p_j}^{(4\lambda_j+1)}} exp\left(-\frac{\lambda_j + 0.25}{T_{p_j}^4 f^4}\right) \tag{2.35}$$

where $\Gamma(.)$ is the gamma function and the j is an index used to define the sea state system. For $j = 1$ we are referring to swell sea system and for $j = 2$ we are referring to wind sea. The calculation of this spectrum requires the knowledge of three parameters: significant wave height (H_s), spectral peak period (f_p), and the shape factor (λ). In particlular, λ corresponds to:

$$\lambda_j = \begin{cases} 3 & \text{for } j = 1 \\ 1.54 \exp(-0.062 H_s) & \text{for } j = 2 \end{cases} \tag{2.36}$$

2.3.3. DIRECTIONAL SPECTRUM MODEL FOR UNI-MODAL SEA STATES

Similar to frequency spectra, various studies have been conducted to develop mathematical formulations that can provide directional spectra in the absence of direct measurements, using only synthetic parameters instead.
The analytic shapes of the directional spectrum are grounded in the principle that directional distributions can be treated as probability distributions of an angular variable, applying theories used for angular probability distributions [59]. Since waves take energy from the wind, it is usually supposed that this distribution has a maximum in the wind direction and that it falls off gradually to the offwind directions.

Mitsuyasu [60] proposed a formulation for directional distribution based on measurements of directional wave spectra recorded at offshore locations in the Japan Sea and the Pacific Ocean. From the collected data, the directional distribution was estimated. The Mitsuyasu's directional distribution takes the following form:

$$D(f,\theta)_{Mitsuyasu} = A(s) cos^{2s}\left(\frac{\theta - \theta_m}{2}\right) \tag{2.37}$$

where the parameter A, depending on s, is the directional dispersion parameter that cor-

responds to the normalization factor that guarantees that Eq. 2.20 is satisfied. It reads:

$$A(s) = \frac{\Gamma(s+1)}{\Gamma(s+\frac{1}{2})2\sqrt{\pi}} \tag{2.38}$$

To determine the parameter s the Mitsuyasu's formulation proposes the following parametrization:

$$s_{Mitsuyasu} = \begin{cases} s_p\left(\frac{f}{f_p}\right)^5 & f < f_p \\ s_p\left(\frac{f}{f_p}\right)^{-2.5} & f \geq f_p \end{cases} \tag{2.39}$$

where the parameter s_p is given by:

$$s_p = 11.5\left(\frac{U_{10}}{c_p}\right)^{-2.5} \tag{2.40}$$

U_{10} corresponds to the value of the wind speed at 10 m above sea level and c_p is the deep water phase speed at the spectral peak and it reads:

$$c_p = \frac{g}{2\pi f_p} \tag{2.41}$$

From the analysis of data recorded during the JONSWAP experiment, *Hasselmann* [61] used the measurements obtained from in-situ campaign to propose an expression for s, which reads:

$$s_{Hasselman} = \begin{cases} 6.97\left(\frac{f}{f_p}\right)^{4.06} & \text{f} < 1.05\ f_p \\ 9.77\left(\frac{f}{f_p}\right)^{\mu} & \text{f} \geq 1.05\ f_p \end{cases} \tag{2.42}$$

where the parameter μ is dependent on the age of the waves as follows:

$$\mu = -2.33 - 1.45\left(\frac{U_{10}}{C_p} - 1.17\right) \tag{2.43}$$

A further formulation of the directional distribution is given by *Donelan* [62], also based on recorded data. Unlike the measurements made by Mitsuyasu and Hasselmann, the data used by Donelan came from waves recorded in Lake Ontario and from an experimental campaign performed in the laboratory. The directional distribution proposed by Donelan is:

$$D_{Donelan}(f,\theta) = \frac{1}{2}\beta sech^2\left\lfloor\beta(\theta-\theta_m)\right\rfloor \tag{2.44}$$

where

$$\beta_{Donelan} = \begin{cases} 2.61\left(\frac{f}{f_p}\right)^{1.3} & 0.56 \leq \frac{f}{f_p} < 0.95 \\ 2.28\left(\frac{f}{f_p}\right)^{-1.3} & 0.95 \leq \frac{f}{f_p} < 1.6 \\ 1.24 & 1.6 \leq \frac{f}{f_p} \end{cases} \tag{2.45}$$

Banner [63] suggested an alternative formulation for the parameter β proposed by Donnelan, assuming that it varies also when the ratio between f and f_p is less than 1.6. The *Donelan–Banner* distribution consists of the Donelan distribution and the Banner definition for β, which reads:

$$\beta_{Banner} = \begin{cases} 2.61\left(\frac{f}{f_p}\right)^{1.3} & 0.56 \leq \frac{f}{f_p} < 0.95 \\ 2.28\left(\frac{f}{f_p}\right)^{-1.3} & 0.95 \leq \frac{f}{f_p} < 1.6 \\ 10^{\left(-0.4+0.8393\exp\left[-0.567\ln\left(\frac{f}{f_p}\right)^2\right]\right)} & 1.6 \leq \frac{f}{f_p} \end{cases} \tag{2.46}$$

2.4. WAVE SPECTRUM PARTITIONING TECHNIQUES

ACCURATELY understanding and modeling the various components of waves is fundamental to improving the design and management of maritime and coastal structures, thus strengthening their safety and effectiveness in the complex marine dynamics. To this end, it is essential to use partitioning techniques, delineating the components related to wind waves from those of swell. These spectral analysis techniques are generally classified into one-dimensional (1D) and two-dimensional (2D) approaches.

2.4.1. ONE-DIMENSIONAL PARTITIONING TECHNIQUES

The 1D approach, due to its practicality, is the most widespread and involves the partitioning wave spectrum based on the frequency. This entails associating lower frequencies with waves generated by swell and higher frequencies with wind waves. Such methods can rely solely on the wave frequency spectrum or incorporate wind speed data, offering a more comprehensive analysis.

Earle [48] proposed a method for partitioning the spectrum based on the idea that wind waves and swells are characterized by different energy distribution over the frequencies, with wind waves having a higher frequency range and swells lower frequency range. The partition is then based on the partitioning frequency (f_s) parameter as follows:

$$f_s = 0.8 f_{PM} \tag{2.47}$$

where f_{PM} is the peak frequency of the Pierson-Moskowitz spectrum and corresponds to:

$$f_{PM} = 0.13 \frac{g}{U_{10}} \tag{2.48}$$

Based on the wave frequency spectrum observed by in-situ instruments, *Wang and Hwang* [64] derive a formulation based on the wave steepness, defined as the ratio between the significant wave height and the wavelength. The frequency value used for the partitioning is mainly influenced by shorter waves, on the contrary, the contribution of the swell components, characterized by longer wavelengths, is almost negligible [65]. As a result, the peak of the wave steepness function aligns closely with the peak of the wind sea. This offers a practical means of delineating wave and wind components without relying on wind data. It reads:

$$f_s = 4.112 f_m^{1.746} \tag{2.49}$$

where f_m is the peak of the steepness function $\alpha(f_*)$ at frequency f_*, having the following formulation:

$$\alpha(f_*) = \frac{8\pi \left[\int_{f_*}^{fmax} f^2 S(f) df \right]}{g \left[\left(\int_{f_*}^{fmax} S(f) df \right]^{\frac{1}{2}} \right.} \tag{2.50}$$

whit f_{max} as upper frequency limit of the spectrum.

Portilla et al. [66] formulated the spectrum partitioning model on the basis of the depression existing between the two adjacent peaks in the spectrum, considering this depression as the boundary of the wave systems. In this way, the wind wave and swell could be separated. The proposed partitioning technique is based on the value assumed by the coefficient λ. Its formulation is:

$$\lambda = \frac{S(f_p)}{S_{PM}(f_p)} \tag{2.51}$$

where $S(.)$ is the measured wave spectrum and $S_{PM}(.)$ is the Pierson-Moskowitz spectrum, both calculated at the peak frequency f_p.
In particular, the technique suggests that the wave system is a wind wave when λ >1, otherwise the wave system is a swell. The assumption underlying the formulation is that the wind wave spectrum will exceed the corresponding PM spectrum before reaching the fully developed state.

2.4.2. TWO-DIMENSIONAL PARTITIONING TECHNIQUES

The first 2D partitioning algorithm was presented by Gerling in [67], offering greater accuracy than the 1D approach. This method simultaneously exploits wind vector information and wave frequency-directional spectra to discriminate between wind waves and swell. Among the algorithms proposed below, Komen's [68] appears to be one of the most

widely adopted.

The two-dimensional partition technique proposed by Komen et al. [68] relies on both the wind vector and the wave directional spectrum, which provides a comprehensive representation of the internal structure of ocean waves in both frequency and direction domains. The formulation established that the wave component can be identified as purely wind-driven, then a wind wave, when the following relationship holds true:

$$\begin{cases} \eta \frac{U_{10}}{c} \cos(\theta - \psi) > 1 \\ |\theta - \psi| < \frac{\pi}{2} \end{cases} \tag{2.52}$$

where c is the phase speed, θ is the wave direction, ψ corresponds to the wind direction and η is a constant equal to 1.3.
Despite its increased accuracy, the practical application of this 2D technique remains limited mainly due to difficulties in acquiring simultaneous measurements of wind vectors and wave directional spectra.

A methodological alternative more suitable for practical applications is represented by the WavSEP method, proposed in [69]. This method partitions the spectrum in the first phase and subsequently categorizes the partitions as wind waves or swells in a second phase. In particular, during the categorization phase, different methodologies can be used, including one that does not require knowledge of the wind speed.
The WavSEP method is based on the idea that the frequency-directional spectrum has a behavior similar to that of topographic surfaces, allowing a partition to be applied by processing the spectral trend as if it were a topographic surface. In particular, the partition is based on a digital watershed image processing algorithm proposed by Vincent and Soille [70], whose applicability for wave analysis is demonstrated in [71]. The spectral frequency-directional surface is then inverted, with the peaks corresponding to the watersheds of the topographic surfaces. In this case, the partition boundaries coincide with the watershed lines derivable using the approach proposed in [70]. In particular, the approach consists in imagining progressively filling the river basins and building dams at the watershed points, i.e. at the points that separate two adjacent river basins. Applying this procedure, each minimum is completely circumscribed by dams that delimit the associated catchment area. The subdivision of the different river basins, here assumed as the subdivision of the spectra, is made up of the dams themselves.
Subsequently, each partition can be categorized as wind wave or swell based on the partitioning frequency (f_s) parameter according to [48] or [64].
This algorithm is implemented in the Wavewatch III numerical wave propagation model code [72] to perform spectrum partitioning and a set of Matlab functions are delivered through GitHub with a free GNU General Public License [73].

2.5. DICUSSION

THIS chapter establishes a solid theoretical basis for ocean wave analysis, highlighting the importance of a detailed understanding of wave characteristics for the efficient design of WECs. The statistical and spectral analysis techniques described are crucial

to accurately evaluate the energy potential of waves and reduce levels of uncertainty in device design. In particular, the short-term statistical analysis of sea waves represents a fundamental step to understand the temporal evolution of sea states in the site of interest. The determination of synthetic wave parameters allows each sea state to be described, proving essential for the design and optimization of WECs. However, it is equally important to consider long-term statistical analysis to identify extreme environmental conditions that could affect device survivability.
The zero-crossing method and spectral analysis emerge as fundamental techniques for wave analysis. The zero-crossing method, although useful for determining synthetic parameters such as significant wave height and energy period, does not provide directional information. Spectral analysis, on the other hand, allows a more advanced description of ocean waves as stochastic processes, decomposing them into sinusoidal components characterized by frequency, amplitude and direction.
The spectral models discussed in the chapter offer tools for reconstructing the frequency and directional spectrum of waves based on synthetic parameters. Spectrum partitioning techniques, both one-dimensional and two-dimensional, are essential to distinguish between wind waves and swell waves, improving the understanding of the sea states that occur at the site of interest.
These concepts are fundamental for the continuation of the study, which aims to evaluate the performance of the PeWEC in different and complex sea conditions.

2.6. CONCLUSION

THE chapter provides the theoretical and methodological foundations necessary for the analysis of ocean waves, demonstrating that a detailed understanding of wave characteristics is complex and a multitude of approaches are possible.
From this chapter it emerges that the short-term statistical analysis of waves is crucial to determine the synthetic parameters necessary for the description of sea states. However, long-term analysis is equally important to identify extreme environmental conditions that could affect the durability of WECs. Furthermore, spectral analysis is more accurate and versatile than the zero-crossing method, providing a more detailed description of the waves. In particular, the directional variability of the different wave components that constitute the sea states is described in detail through the directional spreading parameter.

3

OCEAN WAVES DATA SOURCES & WAVE ENERGY ASSESSMENT STANDARDS

3.1. INTRODUCTION

MANY stakeholders are associated with ocean observation services who benefit from this information, for example in planning, scientific understanding of the ocean, protection of the marine environment, safety of navigation and evaluation of economic gains. Although each stakeholder has different interests and objectives, the acquisition of marine and environmental parameters is fundamental to their activities. The importance of the available data influences both the methodological approach in wave analysis and the quality of the results obtained. In general though, it is essential that wave data meets several requirements to be considered reliable and useful in the long term. These requirements include:

- *High information content*: this implies that the data should provide a wide range of detailed information, allowing the analysis and extraction of all relevant parameters to understand the wave phenomena. This includes not only information on wave heights and frequencies, but also on wave directions and directional spreading [74, 75].

- *Reliability and precision*: data must be accurate and reliable, ensuring that measurements are consistent and truthful over time. This is essential to plan, design and operate in the marine field safely and effectively [75].

- *Good temporal coverage*: it is important that the data covers a sufficiently long period of time to capture the natural variability of the wave motion in the site under consideration. Adequate temporal coverage allows us to observe and analyze sea-

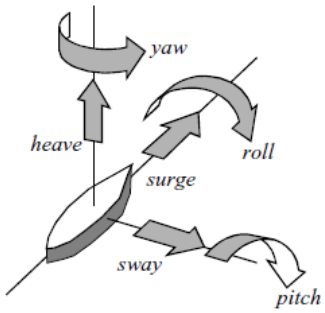

Figure 3.1: The six degrees of freedom of a floating body [77]

sonal variations, extreme events and long-term trends in wave behavior, also due to the effects of climate change.

- *Geographic representativeness*: the data must be relevant and representative for the specific geographical area in which the wave study is conducted. This means that data should be collected from stations or devices strategically placed and representative of site conditions, ensuring that the information obtained is relevant and useful for local wave analysis.

Often no single data source can meet all of these criteria at once. Consequently, it is a common practice combining different data sources, comparing and integrating them, to obtain a complete and reliable overview of the wave phenomenon.

The *in-situ measurements* represent the most accurate and reliable methodology but have the disadvantage of being subject to technical problems and requiring bureaucratic permits for their installation. Furthermore, they are expensive to install and maintain due to harsh marine weather conditions. This data gathering method also affects the total energy cost in offshore renewable energy projects [76]. For these reasons, in-situ instrumentation is sparse in space and, when available, the number of years recorded is often very limited. Furthermore, they describe the environmental conditions and sea states only of the specific installation site and therefore may not provide useful information even at close range. In-situ instruments encompass a variety of operating principles, many of which depend on the wave-induced movements of the device. The movements of a rigid body are described by six degrees of freedom: three translational movements known as surge, sway, and heave, and three rotational movements called pitch, roll, and yaw (Fig. 3.1). Understanding these specific types of motions is crucial for comprehending how sensors that operate on movements, such as those functioning in pitch-heave-roll motion, work effectively.
As for *visual measurements*, although they can be useful for observing and evaluating wave motion from ships at sea in sites where there are no instruments [24], they have little use in the design of Wave Energy Conversion devices (WECs). This is due to the fact that visual observations produce poor dataset, discontinuous in space and time and are

not always compatible with those obtained through instrumental measurements. Visual observations, although simple to make, tend to be approximate compared to instrumental data [38]. For example, visual observations of wave height tend to correspond to significant wave height, but observations of wave period are much less reliable than instrumental ones. Although seafarers are considered expert observers and are able to distinguish multiple wave trains, estimate the height and period of each train, and provide directions of travel of the waves, observations from ships can be affected by location and movement of the ship itself, and therefore may be subject to a certain variability.
Finally, *satellite data* are not yet fully exploited but are generally used for the calibration and validation of numerical wave models [78, 79, 80]. The small number of measurable parameters, the complexity of access and processing, as well as the discontinuous spatial and temporal availability [81], make satellite data particularly promising but not yet fully exploited. In fact, through this observation technique it is possible to collect the significant height of the waves, and other parameters, all over the world, even in areas where the installation of instruments would be unfeasible [82].
It must be notice that, when the measured data are not sufficient or when it is necessary to extend the temporal coverage of the available datasets, the use of *numerical models* represents a valid and widely adopted alternative. These models allow to accurately simulate waves propagation.

3.2. IN-SITU TECHNIQUES

In situ instruments, so named because they can be installed directly on or beneath the sea's surface, or even drill into the surface itself, form an essential part of oceanographic monitoring efforts and wave research. These instruments vary in their configuration and positioning, allowing a wide range of possibilities to choose the appropriate sensor for each case study.
One of the most common types of in situ instruments are floating buoys. Positioned directly on the sea surface providing crucial data on wave patterns. Some buoys can be equipped with additional sensors to also measure other environmental variables, such as temperature, salinity and surface currents.
Other sensors pierce the sea surface, such as wave probe rods. These rods extend from the surface to a point below the surface of the sea.
Other in situ instruments can be mounted on the seabed, such as Acoustic Doppler Current Profilers (ADCPs) providing an accurate assessment of wave characteristics along the vertical water profile.

3.2.1. WAVE BOUYS

One of the most commonly used instruments for open-sea wave measurement is the surface buoy (Fig. 3.2). Typically, a buoy data is processed onboard, and both raw and processed data can be stored or transmitted to shore via radio or satellite link [24]. While buoys generally perform well, they may underestimate short waves and resonate at their natural frequency due to their finite mass and dimensions. Additionally, spherical buoys tend to avoid steep wave parts by rotating around the wave crests, while flat-hulled buoys may even capsize in steep waves [32]. Despite these limitations, buoys are widely used

and perform effectively overall.
Special attention must be paid to mooring design to allow the buoy's free movement without impeding its function. Mooring design should consider the water depth, currents, and wave climate of the deployment site. Typically, at least one section of the moorings is made of elastic material to facilitate the buoy's free movement. Double-anchor mooring configurations may be necessary if the buoy is to be deployed in an area subject to high tidal range and strong currents. A distinction can be made depending on whether the buoy is directional or not.

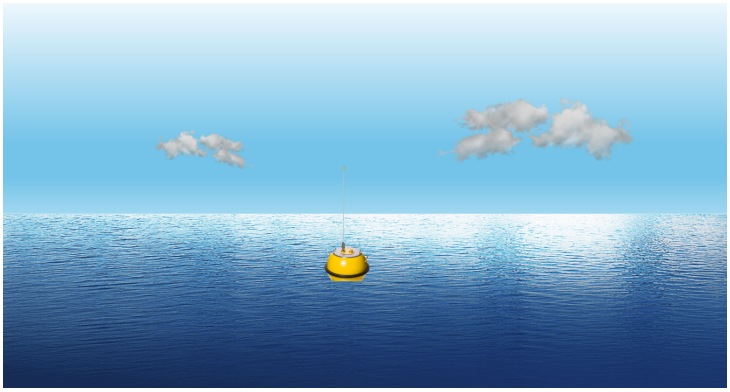

Figure 3.2: An example of wave buoy technique

NON-DIRECTIONAL WAVE BUOY

Non-directional surface instruments are the *accelerometer buoys*, record only the heave motions, representing vertical displacements. By integrating the vertical acceleration twice, these buoys derive the vertical movement and thus the sea surface elevation over time. The most successful non-directional wave buoy is the Datawell Waverider [83], which measures its vertical acceleration on a gravity-stabilized platform.

DIRECTIONAL WAVE BUOY

As for directional surface buoys, two sensors have been developed: the pitch-roll-heave (PRH) buoys and the Displacement buoys.
PRH buoys were first used in the 1960s [84]. They track the slope of the sea surface by measuring the time series of vertical acceleration (heave) and two orthogonal components of the surface slope (pitch and roll). This requires the inclinometer sensors to detect the inclination of the buoy in two orthogonal directions and a sensor to monitor the direction towards true north. The Oceanor Wavescan [85] is the most widely used PRH system. It provides directional wave parameters, sea surface temperature, salinity profiles, and surface current parameters, and it is particularly suitable for measurements in deep waters and areas with strong currents.
Displacement buoys, record their horizontal motion (surge and sway) to identify the directional information. An example of such buoy is the Directional Wavereider by Datawell [83], which employs the Earth's magnetic field to measure the surge and sway motions.

Wave heights and periods can be determined from the analysis of the vertical motion of the buoy, while directional information is obtained from the horizontal displacement of the buoys.

3.2.2. WAVE PROBES

Wave probes are made up of one or more stainless steel rods that exploit the measurement of electrical conductance or capacitance. They are mounted vertically on a fixed platform above water level up to a certain level below the water surface (Fig. 3.3). The level to which the instruments must be submerged is such that one end is always submerged. The wave probes record the temporal evolution of the water surface moving along the measuring rod.

Figure 3.3: An example of resistive wave gauge technique

There are a number of advantages gained by using this device since the probes are robust, easy to calibrate and use [32]. Furthermore, the measurement errors of such instruments are generally small. They depend on the presence of a thin film of water that remains on the rod when the wave attenuates. The water surface is therefore recorded at a slightly higher altitude than the elevation. Like non-directional buoys, these measurement techniques do not provide direction data but it can be otain using an array of wave probes [86]. In this regard, three rods can be positioned in a triangular pattern to obtain information about the direction of the waves.
As a weaknesses there is a decrease in performance in the presence of material on the surface of the water, such as contaminants and oil, which can compromise measurements.
Commonly utilized in experimental campaign, these instruments are less frequently employed in marine environments due to the need for a stable platform and caused by the harsh environments.

CONDUCTANCE WAVE PROBES

The *conductance probes* record the conductance of the exposed part of the rod. In practice, two rods or a rod with a series of electrodes that short-circuit on the surface of the

water are used [32]. These probes are designed on the principle that the electrical conductivity of a medium changes with its composition and ion concentration, which in turn can be used to infer other properties, such as water level.
In typical configurations, conductance probes consist of two rods or a single rod equipped with an array of electrodes. These electrodes are strategically placed along the length of the rod and work by creating a short circuit when they come into contact with the surface of the water. The basic idea is that when the water level reaches the electrodes, an electrical circuit closes between them.

CAPACITIVE WAVE PROBES

The *capacitive probes* measure the electrical capacity of two parallel electrical rods. These probes work on the principle of capacitance, which is the ability of a system to store an electrical charge [32]. Specifically, capacitive level measurement involves two parallel rods that act as electrodes. When the rods are immersed in water, they form a capacitor with the material acting as a dielectric medium between them. The basic principle is that the capacity of this system varies depending on how much the rods are submerged.

3.2.3. ACOUSTIC DOPPLER CURRENT PROFILER

Acoustic Doppler Current Profilers (ADCPs) are instruments used to measure the characteristics of sea waves by emitting sound pulses towards the sea surface and measure the time it takes for the sound to return (Fig. 3.4). By analyzing these travel times and changes in the frequency and amplitude of the reflected sound, the characteristics of the waves can be determined.

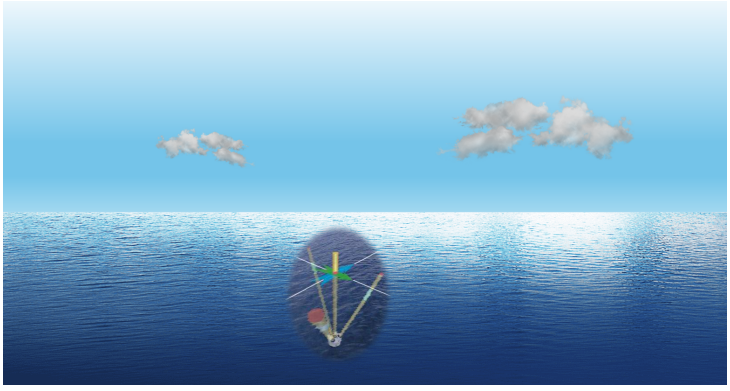

Figure 3.4: An example of ADCP technique

In particular, they measure the speed of water flow through the processing of short sound pulses of known frequency transmitted towards the water surface and by measuring the Doppler shift of the signal reflected towards the sensors [87]. The transmission and reception of acoustic signals generally occurs through 4 transistors which allow the directional spectra to be reconstructed. By means of 3 transistors the flow velocity vector is obtained and the last one provides redundant information for error control [32]. AD-

CPs can be installed on fixed platforms, such as seabeds, or mounted on autonomous underwater vehicles, for more flexible measurements. In both cases they provide a measurement of the flow velocity profile over the entire overlying water column.
It must be kept in mind that as the depth at which the instrument is located increases, the precision and efficiency of the sensor decreases. Typical depth ranges vary between a few meters to a hundred meters. Furthermore, in seas with low suspended particle density, such as in the Tropics, the instrument may provide unreliable measurements as not enough suspended particles are affected by the pulses. Furthermore, measurement errors may exist in the presence of bubbles in turbulent water, such as during breaking waves, or in the presence of schools of fish.

3.3. REMOTE-SENSING TECHNIQUES

REMOTE sensing instruments provide wave information through measurements taken above the sea surface. Such instruments can be installed on an offshore platform, a ship, an aircraft or a satellite. The operating principle, similar to that of ACDP sensors, is based on the reception of signals reflected from the sea surface. Such signals can be visible light, infrared or radar energy. The most important operational difference compared to in-situ techniques is that the recordings do not describe the wave conditions of a fixed point, as for in-situ instruments, but that the sensors interrogate an area of sea, called footprint, and describe its average condition.
Generally, these sensors are not installed in harsh and adverse marine environments. In particular, they are installed in safe environments such as offshore platforms or on satellites. This feature reduces the probability of damage and therefore data loss.

3.3.1. STEREO-PHOTOGRAPHY

Early methods for wave shape measurement relied on *stereo-photography*, where pairs of synchronized photographs were analyzed to reconstruct a 3D map of the sea surface. This technique, pioneered by Schumacher in 1939 [88], involved identifying corresponding points in each image and determining their coordinates. Such images can captured from a single platform, providing insights into localized wave features within a limited area, typically less than 30 m x 30 m. Alternately, a broader coverage can be achieve using pairs of aircraft (Fig. 3.5), [89], facilitating the production of comprehensive directional wave spectra.
Despite effectiveness of this technique, a significant challenge persists due to variable lighting conditions. To address this, alternative approaches have been explored, including the use of infrared or polarization cameras. These advanced technologies, offer promising solutions by mitigating the impact of lighting variations and enhancing texture for more reliable correlation analysis [90].

3.3.2. HIGH FREQUENCY RADAR

High frequency radar, also called *HR radar*, is a system that exploits the radio wave band with frequencies between 3 and 30 MHz and wavelengths from 10 to 100 meters [32]. They were designed mainly to measure surface currents over large areas of sea but also

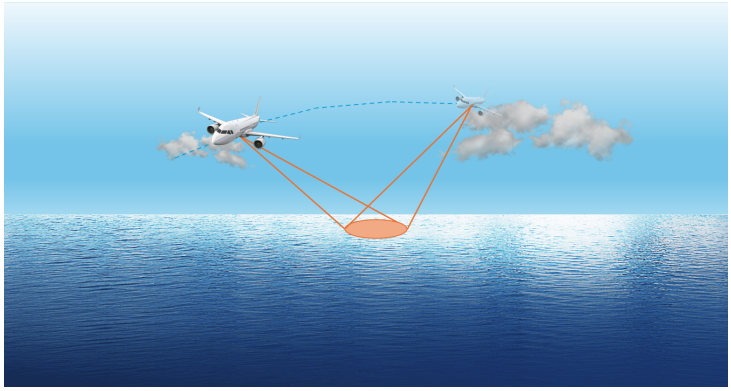

Figure 3.5: An example of stereo-photography technique

allow the description of waves. This type of instrument can be installed on coasts, offshore platforms (Fig. 3.6) or ships and one of its main characteristics is the ability to reach considerable distances, up to 200 km of range, allowing the monitoring of large marine areas.

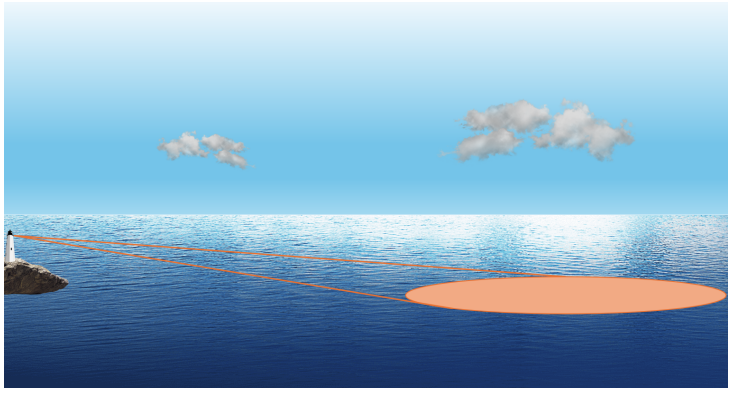

Figure 3.6: An example of HR radar technique

Furthermore, thanks to the triangulation between two or more distant stations, it is possible to generate detailed maps of marine currents and directional spectra.
Although HF radar installations require a significant initial investment to purchase and install, operation and maintenance costs are generally lower than offshore operations [32]. Furthermore, thanks to the permanent connection to electrical and communications networks, HF radars are generally more reliable than marine alternatives.

3.3.3. SATELLITE

While traditional wave recorders retain an important role for detailed short-term observations in specific coastal or shallow water areas, *satellite technology* offers broad spa-

tial coverage and valuable long-term data. Indeed, wave measurement through satellite technologies represents a notable advance compared to traditional methods, as it offers global spatial coverage [91].

The first satellite in orbit, Sputnik I [92], was successfully launched on October 4, 1957, marking the beginning of the space age. Since then, numerous space missions have been completed with the support of governments through their space research organizations, such as NASA (National Aeronautics and Space Administration) [93], ESA (European Space Agency) [94], Roscosmos (Russian State Corporation for Space Activity) [95] and CNSA (China National Space Administration) [96].
Satellites typically carry one or more instruments on board and operate across different bands of the electromagnetic spectrum, from visible to microwave wavelengths. This enables simultaneous measurement of a multitude of environmental parameters through various sensors.
A key distinction from traditional wave recorders, which monitor the temporal movement of the water surface at a fixed point, lies in the fact that satellite sensors interrogate a larger zone, providing measurements of average conditions over an entire area (Fig. 3.7).

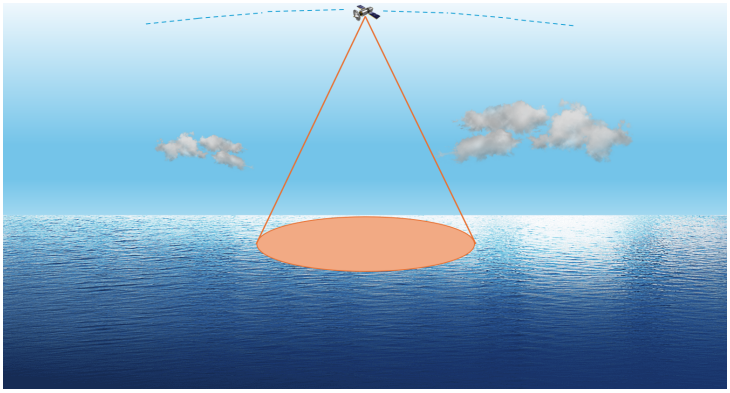

Figure 3.7: An example of active radar sensor technique

Various satellite instruments are employed to observe the ocean surface and measure wave characteristics. These instruments utilize different techniques and technologies to gather valuable data for oceanographic research. In particular, *active radar remote sensing systems* are advanced instruments that play an essential role in acquiring information about wave characteristics. These systems operate by sending a signal and receiving its echo, allowing for the detection and mapping of various attributes of the observed environment. The most significant advantage of these radars is their ability to operate effectively at any time, both day and night, and under any weather conditions, overcoming the limitations of other observation methods that may be impeded by clouds or other adverse weather conditions.
Active radars that measure waves are divided into two main categories: Synthetic Aperture Radar (SAR) and altimeters. *SAR* devices are imaging systems that perform two-

dimensional (2D) measurements. These systems produce reflectivity images that enable detailed mapping of the sea.
On the other hand, *altimeters* are typically used to measure the distance from the land or sea surface to the satellite, providing a one-dimensional (1D) reflectivity profile. Lastly, *SAR altimetry*, also known as delay-Doppler altimetry, is a recent data processing technique in altimetry used to achieve improved spatial resolution in the direction of the satellite's trajectories.

SYNTETIC APERTURE RADAR

The *Synthetic Aperture Radar* (SAR) represents one of the most versatile and useful satellite sensors in the field of oceanography, allowing the measurement of the directional characteristics of ocean wave fields [97]. This instrument is capable of producing high resolution images, from which directional spectra can be derived.
Such images are not direct representations of the surface, but rather raw data that requires complex processing to extract ocean wave information [98]. However, the observation capacity of SAR is limited by a spatial resolution that only makes observations possible on waves with lengths greater than about 50 meters, corresponding to swells [97]. Limitations of spatial resolution can compromise the reliability of measurements, especially in closed seas where waves are shorter and more complex.
The principle of SAR, proposed by Wiley in 1951 [99], exploits the Doppler information coming from the returning echoes in a coordinated manner [100]. In practice, as the sensor moves, it continues to observe the same area from different positions. This method allows the area of interest to be viewed from multiple angles, and the various observations are then combined in a coherent manner to create a composite image. This image offers a detailed and accurate representation of the monitored surface. The use of this principle is particularly effective in oceanography for measuring wave height, as it allows obtaining high-resolution images that show the dynamics of sea surfaces. It is important to note that the specific method used, known as stripmap, means that the radar antenna remains fixed, without orienting itself during data collection. As a result, the angle at which sensor view the target remains constant during the detection process.
Despite spatial and temporal challenges, SAR remains a valuable tool for studying ocean waves in the open ocean, where its ability to detect directional spectra can provide crucial information on sea dynamics. However, the enormous amount of data produced and the costs associated with their processing and transmission still represent significant limitations to the widespread use of SAR for ocean wave observation.

RADAR ALTIMETER

The *radar altimeters* measure the distance from the satellite to the sea surface with an accuracy of a few centimeters [101, 102], allowing the significant height of waves within of the area interrogated by the sensor, i.e. the footprint.
In contrast to other observing systems, the significant wave height is determined directly, without the need for spectral analysis or zero-crossing analysis. Specifically, this technique describes the average marine conditions of the footprint, generally having a footprint radious between 2km and 15km with a spatial resolution between two consecutive

footprint of 7 km [103].
The typical setup involves a radar antenna looking down, at the nadir, towards the sea surface. The operating principle is based on determining the distance, usually referred to as *range*, which is determined by the delay of a radar pulse traveling from the transmitting antenna to the target and back to the receiving antenna [104]. The radar receives echoes first from the crests of the waves and then from the troughs: this difference in travel time between crests and troughs distributes the echoes over time and determines the waveform, i.e., the evolution of the received power over time. The significant wave height is estimated from the leading edge slope of the waveform [105].
It should be noted that for coastal data, validity is not always guaranteed as echoes hitting the mainland compromise the precision and reliability of the measurements. This phenomenon, known as *signal contamination*, can lead to distortions in the data and make it difficult to correctly interpret marine conditions in coastal areas [106].
Moreover, an innovative application of altimetry was developed to overcome the limitations of traditional altimetry. SAR altimetry [107], or delay-Doppler altimetry, was first used in 2010 during the CryoSat-2 mission [108]. It processes altimetric data by exploiting the Doppler effect, which is generated by the relative movements between the satellite and target. This technique allows the spatial resolution of the collected data to be improved, especially in the direction of the satellite's movement, i.e. along-track, reaching 300 m. The transversal resolution, however, remains unchanged. Another advantage concerns the improvement in the precision of the estimated geophysical parameters, higher than conventional altimetry. Furthermore, signal contamination due to proximity to the coast is reduced due to the reduction in spatial resolution. Using SAR altimetry therefore provides a better noise reduction capability in coastal areas.

3.4. NUMERICAL MODEL TECHNIQUES

THE origins of weather forecasting can be traced back to the military needs highlighted during the Crimean War, where a devastating storm led to 38 ships and 3 warships were thus sunk [109]. This induced astronomer Urbain Le Verrier, under the commission of Napoleon III, to explore the potential for predicting such meteorological events. Le Verrier's research laid the groundwork for applying the principles of fluid dynamics and thermodynamics to forecast weather patterns.
Further advancements occurred during World War II when Sverdrup and Munk conducted studies on wave prediction based on statistical analysis of wave heights [110]. However, significant progress in meteorological research awaited the introduction of the wave spectrum concept by Pierson and Marks [111] and the subsequent development of computational technology.
These advancements were not solely aimed at predicting wave conditions but also involved generating statistical data on wave climate. Early spectral models and the first and second-generation models were limited in their interactions and physical terms they accounted for and were based on Miles theory [112]. By the late 1980s, third-generation models were developed [113], offering a comprehensive description of wave physics.
Today, these third-generation numerical wave models continue to be essential for both

hindcasting and forecasting purposes. A well-calibrated and validated wave model is crucial for minimizing uncertainties in assessing both long-term and short-term marine resources. Numerical models remain at the forefront of understanding wave climatology, whether for a specific site, a regional area, or an entire ocean basin. This understanding is crucial for supporting a wide array of activities, including the design and operation of ports, coastal erosion and sediment transport analysis, and the evaluation of wave energy potential. In modeling WECs, knowledge of a long, gap-free, time series is fundamental and the use of modeled data is widely used to meet this need. In fact, sea state information should cover a period of at least 10 years, in order to capture the variability of the resource and conduct statistically robust analyses [114].

All information about the sea state is contained in the energy density spectrum ($E(\sigma,\theta)$), distributing wave energy over radian frequencies (σ) and propagation directions (θ). The third-generation models determine the evolution of the action density in space and time, represented as $N(\sigma,\theta)$=$E(\sigma,\theta)/\sigma$, because, in contrast to energy density, the action one is conserved during propagation along its wave characteristic in the presence of ambient current [115]. Action balance equation, in a non-stationary condition and with spherical coordinates, has the following expression [116]:

$$\frac{\partial N}{\partial t} + \frac{\partial c_\lambda N}{\partial \lambda} + cos^{-1}\varphi \frac{\partial c_\varphi cos\varphi N}{\partial \varphi} + \frac{\partial c_\sigma N}{\partial \sigma} + \frac{\partial \widetilde{c}_\theta N}{\partial \theta} = \frac{S_{tot}}{\sigma} \tag{3.1}$$

where λ is the latitude, φ is the longitude.

The term S_{tot} summarizes the non-conservative source/sink component, encompassing all physical processes that influence the generation, dissipation or redistribution of wave energy at a specific point.

Numerical wave models can be categorized into ocean or coastal models. This differentiation is not deterministic, in fact, each model can be used in a variety of contexts, but it is their computational capacity, efficiency and precision that determine their suitability for specific applications. For example, ocean models are generally designed to handle large areas and open marine conditions, where interactions with the seafloor are less critical. These models, such as the WaveWatch III (WW3) [117] and the WAve Model (WAM) [118], are optimized to simulate large-scale wave dynamics, using global weather data to predict wave movements across entire oceans. For coastal environments, popular models include Simulation Waves Nearshore (SWAN) [116] and MIKE21 [119]. These coastal models are specifically designed to analyze wave dynamics near shorelines, where phenomena such as refraction, diffraction and interaction with structures such as seawalls and reefs play a key role. SWAN, for example, is able to consider the complexity of coastal geometries and the effect of variable seabed. Aside from the MIKE21, most wave models are available in open source format. A complete and detailed overview of the third generation models is available in [120].

3.4.1. WAM

The WAM model, available in open source, specializes in simulating frequency-directional spectra in spherical coordinates, making it ideal for predictions on a global scale or

across large geographical areas. This model considers various phenomena, including the generation of waves by the wind, their propagation and the non-linear interactions between them. Coastal dynamics, however, are examined through a simplified modeling approach.
The current version of WAM is the result of collaborative work carried out by the WAMDI Group [113], an international consortium of researchers in the field of ocean waves.
The model is currently used by several international organizations and agencies, among which the European Center for Medium-Range Weather Forecasts (ECMWF) stands out. The latter developed a customized version of the model, called ECMWAM [121], based on the original WAM structure.

3.4.2. SWAN

The SWAN (Simulating WAves Nearshore) model [122], developed at Delft Technical University in 1999, is an advanced open-source third-generation wave model. This fully frequency-directional spectral model performs simulations of wave generation processes by solving the action balance equation on a nodal grid. It considers crucial factors such as energy transfer from wind to waves, nonlinear interactions between waves, energy dissipation due to breaking, friction with the seabed and other complex physical aspects. SWAN stands out for its ability to specifically analyze interactions with the seabed and for its adaptability to high resolutions, necessary to take bathymetric variations into account. These characteristics make it particularly effective in coastal environments where variable depth leads to breaking waves and the consequent loss of energy.
For its implementation, SWAN involves the definition of a basic grid that represents the bathymetry of the study area. The flexibility in the choice of grids, both in terms of resolution and orientation, allows a detailed approach to physical studies of the interested domain. Nested grids can be used within a coarser main grid to reduce computational load without sacrificing detail and accuracy. These secondary grids use the wave values calculated on the main grid as boundary conditions.
Alternatively, the use of an unstructured grid offers the possibility to adapt the mesh resolution based on the specific geometry of the area, making it ideal for wave propagation near irregular coasts, islands or areas with significant bathymetric variations. Finally, SWAN is applicable in both stationary and non-stationary conditions, using Cartesian coordinates for small scales or spherical coordinates for larger studies.

NUMERICAL MODEL DESCRIPTION

In the SWAN model, the evolution of the action density over space and time is analized and the action balance equation under non-stationary conditions and within spherical coordinates follows the Eq. 3.1.

The non-conservative source/sink term (S_{tot}) is mathematically represented as:

$$S_{tot} = S_{in} + S_{nl3} + S_{nl4} + S_{ds,w} + S_{ds,b} + S_{ds,br} \tag{3.2}$$

here, S_{in} represents the transfer of wind energy to the waves, S_{nls} is associated with triad wave-wave interactions, S_{nl4} corresponds to quadruplet wave-wave interactions, $S_{ds,w}$ accounts for whitecapping dissipation, $S_{ds,b}$ relates to bottom friction dissipation, and

$S_{ds,br}$ pertains to depth-induced breaking dissipation. Below are detailed specifications of the mathematical formulations and assumptions used in the SWAN model.

Prognostic interval

The SWAN model discretizes propagating spectral information within the computational mesh, employing a constant directional resolution and a non-constant resolution for frequency, which adheres to a logarithmic distribution [123]. Regarding frequency discretization, it is imperative to define a cut-in frequency, established as the minimum frequency (f_{min}), and a cut-off frequency, which corresponds to the maximum frequency (f_{max}): these values delineate the prognostic interval of the spectrum within the frequency domain. Within this interval, spectral density can evolve without constraints. Beyond this prognostic range exists the diagnostic range, in which the spectrum is determined by setting frequencies below the cut-in frequency to 0 Hz and introducing a diagnostic tail (f^{-m}) beyond the cut-off frequency. The power of high frequency tail (m) assumes a default value equal to 4 or 5 according to the formulation of physics adopted [124]. Using the Discrete Interaction Approximation (DIA) of Hasselmann [125] the frequency discretization is described by

$$f_i = \begin{cases} 1.1 f_{i-1} & f_{min} \leq f_i \leq f_{max} \\ 0Hz & f_i < f_{min} \\ f^{-m} & f_i > f_{max} \end{cases} \tag{3.3}$$

Fine-tuning the spectral resolution can significantly influence result accuracy contributing to achieving favourable outcomes. In SWAN, the cut-in (f_{min}) and cut-off (f_{max}) frequency values are requested as input and subsequently they are transformed into radian frequency (σ_{min} and σ_{max}, respectively).

Whitecapping

The primary mechanism for dissipating wave energy in open and deep oceans is whitecapping. As waves grow, their slope increases until reaching a critical point where they break. This process is highly nonlinear and limits wave growth. In third-generation wave models, such as SWAN, whitecapping is represented as a sink term in the energy balance equation and formulations are typically grounded in a pulse-based model of Hasselman [126], with Komen [68] and Janssen [127] parametrization. The formulation based on the pulse-based model reads

$$S_{ds,w_{Hasselman}}(\sigma,\theta) = -\Gamma \tilde{\sigma} \frac{k}{\tilde{k}} E(\sigma,\theta) \tag{3.4}$$

here, Γ is a steepness dependent coefficient, k is the wave number, $\tilde{\sigma}$ and $\tilde{k}$ denote a mean radian frequency and a mean wave number, respectively. Where

$$\Gamma = C_{ds} \left| (1-\delta) + \delta \frac{k}{\tilde{k}} \right| \left(\frac{\tilde{s}}{\tilde{s}_{PM}} \right)^p \tag{3.5}$$

here C_{ds} is the coefficient for determining the rate of whitecapping dissipation, δ determines the dependency of the whitecapping on wave number, p is the power of wave

number normalized with the mean wave number, $\widetilde{s}$ is the overall wave steepness and $\widetilde{s}_{PM}$ corresponds to the value of the wave steepness for a Pierson-Moskowitz spectrum. The coefficients C_{ds}, δ and p are tunable and the parametrization provides by Komen establishes $C_{ds} = 2.36 \times 10^{-5}$, $\delta = 1$ and $p = 4$, while Janssen imposes $C_{ds} = 4.10 \times 10^{-5}$, $\delta = 0.5$ and $p = 4$.

Alternatively, multiple formulations for whitecapping are suggested to enhance the precision of SWAN. Rogers [128] introduced a two-stage whitecapping dissipation formulation, which is rooted in intrinsic breakdown related to wave instabilities, expressed by T_1 term, and the dissipation of shorter waves triggered by longer breaking waves, described by T_2 term. The formulation is given as

$$S_{ds,w_{Rogers}}(\sigma,\theta) = T_1(\sigma,\theta) + T_2(\sigma,\theta) \tag{3.6}$$

where

$$T_1(\sigma,\theta) = a_1 A(\sigma) \frac{\sigma}{2\pi} \left\lfloor \frac{E(\sigma) - E_T(\sigma)}{\widetilde{E}(\sigma)} \right\rfloor^{p_1} E(\sigma,\theta) \tag{3.7}$$

and

$$T_2(\sigma,\theta) = a_2 \int_{\sigma_{min}}^{\sigma} \frac{A(\sigma)}{2\pi} \left\lfloor \frac{E(\sigma) - E_T(\sigma)}{\widetilde{E}(\sigma)} \right\rfloor^{p_2} d\sigma E(\sigma,\theta) \tag{3.8}$$

here a_1 and a_2 are coefficients for calibrate the local dissipation term T_1 and cumulative dissipation term T_2, respectively. $A(\sigma)$ is a measure of the narrowness of the directional distribution at radian frequency (σ). $E_T(\sigma)$ is a threshold spectral density, $\widetilde{E}(\sigma)$ is a normalization generic spectral density, which can be either $E(\sigma)$ or $E_T(\sigma)$. The first prognostic radian frequency is σ_{min}, while p_1 and p_2 are the power coefficients controlling strength of dissipation term T_1 and T_2, respectively.

The Westhuysen method [129] represents whitecapping without the dependencies on mean spectral steepness and mean wavenumber, which can be problematic in conditions involving mixed wind sea and swell. This approach is based on experimental results showing that whitecapping is associated with nonlinear hydrodynamics within wave groups. The formulation reads

$$S_{ds,w_{Westhuysen}}(\sigma,\theta) = -C_{ds} \left\lfloor \frac{B(k)}{B_r} \right\rfloor^{\frac{p}{2}} \lfloor tanh(kh) \rfloor^{\frac{2-p_0}{4}} \sqrt{gk} E(\sigma,\theta) \tag{3.9}$$

here the whitecapping parameter C_{ds} accounts to 0.50×10^{-4}, d and g are the water depth and the gravitational acceleration, respectively. $B(k)$ is the azimuthal-integrated spectral saturation, correlated with the probability of wave group-induced breaking, and B_r corresponds to the threshold saturation parameter, while p and p_0 are calibration exponents.

Exponencial wind growth

SWAN provides different formulations for exponential wind grow phenomenon. In general, the process of wind energy transferring to waves is explained by the feedback mechanism as proposed by Miles [112]. This mechanism is exponential and is based on the

concept that wind causes the water surface to descend as the wave crest moves forward and to rise as it moves backward. Consequently, when the sea surface oscillates, pressure variations follow these movements, thereby transferring energy to the wave. This transfer of energy is more effective as the wave amplitude increases. Building upon this mechanism, Janssen [127] explicitly incorporates the interaction between the wind and waves, taking into account roughness length of the sea surface and atmospheric boundary layer effects. The formulation is given as

$$S_{in,exp_{Janssen}}(\sigma,\theta) = max\,[0, cos(\theta-\theta_w)]^2\,\beta\frac{\rho_a}{\rho_w}\left(\frac{U_*}{c_{ph}}\right)^2\sigma E(\sigma,\theta) \tag{3.10}$$

here θ and θ_w depict wave and wind direction, respectively. β is the Miles constant, while ρ_a and ρ_w are the density of air and water. The friction velocity is expressed by U_* and c_{ph} corresponds to the phase speed.

Komen [68] relies on Snyder experimental results [130] and scales this formulation with respect to friction velocity.

$$S_{in,exp_{Komen}}(\sigma,\theta) = max\left[0, 0.25\frac{\rho_a}{\rho_w}\left(28\frac{U_*}{c_{ph}}cos(\theta-\theta_w)-1\right)\right]\sigma E(\sigma,\theta) \tag{3.11}$$

Alternatively, Yan [131] formulation combines the Komen expression with that of experimental results of Plant [132], indicating that the wind-induced wave growth rate varies quadratically with the ratio between friction velocity (U_*) and the phase velocity of waves (c_{ph}). It has the form

$$S_{in,exp_{Yan}} = \left[D\left(\frac{U_*}{c_{ph}}\right)^2 + E\left(\frac{U_*}{c_{ph}}\right) + F\right] cos(\theta-\theta_w)\sigma E(\sigma,\theta) + H\sigma E(\sigma,\theta) \tag{3.12}$$

The parameter values implemented in SWAN are slightly different from those proposed by Yan and they correspond to $D = 4.0\times10^{-2}$, $E = 5.52\times10^{-3}$, $F = 5.2\times10^{-5}$ and $H = -3.02\times10^{-4}$.

Finally, Rogers [128] provides observation-based formulation with three main characteristics: a physical constraint is applied to the total stress, the wind drag coefficient is tunable and the spectral saturation is expressed in terms of wavenumber rather than wave frequency. The formulation assumes the form

$$S_{in,exp_{Rogers}}(\sigma,\theta) = \frac{\rho_a}{\rho_w}G\sqrt{B_n(\sigma)}\sigma W(\sigma,\theta)E(\sigma,\theta) \tag{3.13}$$

here G represents the sheltering coefficient, which factors in the decrease in momentum transfer from the atmosphere to the waves caused by complete airflow separation. $B_n(\sigma)$ corresponds to the spectral saturation and $W(\sigma,\theta)$ describes the wind input. Specifically, the formulation takes into account a negative wind input component, which mitigates wave growth in the portion of the spectrum subject to adverse wind stress. Furthermore, $W(\sigma,\theta)$ is a function of the friction velocity (U_*), which, in turn, depends on the wind drag coefficient (C_d) according to the formula

$$U_* = \sqrt{C_d} U_{10} \tag{3.14}$$

here U_{10} is wind speed at 10 m a.s.l. while C_d assumes varying expressions contingent on the chosen formulation. In accordance with Hwang [133], the wind drag coefficient is only a function of wind speed and is described as

$$C_{d_{Hwang}} = 10^{-4} \left(8.058 + 0.967 U_{10} + 0.016 U_{10}^2\right) \tag{3.15}$$

Alternatively, in Fan [134] C_d is provided as

$$C_{d_{Fan}} = 10^{-3} \left(0.021 + \frac{10.4}{R_w^{1.23} + 1.85}\right) \tag{3.16}$$

here R_w as a dimensionless parameter

$$R_w = ln\left(\frac{zg}{0.2\sqrt{\alpha u_z}}\right) \tag{3.17}$$

here z corresponds to the heigth above the sea level, u_z is the wind speed at a specific z and α represent the high-frequency energy level.

Finally, the ECMWF formulation [113] is given as

$$C_{d_{ECMWF}} = \begin{cases} 1.2875 \times 10^{-3} & U_{10} < 7.5 \frac{m}{s} \\ (0.8 + 0.065 U_{10}) \times 10^{-3} & U_{10} \geq 7.5 \frac{m}{s} \end{cases} \tag{3.18}$$

Linear wind growth

Linear wind growth of waves refers to the process of wave generation, from a sea surface flat, in response to wind. In SWAN, Cavaleri and Malanotte-Rizzoli formulation [86] is implemented and it is based on the resonance mechanism suggested by Phillips [135] for which waves are generated by resonance between propagating wind-induced pressure waves at the water surface. In particular, if the harmonic pressure waves of wind remains in phase with a free harmonic surface wave, then the wind energy is transferred from the pressure wave to the surface wave. The energy input by this mechanism, which contributes to the initial stages of wave growth, varies linearly with time. The formulation is given as

$$S_{in,lin_{Calavalleri}} = \frac{1.5 \times 10^{-3}}{2\pi g^2} U_*^4 max\left[0, cos(\theta - \theta_w)\right]^4 H \tag{3.19}$$

The formulation incorporate the H filter parameter to eliminate wave growth at frequencies lower than the Pierson-Moskowitz frequency [136]

$$H = exp\left\{-\left(\frac{\sigma}{\sigma *_{PM}}\right)^{-4}\right\} \tag{3.20}$$

here $\sigma *_{PM}$ is the peak radian frequency of the fully developed sea state according to Pierson and Moskowitz [52], reformulated in terms of friction velocity.

Bottom friction

Bottom friction pertains to the resistance encountered by water waves as they interact with the seabed in shallow water. The term bottom friction includes all dissipative mechanisms related to the turbulent boundary layer that occur on the bottom, created by the wave-induced movement of the water particle. This phenomenon depends both on the wave field itself and on the characteristics of the seabed. The default model implemented in SWAN is the empirical model of JONSWAP [126], with the following expression

$$S_{bf_{JONSWAP}}(\sigma,\theta) = -C_{bf}\left(\frac{\sigma}{gsinh(kh)}\right)^2 E(\sigma,\theta) \tag{3.21}$$

here C_{bf} is the bottom friction coefficient equal to $0.038 m^2 s^{-3}$ in the JONSWAP formulation. Despite its simplicity, this method appears to perform quite effectively in operational wave models across various scenarios [24].

Triad wave-wave interaction

Triad wave-wave interaction involves the nonlinear interaction of three waves in a shallow water region, where the energy from one wave is transferred to others through resonant interactions. In very shallow water, triad wave-wave interactions transfer the energy from lower frequencies to higher ones, often resulting in higher harmonics. The resonance conditions for three wave components require that the sums of frequencies and wave-number vectors of two freely propagating wave components are equal to the frequency and wave number, respectively, of a third freely propagating wave component. This triad resonance condition is not relevant in deep water but considerable in shallow water, where waves are non-dispersive resulting in an energy transfer and phase-coupling between the wave components involved. The Lumped Triad Approximation (LTA) model, introduced by Eldeberky [137], is implemented in SWAN to compute the evolution of the energy spectrum in shallow water. This model is stochastic and based on the Boussinesq-type deterministic equations [138]. The LTA model includes a source term for triadic wave interactions but does not involve a biphase evolution equation: the biphase of the waves is parameterized on the basis of laboratory observations. The formulation reads

$$S_{nl3}(\sigma,\theta) = S^{+}_{nl3}(\sigma,\theta) + S^{-}_{nl3}(\sigma,\theta) \tag{3.22}$$

The term $S^{+}_{nl3}(\sigma,\theta)$ represents the energy received from radian frequency $\sigma/2$ and the term $S^{-}_{nl3}(\sigma,\theta)$ represents energy lost to radian frequency 2σ. They read as

$$S^{+}_{nl3}(\sigma,\theta) = C_{nl3} c_{ph} c_g \left| sin(\beta_{\sigma_{peak}}) \right| E\left(\frac{\sigma}{2},\theta\right)^2 - 2E\left(\frac{\sigma}{2},\theta\right) E(\sigma,\theta) \tag{3.23}$$

and

$$S^{-}_{nl3}(\sigma,\theta) = -2S^{+}_{nl3}(2\sigma,\theta) \tag{3.24}$$

here c_g is the group velocity and $\beta_{\sigma_{peak}}$ parameterizes the self-interaction of the peak frequency of the biphase components as a function of the local Ursell number [139].

Since $S^{+}_{nl3}(\sigma,\theta)$ assumes only positive values, every wave component within this method gains energy from a component with half its frequency while simultaneously losing energy to a component with twice its frequency. This mechanism guarantees that, within this framework, energy is consistently shifted towards higher frequencies, and there is no return of energy to lower frequencies.

3.5. WAVE DATA PRODUCTS

BASED on specific needs, available time, and economic resources, it is possible to select the most appropriate data source. This choice is essential to ensure that the collected data is suitable for the specific analysis or project. Among various options, a stakeholder can install an in-situ instrument, which entails high costs and long installation times, as well as complex and variable bureaucratic procedures depending on the country. Alternatively, data from pre-existing instruments installed by third parties can be used. This second option can reduce time and costs, but the temporal coverage and location of the dataset may not always align with the user's needs.
Another option is to use data obtained from numerical models implemented either by third parties or in-house. Typically, freely available modeled data offer an hourly temporal resolution, but their spatial resolution is around 50 km [140, 141]. While such data allow for robust statistical analyses based on long time series, they may not meet design standards for accuracy, especially nearshore [142, 143]. These models are generally calibrated and validated using in-situ measurements and satellite observations.
Despite the high accuracy of satellite measurements [144], their reduced temporal resolution, which ranges from several days (e.g. Jason-3 [145]) to a month (e.g. SARAL/Altika [146]), limits their direct usability. Finally, numerical models with high spatial resolution can be employed using commercial data, or by developing an in-house model. This last option allows for the definition of spatial and temporal resolutions tailored to the specific case, as well as the desired temporal coverage of the analysis. However, also numerical model implemented in house requires calibration and validation procedures to ensure its accuracy.

Below is an overview of some of the most widely used open-access datasets from which in-situ, satellite, and modeled data can be obtained.

3.5.1. IN-SITU DATA PRODUCTS

Two distinct open-source datasets of instrumental data are described below. Each dataset covers different oceanographic areas, providing varying geographical coverage. This allows for targeted searches to identify the presence of instrumental data in specific areas of interest. The datasets in question are INSITU_GLO_WAV_DISCRETE_MY_013_045 product and the National Data Buoy Center.

INSITU_GLO_WAV_DISCRETE_MY_013_045 PRODUCT

INSITU_GLO_WAV_DISCRETE_MY_013_045 product provides global validated in-situ measurements [147] obtained mainly from moored buoys and some drifting buoys, i.e. moving with sea currents.

Data validation is carried out through automated procedures, visual inspection, and comparison with other sources, as defined by SeaDataNet [148]. The in-situ instruments distribution of this product are concentrated in the northern hemisphere, specifically in Europe, North America, Japan, and India (Fig. 3.8). In the southern hemisphere, there are some stations in South America and Australia. Coverage in European seas is high, except for the Arctic areas, southern and eastern Mediterranean, and the Black Sea. The time coverage of each instrument is variable and often less than 10 years.

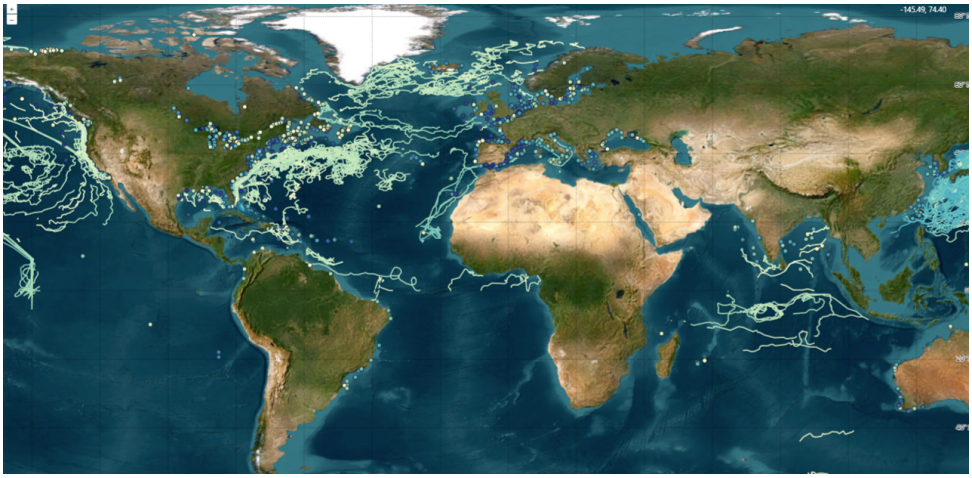

Figure 3.8: In-situ sensors distribution of INSITU_GLO_WAV_DISCRETE_MY_013_045 data product [147]

NATIONAL DATA BUOY CENTER PRODUCT

The National Oceanic and Atmospheric Administration's (NOAA) [149] National Data Buoy Center (NDBC) [150] was established in 1967 to operate and maintain a network of ocean data collection buoys and coastal marine weather stations. This data is open source and available both in real-time and as historical records. The instruments are mainly distributed along the American coasts and along the equatorial belt. Some other stations are located near the North Sea (Fig. 3.9)

Real-time data undergoes an automatic quality control process before publication [151]. The primary user of NDBC's real-time data is the National Weather Service (NWS), which relies on this data to issue alerts, conduct analyses, make forecasts, and initialize numerical models.

Historical data consists of real-time observations that have been accumulated and re-evaluated 45 days after recording. These observations undergo a thorough quality assurance process, including manual review and additional quality checks, before they are archived. Only data that has successfully passed all quality control procedures is included in the historical dataset, ensuring high accuracy and reliability for long-term analyses and research.

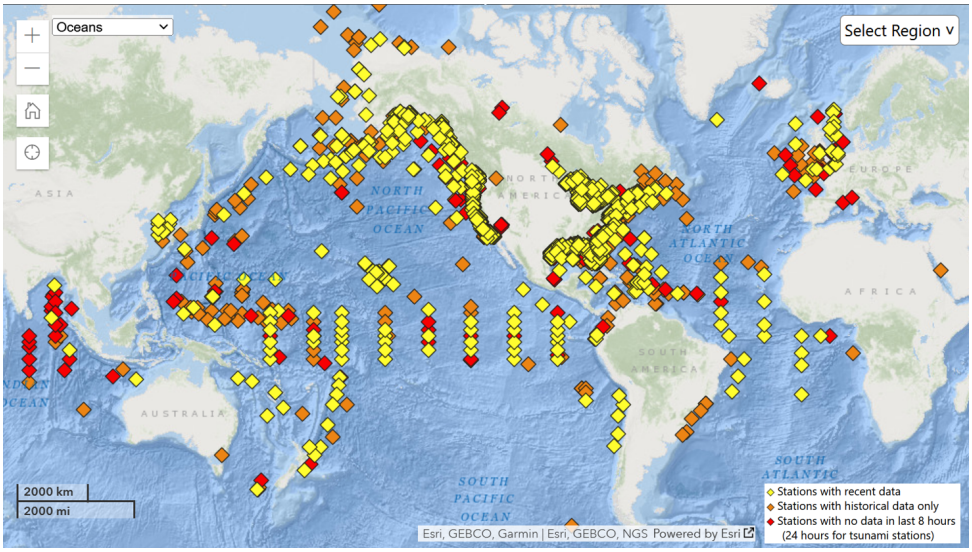

Figure 3.9: In-situ sensors distribution of NDBC data product [150]

3.5.2. SATELLITE DATA PRODUCTS

Generally, the data products resulting from satellite observations are diverse and associated with different levels of data processing:

- *Level-1 (L0):* Raw data resulting from the extraction and decoding of the instrument's source package.
- *Level-1 (L1):* Level-0 data corrected for instrumental effects, with particular attention to date and location variables.
- *Level-2 (L2):* Level-1 data corrected for geophysical effects, with the parameters of interest calculated.
- *Level-3 (L3):* Level-2 data calibrated and validated with in-situ instruments and cross-calibration between different satellite observations.

Usually, only L3 data products are of interest for ocean analyses and numerical model calibration and validation, as they provide corrected and calibrated significant wave height values. The L2 data must be pre-processed before use as they may contain measurement errors, noise and are not calibrated against other satellites and in-situ data.

Several endeavors have been undertaken to generate reliable and cohesive datasets from various altimeter missions [152, 153, 154, 155, 156]. These efforts aim to refine the accuracy and usability of the satellite collected data.
In general, the calibration of satellite data occurs through comparison with in-situ instruments or other satellite measurements recorded in the same location. The in-situ instruments typically considered for the calibration process are positioned at least 50

km from the coast to prevent the satellite return signal from being affected by coastal terrain morphology, which could compromise the measurements. Moreover, satellite measurements recorded in the surrounding area usually have a maximum distance of 100 km from the in-situ instrument and fall within a 30-minute window before and after the in-situ data collection. This allows for comparisons of the same sea state. This procedure is known as *collocation* and ensures that the satellite data is spatially and temporally congruent with the in-situ data. From each collocation, a single satellite data value must be obtained to compare with the in-situ measurements. Different techniques can be used for this purpose. In [157], an extensive sensitivity analysis highlights the impact of the temporal and spatial windows used during the collocation phase. Furthermore, three methodologies are proposed for obtaining the resulting satellite measurement from each collocation. These methodologies include the arithmetic mean of the measurements within the collocation, the linear method of inverse distance weighting (IDW), and distance weighting calculated with a Gaussian function.
The study in [157] investigates the spatial and temporal criteria for the placement of altimetric data, showing that a temporal criterion of 30 minutes and a spatial criterion between 25 km and 50 km produce the best results. Specifically, applying the 25 km spatial criterion leads to slightly better error measurements at the expense of fewer measurements, while increasing the distance results in a larger collocated dataset. Furthermore, the study demonstrates that relying on the single altimeter record closest to the buoy location results in less accurate results than using the temporal and spatial averaging method for collocation.

WAVE_GLO_PHY_SWH_L3_MY_014_005 PRODUCT

WAVE_GLO_PHY_SWH_L3_MY_014_005 [158] is an example of Level-3 significant wave height data product, including several satellite altimeter missions, that are Jason-1 [159], Jason-2 [160], Envisat [161], CryoSat-2 [162], SARAL/AltiKa [146], Jason-3 [145], and CFOSAT [163]. The temporal resolution of the dataset varies depending on the satellite cycle length, for example 10 days for Jason missions [164] and 35 days for SARAL [165]. The temporal coverage of the dataset ranges from 2002 to 2020 but data availability is not constant within this range and varies depending on the satellite considered. The calibration carried forward is a cross-calibration taking the Jason-3 dataset calibrated on instrumental measurements [166] as the reference dataset.In particular, crossover points for calibrations are identified as the intersections of the trajectories of different satellites. Data from these sea areas, with a time difference of less than 3 hours, were analyzed. Finally, a network of 163 offshore buoys was used to validate the satellite data. These buoys are located at least 50 km from the coast, to avoid the influence of the proximity of land on the observations. Finally, the satellite observations used for buoy validation were defined by identifying data recorded within 30 minutes of the buoy recording time.

AODN PRODUCT

The Australian Ocean Data Network (AODN) [79] has produced a unique satellite dataset, representing the first consistently validated, quality-controlled, and calibrated long-duration multimission altimeter and scatterometer dataset. Some of the additional satellites to those included in WAVE_GLO_PHY_SWH_L3_MY_014_005 are GEOSAT [167], TOPEX

[168], ERS-2 [169] and GFO [170].
The database contains global wind speed and wave height data obtained from all altimetry missions flown since 1985 to present. The data are calibrated against NDBC buoy data [150] and validated with independent buoy and crossover point measurements from other altimetry missions. When multiple satellites are in orbit simultaneously, the instruments on board are cross-validated to ensure accuracy.
During the calibration process, only in-situ wave buoys located more than 50 km from the coast were considered to avoid inconsistencies between buoy and satellite data caused by coastal effects. Additionally, the time interval for collocating satellite measurements with buoy data recordings are set to 30 minutes.
As observed, the procedure for positioning and calibrating follows the same method used in WAVE_GLO_PHY_SWH_L3_MY_014_005 product.
This widely used dataset [171, 172, 173, 174] is accessible via the AODN portal, which also provides access to all available Australian marine and climate scientific data.

3.5.3. NUMERICAL MODEL DATA PRODUCTS

Several open source numerical datasets are available to obtain wave and wind time series. These datasets are usually used in the very early stages of wave resource evaluation, as they provide spatially coarse information, not suitable for the detailed understanding of physical phenomena, particularly near the coast. Such datasets are useful for providing a preliminary overview of general wave and wind conditions on a regional or global scale.

These datasets include ERA5 [175], which provides global-scale hourly reanalysis climate data at a spatial resolution of 0.5°x0.5°. Additional numerical models that provide global wave forecasts are MERRA2 [176], ERA-Interim [177] and CFSR [178] reanalyses. As demonstrated by several studies [179, 180, 141], the ERA5 reanalysis models generally show better agreement with both satellite data and in-situ measurements.

ERA5 PRODUCT

ECMWF is an intergovernmental organization dedicated to generating numerical weather forecasts and hindcasts at a global scale [181], offering support services to its Member States and cooperating countries, and making a fundamental contribution to the international scientific and meteorological community. The Center boasts one of the most sophisticated infrastructures in the world for supercomputing and meteorological data storage.
Within the ECMWF, a series of interconnected models work together to produce forecasts. The ECWAM model, in particular, interacts closely with atmospheric models that provide it with surface wind conditions, essential for wave modeling. The ERA5 database [175], an integral part of ECWAM, represents the fifth generation of meteorological reanalysis, the result of the integration of vast volumes of data observed globally via satellites and in-situ sensors, processed through sophisticated meteorological models. The ECMWF wave model has been tested and validated in a variety of locations using in-situ data, demonstrating its reliability and accuracy [182, 183, 184] as well as on a global scale against altimetry data [185, 186]. ERA5 provides detailed estimates of numerous meteorological and climate variables from 1950 to the present day, offering hourly data

with spatial resolution varying between 0.25°, for wind data, and 0.5°, for wave data. Regarding the datasets provided, ERA5 offers a wide range of meteorological parameters, including wind speed at 10 meters above sea level and a wide selection of wave-related variables. These include the significant wave height, the energy period, up to the frequency-directional spectrum. Furthermore, to facilitate detailed analysis of various marine phenomena, wave parameters are also available in partitioned form, allowing users to evaluate different sea states that contribute to the composition of a multi-modal sea states [187].

3.6. WAVE ANALYSIS STANDARDS

THE evaluation of the wave resource and the knowledge of the characteristics of the sea states is essential for the design of efficient and safe WECs. This evaluation must be based on the time series of the synthetic parameters and the reliability of the WECs design itself depends on their reliability. To this end, a number of requirements must be met so that the time series is robust and statistically relevant.
While numerical models are often indispensable due to the limited temporal coverage of in situ instruments, the latter remain crucial for model calibration and validation. Therefore, implementing a rigorous quality control process for instrumental recordings becomes imperative to ensure reliable data for meaningful model comparisons.

3.6.1. IEC/TS 62600-101:2015

The International Electrotechnical Commission (IEC) [188] is a global organization that promotes cooperation on all questions concerning standardization in the electrical and electronic fields. The IEC has 86 member countries (e.g., China, Denmark, Netherlands, Italy), and there are an additional 85 countries in the affiliate country program.
The IEC provides international standards, technical specifications, and technical reports but does not itself offer any attestation of conformity. Independent certification bodies (e.g., DNV [189]) provide conformity assessment services.
The IEC 62600-101 Technical Specification [114] is specifically designed for the wave energy sector and should be applied at all stages of site assessment, from initial investigation to detailed project design. It provides a uniform methodology to ensure consistency and accuracy in:

- *Estimations*, describing the procedure for evaluating the wave energy resource
- *Measurements*, identifying the natural phenomena under study
- *Analysis of measurements*, describing the measurements characteristics
- *Modeling*, providing the numerical model requirements and categorizing them into those that must be considered, those recommended, those acceptable, and those not allowed.
- *Report of results*, supporting in the preparation of the final document
- *Uncertainty estimation of the resource assessment*, to quantify the uncertainty of the results

The minimum requirements and recommendations provided by the Technical Specification vary depending on the *CLASS* of resource assessment. In particular:

- *CLASS 1 - Reconnaissance*: This class involves characterization of the resource with relatively low effort and high uncertainty. It is suitable for large sea areas when determining an installation site for a WEC and there is yet no knowledge of the sea states occurring in the investigated area.
- *CLASS 2 - Feasibility*: This is a characterization of the resource with moderate effort and uncertainty. It is suitable for investigating and comparing one or more potential sites. Typically, potentially interesting spots are identified from the reconnaissance, and through this analysis, a more detailed assessment of the energy potential and specific environmental conditions of the sites is conducted.
- *CLASS 3 - Design*: This is the most advanced phase of resource characterization, where the effort is greater and uncertainty is minimized. In this class, detailed and specific data are collected, often by installing ad hoc in-situ instrumentation, which allows for precise design and development plan. The data collected in this phase are crucial to ensure the reliability and efficiency of the designed WEC system.

DATA COLLECTION OVERVIEW

For an accurate analysis of wave resources, the IEC 62600-101 Technical Specification requires the use of a dataset of at least ten years. This time extension is crucial to fully evaluate seasonal and annual variations, providing a detailed and reliable view of the average conditions and extremes that may occur at the study site.
It is strongly recommended to prefer data collected via in-situ instrumentation, when available. These instruments offer direct and highly precise measurements of marine conditions and should have a data return rate greater than 70% to ensure the validity and representativeness of the information collected. In cases where it is not possible to obtain a complete ten-year in-situ dataset or in the absence of directional sensors, the use of numerical models is permitted. However, the use of numerical datasets, usually derived from simulation models, requires rigorous validation through instrumental data. This validation process is critical to ensuring that models accurately represent different atmospheric and oceanographic conditions throughout the year, avoiding significant distortions due to seasonal variations.
The validated numerical dataset can be used for the overall assessment of the resources, to integrate any gaps in the data collected in-situ, or to provide directional details not available through the instrumentation in use.

In the context of wave resource assessment, it is essential to carry out detailed analyzes based on the collected dataset. Some of the analyzes to be carried out are:

- *Seasonal Variability*: This analysis focuses on the variations in wave conditions that occur at specific times of the year, particularly during the seasons. Understanding seasonal variability is crucial to predict the energy produced by WECs at different times and to optimize the design and management of WECs to maximize their energy efficiency throughout the year.

- *Inter-annual Variability*: The analysis of interannual variability studies the fluctuations in wave conditions from one year to the next. This type of analysis is essential to identify any long-term trends or cyclicality, which may be due to broad climate phenomena. An in-depth understanding of interannual variations can guide strategic decisions related to WECs siting and energy production capacity planning.

- *Prevalence of Multi-modal Wave Systems*: Analyzing the prevalence of multi-modal sea states helps to understand the complexity of the wave field in a given region. This is especially important for directionality-sensitive WECs. These devices maximize energy conversion when the directions of the different wave components are aligned with the direction of operation of the device itself. The sea state that comes closest to this ideal situation is given by a uni-modal wave system. Also in this case, the wave components that form the wave system have a slight variability in the direction of propagation. In the case of multi-modal sea states, however, wave energy is distributed among multiple wave systems, each of which can have a different direction and origin. This energy distribution makes the design and configuration of WEC devices more complex.

- *Variability of Dominant Wave Direction*: This analysis examines how the direction of dominant waves changes over time. The direction of the dominant wave is a critical factor for the optimal orientation of WECs and for evaluating the potential harvesting energy. Understanding directional variability allows to predict the operational efficiency of energy conversion devices and adapt installation strategies to maximize wave energy absorption. This analysis is closely related to that on the prevalence of multi-modal wave systems.

MEASUREMENTS

The measurements necessary for a comprehensive analysis of the wave energy assessment cover a broad range of environmental factors. These factors include waves, winds, tides, currents, and bathymetry, each of which plays a crucial role in the assessment and development of energy projects in marine settings.

WAVE MEASUREMENTS

Regarding wave measurements, depending on the class belonging, different requirements have to met. In particular, only for *CLASS 1* it is possible to carry out analyzes on the basis of the synthetic parameters H_s and T_e. For the other two classes, information derived from the frequency-direction spectrum is required. In particular, the parameters of interest are, in addition to H_s and T_e, P_θ, $\theta_{P_{max}}$, ϵ_0 and the directionality coefficient (d), defined as follows:

$$d = \frac{P_{\theta_{P\text{max}}}}{P} \tag{3.25}$$

This parameter provides an indication of the directional spread of wave power as the ratio of the maximum directionally resolved wave power to the omnidirectional wave

power.

The wave field at a given place and time is often composed of multiple wave systems, each originating from specific wind events that are currently occurring or have occurred previously. The IEC 62600-101 Tecnical Specification foresees that the partitioning of the wave spectra must be carried out in order to distinctly analyze the individual wave systems.

WIND, TIDE, CURREND AND ICE MEASUREMENTS

Wind speed and direction are crucial elements in the numerical modeling of wave conditions, essential for evaluating the climate impact on sea waves. It is essential that these parameters are provided across the entire study domain, ensuring a spatial and temporal resolution adequate for the specific evaluation class. In particular, the wind speed must be referred to the standard altitude of 10 meters above sea level, as commonly adopted in climate prediction models.
Regarding water fluctuation levels due to tides, sensitivity studies need to be conducted to evaluate how these influence the operation of WECs. If the tidal impact is found to be significant, these fluctuations must be integrated into the numerical model. The same attention must be paid to marine currents and the presence of sea ice, both factors that can significantly alter the operating conditions and effectiveness of WECs.

MODELLING

Numerical wave propagation models are a valuable resource for planning and optimizing operations in maritime sectors, including renewable energy, coastal defense and shipping. Boundary conditions and wind forcings should be derived from more extensive validated numerical models or in-situ data. The Table 3.1 summarizes the model requirements according to the class they belong to. These requirements concern the definition of the computational domain, the minimum characteristics of the wind forcing and the boundary conditions, as well as specifics on the model setting.

3.6.2. SEADATANET

SeaDataNet [190] is a comprehensive marine data infrastructure aimed at managing an extensive range of data collected from the seas and oceans. This initiative integrates efforts from numerous professional data centers across Europe, forming a robust network that provides high-quality standardized online databases.
The centralized portal of SeaDataNet offers seamless online access to in-situ data, metadata, and related products. This portal effectively interconnects the interoperable platforms of SeaDataNet's data centers, ensuring smooth data integration and accessibility [148].
To maintain interoperability across platforms, SeaDataNet has established common communication standards and adapted technologies. These measures ensure that data from various sources are of consistent quality, compatible, and coherent. The adoption of standardized data verification methodologies supports the preparation of comprehensive regional and global statistical products from the in-situ datasets provided by SeaDataNet partners.

Additionally, SeaDataNet has developed and adopted the *BODC Vocabulary Dictionary* [191] to provide a standardized description of data.

DATA QUALITY CONTROL PROCEDURES

Data Quality Control procedures are crucial for identifying missing information, detecting errors that occur during data transfer or reformatting, recognizing duplicate entries, and identifying remaining outliers such as spikes or out-of-scale data. SeaDataNet's quality control process includes the following tests:

1. **Date test**: the dates of the measurements are allowable (e.g. the year is made up of 4 digits, the months are between 1 and 12)
2. **Location test:** The coordinates of the instrument fall within the allowable latitude and longitude range:
   i. $-90° \leq$ Latitude $\leq 90°$
   ii. $-180° \leq$ Longitude$\leq 180°$)
3. **Allowable range test**: Value parameters must have a allowable values. In particular:
   i. $0° \leq Dir_m \leq 360°$
   ii. $0° \leq Dir_p \leq 360°$
   iii. $0° \leq s \leq 306°$
4. **Global range test**: Value parameters must fall within expected global bounds. In particular:
   i. $0m \leq H_s \leq 25m$
   ii. $1s \leq T_m \leq 25s$
   iii. $1s \leq T_p \leq 30s$
   iv. $0m \leq H_{s_{max}} \leq 40m$
5. **Regional Range Test**: Value parameters must fall within expected regional extremes. In particular, for the Mediterranean Sea:
   i. $0m \leq H_s \leq 12m$
   ii. $1s \leq T_m \leq 15s$
   iii. $1s \leq T_p \leq 20s$
6. **Spike test**: Confidence limits are determined, and values outside these limits are deemed inaccurate and therefore excluded from the dataset.

$$\left| v_i - \frac{v_{i+1} - v_{i-1}}{2} \right| - \left| \frac{v_{i+1} - v_{i-1}}{2} \right| \leq v_{st} \tag{3.26}$$

with:

$$v_{st=}\begin{cases}3m & \text{for } H_s\\ 4s & \text{for } T_m\\ 15s & \text{for } T_p \text{ in open ocean}\\ 10s & \text{for } T_p \text{ in enclosed sea}\end{cases} \tag{3.27}$$

7. **Anomalies test**: Anomalies in the recordings must be eliminated.
   i. 10 or more consecutive measurements with identical values must be neglected.
   ii. Identify and neglect unrealistic values thought visual check.
8. **Instrument comparison test**: If two different sensors are placed in the same nearby area, exposed to the same environmental conditions and the depth of their installation site is similar, their measurements can be compared to identify inconsistencies.

3.7. DICUSSION

THE chapter focuses on various data sources and their respective acquisition methodologies, examining the advantages and disadvantages of in-situ, remote sensing, and numerical modeling techniques. It is emphasized that no existing data source fully meets all the criteria of reliability and usefulness. In-situ measurements, although highly precise and reliable, are expensive and subject to technical and bureaucratic challenges, limiting their temporal and spatial coverage. These measurements provide data specific to the installation site only. Satellite data, despite being promising for the calibration and validation of numerical models, are still under-utilized due to the complexity of access and their discontinuous availability. Numerical models, on the other hand, offer a viable alternative to extend the temporal and spatial coverage of wave data.
The chapter also introduces various freely available wave data products, detailing their sources, validation processes, and processing methodologies. These products, classified into in-situ data, satellite data, and numerical model data, are particularly useful for obtaining wave information at specific sites.
Additionally, standards for wave analysis, such as IEC/TS 62600-101:2015 and SeaDataNet, are presented to ensure consistency and reliability in data analysis. These standards provide guidance on critical aspects such as the spatial and temporal resolution of wave data obtained from numerical models, acceptable types of wave boundary conditions, and the minimum length of time series required for reliable assessments.

3.8. CONCLUSION

THE analysis of in-situ techniques, remote sensing, and numerical models highlights the strengths and limitations of each approach. This information is crucial for identifying the best data source that meets the specific needs of marine stakeholders.
A significant contribution of this chapter is the collection and discussion of various freely available wave data products. These products, derived from in-situ measurements, satellite observations, and numerical models, offer valuable resources for the research and

design of WECs, as well as for the Blue Economy in general. Combining these data sources allows for a more complete and accurate understanding of wave conditions at a given site, thereby increasing the accuracy of analyses and extending their temporal coverage.

Table 3.1: IEC requirments

Requirments	CLASS 1	CLASS 2	CLASS 3
Computational domain			
Recommended spatial resolution for depth>200m	5km	2km	1km
Recommended spatial resolution for depth<200m	500m	100m	25m
Recommended spatial resolution for depth<20m	100m	50m	10m
Wind forcing & Boundary condition			
Min. wind temporal resolution	3h	3h	1h
Min. wind spatial resolution	100km	50km	25km
Paramatric wave boundary	Acceptable	Not permitted	Not permitted
Spectral wave boundary	Recommended	Recommended	Recommended
Specifications & Numerics of numerical model			
$3^n d$ generation spectral wave model	Recommended	Recommended	Recommended
Spherical coordinates	To be considered	Acceptable	Acceptable
Min. temporal resolution	3h	3h	1h
Min. frequencies discretization	25	25	25
Min. directional discretization	24	36	48
Recommended frequency range	0.04Hz-0.5Hz	0.04Hz-0.5Hz	0.04Hz-0.5Hz
Minimum time series duration	10 years	10 yearsh	10 years

II

NUMERICAL CASE STUDY: PANTELLERIA SEA STATES ANALYS

4

WAVE ENERGY ASSESSMENT IN PANTELLERIA

4.1. INTRODUCTION

AMONG the various renewable energy sources, ocean energy, and especially wave energy has the potential to make a major contribution to the supply of clean and reliable energy [192, 193]. In that context, the characteristics of waves must be properly evaluated to estimate the wave energy resource, design efficient devices and conduct a reliable cost-benefit analysis[194, 195, 114].

The island of Pantelleria is the focal point for this thesis and the evaluation of the wave resource along its coast is analyzed for a WEC performance analysis purpose.
Pantelleria is situated in the Mediterranean Sea and is characterized by strong and consistent wave patterns [196]. The Strait of Sicily, where Pantelleria is located (Fig. 4.1), benefits from strong winds and a considerably long fetch [197]. Consequently, the island is optimal for testing and developing WECs [198, 199]. Over the years, numerous wave energy projects were initiated and tested around the island waters. The specified installation testing site is in the same concession area of the MORE Lab (Marine Offshore Renewable Energy Lab) [200], where in-situ instruments are installed.

4.2. WAVE DATASET AVAILABLE

MULTIPLE data sources are availabe within the designated area of interest of Pantelleria. Specifically, the MOREnergy Lab research group has installed two in-situ instruments and Level-3 satellite dataset is available. Additionally, data from the ERA5 reanalysis dataset is obtained and a SWAN model dataset is implemented through meticulous calibration and validation procedures.
Subsequent sections will delve into these data sources, elucidating their attributes and engaging in detailed discussions thereof.

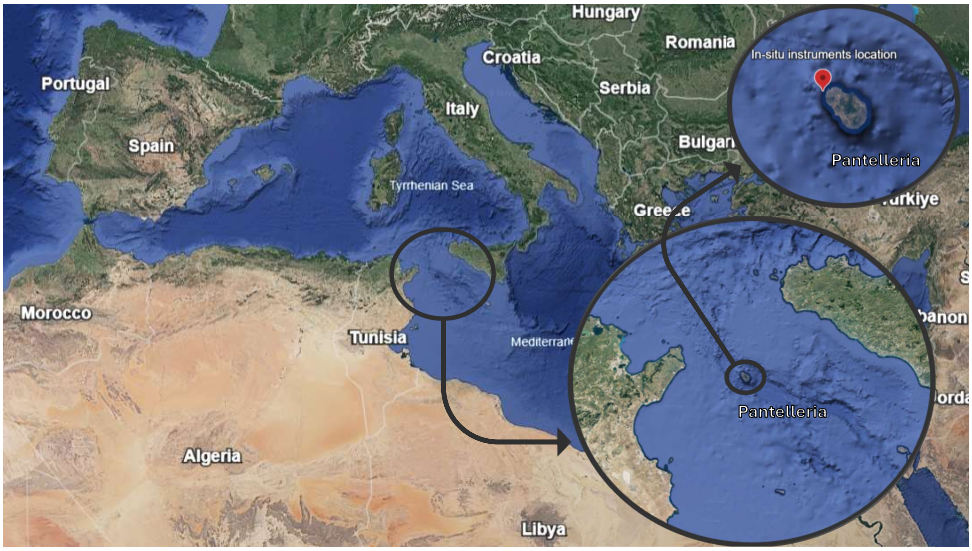

Figure 4.1: Pantelleria island location

4.2.1. IN-SITU DATASET

The in-situ installation site is approximately 800 m from the north-west coast at coordinates 36°49'23"N and 11°55'13"E (Fig. 4.1). This site is located near Cala Modica, in the Mursia area, with a water depth approximately of 30 m. The synthetic data obtained from the in-situ measurements of Nortek AWAC-AST (Acoustic Wave and Currents-Acoustic Surface Tracking) 600 KHz and Datawell Waverider DWR-G buoy underwent rigorous quality control procedures outlined in Section 3.6.2. Through this quality controll process, unreliable data points are identified and removed, resulting in the identification of reliable datasets.
Fig. 4.2 provides an overview of the total coverage of the in situ recordings, as well as the time coverage based on the quality control process described in detail below..

NORTEK AWAC-AST 600 KHZ

The Nortek AWAC-AST 600 KHz is an acoustic profiler positioned on the seabed, specifically designed to monitor ocean currents and waves [201]. It is equipped with a directional wave measurement system that enables the recording and archiving of sea wave profiles. As mentioned earlier, the instrument installation site is situated about 800 meters from the northeast coast, in waters 30 meters deep, at the exact coordinates of 36°49'23"N and 11°55'13"E.
During monitoring operations, the Nortek AWAC-AST sensor acquired data at regular intervals, recording information every hour for a period of 20 minutes with a sampling rate of 2 Hz. This approach allowed for a representative assessment of sea states. The AWAC frequencies range measurements is from 0.01 Hz to 1.0 Hz, covering wave periods from 1 seconds to 100 seconds.

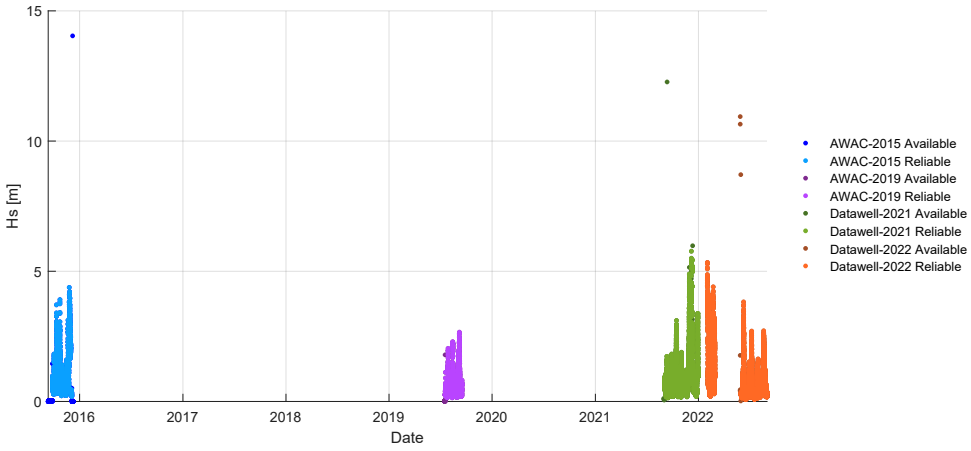

Figure 4.2: Overview of total in situ data coverage and time span achieved after applying the quality control process

AWAC-AST QUALITY CONTROL

Two registration campaigns were conducted using the Nortek AWAC, one in 2015 and the other in 2019, covering different periods of the year. Specifically, the data collected in 2015 ranges from September 26 to December 4, while that of 2019 covers the period from July 18 to September 16.
Tab. 4.2 provides a brief summary of the results obtained through the quality control procedures of AWAC datasets, conducted following the guidelines provided in 3.6.2.

The dataset collected during the 2015 survey campaign includes 2073 data points, but 2140 should have been registered. This discrepancy is due to data loss. Through the quality control process, 99 points are eliminated due to data storage anomalies. Furthermore, additional points, equal to 25, are discarded due to the presence of negative directional values and 4 are discared in the spike test. Finally, 339 points are excluded during the visual evaluation because they corresponded to the installation and recovery data of the instrument. In particular, the AWAC did not have a communication system with the mainland, therefore the data was recorded directly in the device's memory and subsequently extracted once the instrument was recovered from the seabed. As a result, anomalies found in the 2015 registration period were not identified in a timely manner. A return rate of 77.4% is obtained by considering the data reliable compared to those available. However, considering the return rate based on the data that theoretically should have been recorded, the percentage is 75%

Regarding the 2019 measurement campaign, only 4 points are eliminated due to negative directional parameters, while only one is discared by the spike test. Throughout the anomalies test, in particular throughout the visual evaluation, 51 points are excluded and they corresponded to the installation and recovery operations of the sensor.
The implemented quality control process showes a return rate of 96.2% both considering

Table 4.1: AWAC-AST datasets

Quality Control Process		
Assessment	**2015-Unreliable data**	**2019-Unreliable data**
Date test	99	0
Location test	0	0
Allowable test	25	4
Global range test	0	0
Regional range test	0	0
Spike test	4	1
Anomalies test	339	51
Instrument comparison test	No additional instruments available	No additional instruments available
Measurements	2015-Dataset	2019-Dataset
Theoretical	2140	1500
Available	2073	1500
Reliable	1606	1444
Return rate	2021/2022-Dataset	
Reliable on theoretical	75.0%	96.2%
Reliable on available	77.4%	96.2%

the reliable data versus the reliable and theoretical ones.

DATAWELL WAVERIDER DWR-G

The Datawell Waverider DWR-G buoy [83] recorded wave sea states in Pantelleria in 2021 and 2022. Like the Nortek AWAC-AST instrument, the Datawell was also installed at the same site, located in the center of the sea area granted under the MORELab concession. The buoy is equipped with a Global Positioning System (GPS) module that facilitates directional wave measurements. It is equipped with a sensor package for measuring accelerations along the x-, y-, and z-axes, magnetic field readings along these axes, and pitch and roll motions. Analyzing the pitch and roll angles of the buoy and its heave motion makes it possible to characterize the incident wave fully. A disc-shaped device located at the pivot point of the buoy's motion is employed to determine the wave direction, focusing on the two-dimensional horizontal aspect of the wave.
The duration of data acquisition is equivalently 30 minutes and occurs every 30 minutes, obtaining a continuous recording of sea states. Moreover, the buoy detectes frequencies spanning from 0.01 Hz to 0.64 Hz, corresponding to wave periods between 1.6 seconds and 100 seconds.

DATAWELL WAVERIDER DWR-G QUALITY CONTROL

The buoy was deployed in early September 2021 with an expected operational lifespan of 12 months. However, due to failures in the battery packs, it was decommissioned prematurely at the end of February 2022 and only in June 2022 was the buoy reinstalled, returning to record sea states until the end of August 2022. Additionally, intermittent interruptions in communication between the transmitting and receiving antennas occurred, resulting in a overall data loss.
Tab. 4.2 offers a concise summary of the outcomes derived from the quality control procedures of Datawell datasets.

Table 4.2: Datawell datasets

Quality Control Process	
Assessment	2021/2022-Dataset
Date test	0
Location test	0
Allowable test	2
Global range test	0
Regional range test	0
Spike test	41
Anomalies test	28
Instrument comparison test	No additional instruments available
Measurements	2021/2022-Dataset
Theoretical	17567
Available	10247
Reliable	10176
Return rate	2021/2022-Dataset
Reliable on theoretical	57.9%
Reliable on available	99.3%

The rate of return of reliable data out of those available is equal to 99.3% but is reduced to 57.9% if theoretical data is considered. This highlights that, although the quality control process eliminated only a negligible percentage of points, and therefore the data provided is accurate, the sensor is unreliable. This is because nearly half of the expected recording time was lost due to battery failure and the time required to recover, repair and reinstall the instrument. Importantly, recovery and installation operations involve activities such as renting a vessel, finding a qualified crew, and waiting for an adequate time window for navigation and operations at sea, all of these activities are time consuming.

4.2.2. SATELLITE DATASET

Satellite observations are a valuable resource in understanding global wave trends [202] and in validating global [202, 203] or local [204, 205] numerical models. However, they have no application in offshore design support when used alone. In fact, once a site has been identified, the temporal resolution with which satellite observations provide information could vary between 10 days (e.g. Jason-3 [145]) and 35 days (e.g. SARAL/Altika [146]). Furthermore, as the distance from the coast decreases, the uncertainty and error of the data increases, consequently some measurements must be discarded because their unreliability, further reducing the original dataset.

AODN DATASET

Among the Level-3 datasets available, the Australian Ocean Data Network (AODN) [79] has identified as the best one for acquiring satellite data pertinent to the area of interest. What distinguishes this dataset from others at Level-3 is its notably extensive temporal coverage. While there are alternative Level-3 datasets accessible, they exhibit comparatively shorter temporal spans, thereby affirming the selected one as the preferable option for ensuring a thorough and continuous portrayal of temporal dynamics. An example is the WAVE_GLO_PHY_SWH_L3_MY_014_005 product [158], which has limited time coverage, spanning from 2002 to 2020, and includes data from less satellites.

Various performance indicators are used to evaluate the applicability of satellite data to the Pantelleria case study. This analysis involves assessing the accuracy of satellite data compared to in situ measurements, considering variations in spatial criteria for the collocation phase and methodologies for determining satellite values at each collocation.
The primary objective is to evaluate the congruence of satellite data with in situ measurements, despite the instrument's proximity to the coast and the nearby presence of Tunisia and Sicily. Many studies validate satellite data under more favorable conditions, typically in open ocean environments with instruments located at least 50 km from the coast [157, 206, 79]. In contrast, this study aims to determine the feasibility of using satellite data in less favorable conditions, such as those presented by the Pantelleria case study. This approach seeks to demonstrate the applicability of satellite data for validating numerical models, showing that satellite data can be reliable even in challenging coastal environments.
The ultimate goal is to obtain a satellite dataset that provides significant wave heights during time periods when in-situ measurements are unavailable. The accuracy of the satellite dataset is assessed by comparing satellite data with in-situ data recorded during the same time periods. Once the reliability of the satellite data is verified, these measurements can be used to fill gaps in the in-situ dataset, thereby improving the validation of numerical models. By leveraging satellite data to supplement periods without in-situ measurements, a continuous and comprehensive coverage of significant wave height data can be achieved. Ensuring the satellite data's reliability through rigorous comparison with in-situ measurements is a critical step in this process, as it provides confidence in the satellite data's applicability for model validation purposes.

PERFORMANCE INDICATOR

The Root Mean Square Deviation ($RMSD$) is useful to evaluate the average error magnitude in the satellite dataset (x_s), and it reads

$$RMSD = \sqrt{\frac{\sum_{n=1}^{N} \left[\left(x_s - \overline{x}_s \right) - \left(x_o - \overline{x}_o \right) \right]^2}{N}} \tag{4.1}$$

where N is the length of the datasets and x_o correspond to the in-situ observations.

The Pearson Correlation Coefficient (CC) measures the linear relationship between two variables and determines the strength of the relationship between satellite and in-situ data. It is described by

$$CC = \frac{\sum_{n=1}^{N} \left| \left(x_s - \overline{x}_s \right) \left(x_o - \overline{x}_o \right) \right|}{N s_{d_{x_s}} s_{d_{x_o}}} \tag{4.2}$$

where s_d is the standard deviation, a statistical measure that quantifies the degree of dispersion of a dataset from the mean value. It has the form

$$s_{d_i} = \sqrt{\frac{\sum_{n=1}^{N} \left(x_i - \overline{x}_i \right)^2}{N}} \tag{4.3}$$

where $_i$ may refer to the satellite dataset (x_s) or in-situ observations (x_o).

Other performance parameters used to evaluate the satellite applicability are $BIAS$ and the Symetric slope (S). The formulations for these parameters are as follows

$$BIAS = \frac{\sum_{n=1}^{N} (x_s - x_o)}{N} \tag{4.4}$$

$$S = \sqrt{\frac{\sum_{n=1}^{N} x_s^2}{\sum_{n=1}^{N} x_o^2}} \tag{4.5}$$

DATA COLLOCATION ANALYSIS

All available altimetric satellite data, for the area of interest, are obtained from the AODN portal, resulting in 14 satellite missions. Fig. 4.3 provides a spatial overview of the distribution of satellite measurements based on each satellite's track.

As observed, Pantelleria's position is particularly favorable, lying almost entirely at the crossover point of the ERS-2 satellite. Additionally, the crossover point of the ENVISAT satellite is located near the west coast of the island, and the CFOSAT trajectory bands run along the island's west coast.

The overall temporal coverage of the altimetric data ranges from 1985 to the present, with a gap between 1988 and 1992 (Fig. 4.4).

Tab. 4.3 provides a more detailed overview of the individual time coverages of the different satellite missions.

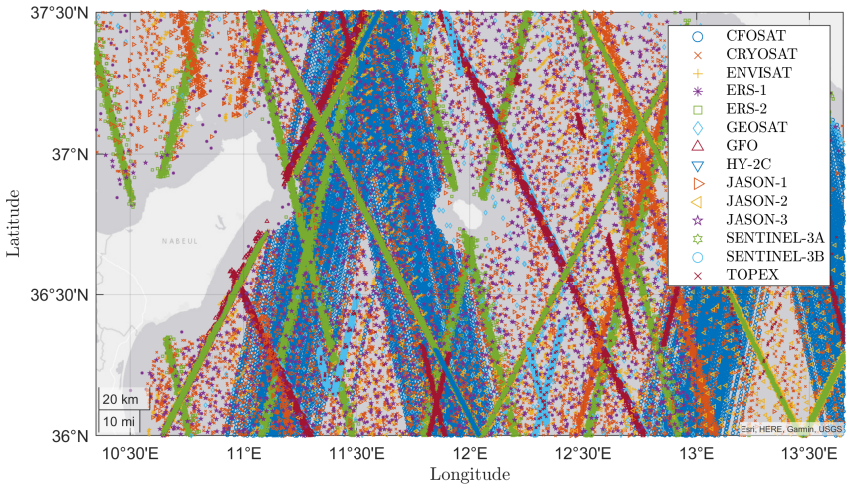

Figure 4.3: Spatial distribution of all available altimetric satellite measurements provided by AODN

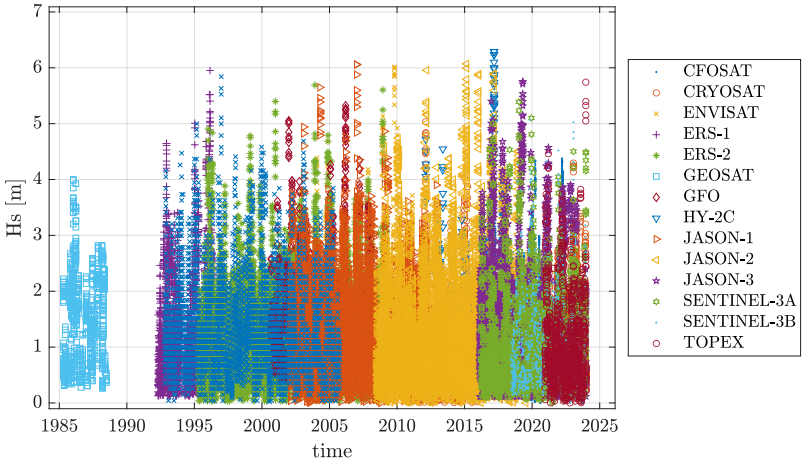

Figure 4.4: Time coverage of all available altimetric satellite measurements provided by AODN

There are several instances of temporal overlap between satellite missions, which enhance the continuity and reliability of significant wave height data. Currently, five satellites are active and providing significant wave height information. This active fleet ensures a robust and comprehensive dataset, facilitating more accurate and timely analysis of oceanographic conditions. The overlapping periods between these satellite missions allow for cross-validation of data, improving the overall quality and consistency of the wave height measurements.

Table 4.3: Detailed overview of time coverage of all available altimetric satellite measurements provided by AODN

Satellite	Start mission	End mission
CFOSAT [163]	Oct 2018	Present
CRYOSAT-2 [162]	Apr 2010	Present
ENVISAT [161]	Mar 2002	Apr 2012
ERS-1 [207]	Jul 1991	Mar 2000
ERS-2 [169]	Apr 1995	Jul 2011
GEOSAT [167]	Mar 1985	Jan 1990
GFO [170]	Feb 1998	Oct 2008
HY-2C [208]	Sep 2020	Jan 1990
JASON-1[159]	Dec 2001	Jul 2013
JASON-2 [209]	Jun 2008	Oct 2019
JASON-3 [145]	Jan 2016	Present
SENTINEL-3A [210]	Feb 2016	Present
SENTINEL-3B [211]	Apr 2018	Present
TOPEX [212]	Aug 1992	Jan 2006

The reliability analysis of the satellite data in the case study progressed by assuming a time criterion for data collocation of 30 minutes. Regarding the spatial criterion, various distances from the buoy installation site are analyzed, ranging from 10 km to 90 km, with increments of 10 km. Fig. 4.5 provides an overview of the spatial extents within which the analysis is conducted. This figure illustrates the different radii around the buoy, systematically varyed to determine the optimal spatial range for integrating satellite data with in situ buoy data. This approach ensures a comprehensive understanding of how spatial factors influence the congruence between satellite and buoy measurements, ultimately enhancing the precision of oceanographic data analysis.
Given the proximity to Tunisia, the maximum distance considered is 90 km. Furthermore, considering the installation site of the in-situ instruments, which is located 800 meters from the northwest coast, a sensitivity analysis is conducted to assess the impact of including or excluding satellite measurements from the southeast quadrant relative to the buoy. Taking these geographical factors into account, the study aims to evaluate the influence of spatial orientation and distance on the reliability of satellite data. This comprehensive approach ensures that the data integration process is robust and reliable.

Regarding the identification of the satellite significant wave height value resulting from each collocation, two methodologies are followed. The first methodology involves determining this value as the measurement nearest to the installation site of the in-situ instruments for each collocation. The second methodology considers the significant

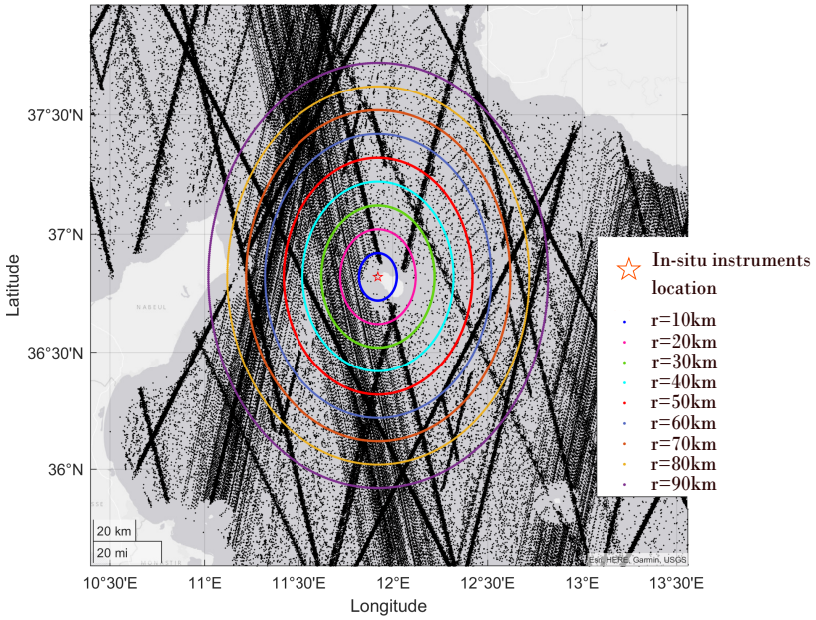

Figure 4.5: Overview of the spatial extents analyzed for evaluating satellite data reliability

wave height value of each collocation to be the mean value of the measurements at each collocation.
Consequently, four different case studies are analyzed. The case defined as MDQ (Mean-Distance-Quadrant) assigns the significant wave height value as the mean of the measurements at each collocation, at varying distances r from the installation site, excluding measurements from the southeast quadrant. The NDQ (Near-Distance-Quadrant) case study is similar to MDQ but defines the significant wave height value as the measurement nearest to the installation site. The MD (Mean-Distance) and ND (Near-Distance) cases are analogous to MDQ and NDQ, respectively, but do not exclude measurements from the southeast quadrant.
Fig. 4.6 illustrates the number of satellite data points obtained from the four different cases, varying the distance from the installation site and considering the entire recording period provided by the AWAC and Datawell buoy.
By grouping the different measurement campaigns, a total of 13226 in-situ data points are obtained. In contrast, the number of satellite data points derived from collocations with the in-situ instruments ranged from a minimum of 5 to a maximum of 206 measurements. This discrepancy is primarily due to the temporal resolution of the satellite measurements, which, as previously discussed, can vary between a few days to just over a month. Consequently, the availability of satellite data is limited by the frequency of satellite passes over the area of interest. As expected, the number of satellite data points

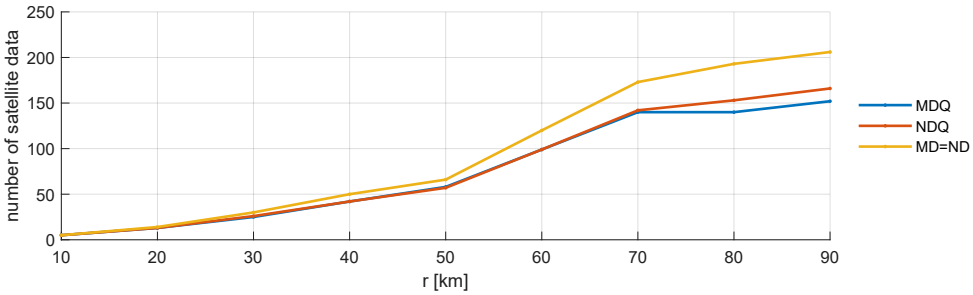

Figure 4.6: Number of satellite data obtained by the different collocation cases in regard to the distance from the in-situ installation site

in the MD and ND cases is overall greater than in the MDQ and NDQ cases. This difference arises because the latter cases exclude satellite data from the southeast quadrant of the installation site. The slight discrepancy between the MDQ and NDQ cases is due to the methodology used for determining the significant wave height value and the location of the resulting measurement. In the MDQ case, the location of the resulting measurements is defined as the centroid of the different satellite measurements for each collocation. Specifically, this procedure involves assigning the value and position of the significant wave height data corresponding to each collocation and subsequently skimming for removing the resulting values within the exclusion quadrant. Conversely, in the NDQ case, the value of the significant wave height is determined by identifying the measurement closest to the instrument installation site, excluding in advance any measurements within the exclusion quadrant. In this way, the identification of the measurement used to assign the significant wave height is done by selecting from a pool of pre-qualified measurements. This distinction in methodology affects the data density and spatial representation of the satellite measurements. By excluding the southeast quadrant, the MDQ and NDQ cases cleanse the dataset, potentially increasing its accuracy.
The significantly higher number of in-situ measurements provides a robust dataset for numerical model validation. In contrast, the variability in the number of satellite measurements underscores the importance of optimizing the collocation method. The goal is to strike an optimal balance between obtaining a high number of measurements, which can be achieved by increasing the distance from the site of interest, and maintaining high accuracy to ensure the reliability of the dataset. This careful balance ensures that the integration of satellite and in-situ data is both accurate and reliable, ultimately enhancing the precision and credibility of the oceanographic analysis.

Quantile-Quantile (Q-Q) scatter plots are employed to evaluate the congruence between satellite data and in-situ data for each case study (Fig. 4.7). For this analysis, the complete historical series of instrumental data considered reliable is used for comparison. This includes both AWAC and Datawell data, encompassing their full time coverage, with only the data deemed reliable after quality control being considered. In particular, for each in-situ measurement, the corresponding satellite measurement is identified us-

ing the four previously described techniques. Q-Q plots are generated by comparing pairs of in-situ and satellite measurements that represent the same sea state, allowing for a detailed comparison of the data. This approach ensures that both datasets are temporally aligned, as each satellite value is based on the crossover concept, following a 30-minute time interval criterion. The Q-Q plots reveal that at shorter distances from

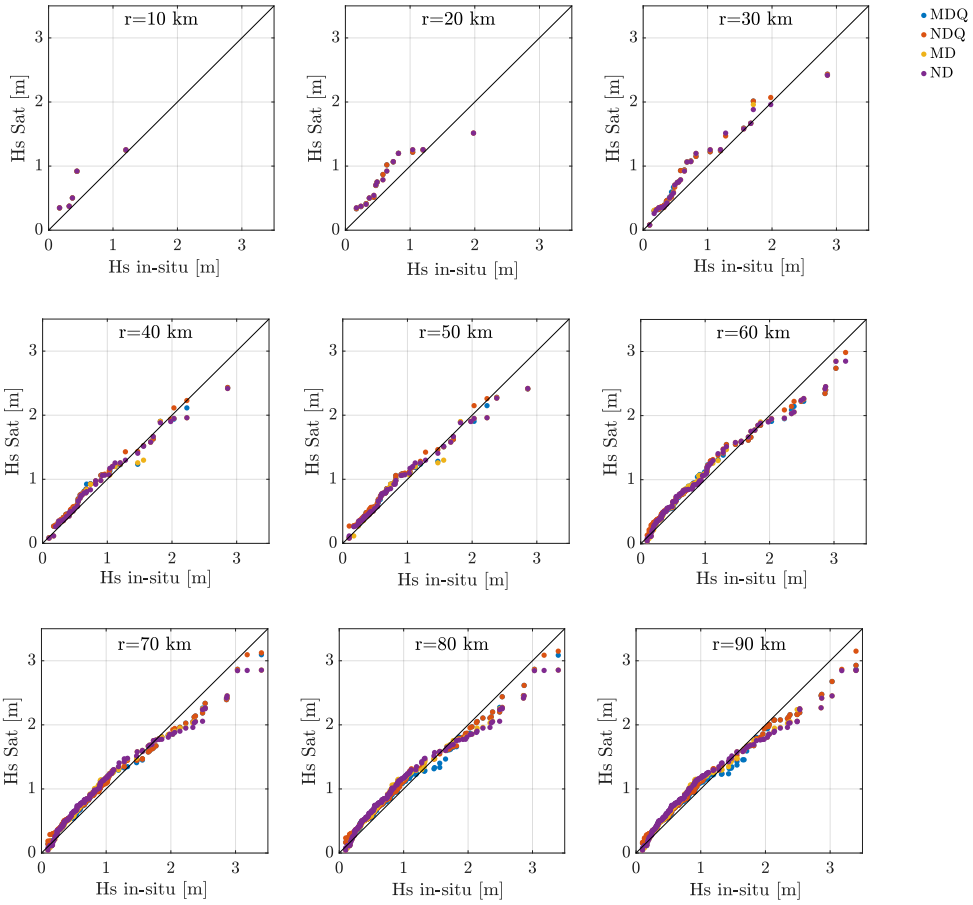

Figure 4.7: Quantile-Quantile plots for comparing satellite and in-situ significant wave height data as the distance varies, for the different cases analyzed

the installation site, specifically between 10 and 30 km, there is a noticeable deviation in the data. Specifically, it is evident that satellite data generally overestimate significant wave heights compared to in-situ measurements. This deviation is likely attributable to the proximity to the coast, which may have introduced noise or contamination into the satellite measurements.

As the distance from the coast increases, the resulting satellite dataset expands, increasing the probability of covering a significantly wider range of wave heights. For instance, at a distance of 10 km, only 5 satellite data points are obtained from the collocation. At 20

km, this number increases to 13 measurements. With a distance of 30 km from the coast, the number reaches approximately thirty, thereby enhancing the likelihood of recording various wave heights.
Overall, the trends observed in the Q-Q plots indicate that up to a significant wave height of 1.5 meters, the satellite data are well-aligned with the in-situ measurements, showing only a slight overestimation. However, for wave heights above 1.5 meters, satellite measurements tend to underestimate compared to in-situ measurements. This underestimation could be due to several factors. One of these is the location of the instrument in a nearshore sea area, which leads to a greater influence of coastal conditions and physical phenomena related to seabed interactions.

Table 4.4 presents the performance parameter values for the different cases analyzed, offering detailed information on the accuracy of the satellite data. It is important to highlight that, in addition to the performance parameters, the number of significant wave heights obtained from the collocation process is also reported. This inclusion provides context for the analysis and offers insight into the size of the datasets being compared. By considering both the performance metrics and the dataset sizes, the table enables a comprehensive evaluation of the satellite data's reliability and its effectiveness in capturing significant wave heights.
Cases with a radius of 10 and 20 km are excluded from the performance analysis due to the small dataset obtained and the poor adherence to the in-situ data shown in the Q-Q plots.
The general trend observed from comparing the various performances indicates that increasing the radius of the spatial collocation criterion improves the adherence of the satellite data to the in-situ data. This is probably linked to the correlation between the number of satellite data and the distance from the installation site. In fact, as the distance increases the dataset increases and more sea conditions can be compared. Furthermore, when comparing the MDQ cases with the respective MD cases and the NDQ cases with the respective ND cases, it becomes that excluding satellite data from the southeast quadrant reduces overall performance. This unexpected result suggests the need for further investigation. One possible explanation is that including the southeast quadrant results in a larger dataset, which could enhance the robustness of the analysis. This correlation should be further investigated using an instrumental dataset with higher temporal coverage to increase the number of collocations. Additionally, a similar geographical configuration should be sought to validate these findings.
Regarding the best performance among the analyzed cases, the MD case with a radius of 80 km stands out, achieving a correlation coefficient CC of 0.878% and a $RMSD$ of 0.316 m. These results demonstrate good adherence of the satellite data to the in-situ data, especially considering the buoy's proximity to the coast and the fact that the study area is a closed sea surrounded by two land masses.

In conclusion, the results demonstrate the satellite data potential even in unfavorable locations, and that analyzing the spatial criterion can help identify the optimal conditions for performance. To further validate these findings, similar analyses in different locations would be necessary. For the purposes of this thesis, the satellite data provided by AODN are used as a benchmark for the validation of the SWAN numerical model. This

Table 4.4: Performance parameter values for the different cases analyzed

r [km]	Technique	N data	RMSD [m]	SI [-]	BIAS [m]	CC [-]	S [-]
30	NDQ	26	0.278	0.293	0.121	0.857	0.934
	MDQ	25	0.294	0.305	0.135	0.847	0.925
	ND	30	0.294	0.298	0.115	0.858	0.940
	MD	30	0.270	0.274	0.129	0.876	0.925
40	NDQ	42	0.341	0.333	0.028	0.815	1.021
	MDQ	42	0.344	0.336	0.059	0.812	0.994
	ND	50	0.343	0.334	0.042	0.812	1.001
	MD	50	0.328	0.319	0.077	0.829	0.968
50	NDQ	57	0.321	0.329	0.052	0.826	0.997
	MDQ	57	0.318	0.326	0.074	0.827	0.978
	ND	66	0.324	0.332	0.064	0.824	0.983
	MD	66	0.306	0.313	0.092	0.843	0.955
60	NDQ	99	0.342	0.320	0.070	0.856	0.994
	MDQ	99	0.341	0.318	0.073	0.856	0.999
	ND	120	0.341	0.318	0.071	0.859	0.992
	MD	120	0.332	0.309	0.084	0.867	0.986
70	NDQ	142	0.357	0.322	0.067	0.848	0.999
	MDQ	140	0.341	0.305	0.055	0.862	1.011
	ND	173	0.361	0.329	0.073	0.845	0.997
	MD	173	0.326	0.296	0.070	0.875	1.000
80	NDQ	153	0.374	0.341	0.066	0.829	1.001
	MDQ	140	0.328	0.291	0.042	0.876	1.020
	ND	193	0.374	0.347	0.080	0.827	0.993
	MD	**193**	**0.316**	**0.293**	**0.073**	**0.878**	**0.990**
90	NDQ	166	0.409	0.367	0.050	0.804	1.026
	MDQ	152	0.364	0.317	0.025	0.854	1.044
	ND	206	0.402	0.367	0.066	0.806	1.014
	MD	206	0.345	0.315	0.057	0.860	1.010

approach extends the temporal coverage of the validation beyond what is available from the in-situ data alone. By leveraging the extended dataset from AODN, the study aims to enhance the robustness and accuracy of the SWAN model's predictions.

4.2.3. NUMERICAL MODEL DATASET

The use of numerical models is particularly useful in the absence of a long time-series provided by in-situ sensors. Additionally, these models are also employed when the available instrumentation covers a vast time period, but the installation site differs from the site of interest for the deployment of WECs or other offshore projects. In this context, numerical models must be carefully calibrated and validated to optimize their performance and accuracy. In this regard, the calibration dataset is selected from the Datawell measurements, covering the period from September 2021 to February 2022. The remaining in-situ measurements, from both Datawell and AWAC, are used together with the satellite dataset for validation purposes.

SWAN DATASET

The ten-year numerical dataset of synthetic wave parameters and the frequency-directional spectrum are obtained from the SWAN model. In particular, the temporal coverage of the time series spans from 2013 to 2022, as a 30-minute temporal resolution. An innovative calibration procedure is presented and used to identify the optimal setting in terms of performance and computational time. Indeed, the present thesis not only delves into an in-depth analysis of the SWAN model accuracy concerning wind inputs, whitecapping and exponential wind growth, but also assesses the model performance across a broad spectrum of cases. These cases encompass variations bathymetric inputs, mesh resolution, computational time-step, boundary conditions, and frequency discretisation. The investigation further delves into the model's response concerning the linear wind growth, bottom friction, and triad-triad wave interactions. The analysis encompasses an extensive assessment of wind drag formulation, and the calibration of physical parameters.

SWAN IMPLEMENTATION

In the setting up of SWAN model, much attention is paid to the choice of the wind input and the models and parameters of the physical process. Many studies [213, 214, 215, 216, 217, 218, 219, 220] have carried out sensitivity analyzes of the SWAN model about the imposed wind conditions. In particular, several wind databases are investigated, and Table 4.5 provides an overview.

The results demonstrated that the choice of the wind field database is crucial to obtain precise outputs from the wave model. In particular, [213] states that the model accuracy varies mainly according to the spatial resolution and less according to the temporal resolution of the wind fields. Then, the finer spatial resolution of the wind leads to improved wave model predictions. In [218] and [219] ERA5 appears to be the database that produces the best performances in the Mediterranean Sea, respectively, compared to ERA-Interim and CCMP for [218] and CCMPv2 [232], JRA-55 [223], MERRA 2 [229], ERA-Interim [226], NCEP 2 [228] and NCEP FNL [233] for [219]. Generally, the implemented models have a good prediction capability for the average wave conditions through tuning but show underestimating the maximum wave conditions [218, 220].

Another common method to increase SWAN model performance is the setting of whitecapping and exponential wind grow physics [214, 215, 234, 218, 220, 235, 236]. The exponential wind grow pertains to the process of energy transfer from wind to waves,

Table 4.5: Overview of widely-used wind datasets as wind forcing for the SWAN model, with temporal and spatial specifications and corresponding research papers references

Wind database	Temporal coverage	Temporal resolution	Spatial resolution	References
ERA5 [221]	1950-present	1-hourly	0.25° × 0.25°	[215, 218, 219, 220]
ERA-40 [222]	1957–2002	6-hourly	1.5° × 1.5°	[213, 214]
JRA-55 [223]	1958-present	3-hourly	1.25°x 1.25°	[219]
JRA-25 [224]	1979–2004	6-hourly	1.125° × 1.125°	[213]
NCEP CFSR [225]	1979–2010	6-hourly	0.34° × 0.34°	[213, 216, 217, 220]
ERA-Interim [226]	1979–present	6-hourly	0.75° × 0.75°	[213, 214, 215, 217, 218, 219]
MERRA [227]	1979–present	1-hourly	0.5° × 0.667°	[213, 214]
NCEP 2 [228]	1979-present	6-hourly	1.875° x 1.875°	[219]
MERRA 2 [229]	1980-present	3-hourly	0.5° x 0.625°	[219]
NCEP CFSv2 [230]	1982–present	6-hourly	0.25° × 0.25°	[215, 216]
CCMP [231]	1987-present	6-hourly	0.25° × 0.25°	[218]
CCMPv2 [232]	1987-present	6-hourly	0.25° × 0.25°	[219]
NCEP FNL [233]	1999-present	6-hourly	1°x 1°	[219]

with various formulations incorporated into SWAN [116]. Janssen [127] and Komen [68] models are grounded in the feedback mechanism, Yan [131] is based on the saturation-based parameterization while Rogers [237] relies on an observation-based approach. Whitecapping is the primary process of dissipating wave energy in open and deep oceans, characterized by waves reaching a critical point where their slopes increase and they break, effectively limiting further wave growth. SWAN [116] has adapted several physics scheme for wind and whitecapping such as Janssen [127], Komen [68], Westuyasen [129] and Rogers [128] (see Table 4.6), with wind growth and whitecapping being tunable independent parameters.

In [215], the SWAN performance has been evaluated with different whitecapping and exponential wind grow models, revealing that the wind scaling parameter is among the most affecting for wave height regulation. It has also been demonstrated in Akpinar et al [214] that the value of the whitecapping coefficient with greater consistency, compared to the wave observations, varies with the variation of the wind reanalysis database used. Additionally, the study [234] highlights the importance of conducting sensitivity anal-

Table 4.6: SWAN physics packages

Packages	Exponential wind grow	Whitecapping	Combinations acronym
GEN3 JANSsen	Janssen [127]	Komen [68]	J-K
GEN3 KOMen	Komen [68]	Komen [68]	K-K
GEN3 WESTHuysen	Yan [131]	Westhuysen [129]	Y-K
GEN3 ST6	Rogers [237]	Rogers [128]	R-R

yses of the SWAN model to identify the optimal physics combinations for the specific study site. The model is calibrated and validated against data from five buoys placed at sites with different wave characteristics in the west coast of Norway and shows that GEN3 WESTHuysen package generally provides wave heights at locations with mixed swell-wind sea conditions with good agreement. GEN3 KOMen package is the most accurate for measuring wave heights in locations not exposed to the open sea, in contrast to the GEN3 ST6 package, which tends to overestimate wave heights in sheltered areas. Additionally, GEN3 ST6 package is more sensitive to narrow fetch geometry and local wind speed variations than the other packages [234].

Although many studies have dealt with the optimal choice of wind database [213, 216, 217, 219, 238] and/or physics setting [214, 215, 218, 220, 234, 235, 236], the optimal model setting is not always the same for every region [239, 240, 241, 236]. Furthermore, only a few of these studies have attempted to reduce the calculation time of their model [218, 220, 235, 242].

IN-SITU CALIBRATION AND VALIDATION DATASETS

The calibration is conducted by assessing the accuracy of different configurations, relying on Datawell time series data covering the period from September 3, 2021, to February 28, 2022, with a half-hour temporal resolution. For validation purposes, Datawell Waverider DWR-G data from June 1, 2022, to September 1, 2022, is used. Additional instrumental hourly data is provided by measurements from the Nortek AWAC-AST, covering the periods from September 20, 2015, to December 4, 2015, and from July 18, 2019, to September 16, 2019. No other in-situ instruments are available in the study area, not even from open-source databases such as the National Data Buoy Center (NDBC) or INSITU_GLO_WAV_DISCRETE_MY_013_045. Finally, altimetric satellite data provided by AODN is used to carry out validation for the time periods in which the in-situ instruments did not provide data.

This comprehensive approach ensures that the calibration and validation processes are robust and thorough. By utilizing a diverse range of datasets, the study aims to provide a detailed assessment of the SWAN numerical model's performance. The inclusion of satellite data helps to fill gaps in the temporal coverage, thereby extending the validation period and enhancing the overall reliability of the model.

WAVE AND WIND FORCING DATASET

Wave characteristics are downscaled by implementing wave and wind forcing in the SWAN model. These forces are sourced from the ERA5 reanalysis dataset, which is generated by the European Centre for Medium-Range Weather Forecasts (ECMWF). Specifically, the ERA5 encompasses data on wave and wind parameters, derived from a combination of satellite altimetry, buoy observations, and numerical models.
To produce a highly representative model, different types of boundary conditions are analyzed. In particular, the frequency-directional spectrum (2D wave spectrum), the synthetic parameters of the wind waves combined with the swell and the synthetic parameters of the only swell are used as different wave forcing, testing their performance. All wave condition information are acquired from the ERA5 database, characterised by a spatial resolution of 0.5°x0.5° and an hourly temporal resolution. The 2D spectrum provided by ERA5 has 24 directions and 30 frequencies, covering the range 0.0345 Hz and 0.54775 Hz. The synthetic parameters of wind waves combined with swell and the synthetic parameters of only swell include significant wave height (H_s), the peak period (T_p), the wave direction (Dir) and the directional spreading (s).

Wind conditions, like wave conditions, are acquired by ERA5. Unlike wave information, wind data are provided with a spatial resolution of 0.25°x0.25° and updated hourly. In particular, the available dataset includes the eastward component of the wind at 10 meters (u10m) and the northerly component of the wind at 10 meters (v10m), i.e. the components of the horizontal wind speed at a height of 10 meters above the surface of the sea. The wind direction components provided by ERA5 adhere to meteorological convention, indicating the direction from which the wind is blowing. Both conventional and neutral wind at 10 m above sea level are analyzed to identify the most suitable dataset. Notably, using conventional wind is a common practice [215, 218, 219, 220], however the results shown in [243], and confirmed in [244], highlight how the neutral wind at 10 meters above sea level is slightly more suitable than the conventional one when referring to satellite observations. This result is based on the global comparison of the wind speed obtained from the ENVISAT [161], Jason-1 [245], Jason-2 [209] and CryoSat-2 [246] satellites and the wind speeds provided by ERA5 for the conventional and neutral wind datasets. Both datasets have a correlation coefficient (CC) equal to 0.95% and a scatter index (SI) of 0.14 but the Root Mean Square Error ($RMSE$) of the neutral dataset is equal to 1.16 m s^{-1}, slightly better than the conventional one corresponding to 1.22 m s^{-1}. Furthermore, [244] demonstrated that using ERA5 neutral wind-forced has a slight advantage over conventional wind-forced in terms of wave model performance.

BATHYMETRIC DATASET

The study researches the best bathymetric datasets by comparing the results obtained from using the General Bathymetric Chart of the Oceans (GEBCO) [247] and European Marine Observation and Data Network (EMODnet) [248] bathymetry. GEBCO is a collaborative project between the International Hydrographic Organization (IHO) and the Intergovernmental Oceanographic Commission (IOC) of UNESCO, which offers a global coverage bathymetric map of the ocean seabed, collecting data from a variety of sources,

such as ship soundings, satellite altimetry, and gravity models. On the other hand, EMODnet Bathymetry is a digital terrain model that provides harmonized bathymetric data from multiple sources, including industry, government agencies, and research institutes, with the goal of offering the most comprehensive and high-resolution depth data for European waters. The main difference of the two bathymetric databases is the spatial resolution: GEBCO has a resolution of approximately 15 arc-sec (around 460 m) while EMODnet provides the bathymetric trend every 3.75 arc-sec (around 115 m). In both cases, the Mean Sea Level (MSL) is used as a reference. Fig. 4.8 shows the bathymetric trend with respect to the two data sources used.

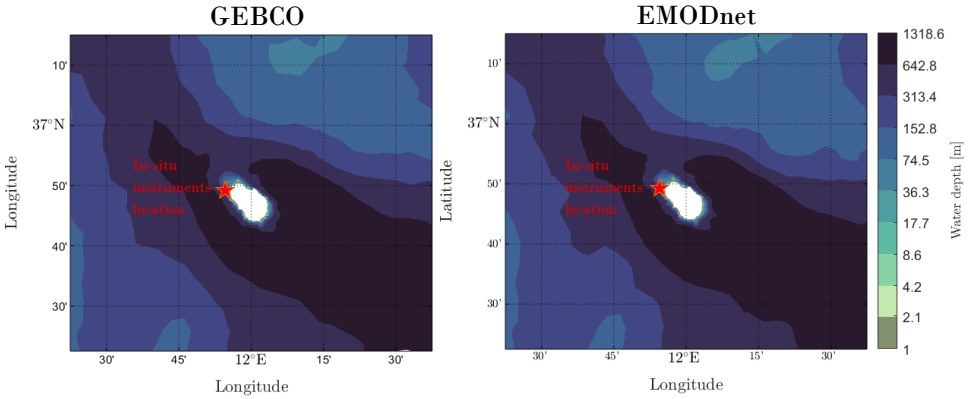

Figure 4.8: Bathymetric trend in reference to the information provided by GEBCO (left panel) and by EMODnet (right panel)

SWAN CALIBRATION

Considering all possible combinations of such an extensive parameters space would be unfeasible in any reasonable time frame, which is indeed the reason why no similar study is found in the literature. To cope with this intrinsic limitation, but still achieving the objectives of this thesis, a novel incremental Stage Gate approach is herein suggested. The Stage Gate approach is indeed employed to investigate the numerous case scenarios and pinpoint optimal configurations at each stage. This approach divides the problem into manageable sub-problems, and finds the best solution for each stage. At each gate, the best solution is identified and serves as a starting point for the subsequent gate, effectively exploring various settings and considering both performance outcomes and computation time requirements. The study assesses the precision of results, focusing on the accuracy of significant wave height and energy period, both of which are crucial parameters for evaluating the energy resource. The island of Pantelleria is used as a case study, comparing the results produced by the different configurations with the available in-situ measurements. Statistical performance indicators are used to assess the accuracy of the results, and the computational time is also considered to find the optimal configurations.

Performance indicator

Various metrics are used to assess the accuracy of the different configurations, in terms of H_s and T_e, and determine the best setup. In addiction to $RMSD$, CC, $BIAS$ and S, other performance parameters used are the Root Mean Square Error ($RMSE$), and the Scatter Index (SI) . The formulations for these parameters are as follows

$$RMSE = \sqrt{\frac{\sum_{n=1}^{N}(x_m - x_o)^2}{N}} \tag{4.6}$$

$$SI = \sqrt{\frac{\sum_{n=1}^{N}[(x_m - \bar{x}_m) - (x_o - \bar{x}_o)]^2}{\sum_{n=1}^{N} x_o^2}} \tag{4.7}$$

In order to gauge the precision of the outcomes, the Taylor diagram, as described in [249] and relying on $RMSD$, CC, and s_d metrics, is employed for every gate. This methodology is applied to appraise different SWAN configurations by examining how closely the computed values for significant wave height (H_s) and energy period (T_e) align with observed data. Furthermore, the normalized computational time for each configuration (N_{ct}), relative to the specific Stage-Gate results, is considered to assess its computational efficiency.

MODEL SET-UP

The SWAN model is set up in a spherical coordinate system as it better accommodates small- and large-scale calculations than the Cartesian system. The non-stationary mode is adopted to describe sea state evolution in detail, evaluating the interaction between incoming waves and those already developed in the computational grid. Wind inputs and wave boundaries are provided hourly. The explicit scheme is preferred over the implicit one for the wave propagation scheme. In the case of implicit models, the Courant Friedrichs Lewy criterion [250] must be considered, ensuring that wave energy travels through at least one geographical cell within a time-step. In other words, it must be ascertained that the maximum time-step is less than the spatial resolution divided by the velocity of the shallow water group of the fastest component. In practice, this means that for a resolution of 100 m and a frequency of 0.04 Hz, the time-step should not exceed 2.5 s, which would result in a high computational time. To address this problem, the Backward Space Backward Time (BSBT) method [123] is used since it is an explicit scheme and guarantees numerical stability, regardless of the chosen temporal resolution.

A maximum of 10 iterations per time-step is used. This means that if the convergence of H_s is not reached within 10 iterations, the calculation proceeds to the next time-step. It is important to highlight that in non-stationary analysis, the maximum number of iterations typically falls from 1 to 4. However, increasing this value significantly reduces the risk of obtaining inaccurate results, and usually, the number of challenging-to-compute time-steps is limited.

Table 4.7 summarises the SWAN model setup characteristics before the Stage-Gate analysis. In particular, the characteristics reported as predefined (P) are defined at the beginning of the analysis and not explored during the present work. Otherwise, the examined features are marked as tuned (T).

Table 4.7: SWAN model set-up, distinguishing between predefined (P) features at the beginning of the analysis and tuned (T) ones during the study

Features	Setting	Type
Mode	Non-stationary	P
Scheme	BSBT [123]	P
Number of directions	36	P
Number of frequency	36	P
Minimum frequency	0.04 Hz	T
Maximum frequency	1 Hz	T
Maximum iteration number	10	P
Wind forcing	Conventional wind	T
Wave boundary conditions	Synthetic parameters of the wind waves combined with the swell	T
Exponential wind growth	Default (Komen [68])	T
Whitecapping	Default (Komen [68])	T
Depth-induced breaking	Default (Battjes and Janssen [251])	P
Quadruplets	DIA (Hasselmann et al. [125])	P
Wind drag formula	Default (Hwang [133])	T
Output calculation	30 min	P
Time-step	30 min	T

STAGE-GATES APPROACH

The Stage-Gate process methodology is utilized to fine-tune and select the most suitable configuration for the SWAN model based on quantitative performance indicators. This approach simplifies problem-solving by breaking it down into smaller elements. At each stage, the aim is to pinpoint the best configuration of one variable, which then serves as the starting point for the subsequent phase. This methodology facilitates a systematic analysis and in-depth examination of various components of the SWAN model, allowing each element to be investigated individually.

Moreover, this approach establishes a structured framework for decision-making, streamlining the identification of the best configuration at each gate. One of the primary merits of this methodology lies in its capacity to simplify the tuning and calibration process while efficiently identifying the optimal parameters. Through a methodical progression through each gate and consideration of both model performance and computation time, sensitivity studies are conducted on various model aspects, resulting in

effective model calibration.

If an analysis of all the settings combinations had been undertaken, the scope of the problem would have expanded significantly, increasing from the 40 configurations evaluated in the Stage-Gate process to over 250,000 distinct variations.

Fig. 4.9 provides a concise overview of the specific elements addressed in each process phase.

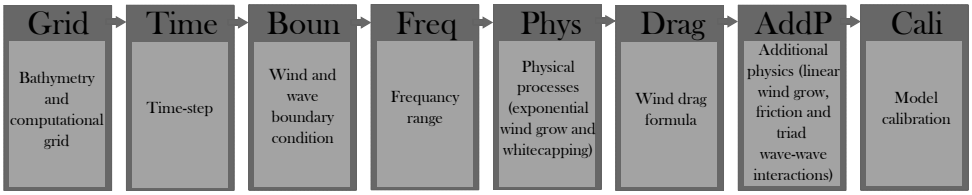

Figure 4.9: Diagram depicting the sequential application of the Stage-Gate approach for the SWAN model set-up

The initial stage involves selecting bathymetric input and configuring the computational grid, marking a critical decision in model establishment. Subsequently, the second stage involves exploring the time-step to identify a configuration that achieves an best balance between computational efficiency and accuracy. Based on these findings, all subsequent configurations are then refined. Following this, an analysis of wave boundary conditions and the wind field is conducted to identify the crucial inputs of model forcing. Examining the frequency range represents the first real step in model tuning. This is followed by identifying best formulations for the physics of exponential wind growth and withecapping, both crucial aspects of model configuration. Following, the sensitivity analysis of the wind drag formulation is carried out, and the inclusion of additional physics is investigated. Finally, the resulting best configuration undergoes calibration.

Tables are used at each Stage-Gate subsection as a means to encapsulate the features of the configurations examined at various gates. To maintain clarity regarding the best configuration transition between one gate and the next, each Stage-Gate table adheres to the following convention: the best configuration for each gate is indicated using **bold** text, and the best configuration from the preceding gate is marked with a superscript *.

Bathymetric source and mesh resolution

Different configurations regarding the bathymetric source and spatial mesh resolutions are investigated. The use of unstructured computational grids is adopted to accurately describe the spatial variability of the seabed and reduce computation times: a greater resolution is defined in the areas near the coast, imposing a minimum resolution of 100 m and a maximum one of 500 m, while a broad one is used for the offshore area. Different configurations are identified by varying the maximum offshore resolution (Max_{el}=5000 m and Max_{el}=10000 m) and the grade parameter (α=0.15 and α=0.2), which defines the percentage of the increase in the spatial resolution of the offshore cells. The GEBCO and EMODnet databases are used to create two subgroups of analyses having the same mesh characteristics but different bathymetry sources. Table 4.8 summarizes the differ-

ent characteristics of the configurations investigated during the *bathymetric source and mesh resolution* Stage-Gate.

Table 4.8: Configurations features analyzed in the *bathymetric source and mesh resolution* Stage-Gate

Configurations	Bathymetry	Max_el [m]	α
$Grid_1$	GEBCO	5000	0.15
$Grid_2$	GEBCO	5000	0.2
$Grid_3$	GEBCO	10000	0.2
$Grid_4$	EMODnet	5000	0.15
$Grid_5$	EMODnet	5000	0.2
$Grid_6$	**EMODnet**	**10000**	**0.2**

Fig. 4.10 is the representation of the different meshes used in the Stage-Gate to identify the best computational grid.

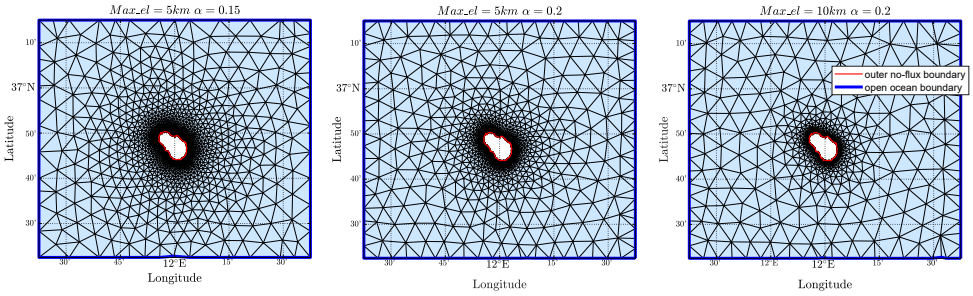

Figure 4.10: Representation of the different meshes used in the Stage-Gate to identify the best computational grid. The three images show meshes with varying parameters: Max_el set to 5 km and α varying between 0.15 and 0.2 in the first two, and Max_el set to 10 km with α=0.2 in the third image. The red lines represent the outer no-flux boundary, while the blue lines indicate the open ocean boundary.

Fig. 4.11 represents the Taylor diagram of the H_s and T_e, referring to the different configurations, as well as the respective N_{ct}.

Tab. 4.9 and 4.10 provide the values of the performance parameters for the different configurations for H_s and T_e, respectively.

The comparison between the parameters modelled by SWAN and those measured by the buoy indicates that the best configuration is $Grid_6$, with $RMSD$ and CC values of 0.242 m and 96.8% for H_s, and 0.665 s and 88.1% for T_e, respectively. It also results in a 23% reduction in calculation times compared to the $Grid_4$ configuration, which employs the same bathymetric dataset but with a higher computational mesh resolution. This outcome is primarily attributed to two factors. Firstly, the bathymetric trend provided by EMODnet has a higher resolution than that provided by GEBCO, resulting in a more precise outcome. Comparing $Grid_3$ and $Grid_6$, which differ only in the bathymetric dataset adopted, there is an improvement of 2.4% on the $RMSD_{Hs}$ and of 8.4%

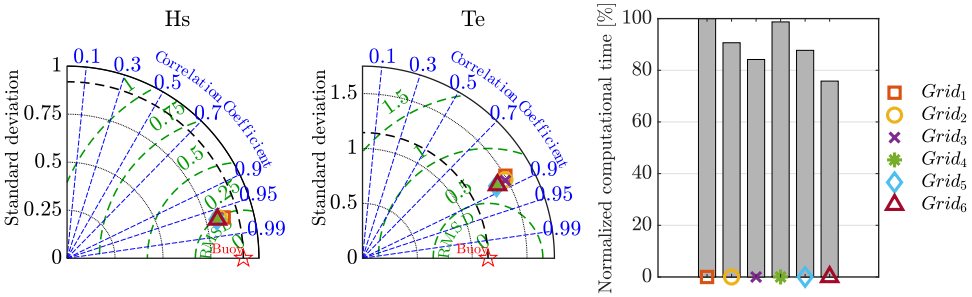

Figure 4.11: Taylor diagrams, applied to H_s and T_e, and comparison of normalized computational times regarding the different configurations analyzed in the *bathymetric source and mesh resolution* Stage-Gate

Table 4.9: H_s Performance indicator for *bathymetric source and mesh resolution* Stage-Gate

	H_s							
Config.	*RMSE* [s]	*RMSD* [s]	*BIAS* [s]	*CC*[-]	s_{d_m} [s]	s_{d_o} [s]	*SI* [-]	*S* [-]
$Grid_1$	0.272	0.236	-0.136	0.968	0.844	0.919	0.159	1.115
$Grid_2$	0.289	0.245	-0.155	0.967	0.821	0.919	0.165	1.140
$Grid_3$	0.297	0.248	-0.163	0.966	0.815	0.919	0.167	1.149
$Grid_4$	0.263	0.243	-0.101	0.968	0.812	0.919	0.164	1.109
$Grid_5$	0.269	0.244	-0.113	0.968	0.807	0.919	0.165	1.119
***Grid*$_6$**	**0.266**	**0.242**	**-0.111**	**0.968**	**0.811**	**0.919**	**0.163**	**1.115**

Table 4.10: T_e Performance indicator for *bathymetric source and mesh resolution* Stage-Gate

	T_e							
Config.	*RMSE* [s]	*RMSD* [s]	*BIAS* [s]	*CC*[-]	s_{d_m} [s]	s_{d_o} [s]	*SI* [-]	*S* [-]
$Grid_1$	0.812	0.768	0.262	0.866	1.504	1.145	0.165	0.930
$Grid_2$	0.764	0.726	0.238	0.877	1.479	1.145	0.155	0.936
$Grid_3$	0.762	0.726	0.232	0.878	1.483	1.145	0.155	0.937
$Grid_4$	0.749	0.660	0.354	0.882	1.390	1.145	0.141	0.920
$Grid_5$	0.749	0.661	0.352	0.881	1.387	1.145	0.142	0.921
***Grid*$_6$**	**0.745**	**0.665**	**0.338**	**0.881**	**1.396**	**1.145**	**0.142**	**0.923**

on the $RMSD_{Te}$, going from 0.248 m to 0.242 m and 0.726 s to 0.665 s, respectively. Secondly, among the three configurations based on EMODnet bathymetric information, the

metrics of H_s and T_e were slightly different but with a substantial decrease in N_{ct}.

Time-step

The analysis focuses on the computational time-step to find the most balanced solution between performance and computational efficiency. Four distinct configurations with time-steps of 5, 10, 15, and 30 minutes, as outlined in Table 4.11, are examined.

Table 4.11: Configurations features analyzed in the *time-step* Stage-Gate

Configurations	Time-step [minutes]
$Time_1$	5
$Time_2$	10
$Time_3$	15
Time*$_4$	**30**

The Taylor diagram for H_s and T_e (Fig. 4.12) reveals that the performances of these configurations are quite similar. Nevertheless, there is only a marginal performance gain associated with increasing the computational time, maintaining the same maximum number of iterations.

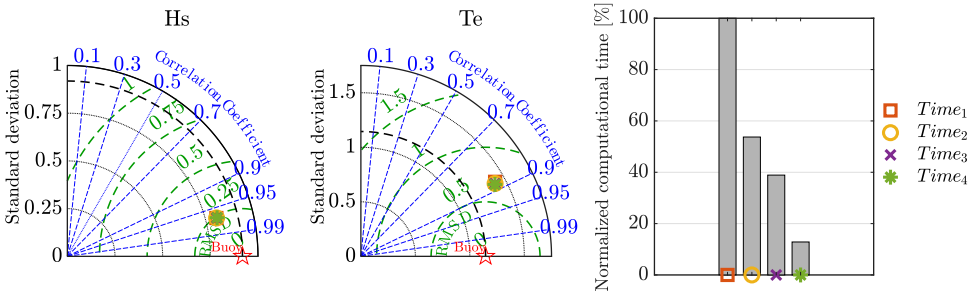

Figure 4.12: Taylor diagrams, applied to H_s and T_e, and comparison of normalized computational times regarding the different configurations analyzed in the *time-step* Stage-Gate

Table 4.12 and 4.13 present the performance parameter values for the various configurations.

As previously discussed in [215], reducing the time-step without a concurrent increase in the maximum number of iterations does not automatically enhance precision but certainly extends the computational time, as sea state propagation becomes more computationally intensive. To boost model performance, it is advisable to augment both the maximum number of iterations and decrease the time-step.

In this analysis, the number of iterations is not further increased to limit the increase in computational time, considering 10 iterations are already sufficiently expensive from the point of view of computational cost. Given that variations in the time-step do not

Table 4.12: H_s Performance indicator for *time-step* Stage-Gate

	H_s							
Config.	$RMSE$ [s]	$RMSD$ [s]	$BIAS$ [s]	CC[-]	s_{d_m} [s]	s_{d_o} [s]	SI [-]	S [-]
$Time_1$	0.271	0.243	-0.120	0.968	0.807	0.919	0.164	1.124
$Time_2$	0.269	0.243	-0.116	0.968	0.808	0.919	0.164	1.121
$Time_3$	0.268	0.243	-0.114	0.968	0.809	0.919	0.164	1.119
Time*$_4$	**0.266**	**0.242**	**-0.111**	**0.968**	**0.811**	**0.919**	**0.163**	**1.115**

Table 4.13: T_e Performance indicator for *time-step* Stage-Gate

	T_e							
Config.	$RMSE$ [s]	$RMSD$ [s]	$BIAS$ [s]	CC[-]	s_{d_m} [s]	s_{d_o} [s]	SI [-]	S [-]
$Time_1$	0.777	0.689	0.358	0.874	1.409	1.145	0.148	0.918
$Time_2$	0.756	0.673	0.343	0.879	1.401	1.145	0.144	0.921
$Time_3$	0.754	0.672	0.341	0.879	1.400	1.145	0.144	0.922
Time*$_4$	**0.745**	**0.665**	**0.338**	**0.881**	**1.396**	**1.145**	**0.142**	**0.923**

affect result quality of H_s but mainly influence computational time and a slight improvement in performance in T_e is observed, the best choice is the $Time_4$ configuration. Indeed, the $Time_4$ configuration reduces the computational burden by 87% compared to the $Time_1$ configuration, with similar result accuracy for H_s and an improvement for T_e.

Wind and Wave boundary condition

Different wave boundary conditions and forcing wind fields are analyzed to identify the configuration that strikes a well-balanced compromise between accuracy and computational efficiency (Table 4.14).

Both wind and wave information are acquired from the ERA5 database. Different configurations are analyzed regarding wave boundary conditions, using synthetic parameters referring to the combination of wind waves and swell, synthetic ones based on the only swell, and the 2D frequency-directional spectrum. Furthermore, for each wave boundary condition studied, two subcategories are created using conventional and neutral wind at 10 m above sea level as a forcing wind field. Observing the Taylor diagram (Fig. 4.13) regarding the T_e, it emerges that the use of the 2D frequency-directional spectrum drastically increases the accuracy of the results compared to the configuration based on the synthetic parameters of combined wind waves and swell.

The performance parameter values for the different configurations, in reference to H_s and T_e, are shown in Tables 4.15 and 4.16.

Table 4.14: Configurations features analyzed in the *wind and wave boundary conditions* Stage-Gate

Configurations	Wave boundary condition	Wind forcing at 10 m a.s.l.
$Boun_1$	2D frequency-directional wave spectrum	Conventional wind
***Boun*$_2$**	**2D frequency-directional wave spectrum**	**Neutral wind**
$Boun_3*$	Shyntetic parameters of combined wind waves and swell	Conventional wind
$Boun_4$	Shyntetic parameters of combined wind waves and swell	Neutral wind
$Boun_5$	Shyntetic parameters of swell	Conventional wind
$Boun_6$	Shyntetic parameters of swell	Neutral wind

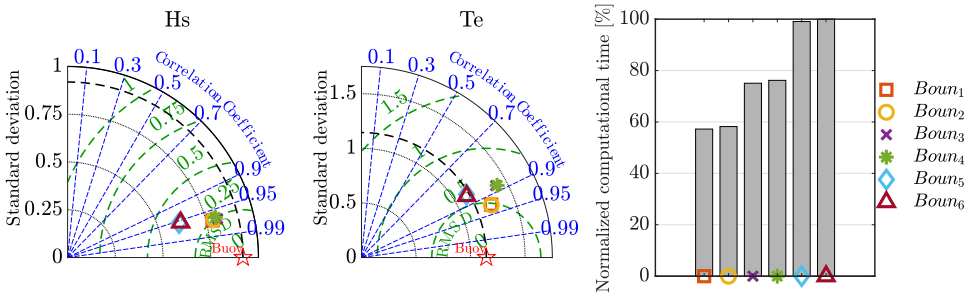

Figure 4.13: Taylor diagrams, applied to H_s and T_e, and comparison of normalized computational times regarding the different configurations analyzed in the *wind and wave boundary conditions* Stage-Gate

The reason for this result is mainly linked to the almost constant simultaneous overlap of different sea states, as described in [36]. In particular, the analysis is conducted based on the wave conditions of 2022, and the co-presence of the swell with the wind waves is not negligible, as swell represents approximately 35% of the total wave energy in Pantelleria during that year. The absolute angular difference of the average direction of swell and wind waves is less than $\pi/4$ approximately 64% of the time. The remaining maritime states are characterized by swell, which has a significantly distinct mean direction from that of the wind waves. Consequently, even the assignment of a single mean direction for both sea states involves non-negligible errors. In fact, the use of synthetic parameters is valid only in the cases of single sea states.

Table 4.15: H_s Performance indicator for *wind and wave boundary conditions* Stage-Gate

	H_s							
Config.	$RMSE$ [s]	$RMSD$ [s]	$BIAS$ [s]	CC[-]	s_{d_m} [s]	s_{d_o} [s]	SI [-]	S [-]
$Boun_1$	0.286	0.251	-0.137	0.969	0.783	0.919	0.169	1.148
***Boun*$_4$**	**0.277**	**0.250**	**-0.120**	**0.968**	**0.791**	**0.919**	**0.169**	**1.132**
$Boun_3*$	0.266	0.242	-0.111	0.968	0.811	0.919	0.163	1.115
$Boun_4$	0.294	0.255	-0.146	0.965	0.801	0.919	0.172	1.145
$Boun_5$	0.473	0.380	-0.282	0.956	0.611	0.919	0.256	1.382
$Boun_6$	0.457	0.374	-0.263	0.955	0.620	0.919	0.252	1.356

Table 4.16: T_e Performance indicator for *wind and wave boundary conditions* Stage-Gate

	T_e							
Config.	$RMSE$ [s]	$RMSD$ [s]	$BIAS$ [s]	CC[-]	s_{d_m} [s]	s_{d_o} [s]	SI [-]	S [-]
$Boun_1$	0.520	0.487	0.183	0.926	1.284	1.145	0.104	0.956
***Boun*$_4$**	**0.509**	**0.482**	**0.164**	**0.927**	**1.284**	**1.145**	**0.103**	**0.960**
$Boun_3*$	0.745	0.665	0.338	0.881	1.396	1.145	0.142	0.923
$Boun_4$	0.674	0.669	0.085	0.883	1.409	1.145	0.143	0.968
$Boun_5$	0.676	0.605	-0.301	0.858	1.122	1.145	0.130	1.068
$Boun_6$	0.667	0.592	-0.307	0.863	1.117	1.145	0.127	1.070

The configurations $Boun_5$ and $Boun_6$ are defined using the synthetic parameters derived only from the swell sea states to avoid the incorrect assumption regarding the occurrence of exclusively monopeak sea states, as described above. The results show that there is inadequate congruence between the results of the SWAN model and the buoy observations. The main reason is linked to the lower energy supplied to the system, which is not compensated by that supplied by the wind, as the analysis area is relatively small: the wind, in fact, does not have a sufficiently large fetch to transfer energy to the sea. Consequently, the 2D frequency-directional spectrum is the best wave boundary condition.

Regarding the wind field, the $Boun_2$ configuration based on neutral wind is better than the $Boun_1$ configuration based on conventional one. From a computational time point of view, $Boun_2$ requires only 1.6% more time than $Boun_1$. In conclusion, the $Boun_2$ configuration is chosen as the best configuration in the *wind and wave boundary condition* Stage-Gate, having an $RMSD_{Hs}$ equal to 0.250 m, CC_{Hs} equal to 96.8%, $RMSD_{Te}$ equal to 0.482 s and CC_{Hs} equal to 92.7%, with a reduction in N_{CT} of almost

30% compared to the optimal configuration of the previous gate, i.e. $Boun_3$.

Frequency range

In this Stage-Gate, variations are introduced in both the frequency range of the prognostic interval and the range used for calculating integral parameters. Users are given the flexibility to set minimum and maximum frequencies for computing integral output parameters. In the $Freq_1$ configuration, the same frequency range as the Datawell Waverider DWR-G buoy is applied for both the prognostic range and the range used to compute integral parameters. For the $Freq_2$ configuration, the interval for spectral density propagation aligns with the recommendations found in the SWAN manual [116], utilizing the buoy frequency range for the output calculations as well. Lastly, the $Freq_3$ configuration is established using the SWAN manual suggested minimum and maximum frequency values for both frequency categories. Details of the minimum and maximum frequency values for these configurations are summarized in Table 4.17.

Table 4.17: Configurations features analyzed in the *frequancy range* Stage-Gate

Configurations	Prognostic range	Output range
***Freq*$_1$**	**0.01 Hz - 0.64 Hz**	**0.01 Hz - 0.64 Hz**
$Freq_2$	0.04 Hz - 1Hz	0.01Hz - 0.64Hz
$Freq_3*$	0.04 Hz - 1Hz	0.04Hz - 1Hz

Fig. 5.4 offers a concise overview of the performance of these studied configurations

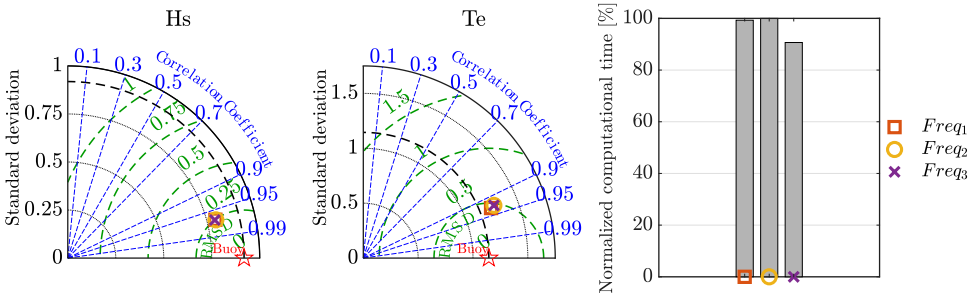

Figure 4.14: Taylor diagrams, applied to H_s and T_e, and comparison of normalized computational times regarding the different configurations analyzed in the *frequancy range* Stage-Gate

Tables 4.18 and 4.19 detail the performance parameters for each configuration in regard to H_s and T_e, respectively.

It is evident that there is no substantial improvement in the accuracy of H_s. When it comes to T_e, the $Freq_1$ configuration yields results more closely aligned with those measured by the buoy. Specifically, $RMSD_{Te}$ decreases from 0.482 s to 0.456 s, and CC_{Te} improves from 92.7% to 93.1% when comparing $Freq_3$ and $Freq_1$.

Table 4.18: H_s Performance indicator for *frequancy range* Stage-Gate

	H_s							
Config.	$RMSE$ [s]	$RMSD$ [s]	$BIAS$ [s]	CC[-]	s_{d_m} [s]	s_{d_o} [s]	SI [-]	S [-]
$Freq_1$	**0.277**	**0.250**	**-0.121**	**0.968**	**0.795**	**0.919**	**0.168**	**1.131**
$Freq_2$	0.280	0.247	-0.131	0.968	0.797	0.919	0.167	1.137
$Freq_3*$	0.277	0.250	-0.120	0.968	0.791	0.919	0.169	1.132

Table 4.19: T_e Performance indicator for *frequancy range* Stage-Gate

	T_e							
Config.	$RMSE$ [s]	$RMSD$ [s]	$BIAS$ [s]	CC[-]	s_{d_m} [s]	s_{d_o} [s]	SI [-]	S [-]
$Freq_1$	**0.497**	**0.456**	**0.196**	**0.931**	**1.251**	**1.145**	**0.098**	**0.956**
$Freq_2$	0.509	0.482	0.164	0.927	1.284	1.145	0.103	0.960
$Freq_3*$	0.509	0.482	0.164	0.927	1.284	1.145	0.103	0.960

This outcome can be attributed to narrowing the frequency range used for spectrum propagation, which, with the same number of frequencies used for discretizing the frequency space, provides a more accurate spectrum description. Despite an 8% increase in computational time, the $Freq_1$ configuration is preferred over the $Freq_3$ configuration.

Whitecapping and exponencial wind grow

The study involves an assessment of the SWAN model performance with respect to various physical models related to whitecapping and exponential wind growth. Table 4.20 designates the specific whitecapping and exponential wind growth models employed in each configuration.

Among the array of configurations scrutinized, the $Phys_2$ configuration stands out as the most accurate in terms of both H_s and T_e. This distinction is evident in Fig. 4.15, in fact, the alignment of the $Phys_2$ configuration with the buoy data emerges from the Taylor diagram.

In Tables 4.21 and 4.22, the performance parameters for the different configurations, in regard to H_s and T_e, respectively, are provided.

When comparing $Phys_2$ to the $Phys_3$ configuration, which corresponds to the best choice from the *frequency range* Stage-Gate, it is observed that the $RMSD_{Hs}$ decreases from 0.250 m to 0.236 m, while CC_{Hs} remains relatively constant at 96.8%. The most notable improvement pertains to T_e, with $RMSD_{Te}$ dropping from 0.482 s to 0.439 s, and CC_{Te} increasing from 92.7% to 93.4%. Nevertheless, it is worth noting that there is a 24% increase in computational time.

Table 4.20: Configurations features analyzed in the *whitecapping and exponential wind growth* Stage-Gate

Configurations	Exponential wind growth	Whitecapping
$Phys_1$	Janssen	Janssen
***Phys*$_2$**	**Rogers**	**Rogers**
$Phys_3$*	Komen	Komen
$Phys_4$	Yan	Westhuysen
$Phys_5$	Komen	Janssen
$Phys_6$	Rogers	Janssen
$Phys_7$	Rogers	Komen
$Phys_8$	Yan	Komen

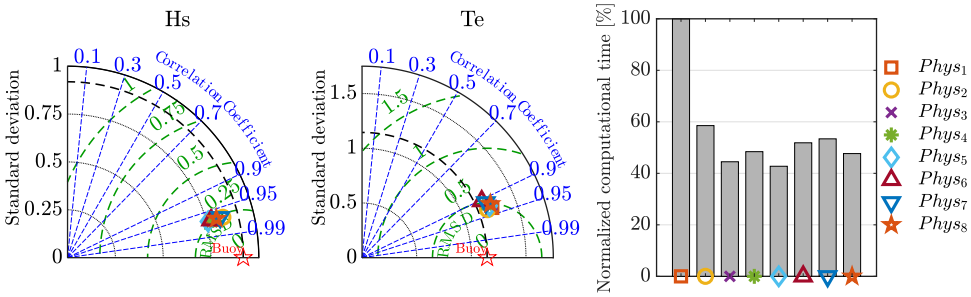

Figure 4.15: Taylor diagrams, applied to H_s and T_e, and comparison of normalized computational times regarding the different configurations analyzed in the *whitecapping and exponential wind growth* Stage-Gate

In the broader context, the Taylor diagram for H_s reveals a significant variation in s_d, ranging from 0.784 m for $Phys_4$ to 0.839 m for $Phys_2$, while the buoy dataset registers s_d at 0.919 m.

Turning attention to the model sensitivity concerning T_e performance, there is considerable variability in terms of CC. For instance, $Phys_6$ records a CC_{Te} value of 90.4%, whereas the top-performing configuration, $Phys_2$, achieves a value of 93.4%.

Wind drag

The three available wind drag formulations within the ST6 package are examined to assess the model sensitivity, as summarized in Table 4.23.

The *HWANG* formulation, as suggested by Hwang et al. [133], serves as the default choice and is recommended for use. The other two options, namely *FAN* [134] and *ECMWF* [113], employ iterative procedures. It is important to note that selecting non-default formulations is an option advised in the SWAN manual due to results in a significant decrease in wave height values [123].

Following a comparative analysis of the results (Fig. 4.16), it becomes evident that the default formulation outperforms the others both in terms of conformity with observed

Table 4.21: H_s Performance indicator for *whitecapping and exponential wind growth* Stage-Gate

	H_s							
Config.	$RMSE$ **[s]**	$RMSD$ **[s]**	$BIAS$ **[s]**	CC[-]	s_{d_m} **[s]**	s_{d_o} **[s]**	SI [-]	S [-]
$Phys_1$	0.277	0.254	-0.111	0.968	0.786	0.919	0.171	1.129
***Phys*$_2$**	**0.245**	**0.236**	**-0.064**	**0.968**	**0.839**	**0.919**	**0.159**	**1.072**
$Phys_3*$	0.277	0.250	-0.121	0.968	0.795	0.919	0.168	1.131
$Phys_4$	0.296	0.252	-0.155	0.968	0.784	0.919	0.170	1.161
$Phys_5$	0.310	0.263	-0.164	0.968	0.759	0.919	0.178	1.181
$Phys_6$	0.309	0.258	-0.169	0.968	0.775	0.919	0.174	1.176
$Phys_7$	0.269	0.243	-0.117	0.967	0.826	0.919	0.164	1.112
$Phys_8$	0.269	0.248	-0.105	0.967	0.804	0.919	0.167	1.115

Table 4.22: T_e Performance indicator for *whitecapping and exponential wind growth* Stage-Gate

	T_e							
Config.	$RMSE$ **[s]**	$RMSD$ **[s]**	$BIAS$ **[s]**	CC[-]	s_{d_m} **[s]**	s_{d_o} **[s]**	SI [-]	S [-]
$Phys_1$	0.504	0.457	0.212	0.934	1.275	1.145	0.098	0.951
***Phys*$_2$**	**0.464**	**0.439**	**0.150**	**0.934**	**1.229**	**1.145**	**0.094**	**0.966**
$Phys_3*$	0.497	0.456	0.196	0.931	1.251	1.145	0.098	0.956
$Phys_4$	0.494	0.482	0.108	0.921	1.239	1.145	0.103	0.973
$Phys_5$	0.496	0.474	0.147	0.926	1.258	1.145	0.101	0.965
$Phys_6$	0.524	0.520	0.065	0.904	1.211	1.145	0.111	0.983
$Phys_7$	0.515	0.505	0.099	0.913	1.240	1.145	0.108	0.975
$Phys_8$	0.500	0.492	0.089	0.922	1.273	1.145	0.105	0.975

Table 4.23: Configurations features analyzed in the *wind drag formula* Stage-Gate

Configurations	**Wind drag formula**
$Drag_1$	ECMWF
$Drag_2$	FAN
***Drag*$_3*$**	**HWANG**

data and computational efficiency. The performance parameters for the various config-

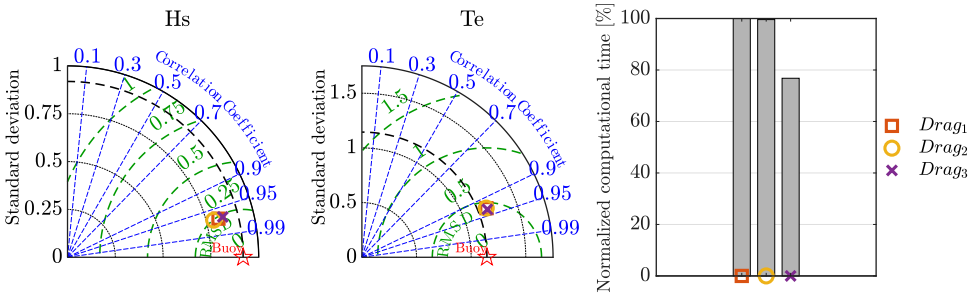

Figure 4.16: Taylor diagrams, applied to H_s and T_e, and comparison of normalized computational times regarding the different configurations analyzed in the *wind drag formula* Stage-Gate

urations, in regard to H_s and T_e, are summarized in Tables 4.24 and 4.25, respectively.

Table 4.24: H_s Performance indicator for *wind drag formula* Stage-Gate

	H_s							
Config.	*RMSE* **[s]**	*RMSD* **[s]**	*BIAS* **[s]**	*CC*[-]	s_{d_m} **[s]**	s_{d_o} **[s]**	*SI* [-]	*S* [-]
$Drag_1$	0.262	0.239	-0.107	0.969	0.815	0.919	0.161	1.111
$Drag_2$	0.275	0.248	-0.121	0.969	0.789	0.919	0.167	1.134
***Drag*$_3$∗**	**0.245**	**0.236**	**-0.064**	**0.968**	**0.839**	**0.919**	**0.159**	**1.072**

Table 4.25: T_e Performance indicator for *wind drag formula* Stage-Gate

	T_e							
Config.	*RMSE* **[s]**	*RMSD* **[s]**	*BIAS* **[s]**	*CC*[-]	s_{d_m} **[s]**	s_{d_o} **[s]**	*SI* [-]	*S* [-]
$Drag_1$	0.480	0.449	0.172	0.930	1.225	1.145	0.096	0.962
$Drag_2$	0.480	0.450	0.168	0.930	1.224	1.145	0.096	0.962
***Drag*$_3$∗**	**0.464**	**0.439**	**0.150**	**0.934**	**1.229**	**1.145**	**0.094**	**0.966**

As a result, the $Drag_3$ configuration is adopted to designate the most appropriate wind drag formulation for the subsequent Stage-Gate.

In terms of computational times, the $Drag_1$ and $Drag_2$ configurations exhibit similar performance, with N_{cd} increased by approximately 23% compared to that of the $Drag_3$ configuration. As for the accuracy of H_s, the s_d parameter varies significantly depending on the wind drag formulation. The buoy-measured data corresponds to an

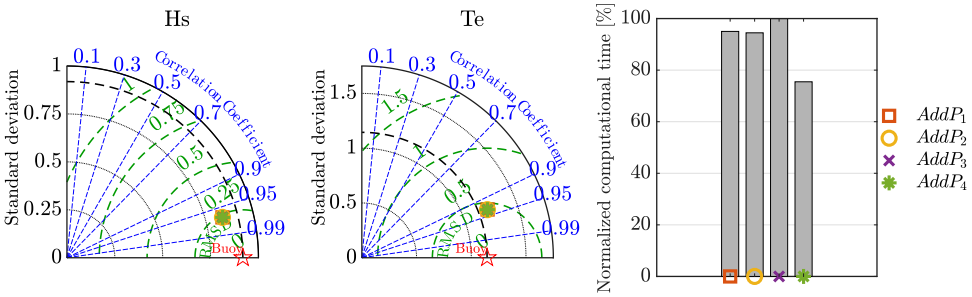

Figure 4.17: Taylor diagrams, applied to H_s and T_e, and comparison of normalized computational times regarding the different configurations analyzed in the *linear wind growth, friction and triad* Stage-Gate

s_d of 0.919 m, while the different configurations yield datasets with s_d values of 0.815 m, 0.789 m, and 0.968 m for $Drag_1$, $Drag_2$, and $Drag_3$, respectively. Nevertheless, the performance of the T_e parameter remains consistent regardless of the wind drag formulation employed.

Linear wind grow, friction and triad wave-wave interaction

The investigation delves into the influence of additional physics as part of the quest for the optimal settings of the SWAN model. Specifically, attention is directed toward examining the effects of linear wind growth, bottom friction, and the wave-wave interaction of the triad.

Each additional physical aspect is individually scrutinized to gauge its impact on the SWAN model's performance. Table 4.26 enumerates the phenomena under consideration for each configuration.

Table 4.26: Configurations features analyzed in the *linear wind growth, friction and triad* Stage-Gate

Configurations	Linear wind growth	Friction	Triad
$AddP_1$	Cavaleri and Malanotte-Rizzoli	deactivated	deactivated
$AddP_2$	deactivated	JONSWAP	deactivated
$AddP_3$	deactivated	deactivated	LTA method of Elderberky
AddP*$_4$	**deactivated**	**deactivated**	**deactivated**

Upon comparing the results across various configurations, as illustrated in Fig. 4.17, it becomes evident that there are minimal discernible variations in performance. However, significant discrepancies emerge in terms of computational time. Notably, the $AddP_4$ configuration emerges as the best choice, boasting a lower computational time than the others.

Tables 4.27 and 4.28 outline the performance parameters for the different configurations in regard to H_s and T_e, respectively.

Table 4.27: H_s Performance indicator for *linear wind growth, friction and triad* Stage-Gate

	H_s							
Config.	$RMSE$ **[s]**	$RMSD$ **[s]**	$BIAS$ **[s]**	CC[-]	s_{d_m} **[s]**	s_{d_o} **[s]**	SI [-]	S [-]
$AddP_1$	0.244	0.236	-0.063	0.968	0.839	0.919	0.159	1.071
$AddP_2$	0.244	0.236	-0.064	0.968	0.839	0.919	0.159	1.072
$AddP_3$	0.245	0.236	-0.064	0.968	0.839	0.919	0.159	1.072
AddP*$_4$	**0.245**	**0.236**	**-0.064**	**0.968**	**0.839**	**0.919**	**0.159**	**1.072**

Table 4.28: T_e Performance indicator for *linear wind growth, friction and triad* Stage-Gate

	T_e							
Config.	$RMSE$ **[s]**	$RMSD$ **[s]**	$BIAS$ **[s]**	CC[-]	s_{d_m} **[s]**	s_{d_o} **[s]**	SI [-]	S [-]
$AddP_1$	0.465	0.440	0.148	0.934	1.231	1.145	0.094	0.966
$AddP_2$	0.463	0.439	0.148	0.934	1.228	1.145	0.094	0.966
$AddP_3$	0.464	0.439	0.150	0.934	1.229	1.145	0.094	0.966
AddP*$_4$	**0.464**	**0.439**	**0.150**	**0.934**	**1.229**	**1.145**	**0.094**	**0.966**

Physics calibration

The *physics calibration* Stage-Gate is implemented to assess the model sensitivity regarding the coefficients within Rogers exponential wind growth and whitecapping formulations. Specifically, two different windscaling (W_s) values, W_s=32 and W_s=35, are employed in conjunction with three distinct combinations of a_1 and a_2 dissipation coefficients. It is important to note that as the W_s value increases, the impact of wind-induced wave growth intensifies, while a decrease in W_s diminishes the wind influence on wave development. The whitecapping dissipation coefficients a_1 and a_2 are associated with intrinsic wave breaking and the modulation of longer waves leading to relatively short wave breaking, as detailed in [252].

Table 4.29 provides an overview of the calibration parameter values for each configuration.

Upon comparing the computational time (N_{ct}) across configurations, as depicted in Fig. 4.18, it becomes apparent that the results exhibit similarity, with the use of W_s equal to 35, resulting in a slight increase in computational time, approximately 3%. The perfor-

Table 4.29: Configurations features analyzed in the *calibration* Stage-Gate

Configurations	a1	a2	W_s
$Cali_1$	6.50E-06	8.50E-05	32
$Cali_2$	6.50E-06	8.50E-05	35
$Cali_3$	**5.70E-07**	**8.00E-06**	**32**
$Cali_4$	5.70E-07	8.00E-06	35
$Cali_5*$	2.80E-06	3.50E-05	32
$Cali_6$	2.80E-06	3.50E-05	35

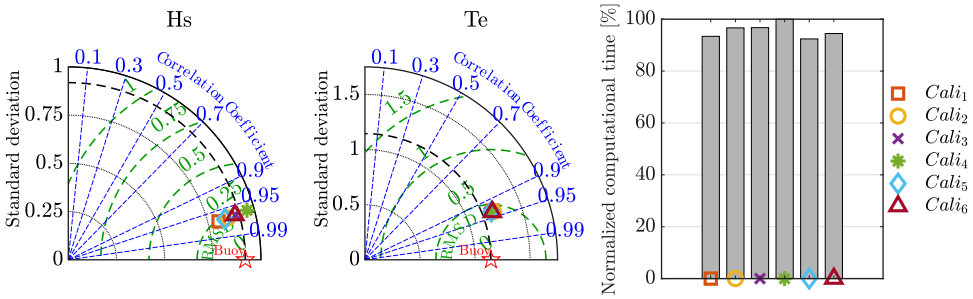

Figure 4.18: Taylor diagrams, applied to H_s and T_e, and comparison of normalized computational times regarding the different configurations analyzed in the *calibration* Stage-Gate

mance parameters for the various configurations in regard to H_s and T_e are summarized in Tables 4.30 and 4.31, respectively.

Table 4.30: H_s Performance indicator for *calibration* Stage-Gate

	H_s							
Config.	$RMSE$ [s]	$RMSD$ [s]	$BIAS$ [s]	CC[-]	s_{d_m} [s]	s_{d_o} [s]	SI [-]	S [-]
$Cali_1$	0.264	0.243	-0.103	0.969	0.805	0.919	0.164	1.114
$Cali_2$	0.240	0.235	-0.045	0.967	0.855	0.919	0.159	1.053
$Cali_3$	**0.237**	**0.237**	**0.008**	**0.966**	**0.899**	**0.919**	**0.160**	**1.004**
$Cali_4$	0.269	0.257	0.080	0.964	0.962	0.919	0.173	0.943
$Cali_5*$	0.245	0.236	-0.064	0.968	0.839	0.919	0.159	1.072
$Cali_6$	0.238	0.238	0.000	0.966	0.895	0.919	0.160	1.009

When considering H_s, significant variations become apparent in the shifts of s_d values. For example, the s_d value for the $Cali_1$ configuration is 0.805 m, in contrast to the

Table 4.31: T_e Performance indicator for *calibration* Stage-Gate

	T_e							
Config.	$RMSE$ [s]	$RMSD$ [s]	$BIAS$ [s]	CC[-]	s_{d_m} [s]	s_{d_o} [s]	SI [-]	S [-]
$Cali_1$	0.491	0.446	0.206	0.933	1.243	1.145	0.096	0.954
$Cali_2$	0.487	0.439	0.211	0.936	1.248	1.145	0.094	0.953
***Cali*$_3$**	**0.435**	**0.432**	**0.053**	**0.934**	**1.208**	**1.145**	**0.092**	**0.986**
$Cali_4$	0.439	0.432	0.075	0.935	1.218	1.145	0.093	0.981
$Cali_5*$	0.464	0.439	0.150	0.934	1.229	1.145	0.094	0.966
$Cali_6$	0.463	0.434	0.162	0.936	1.236	1.145	0.093	0.963

0.962 m value for the $Cali_4$ configuration, whereas the buoy data records a value of 0.919 m. Although the values of $RMSD_{Hs}$ and CC_{Hs} are less sensitive to calibration, they also exhibit variations.

The statistical values characterizing T_e show less dispersion in the Taylor diagram between various configurations compared to those of H_s. However, it is important to note that both $RMSD_{Te}$ and $s_{d_{Te}}$ are affected by the calibration process. Most significantly, an improvement in accuracy is observed when moving from the $Cali_5$ configuration to the $Cali_3$ configuration, resulting in $RMSD_{Te}$ of 0.432 s and $s_{d_{Te}}$ of 1.208 s, compared to 1.145 s of the buoy. Therefore, the $Cali_3$ configuration is the most favorable choice, offering a balance between result accuracy and computational efficiency.

SWAN CALIBRATION PERFORMANCE RESULTS

Using a Stage-Gate approach, the problem is divided into subproblems, each dedicated to specific aspects of the model. Fig. 4.19 encapsulates the summary of performance parameters (CC and $RMSD$) and normalized computation time (N_{tc}) for both H_s and T_e, providing a complete view of the improvements achieved through this approach.

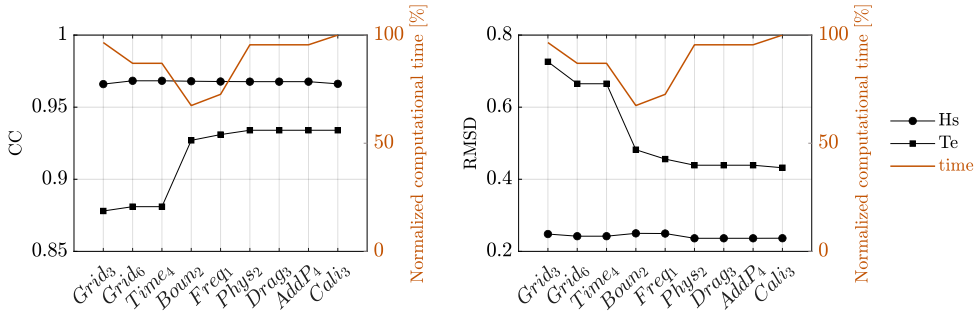

Figure 4.19: Comparative trend of CC, $RMSD$ and the normalized computational time considering the best configurations of each Stage-Gate

In summary, the results reveal that no significant improvements in H_s accuracy are achieved, with $RMSD_{H_s}$ consistently hovering around 0.241m and CC_{H_s} remaining stable at around 96.7%. In contrast, the accuracy in predicting T_e sees significant improvements, with $RMSD_{T_e}$ decreasing from 0.726 s in the initial configuration ($Grid_3$) to 0.432 s in the final configuration ($Cali_3$). In terms of CC_{T_e}, it increases from 87.8% to 93.4% the first and last configurations obtained via the Stage-Gate approach.

The most notable improvements are observed during the *bathymetric source and mesh resolution* Stage-Gate, resulting in reduced computation time and improved accuracy in the T_e parameter. The Stage-Gates about *time-step, wind frag formula* and *linear wind growth, friction and triad physics* do not contribute to the improvement of the model performance. The study highlights that reducing the computational time-step does not consistently improve accuracy when the maximum number of iterations is held constant. In this regard, [215] suggests decreasing the time-step together with an increase in the number of iterations. An underestimation of H_s is found using the FAN and $ECMWF$ wind drag coefficient formulations, as the SWAN manual warns [123]. Furthermore, considering the phenomena of linear wind growth, bottom friction and triad-triad wave interaction increase the calculation times without a change in performance, requiring a careful evaluation of their necessity of inclusion in the model.

To improve the accuracy in predicting T_e, it is recommended to evaluate the optimal cut-in and cut-off frequencies for the prognostic interval and the calculation of synthetic parameters. An in-depth investigation into the physics of whitecapping and exponential wind growth is also suggested to optimize both H_s and T_e, as both parameters are sensitive to these aspects. Either the Stage-Gate *frequency range* and *whitecapping and exponential wind growth* contribute to setting the model and increasing its accuracy. This comprehensive investigation systematically examines and assesses various stages of configuration within the SWAN model. The study employs a Stage-Gate approach to fine-tune the model performance, taking into account considerations of result accuracy and computational efficiency for diverse configurations. The approach simplifies problem-solving by breaking it into manageable subproblems, aiming for optimal setups at each stage. The ultimate optimal SWAN model configuration results from specific adjustments made at each Stage-Gate, providing a reliable and efficient tool for obtaining accurate data in a reasonable computational time. In contrast to conventional model setups, this analysis considers various aspects beyond the choice of wind database and formulations for whitecapping and exponential wind growth. Specifically, it compares 40 different configurations across eight distinct Stage-Gates.

In this analysis, the island of Pantelleria, located in the Mediterranean Sea, renowned for its strong winds and substantial fetch facilitating energy transfer to sea waves, is utilized as a case study. Pantelleria serves as an optimal testbed for applying the Stage-Gate approach to the SWAN model, aided by the availability of a time series of recordings provided by the Datawell Waverider DWR-G buoy.

The first Stage-Gate is the *bathymetric source and mesh resolution* one and reveales that utilizing the EMODnet bathymetry source, as opposed to GEBCO, yields the most accurate representation of H_s and T_e. Indeed, the higher-resolution bathymetry data significantly enhances accuracy, with EMODnet providing bathymetric information at a spatial resolution of approximately 115 m, whereas GEBCO offers data at a coarser 460

m resolution.

In the analysis of the *time-step* Stage-Gate, the configuration with a 30-minute time-step stands out as the most efficient option when compared to those utilizing time-steps of 5, 10, and 15 minutes, all with an equal maximum number of iterations arranged at 10. This 30-minute configuration presents a significant 87% reduction in computational time compared to the 5-minute time-step configuration, all while maintaining the same level of accuracy. This highlights the importance of striking a balance between the time-step and maximum iterations to achieve optimal model performance, underscoring the critical nature of this equilibrium in optimizing the model performance.

In the assessment of *wind and wave boundary condition*, the chosen configuration is characterized by neutral wind and waves described through the 2D frequency-directional spectrum. This selection results in enhanced accuracy for both H_s and T_e, all with a minimal 22.5% increase in computational time when compared to conventional wind and wave descriptions based on synthetic parameters of the wind waves combined with the swell.

During the *frequency range* Stage-Gate analysis, the chosen configuration aligns its frequency range with that of the buoy for spectral density propagation and output calculations, attains the utmost precision. This holds particularly true for the T_e parameter, as this configuration carefully represents the wave spectrum. In particular, since the number of discrete frequencies in the spectrum is kept constant, the narrowing of the frequency range resulted in a better description of the spectrum.

The investigation of *whitecapping and exponential wind growth* models leads to the selection of the configuration based on Rogers formulations, which improves accuracy for both H_s and T_e. The trade-off is a 24% increase in computational time compared to the configuration based on the default formulations, emphasizing the importance of selecting the right combination of models for accurate results.

The analysis of the *wind drag* Stage-Gate identifies the configuration based on the default formulation as the most accurate. Indeed, it provides the best accuracy in terms of H_s and T_e while maintaining a similar computational time compared to other wind drag formulations.

The evaluation of *additional physics* components underscores to carefully assess the need for analyzing further physical phenomena like linear wind growth, bottom friction, and triad-triad wave physics. Their inclusion, in this specific case, does not lead to an increase in accuracy despite a light rise in computational time.

The results from the analyses underline how the choice of bathymetric source and mesh resolution significantly influences model accuracy. Furthermore, striking a balance between time-step and maximum iterations is crucial for optimal model performance, just as careful selection of the physical model for whitecapping and exponential wind growth is essential for enhancing model accuracy.
Finally, the comparison of the wave patterns obtained from the in-situ data and the numerical data produced by the SWAN model is conducted to evaluate the congruence between the in-situ observations and the model simulations. The analysis focuses on SWAN numerical data from the centroid of the triangular cell closest to the instrument installation site (36°49'23"N, 11°55'13"E), with the centroid located at coordinates 36°49'30"N, 11°55'19"E. This comparison allows for the identification of any discrepancies and the

assessment of the model's accuracy.
In particular, the calibration datasets span the period from September 2021 to February 2022 and consist of 6031 value pairs, obtained by Datawell in-situ survey and SWAN numerical model respectively. While the SWAN numerical model covers this time frame without gaps, the in-situ measurements used for calibration correspond precisely to the 6031 data corresponding to the measurements recorded by Datawell between September 2021 and February 2022 and which passed the quality control. The theoretical number of measurements that could have been obtained from the in situ survery, if no gaps had occurred, is 8591. The calibration results between in-situ measurements and SWAN model outputs are shown in the scatterplots for significant wave height (H_s) and energy period (T_e) in Fig. 4.20. These plots illustrate the agreement between the SWAN model outputs and the in-situ data. For significant wave height, there is a strong correlation between the two datasets, with the points closely aligned along the diagonal, indicating that the SWAN model effectively captures wave height variations across the entire range of values. However, slight deviations are noticeable at higher wave heights, suggesting a potential underestimation by the model in extreme cases. Similarly, for the energy period, there is a good correlation between the in-situ and SWAN data. Most points fall near the diagonal, confirming that the model performs well in replicating the energy period. Nevertheless, minor discrepancies are seen at higher T_e values, where the model appears to slightly underestimate longer periods. Overall, despite these small deviations, the SWAN model shows satisfactory performance in simulating both significant wave height and energy period, with strong agreement to the in-situ observations.

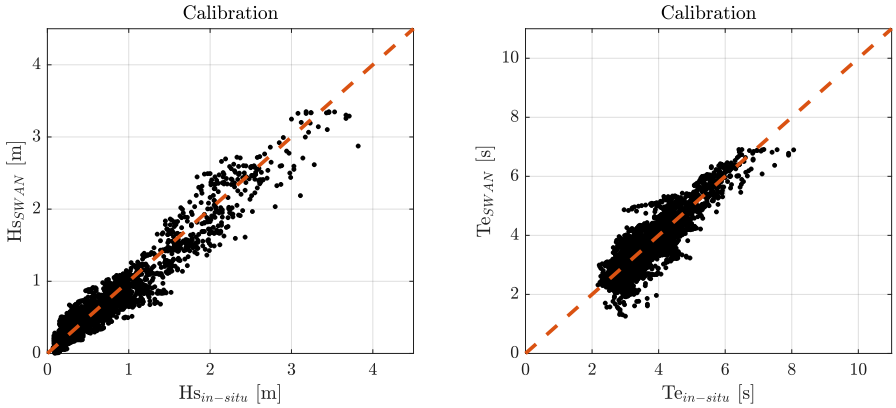

(a) H_s comparison between SWAN model outputs and in-situ measurements, considering the calibration dataset, based on Datawell measurements

(b) T_e comparison between SWAN model outputs and in-situ measurements, considering the calibration dataset, based on Datawell measurements

Figure 4.20: Comparison of the scatter plot of H_s and T_e, respectively, considering the Datawell calibration dataset

Furthermore, as evidenced by Fig. 4.21, the model provides a fitting directional description. Specifically, the peak wave directions obtained from the in-situ Datawell instrument and those from the SWAN model are used for this analysis.
Since the numerical model discretizes the directions in 36 bins, the in-situ instrument

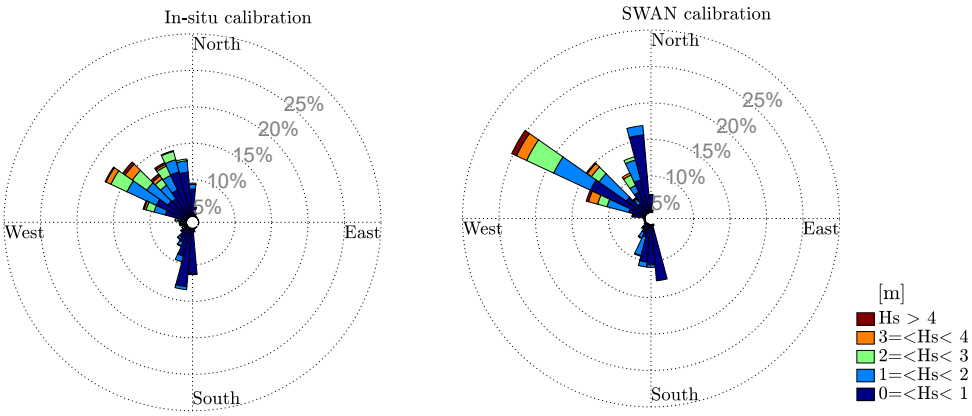

Figure 4.21: Comparative rose plots ($Dir_p - H_s$) obtained with the calibration dataset: in-situ data (left panel) SWAN data (right panel)

directions are processed to approximate the peak instrument directions to the nearest discretized model directions. This processing allows for the comparison of datasets with the same discretizations, enabling a direct and accurate comparison between the two data sets.
As shown in the wave rose plots, the northeast quadrant is the most energetic and frequent, making the occurrence of higher wave heights more probable. Specifically, the most frequent direction with the greatest wave heights is 300°. Regarding the other wave directions, the east sector is almost completely shielded from incoming waves. This characteristic is due to both the instrument's installation location, near the northeast coast of the island, and the prevailing sea states around Pantelleria. Indeed, the waves and winds arriving from the North-West and South-West sectors do not find obstacles due to the presence of lands or islands. Moreover, the island is situated in the Strait of Sicily and is exposed to strong Mistral winds, which generate energetic waves [36].

The analysis of wave roses allows for a better understanding of the prevailing wave directions, their significant heights, and the sea conditions influencing the study area. This comparison is crucial for validating the model's effectiveness and ensuring it can be confidently used for design purposes, especially in tasks requiring knowledge of wave direction. For instance, in the design of energy converters, accurately knowing the directionality of the sea states allows for the optimization of the device's response. Identifying the most frequent wave direction with the greatest energy helps define the most effective orientation for installing the device.
Furthermore, detailed wave direction information can influence the design of coastal infrastructure, such as ports and seawalls, by improving their ability to impede wave entry into the port basin.

SWAN VALIDATION PERFORMANCE RESULTS

A validation analysis is conducted to evaluate the reliability and performance of the SWAN model under different sea states than the calibration ones. Specifically, wave

information recorded by the AWAC instrument in 2015 and 2019, and by the Datawell instrument at the end of 2022, are used for comparative analyses with numerical data. Additionally, the accuracy of significant wave height is assessed by comparing numerical data with satellite data obtained from AODN.
The instrumental data used for the analysis undergos a rigorous quality control process to ensure its reliability. The satellite data, on the other hand, are processed through a collocation method with a temporal critera of 30 minutes and a spatial critera of 80 km. The significant wave height values are determined as the mean values of the satellite measurements within each collocation.

This comprehensive approach ensures that the SWAN model's performance is thoroughly evaluated across different datasets and sea conditions. By incorporating both in-situ and satellite data, the analysis provides a robust validation framework that highlights the model's strengths and identifies areas for improvement.
Tab. 4.32 summarizes the values of the main performance indicators for significant wave height and energy period regarding the comparison with the in-situ data, as well as significant wave height from the comparison with the satellite data.

Table 4.32: H_s and T_e performance indicator in regard to in-situ and satellite data

	RMSE	*RMSD*	*BIAS*	*CC*	*SI*	*S*
			In – situ			
H_s	0.187 m	0.185 m	0.026 m	0.957	0.200	0.969
T_e	0.665 s	0.594 s	0.300 s	0.859	0.147	0.934
			Satellite			
H_s	0.504 m	0.486 m	0.134 m	0.828	0.374	0.933

The results show a good consistency with satellite data, with a *CC* of 82.8%. This value is lower than the *CC* obtained from the comparison between the entire in-situ dataset and the satellite dataset, which is 87.8%. However, considering the unfavorable geographical position of the site of interest, the results suggest that satellite datasets can still be used as useful validation benchmarks. Indeed, the data analysis demonstrates that, despite the challenges posed by proximity to the coast and the influence of local conditions, the SWAN model and satellite data exhibit a reasonably precise correlation. This is particularly significant in contexts where in-situ data are limited or difficult to obtain. Additionally, the comparison with satellite data, which covers a larger area and longer observation periods, reinforces their usefulness even under less ideal conditions. The observed discrepancy between the two *CC* values could be attributed to various factors, including the spatial resolution of satellite data and the complexity of coastal dynamics that are not fully captured by the model, as well as the different sea conditions recorded given by the different seasonal coverage of in-situ data compared to the ten-year time series of the model data.

As regards the performances resulting from the comparison with in-situ data, there is a decrease in accuracy for both H_s and T_e. In fact, in the calibration analysis, the CC is equal to 96.6% for H_s and 93.4% for T_e. In the validation study, however, these values drop to 95.7% and 85.9%, respectively, with a clear decrease in accuracy for T_e. For this reason, an investigation is carry out to understand the reasons related to this reduction in accuracy.
The analysis focuses on two main aspects. The first concerns the impact of seasonality on the results, looking for a correlation between the congruence of the data and the different months of the year. Secondly, aggregate and separate analyzes are carried out with respect to the two sensors used, to identify any specific discrepancies and understand how these may affect the overall results.

To gain a comprehensive understanding of the impact of seasonality on the model's accuracy, performance indicators for the different months of Datawell recordings used in the calibration are analyzed (Fig. 4.33).

Table 4.33: H_s performance indicator in regard to Datawell in calibration phase in regard to different months

Month	*N data*	*RMSE* [m]	*RMSD* [m]	*BIAS* [m]	*CC*	*SI*	*S*
			H_s **- calibration with Datawell**				
Feb	1240	0.302	0.288	-0.093	0.967	0.144	1.064
Sep	1116	0.144	0.140	-0.032	0.892	0.194	1.038
Oct	1013	0.186	0.186	-0.008	0.951	0.180	1.008
Nov	1227	0.213	0.206	0.053	0.974	0.166	0.924
Dec	1288	0.275	0.249	0.115	0.970	0.141	0.955
Tot.	5884	0.235	0.235	0.009	0.967	0.160	0.997

For the months of September and October, a negative BIAS is recorded, suggesting a slight underestimation of wave heights. Furthermore, during these months, the CC value is lower than in other months, despite low $RMSE$ values. This combination indicates that although the model predictions are close to the in-situ values, as shown by the low $RMSE$, they do not always follow the pattern of changes in the actual data, as indicated by the low CC. Consequently, the model can make accurate predictions in terms of mean value but slightly lacks in replicating the variability of the data.
For the months of November and December, the $RMSE$ is relatively low and the $BIAS$ is positive, indicating a slight overestimation of wave heights. The high CC value suggests a strong correlation between the modelled and observed data. This means that the model is not only accurate in its predictions but also tracks variations in the in-situ data well.
In February, a relatively high $RMSE$ and negative $BIAS$ are observed, indicating an underestimation of wave heights. However, the high CC suggests that, despite errors in magnitude, the model captures the data trend well. This implies that the model predic-

tions correctly follow the variations in the real data, even though they tend to be slightly underestimated in terms of height.

Tab. 4.34 presents a meticulous analysis of performance indicators, based on validation data collected by both AWAC and Datawell.

Table 4.34: H_s performance indicator in regard to AWAC and Datawell in validation phase in regard to different months

Month	*N data*	*RMSE* [m]	*RMSD* [m]	*BIAS* [m]	*CC*	*SI*	*S*
			H_s **- validation with AWAC and Datawell**				
Jun	1338	0.151	0.150	0.012	0.972	0.173	1.028
Jul	1728	0.146	0.146	-0.016	0.947	0.211	1.032
Aug	2046	0.169	0.160	-0.052	0.949	0.189	1.069
Sep	490	0.236	0.201	-0.123	0.947	0.210	1.213
Oct	741	0.227	0.226	-0.021	0.941	0.198	1.034
Nov	718	0.282	0.281	0.018	0.957	0.181	0.971
Dec	37	0.080	0.061	-0.051	0.969	0.065	1.035
Tot.	7098	0.187	0.185	-0.026	0.957	0.194	1.032

During the summer and autumn months, specifically from July to October, a negative bias emerges indicating a slight underestimation of wave height. This trend aligns with the results of the calibration analysis, with a $BIAS$ of -0.032 m and -0.008 m for September and October respectively. However, a discrepancy is noted for these months in the trend of $RMSE$ values during validation, which are lower than in other periods. December stands out for a negative bias and for the lowest $RMSE$ value found in the analysis, but the scarcity of the data considered, only 37, limits the robustness of the results. November data indicates a lower match between instrumental measurements and the model compared to calibration. In fact, the correlation coefficient (CC) obtained in November during calibration is 97%, while in validation it drops to 95.7%.

A more in-depth examination to better understand the relationships between the validation performance indicators and the tools used was conducted by analyzing the AWAC (Tab. 4.35) and Datawell (Tab. 4.36) data separately.

The results show that $BIAS$ arising solely from the use of the AWAC dataset are generally negative, signaling a significant underestimation of H_s. Furthermore, the CC obtained from AWAC is generally lower than that derived from Datawell data, which underlines a greater accuracy of the model when compared with the latter's data, recording an overall CC of 96.3% against 95.1% for AWAC. The $BIAS$ values for the months of July and August confirm this trend.

In conclusion, the results indicate that the model provides a more precise estimate of

Table 4.35: H_s performance indicator in regard to AWAC in validation phase in regard to different months

Month	*N data*	*RMSE* [m]	*RMSD* [m]	*BIAS* [m]	*CC*	*SI*	*S*
			H_s - validation with AWAC				
Jul	317	0.166	0.164	-0.022	0.905	0.232	1.055
Aug	743	0.176	0.160	-0.072	0.929	0.222	1.084
Sep	490	0.236	0.201	-0.123	0.947	0.210	1.213
Oct	741	0.227	0.226	-0.021	0.941	0.198	1.034
Nov	718	0.282	0.281	0.018	0.957	0.181	0.971
Dec	37	0.080	0.061	-0.051	0.969	0.065	1.035
Tot.	3046	0.225	0.221	-0.041	0.951	0.200	1.025

Table 4.36: H_s performance indicator in regard to Datawell in validation phase in regard to different months

Month	*N data*	*RMSE* [m]	*RMSD* [m]	*BIAS* [m]	*CC*	*SI*	*S*
			H_s - validation with Datawell				
Jun	1338	0.151	0.150	0.012	0.972	0.173	1.028
Jul	1411	0.142	0.141	-0.014	0.953	0.2058	1.026
Aug	1303	0.164	0.159	-0.040	0.956	0.174	1.063
Tot.	4052	0.152	0.152	-0.014	0.963	0.184	1.041

wave heights when validated with Datawell data rather than AWAC data. A widespread underestimation of waves in the summer months and a trend towards greater accuracy in the autumn months is resulted. Moreover, a Datawell's superior ability to accurately record waves, could be the reason for the greater congruence of the numerical dataset compared to the in-situ one.

The same analysis carried out for the height H_s is also applied to the T_e. The monthly results of the performance indicators during the calibration phase (Fig. 4.37) reveal a high correspondence between the calculated and observed Te, with the exception of September, which recorded a *CC* of 64.9%. This lower result can be attributed to the complexity of some sea states that occurred in that month, leading to inaccurate model estimates. Regarding the BIAS, the values are generally positive, indicating a tendency to overestimate the numerical data, except for September where an underestimation is observed.
In terms of better performance, the winter months, in particular December and February, show greater adherence between the numerical dataset and the one used for calibration.

Table 4.37: T_e performance indicator in regard to Datawell in calibration phase in regard to different months

Month	*N data*	*RMSE* [s]	*RMSD* [s]	*BIAS* [s]	*CC*	*SI*	*S*
			T_e **- calibration with Datawell**				
Feb	1240	0.461	0.441	0.134	0.951	0.084	0.974
Sep	1116	0.425	0.414	-0.098	0.649	0.104	1.024
Oct	1013	0.418	0.400	0.121	0.925	0.093	0.966
Nov	1227	0.545	0.465	0.283	0.910	0.101	0.937
Dec	1288	0.535	0.414	0.338	0.948	0.085	0.933
Tot.	5884	0.483	0.455	0.163	0.931	0.098	0.961

Tab. 4.38 provides a comprehensive overview of the model's performance relative to the in-situ data used for validation, presented on a monthly basis. Notably, there is no discernible linear trend in the data. For instance, the accuracy results in the winter months are inconsistent, with the correlation coefficient (*CC*) fluctuating significantly, dropping from 86.9% in January to only 67.5% in December. Moreover, the model generally tends to underestimate the values of T_e, a trend that diverges from the observations made during the calibration performance analysis. This underestimation suggests a potential discrepancy or a unique characteristic of the model that warrants further exploration. To better understand these differences, a detailed analysis of the model's performance in relation to each dataset is undertaken, aiming to pinpoint the reasons behind these variations and enhance our interpretation of the results.

Table 4.38: T_e performance indicator in regard to AWAC and Datawell in validation phase in regard to different months

Month	*N data*	*RMSE* [s]	*RMSD* [s]	*BIAS* [s]	*CC*	*SI*	*S*
			T_e **- validation with AWAC and Datawell**				
Jun	1338	0.494	0.492	0.041	0.869	0.130	0.984
Jul	1728	0.552	0.464	-0.298	0.860	0.122	1.080
Aug	2046	0.662	0.596	-0.288	0.778	0.143	1.069
Sep	490	0.963	0.568	-0.778	0.810	0.112	1.181
Oct	741	0.763	0.576	-0.500	0.864	0.112	1.103
Nov	718	0.774	0.666	-0.394	0.898	0.124	1.063
Dec	37	1.434	0.794	-1.195	0.675	0.157	1.271
Tot.	7098	0.665	0.594	-0.300	0.859	0.137	1.071

Significant findings emerge from comparing the performance indicators between AWAC data (Fig. 4.39) and Datawell data (Fig. 4.40). Notably, the comparison with AWAC data reveals particularly high and negative $BIAS$ values, indicating a marked underestimation of T_e. Similarly, the comparison with Datawell data also shows a general tendency to underestimate T_e, although the $BIAS$ values are less extreme, ranging from 0.041 s to -0.202 s. In contrast, the $BIAS$ values associated with AWAC data are much more pronounced, varying between -1.195 s and -0.394 s. This discrepancy suggests that the model exhibits greater deviations with AWAC data compared to Datawell data, which may point to differences in the accuracy of the instruments. Indeed, seasonal variations are ruled out as a cause, since the calibration performance indicators based on Datawell data show a $BIAS$ ranging from -0.098 s to 0.338 s.

Table 4.39: T_e performance indicator in regard to AWAC in validation phase in regard to different months

Month	*N data*	*RMSE* [s]	*RMSD* [s]	*BIAS* [s]	*CC*	*SI*	*S*
T_e - validation with AWAC							
Jul	317	0.924	0.573	-0.725	0.781	0.126	1.182
Aug	743	0.957	0.629	-0.721	0.791	0.136	1.164
Sep	490	0.963	0.568	-0.778	0.810	0.112	1.181
Oct	741	0.763	0.576	-0.500	0.864	0.112	1.103
Nov	718	0.774	0.666	-0.394	0.898	0.124	1.063
Dec	37	1.434	0.794	-1.195	0.675	0.157	1.271
Tot.	3046	0.877	0.634	-0.605	0.855	0.127	1.123

Table 4.40: T_e performance indicator in regard to Datawell in validation phase in regard to different months

Month	*N data*	*RMSE* [s]	*RMSD* [s]	*BIAS* [s]	*CC*	*SI*	*S*
T_e - validation with Datawell							
Jun	1338	0.494	0.492	0.041	0.869	0.130	0.984
Jul	1411	0.426	0.375	-0.202	0.903	0.104	1.050
Aug	1303	0.407	0.405	-0.041	0.881	0.104	1.0063
Tot.	4052	0.444	0.438	-0.070	0.882	0.117	1.012

The directly comparable results pertain to the months of July and August, during which both instruments recorded data useful for the validation. From this comparison, it becomes apparent that the CC derived from the match between numerical data and those obtained from Datawell are significantly higher than those for AWAC. Specifically,

for the month of June, AWAC's CC stands at 78.1%, whereas Datawell reaches 86.9%. In August, the CC for AWAC is 79.1%, while Datawell scores 88.1%.
Despite these clear differences, it's important to emphasize that since the AWAC and Datawell recordings were conducted in different years, merely observing performance indicators by month may not provide a comprehensive analysis. Concurrent measurement campaigns using both AWAC and Datawell could offer more definitive insights and potentially highlight whether Datawell consistently exhibits greater accuracy. This approach would help to eliminate any variability due to differing environmental conditions or other seasonal factors that could affect the data year-on-year. Additionally, the optimal scenario would involve installing both instruments at the same site of interest during the same analysis period, ideally with coverage extending over at least a full year. This arrangement would enable more robust analyses of the seasonal variability of sea states and enhance the evaluation of the SWAN model's ability to deliver accurate results. By synchronizing the data collection in this manner, discrepancies due to environmental changes or instrumental differences could be minimized, providing a clearer understanding of the model's performance across various conditions.

The scatterplots for the Datawell and AWAC (Fig. 4.22) validation datasets offer valuable insights into the performance of the SWAN model in predicting significant wave height (H_s) and energy period (T_e). For the Datawell dataset, the scatterplot of H_s shows a strong correlation, with most points closely aligned along the diagonal, indicating that the model effectively captures wave height variations. Similarly, the AWAC dataset also demonstrates a good correlation between the SWAN model and the in-situ measurements. However, compared to the Datawell validation, the AWAC results show a slightly broader spread of points, particularly at higher wave heights.
Regarding the energy period (T_e), the comparison with the Datawell dataset again demonstrates a strong correlation, with most data points situated near the diagonal, confirming the SWAN model's accuracy in replicating energy periods. In contrast, the AWAC validation reveals a slightly broader distribution of points, especially for larger energy periods, although the correlation remains strong. The increased dispersion around the diagonal suggests a slight decrease in the model's precision for the AWAC dataset at higher T_e values.
Overall, the SWAN model performs well with both the Datawell and AWAC in-situ datasets, showing strong agreement between model outputs and in-situ observations. However, there are evidentdifferences in performance between the two validation datasets. These results suggest that the performance analysis may be partially influenced by the measurement instruments used. Specifically, the key differences between the two comparisons stem from the use of different instruments and the varying temporal coverage of the measurement campaigns. To assess the impact of these discrepancies, it would be necessary to compare the measurements from the different instruments at the same location and over the same time period.

Ultimately, the wave rose analysis is conducted to ascertain the alignment between directional information provided by the SWAN model and that recorded by various instruments. In this instance, a dual analysis approach is employed, utilizing both the en-

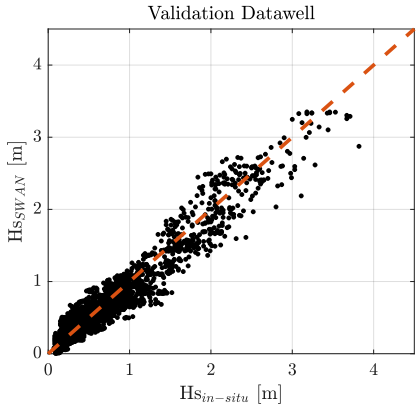

(a) H_s comparison between SWAN model outputs and in-situ measurements, considering the Datawell validation dataset

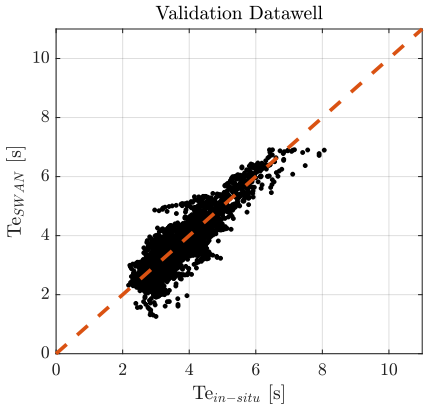

(b) T_e comparison between SWAN model outputs and in-situ measurements, considering the Datawell validation dataset

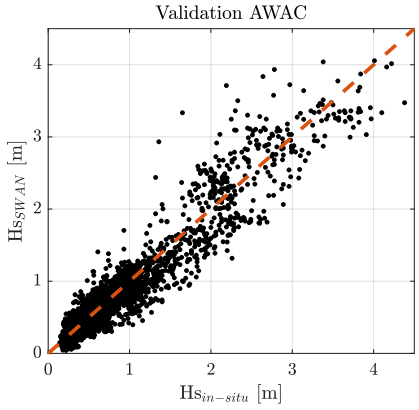

(c) H_s comparison between SWAN model outputs and in-situ measurements, considering the AWAC validation dataset

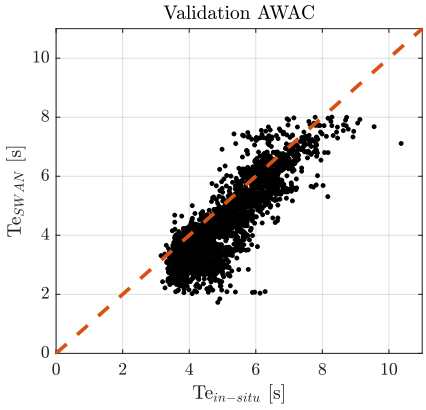

(d) T_e comparison between SWAN model outputs and in-situ measurements, considering the AWAC validation dataset

Figure 4.22: Comparison of the scatter plots of H_s and T_e, considering the validation dataset of Datawell and AWAC, respectively

tire validation dataset and subdividing the analysis according to the specific instruments installed. Similar to the process used in the wave rose analysis for the calibration results evaluation, a preprocessing step of the peak directions from the instrumental data is carried out to harmonize the datasets for comparison.

Specifically, the directions obtained from the in-situ instruments are approximated to the nearest directions derived from the SWAN model. Fig. 4.23 illustrates a comparison between the wave rose generated from the entire in-situ dataset and the wave rose derived from the SWAN data, referring to the same time period. The complete validation dataset consists of 7195 in-situ measurements, matched with 7195 data points from the SWAN model, corresponding to the same time instants and the triangular numerical cell closest to the instrument installation site. Specifically, 4145 of the instrumental measurements come from the Datawell campaign conducted between June and August

2022, while the remaining 3050 measurements were gathered during two AWAC campaigns, carried out from September to December 2015 and from July to September 2019.

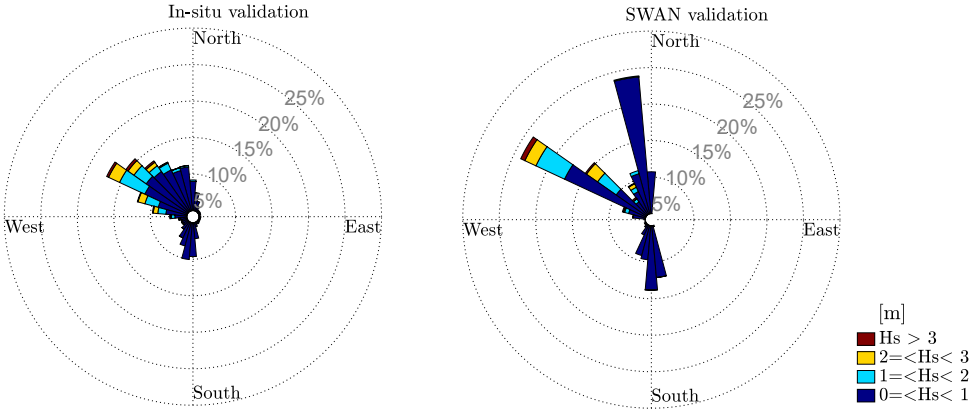

Figure 4.23: Comparative rose plots ($Dir_p - H_s$) in validation phase for AWAC and Datawell data (left panel) and SWAN data (right panel)

It is noticeable that the dominant peak direction in both cases is 300°. In the wave rose generated from the in-situ instruments, this direction occurs between 10% and 15% of the time, whereas in the modeled data, the occurrence exceeds 15%. This discrepancy might be attributed to adjacent directions around 300°, which account for occurrences ranging from 5% to 10% in the validation wave rose.

Furthermore, less energetic but notably frequent waves, generally originating from the north and south, appear to be more evenly distributed in the in-situ validation dataset. In contrast, in the SWAN wave rose, prominent directions are highlighted, particularly the direction of 340°, which occurs about 15% of the time, and the directions of 180° and 190°, each also with an occurrence of approximately 15%.

Fig. 4.24 and 4.25 provide wave roses with reference to the individual instruments and the corresponding model datasets.

In both comparisons, it becomes evident that the instrumental data are more widely distributed across various directions compared to the data obtained from the model. However, the presence of waves from the northeast and southwest is exclusive to the AWAC dataset. Specifically, the geographical layout of the instrument installation site is such that the waves are influenced by the presence of the coast, preventing their arrival from these directions due to the island blocking their propagation along these paths. This result suggests AWAC inaccuracies in accurately reconstructing sea states.
In both instances, however, the predominance of the more energetic waves coming from the northwest direction, particularly around 300°, is clear.

4.3. WAVE ENERGY ASSESSMENT

THE wave energy assessment analysis of the wave is conducted in reference to the IEC/TS 62600-101:2015 standards, in addition to analyzing the occurrences of sea

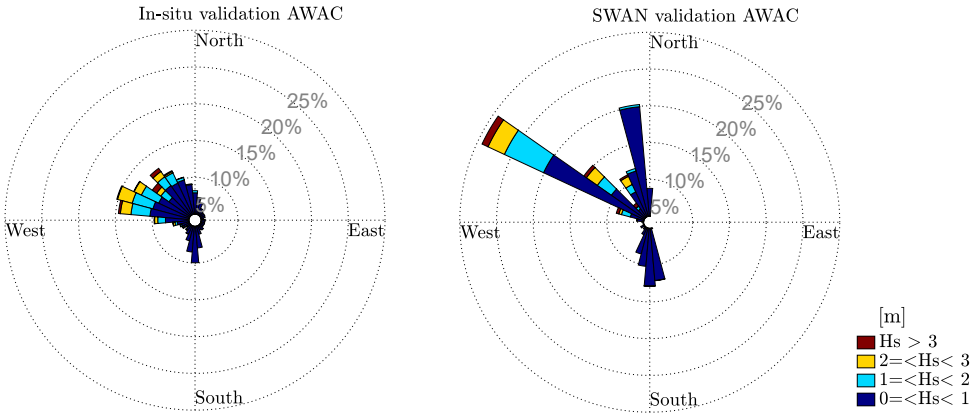

Figure 4.24: Comparative rose plots ($Dir_p - H_s$) in validation phase for AWAC data (left panel) and SWAN data (right panel)

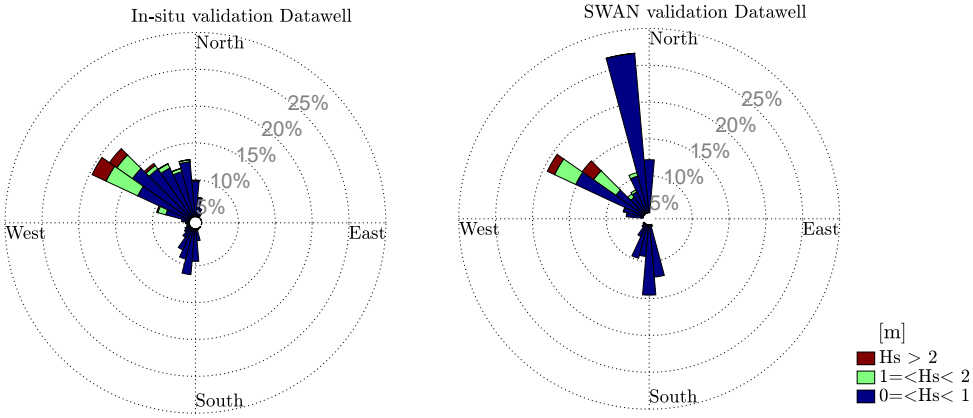

Figure 4.25: Comparative rose plots ($Dir_p - H_s$) in validation phase for Datawell data (left panel) and SWAN data (right panel)

states. These analyses are based on the decadal historical series obtained from the SWAN model previously discussed. In particular, the analysis is based on numerical data referencing the centroid of the triangular cell closest to the instrument installation site (36°49'23"N, 11°55'13"E), with this centroid located at coordinates 36°49'30"N, 11°55'19"E. Both the synthetic parameters and the frequency-directional spectrum are obtained every half hour covering the period from 2013 to 2022. Specifically, the synthetic parameters are obtained as descriptive parameters of the overall sea state, as well as from the partitioning of the respective spectra. Regarding the spectra, they cover all directions with a constant bin of 10°, while the 36 frequencies vary between 0.01Hz and 0.64Hz, following a logarithmic progression.

4.3.1. PREVALENCE OF MULTI-MODAL WAVE SYSTEM

The analysis of the predominance of multi-modal sea states is carried out through the examination of partitioned spectra. Initially, the SWAN model generates spectra which are then partitioned using the two-dimensional WavSEP technique. For each partitioned spectrum, the zero-order moment (m_0) is calculated, and its frequency of occurrence and prevalence within each sea state are analyzed.
The analysis of occurrences is carried out by quantifying the number of sea states simultaneously coexisting. However, this analysis does not provide information on the energy contribution of individual sea states in relation to the overall wave obtained. For such analysis, the percentage of energy corresponding to each sea state is determined. In particular, the parameter m_0 is used as a proxy for the evaluation of the energy of each sea state, corresponding to the volume underlying the corresponding frequency-directional spectrum.

Fig. 4.26 displays the time series of the zero-order moments corresponding to various sea states that occurred simultaneously in Pantelleria. As illustrated, the sime series of the different sea states is characterized by the overlapping of three or four distinct sea states.

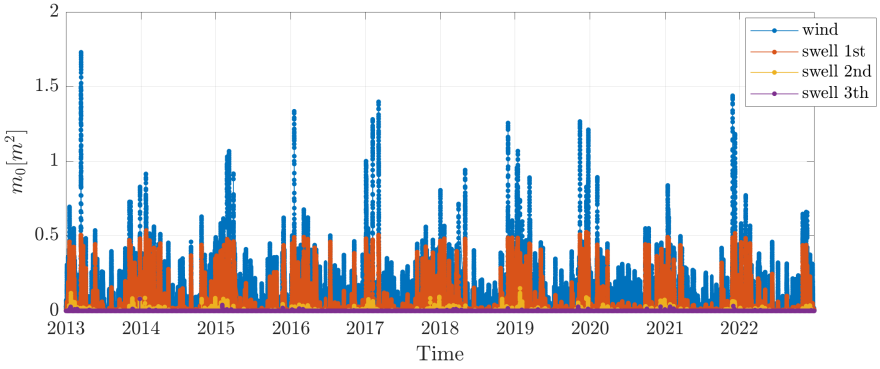

Figure 4.26: Time-seris of m_0 for the different sea states occurred over the 10 years of simulation

Seasonal and inter-annual synthetic analyses are conducted to understand the average energy contribution from wind waves and swells in relation to each sea state. Fig. 4.27 illustrates the occurrence of different sea states.

There is a predominance of bi-modal sea states characterized by the combination of wind waves and the first swell. These bi-modal sea states show a high frequency of occurrence, varying from 83.7% in February to an overwhelming 99.9% in August. This indicates that for most of the year, the sea conditions are primarily influenced by these two interacting wave systems.
The remaining sea states are predominantly composed of a superposition of wind waves and two swell components. The highest occurrence of these 4 sea states is observed in April, reaching up to 6.5%. These complex sea states are characterized by frequency-directional spectra that exhibit four distinct peaks, corresponding to the wind waves and

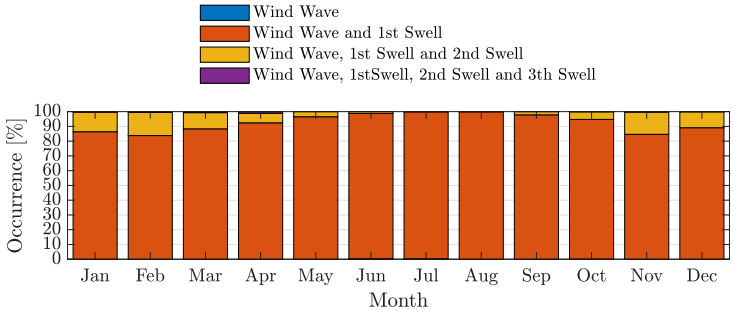

Figure 4.27: Season variability of wind waves and swells occurrence

the two swell systems.

This distribution of sea state occurrences highlights the dynamic nature of the maritime environment, with a significant prevalence of bi-modal conditions. The presence of 4 states, though less frequent, adds complexity to the wave climate, especially during certain months like April.
An interesting trend observed is that bi-modal sea states tend to dominate in the summer months, when weather conditions are generally more stable and swell waves are more pronounced. In contrast, during the winter months, increased storm activity leads to greater variability and the possible formation of tri-modal sea states.

Fig. 4.28 The inter-annual analysis of the occurrence of multimodal sea states is carried out to identify any trends and variations over years.

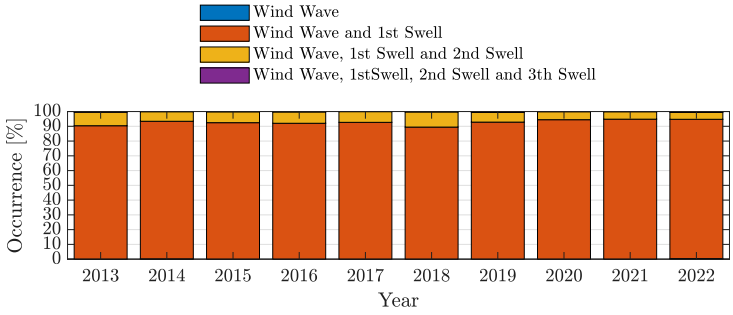

Figure 4.28: Inter-annual variability of wind waves and swells occurrence

The results show how the inter-annual variability is not particularly pronounced. In particular, the occurrence of bi-modal sea states varies between 89.5% in 2018 and 94.8% in 2021. Almost all of the remaining occurrences correspond to waves obtained from the simultaneous coexistence of three different sea states. The year in which the greatest waves characterized by 4 different sea states modelled corresponds to 2019, with an occurrence of 6.6%.

The results shown in Fig. 4.29 highlight the seasonal variability of the average contribution of individual sea states in reference to the overall m_0.

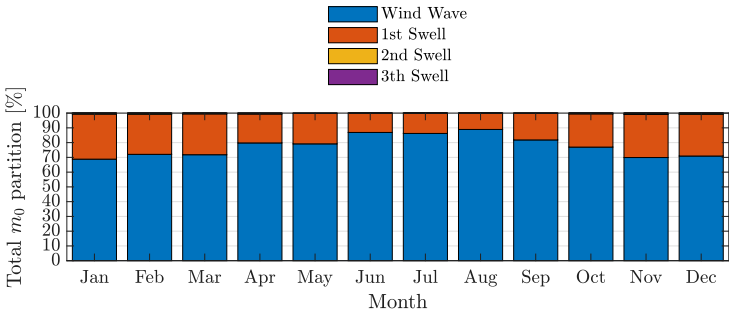

Figure 4.29: Seasonal variability of the average contribution of individual sea states in reference to the overall m_0

The graph demonstrates a greater contribution from wind waves compared to the 1st swell waves. Notably, during the summer months, there is a pronounced dominance of wind wave contributions, reaching up to 88.9% in August. Conversely, in the winter months, there is an increased contribution from swell waves, peaking at 29.1% in December.
This pattern suggests that wind waves dominate during the calmer summer months when the weather is generally more stable, leading to a higher percentage of wind wave activity. On the other hand, during the winter months, the increased storm activity results in a higher contribution from swell waves. This is particularly evident in December, where the swell wave contribution is at its highest.
The seasonal shift in the contributions of wind waves and swell waves is crucial for understanding the overall wave climate and its impact on maritime activities. During the summer, the higher prevalence of wind waves indicates that the sea conditions are more influenced by local wind patterns, which could affect activities such as boating and coastal construction. In contrast, the winter months, with their higher swell wave contributions, suggest that sea conditions are more affected by distant storm events, impacting long-range swell propagation and potentially affecting offshore structures and operations.

Finally, the inter-annual analysis of the contribution of individual sea states is carried out (Fig. 4.30).

The figure shows a consistent pattern where wind waves have the predominant contribution compared to the 1st swell waves across all years. Wind waves consistently make up the majority of the total wave energy, with contributions typically ranging around 75% each year. This indicates that local wind-driven waves are the dominant sea state in the studied area throughout the entire decade.
The contribution of the 1st swell waves, while less than that of the wind waves, is still significant, generally constituting around 25% of the total wave energy. This steady contribution from swell waves suggests a consistent presence of longer-period waves generated by distant weather systems, which reach the study area after traveling across the

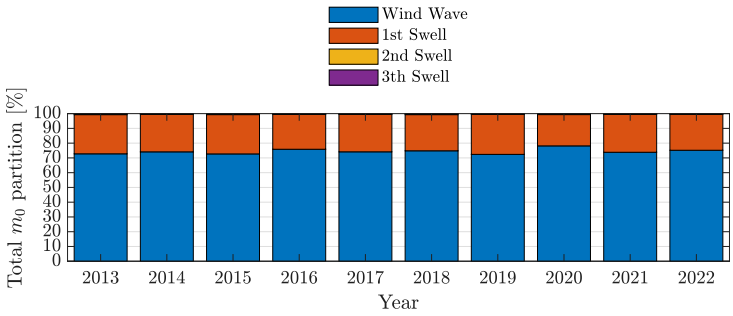

Figure 4.30: Inter-annual variability of the average contribution of individual sea states in reference to the overall m_0.

Mediterranean Sea.
Interestingly, there is little to no contribution from the 2nd and 3rd swell waves, as indicated by the absence of yellow and purple segments in the graph. This lack of higher-order swell components implies that the wave climate is largely influenced by primary wind waves and the dominant first swell, with minimal impact from additional swell sources.
The stability in the proportions of wind wave and swell contributions over the years suggests a relatively stable wave climate in the region, with no significant inter-annual changes in the dominance of wave types. This consistency can be advantageous for long-term maritime planning and operations, as it allows for more predictable and reliable forecasting of sea conditions. The variability ranges from a 72.7% contribution of wind waves in 2013 to 78.1% in 2020, highlighting a narrow range of variability. This limited range of fluctuation emphasizes the consistency in the dominance of wind waves over the studied period.

4.3.2. SEASON VARIABILITY

The seasonal variability of Hs, Te, s and P is studied in detail to deepen the understanding of their trends. Specifically, the synthetic parameters under study belong to three categories of sea states. First of all, the synthetic parameters of the sea states present in Pantelleria are analysed, obtained from the spectral analysis of the frequency-directional spectra provided by SWAN. Furthermore, the synthetic parameters of the unimodal marine states of the wind waves and storm surges that occurred in Pantelleria are studied to evaluate the characteristics of the individual sea states. These parameters are also obtained from spectral analysis but in this case with reference to the directional frequency spectra of wind waves and swells only, obtained by partitioning the overall spectrum with the WaveSep method.
To conduct the seasonal variability study, wave data over several years are examined to identify any recurring seasonal trends in wave characteristics. This analysis involves the comparison between the monthly averages, maximums and minimums of the synthetic parameters analyzed. Additionally, for each month, the 5th and 95th percentiles are determined to provide information on the distribution of values over the months. Each pa-

rameter is analyzed based on the general state of the sea as well as the individual types of waves.
This analysis is critical for predicting seasonal changes in wave behavior, which is essential for various maritime and coastal activities, including shipping, coastal development, and the operation of marine renewable energy systems. Identifying the least energetic seasons is particularly crucial for identifying optimal renewable energy sources to compensate for energy shortages in the context of decarbonization. Specifically, energy mix analysis simultaneously explores different renewable energy sources to determine their compatibility and maximize their strengths, as exemplified by the integration of wave motion with wind and/or solar energy [5, 253].

SIGNIFICANT WAVE HEIGHT SEASON VARIABILITY

Fig. 4.31 show the distributions of H_s values for the three sea state conditions analyzed, respectively, in the different months. In Figure 4.31a, depicting the seasonal variability of H_s for wind waves and swells combined, a clear pattern emerges. The maximum H_s values (red dashed line) are consistently higher during the winter months, peaking notably in November and March, likely due to increased storm activity. The mean H_s (green line) and the 95^{th} percentile (black dotted line) show a smoother trend than the maximum values, indicating a general increase in wave energy during the winter. January records the highest average significant wave height at 1.45m, while August has the lowest at 0.58m. The minimum values (blue dashed line) and the 5^{th} percentile (purple dotted line) remain relatively low and stable across all months, suggesting that while high-energy events are more frequent in winter, low-energy conditions are prevalent year-round.

Figure 4.31b focuses on the seasonal variability of H_s for wind waves only, showing a similar trend compared to the combined sea state. In this case, the maximum H_s values remain nearly constant around 2.7m, while the seasonal variability of the average values and the 95^{th} percentile show higher values in the winter months and lower values in the summer months. January again records the highest average significant height at 1.16m, with August showing the lowest at 0.54m.

Figure 4.31c presents the seasonal distribution of significant wave height values for swells only. The maximum H_s values remain almost constant throughout the year, around 2.77m, with notable variability in the summer months, likely due to a specific storm event in July. The average significant height values and the 95^{th} percentile follow a similar trend to the combined wind waves and swells, and wind waves alone. Higher values correspond to the winter months, while the lowest values are observed in the summer months. January shows the highest average H_s at 0.71m, and August the lowest at 0.17m.

These results highlight the pronounced seasonal fluctuations in significant wave heights overall and with respect to individual sea states. The highest average values occur in the winter months, driven by storm activity. In contrast, the summer months show a decrease in Hs, likely resulting from more stable weather conditions.

ENERGY PERIOD SEASON VARIABILITY

Figures 4.32 illustrate the seasonal variability of the energy period (Te) for different wave conditions: combined wind waves and storm surges, wind waves alone, and storm surges

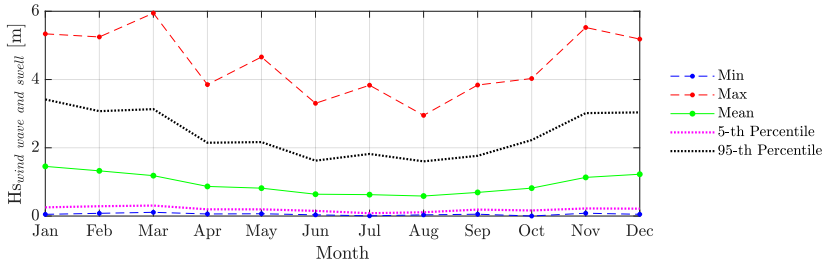

(a) $Hs_{wind\ wave\ and\ swell}$ seasonal variability

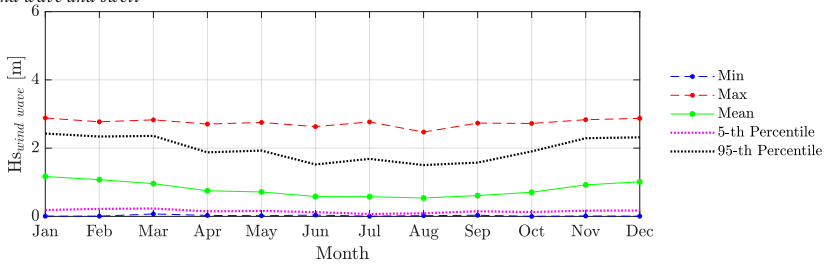

(b) $Hs_{wind\ wave}$ seasonal variability

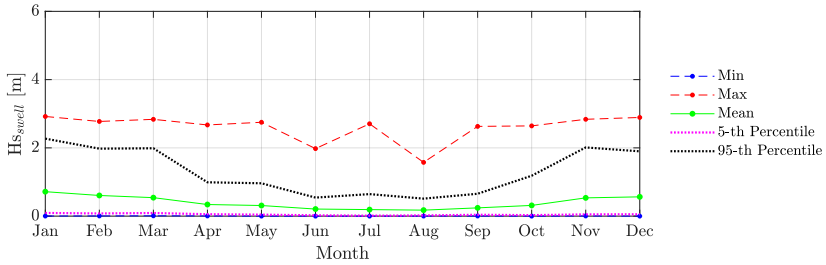

(c) Hs_{swell} season variability

Figure 4.31: Seasonal variability of H_s

alone. The trends of the average energy period values for the three wave conditions show higher values during the winter months and lower values in the summer months. However, the trend of the maximum monthly values and the 95^{th} percentile differs slightly.

Figure 4.32a shows the seasonal variability of T_e for combined wind waves and storm surges. The maximum T_e values (red dashed line) increase during the winter months, particularly in January, and decrease in the summer months. The average T_e (green line) and the 95^{th} percentile (black dashed line) follow the same trend, indicating an overall increase in the energy period during the winter. The minimum values (blue dashed line) and the 5^{th} percentile (purple dashed line) remain low and stable, reflecting consistently low energy conditions throughout the year.

Figure 4.32b examines the seasonal variability of T_e for wind waves alone. Here, the maximum T_e values remain almost constant throughout the year, around 6.3 seconds, with some variability likely due to specific storm events. The mean T_e values and the 95^{th}

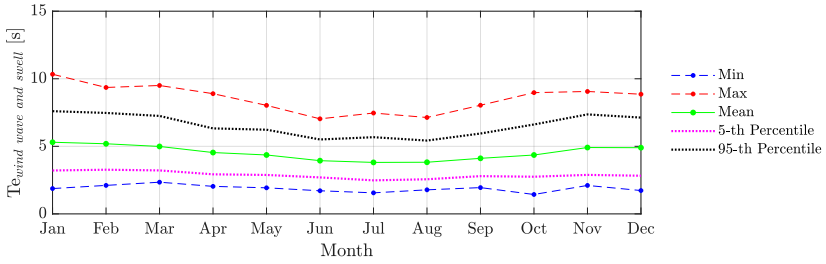

(a) $Te_{wind\ wave\ and\ swell}$ seasonal variability

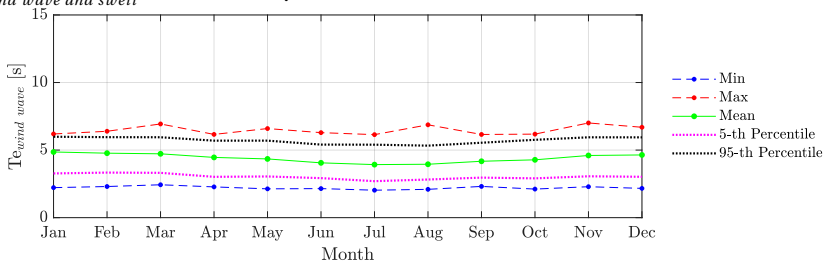

(b) $Te_{wind\ wave}$ seasonal variability

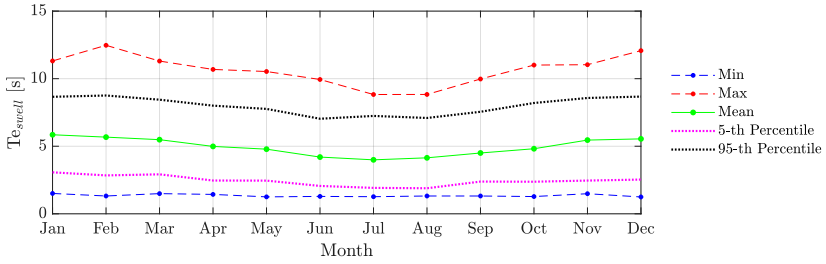

(c) Te_{swell} seasonal variability

Figure 4.32: Season variability of Te

percentile show a similar pattern to the combined wind waves and storm surges, with higher values during winter and lower values in summer. This trend highlights the influence of winter storms in increasing the energy period for wind waves, while the summer months maintain more stable conditions.

It is noteworthy that the dispersion of points around the average values is more pronounced for the energy periods of wind waves and swells (Fig. 4.32a) and for swells alone (Fig. 4.32c), whereas in the case of only wind waves, the variability is much less accentuated. This is demonstrated by the closer proximity of the different curves around the average values. In particular, swell waves show more pronounced inter-monthly variability compared to the three cases analyzed. This implies that within a month, there is high variability in the energy period, ranging from low values (the average 5^{th} percentile is equalt to 2.1 s) to high values (the average 95^{th} percentile corresponds to 7.7s).

DIRECTIONAL SPREADING SEASON VARIABILITY

The monthly variability of directional spreading (s) is analyzed for the three sea states of interest (Fig. 4.33). Specifically, the directional spreading values are determined and analyzed from the spectral analysis of the directional frequency spectrum and the 2D spectra of individual sea states.

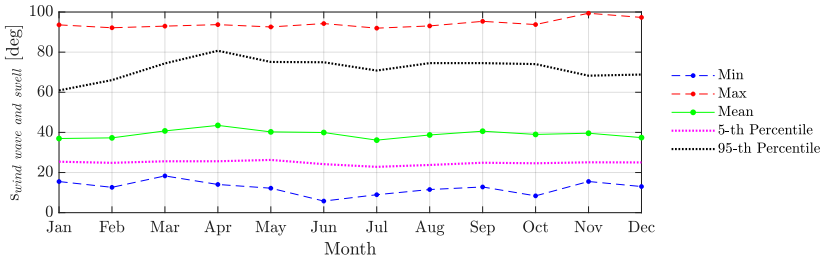

(a) $s_{wind\ wave\ and\ swell}$ seasonal variability

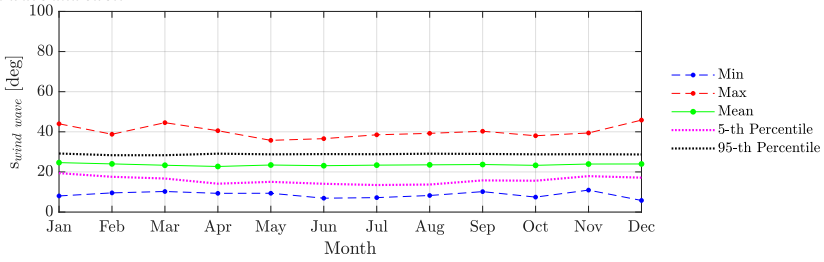

(b) $s_{wind\ wave}$ seasonal variability

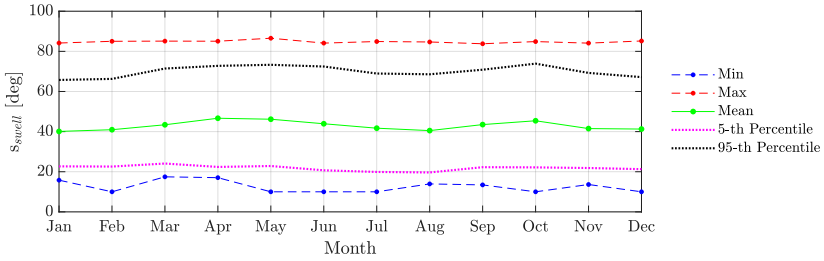

(c) s_{swell} seasonal variability

Figure 4.33: Season variability of s

Figure 4.33 illustrates the variation of minimum, maximum, average values, and percentiles throughout the year for the analyzed sea states. It is notable that in the case of directional spreading referring only to wind waves (Figure 4.33b), the dispersion around the average values is not very pronounced, varying between minimum values averaging 7.2 ° and maximum values averaging 38.5°. In contrast, for swell waves (Figure 4.33c), this variability is more pronounced, oscillating between a minimum average value of 13 ° and a maximum of 85.3°. This trend is attributable to the specific geographical area of study. Swell waves do not have a geographic fetch free from obstacles. The existence of

islands, archipelagos, and irregular coastlines limits the development of fully developed waves that can propagate freely for long stretches of sea. Consequently, some waves are able to develop and manifest through particularly narrow directional spectra, while other swells show a more pronounced dispersion of energy around the average wave direction.

For the combination of wind and swell waves (Figure 4.33a), the maximum values (red dashed line) and the 95^{th} percentile (black dotted line) remain relatively high and stable throughout the year characterizing waves with reduced directional variability. The mean values (green line) and the 5^{th} percentile (purple dashed line) show minimal seasonal variability, maintaining a constant distribution across all months. The minimum values (blue dashed line) show slight fluctuations but remain generally low, describing waves with high directional dispersion and indicating that the waves consistently come from a wide range of directions. The coexistence of at least two distinct sea states leads to a more accentuated energy distribution compared to uni-modal sea states.

These observations underline the importance of understanding the directional spreading of waves throughout the year. The consistently high values of maximum directional spreading suggest that, regardless of the season, waves come from a wide range of directions, which is critical for maritime and coastal planning. The stable mean values indicate that, on average, the directional spreading does not fluctuate significantly with the seasons. This can help in predicting and managing wave energy and its impact on coastal structures and activities. The variability observed in swell waves highlights the influence of geographical features on wave development and propagation, emphasizing the need for localized studies in different maritime regions.

4.3.3. INTER-ANNUAL VARIABILITY

Similarly to the analysis conducted on monthly variability, an investigation into inter-annual variability is also carried out. This research focuses on identifying long-term trends and fluctuations in H_s, T_e and s over several years. By examining SWAN data provided over extended period, this study aims to detect any patterns or significant changes that might be influenced by broader climatic or environmental shifts.

This approach not only enriches our understanding of wave dynamics over time but also aids in the assessment of potential impacts due to climate change. For instance, it helps to evaluate whether there is a trend towards more extreme weather events that could result in higher waves and more energy, or conversely, a shift towards calmer sea conditions. The results of this analysis are crucial for long-term planning in a strategic deployment of marine renewable energy infrastructures.

SIGNIFICANT WAVE HEIGHT INTER-ANNUAL VARIABILITY

Figure 4.34 shows the inter-annual trends of significant wave height (Hs) for multimodal sea states, wind waves alone, and swells alone.

In Figure 4.34a, the maximum H_s values, derived from the full frequency-direction spectrum of waves observed in Pantelleria, display notable variability. This trend differs from what is observed for wind waves alone (Figure 4.34b) and swells alone (Figure 4.34c). Specifically, the maximum H_s values for individual unimodal sea states do not

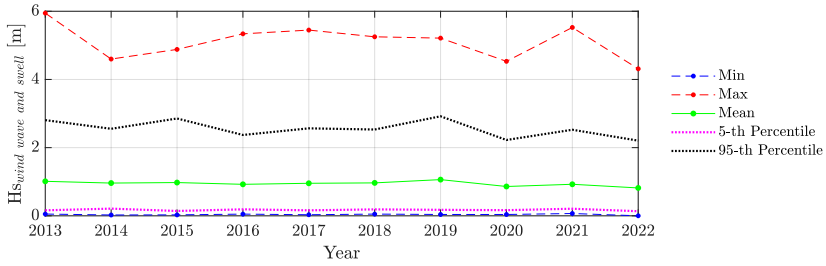

(a) $Hs_{wind\ wave\ and\ swell}$ inter-annual variability

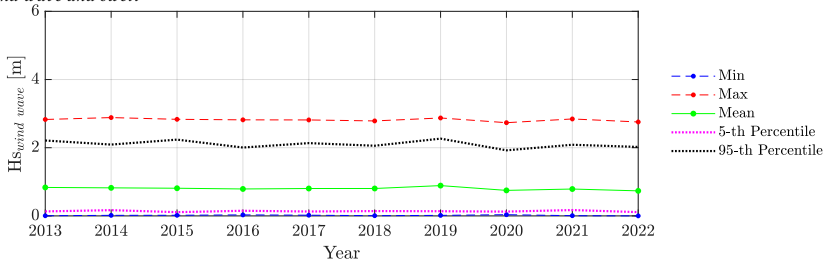

(b) $Hs_{wind\ wave}$ inter-annual variability

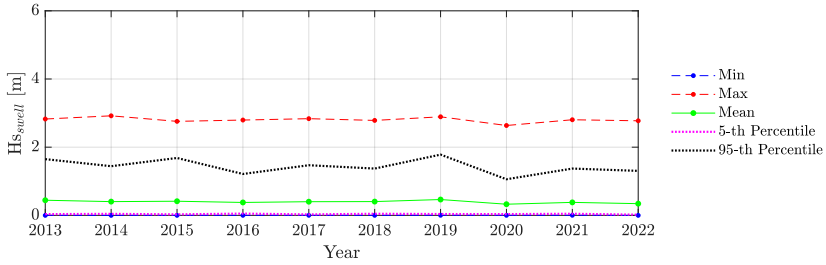

(c) Hs_{swell} inter-annual variability

Figure 4.34: Inter-annual variability of H_s

exhibit significant inter-annual variability. This comparison suggests that the variability in the significant wave height of multimodal sea states is due to the random combination of wind waves and swells. The pronounced peaks in H_s for combined wind waves and swells indicate that high-energy wind waves and swells coincided, resulting in higher waves. Conversely, the lower maximum H_s values for the years 2014 and 2022 suggest that the combined energy content of wind waves and swells was lower, leading to smaller waves.

Examining the average H_s values for the three analyzed sea states reveals a consistent trend. The average significant wave height from the analysis of combined wind waves and swells is 0.94m. For wind waves alone, the average H_s is 0.81m, and for swells alone, it is 0.35m. These stable average values across the years indicate a predictable wave climate, despite the occasional peaks in maximum H_s values.

In summary, while the maximum H_s values for multimodal sea states show significant

variability due to the random combination of wind waves and swells, the average H_s values remain stable.

ENERGY PERIOD INTER-ANNUAL VARIABILITY

The energy period, along with the other syntetic parameters, is analyzed in detail according to the inter-annual variability (Figure 4.35). The energy period of wind waves exhibits

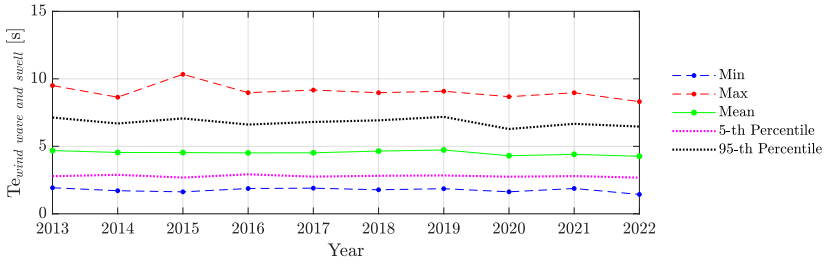

(a) $Te_{wind\ wave\ and\ swell}$ inter-annual variability

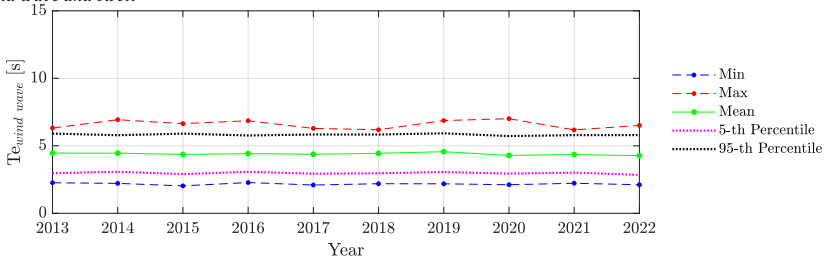

(b) $Te_{wind\ wave}$ inter-annual variability

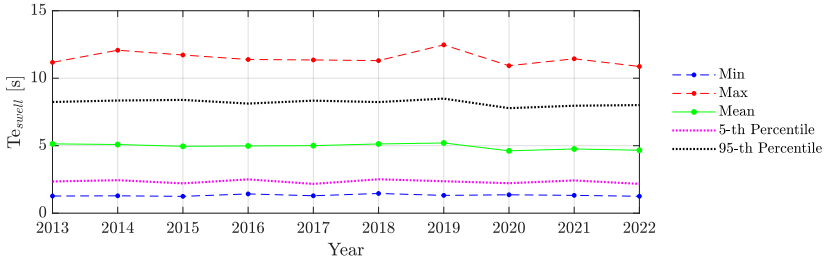

(c) Te_{swell} inter-annual variability

Figure 4.35: Inter-annual variability of Te

reduced intra-annual variability (Fig. 4.35b), with minimum and maximum values that are closer to the average compared to the energy periods of combined wind waves and swells (Fig. 4.35a), as well as swells alone (Fig. 4.35c). This observation aligns with the previous analysis of monthly variability, indicating that wind waves occurring in Pantelleria have a lower variability range compared to other sea states. Specifically, the greatest variability is recorded for swell waves (Figure 4.35c).
Regarding the average values, they remain nearly constant across different years and for

the various sea states analyzed. The average energy period over the ten-year multimodal dataset is approximately 4.5 s for multimodal waves, 4.3 s for wind waves alone, and 5 s for swell waves alone.

These results suggest that while there is some variability in the energy period of the waves, wind waves show more stability compared to swell waves and combined sea states. The consistent average energy periods across the years further confirm the predictable nature of the wave climate in Pantelleria.

DIRECTIONAL SPREADING INTER-ANNUAL VARIABILITY

the inter-annual analysis of the directional spreading corresponding to the multi-modal sea states occurring in Pantelleria and the uni-modal sea states of wind wave and swell is investigated (Fig. 4.36).

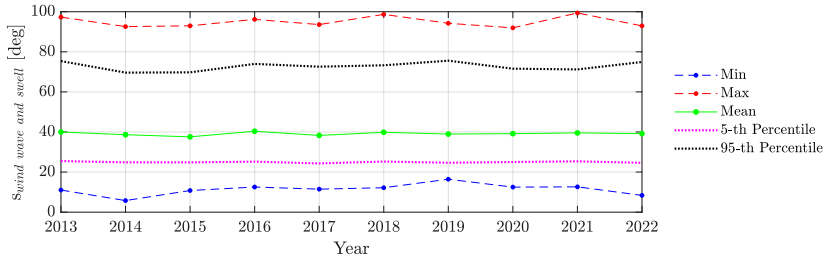

(a) $s_{wind\ wave\ and\ swell}$ inter-annual variability

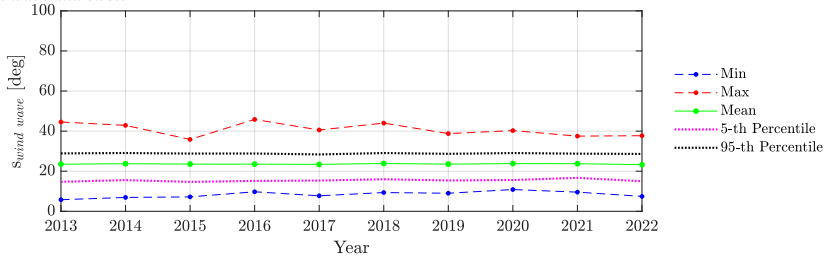

(b) $s_{wind\ wave}$ inter-annual variability

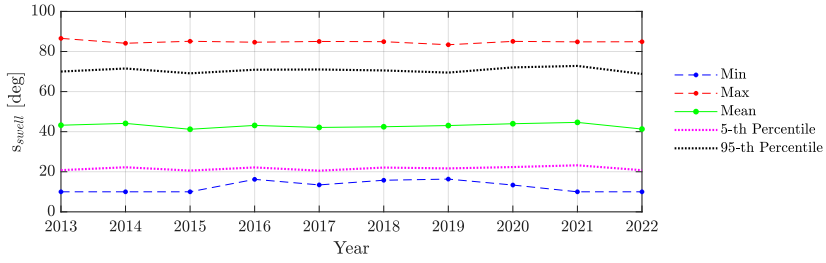

(c) s_{swell} inter-annual variability

Figure 4.36: Inter-annual variability of s

In Figure 4.36a, the interannual variability of directional spreading for the combination of wind waves and swells shows a relatively stable trend over the years. The maximum values and the 95^{th} percentile remain consistently high, indicating that each year a large number of waves are characterized by a narrow range of directions. The average values show minimal change, suggesting that the overall directional spread remains relatively unchanged. The minimum values and the 5^{th} percentile show slight fluctuations but generally remain low, indicating conditions of high directional wave diffusion. This result aligns with predictions, as a high predominance of bi-modal sea states is found, resulting in greater directional variability of the wave components that, by overlapping, generate the sea states characterizing Pantelleria.

Fig. 4.36b focuses on the interannual variability of the directional spread for wind waves only. Similar to the combined sea states, the maximum values remain relatively stable with minor fluctuations, highlighting a consistent directional diffusion pattern. The mean values and the 95^{th} percentile follow a constant trend with minor variations, reflecting the stable nature of the directional spread of wind waves. The minimum values and the 5^{th}percentile remain consistently low, indicating that these wind waves are characterized by wider directional spreads.

Fig. 4.36c presents the interannual variability of the directional diffusion for swells only. The maximum values and the 95^{th} percentile show more pronounced stability over the years, indicating that swell waves also consistently come from a narrow range of directions. The average values show slight variability but maintain a constant trend similar to other wave conditions. The minimum values and the 5^{th} percentile remain low, indicating that wave conditions characterized by high directional variability occur every year.

Consequently, the interannual stability in directional diffusion, combined with previously observed seasonal trends, provides a comprehensive understanding of the wave climate at the site of interest.

Ultimately, the average directional spreading of the waves occurring in Pantelleria, in reference to multimodal sea states, is approximately 39.8°. For swell waves, this value corresponds to 42.4°. In contrast, for wind waves, the value is around 23.5°.

4.3.4. VARIABILITY OF DOMINANT WAVE DIRECTION

The directional distribution of waves is analyzed using wave rose plots, which show the percentage of wave height occurrences from different directions. To draw coherent conclusions, both the wave rose for the multimodal maritime states occurring in Pantelleria and those for the only wind wave and swell are provided (Figure 4.37).

In the wave pattern of combined wind waves and swell, the waves mainly come from the west and north-west directions. The color distribution shows that a significant portion of the waves are between 0 and 2 m of significant wave high, with occasional higher waves exceeding 4 meters, particularly from the northwest.
Likewise, in the rose plot of the wind wave only, the waves mainly come from the west and northwest. The distribution reveals a greater proportion of waves with heights between 1 and 3 metres, suggesting that wind-generated waves contribute significantly to overall wave energy. The absence of higher waves (over 4 m) compared to the combined sea state graph suggests that the extreme wave heights are mainly due to the combined

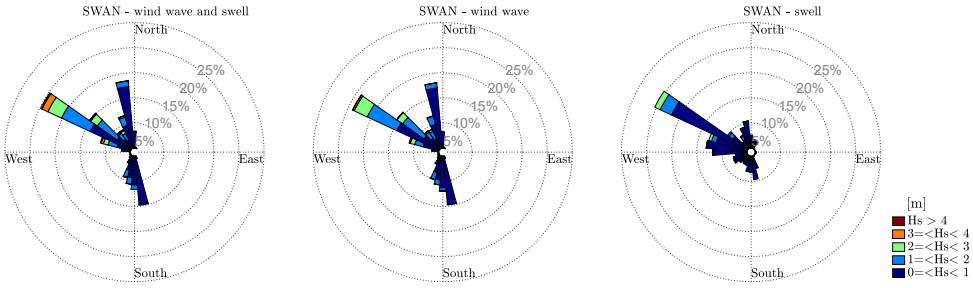

Figure 4.37: Rose plot ($Dir_p - H_s$) according to the different sea states: combination of wind waves and swell (left panel), wind wave (central panel) and swell (right panel)

influence of wind waves and storm surges.
Finally, the wave pattern relating to swell shows a narrower directional spread compared to wind waves. Most significant wave height of the swell are between 1 and 2 m, some reaching up to 3 m. This directional concentration indicates that swell waves are generated primarily by distant storms propagating from the west.
Overall, these rose plots highlight the predominant wave directions and the contribution of different wave heights to Pantelleria's wave climate.

4.3.5. SEA STATE OCCURRENCE

The analysis of the occurrence and energy of sea states is conducted through a conventional method, which consists in determining the probability of occurrence of a specific combination of height H_s and T_e, and in calculating the energy of the sea states waves as a function of this probability.

For this investigation, the values of H_s and T_e are discretized using bins of 0.25 m and 0.5 s, respectively. The Fig. 4.38 provides the probability of occurrence for both the $H_s - T_e$ pairs and the individual parameters. It is observed that the most frequent significant wave height, accounting for 23.84% of events, ranges between 0.5 m and 0.75 m. As for the T_e, it most commonly occurs, with a frequency of 16.48%, between 3.5 s and 4 s. The most frequent $H_s - T_e$ pair occurs with H_s ranging between 0.25 m and 0.5m and T_e between 3s and 3.5s, accounting for 6.7% of occurrences.

In this context, a scatter plot of energy is provided (Fig. 4.39) showing the yearly energy sea state corresponding to the $H_s - T_e$ pairs. From this analysis, the sea state with an occurrence of only 0.89%, chacarterized by H_s ranging between 2.5 m and 2.75 m and T_e ranging between 6 s and 6.5 s is characterized by the maximum value of average annual energy equal to 1.65 MWh/m.

This approach provides a general overview of the wave resource of the site of interest. However, as observed in the case of Pantelleria, the prevalence of multi-modal sea states limits the precision of these analyzes providing more general information. In particular, for devices that are sensitive to wave direction, such as the PeWEC, the coexistence of wind waves and swells leads to a superposition of sea states that can originate from different directions. As a result, the energy distribution is not concentrated around a single

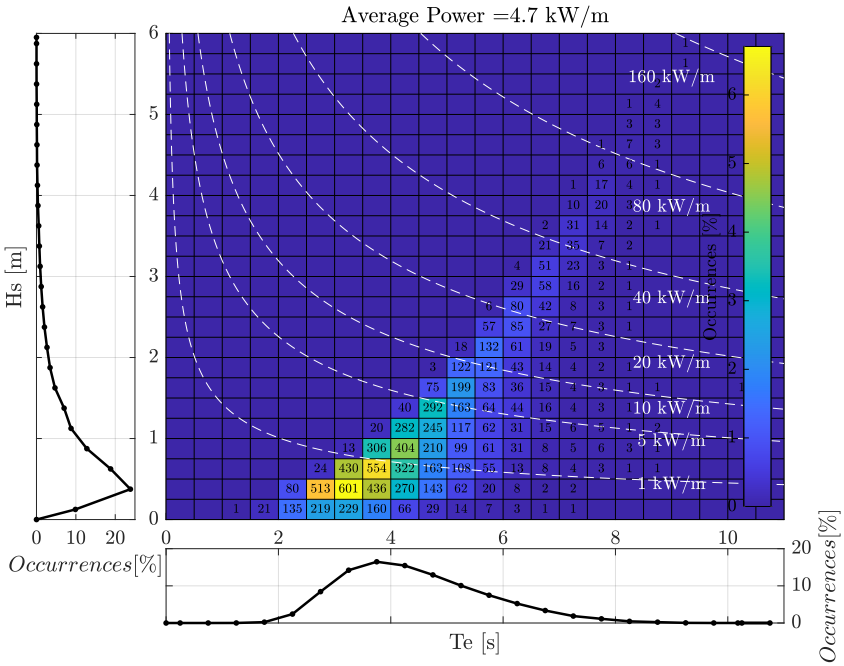

Figure 4.38: Scatter of occurrence in Pantelleria

peak direction of the spectrum, but is dispersed between two or more principal directions. This phenomenon leads to a dispersion of wave energy over a wide spectrum of directions, which, consequently, reduces the extractable energy.

4.4. DICUSSION

THIS chapter addresses the assessment of the wave energy resource at Pantelleria. To achieve this objective, various available data sources are analyzed, processed, and evaluated to identify accurate and reliable in-situ and satellite datasets for use in the calibration and validation of the SWAN model. The difficulty in obtaining a long-term series of in-situ data is highlighted, along with the use of a collocation technique based on a temporal criterion of 30 minutes and a spatial criterion evaluated at various distances.

Moreover, the SWAN model is calibrated and validated using these instrumental data, assessing both the accuracy of significant wave height (H_s) and energy period (T_e), as well as the computational time of different configurations. The use of a Stage-Gate approach significantly reduced the number of configurations to investigate, streamlining the calibration process and focusing on key aspects.

Once the model is validated, the resulting decadal time series is used to conduct a com-

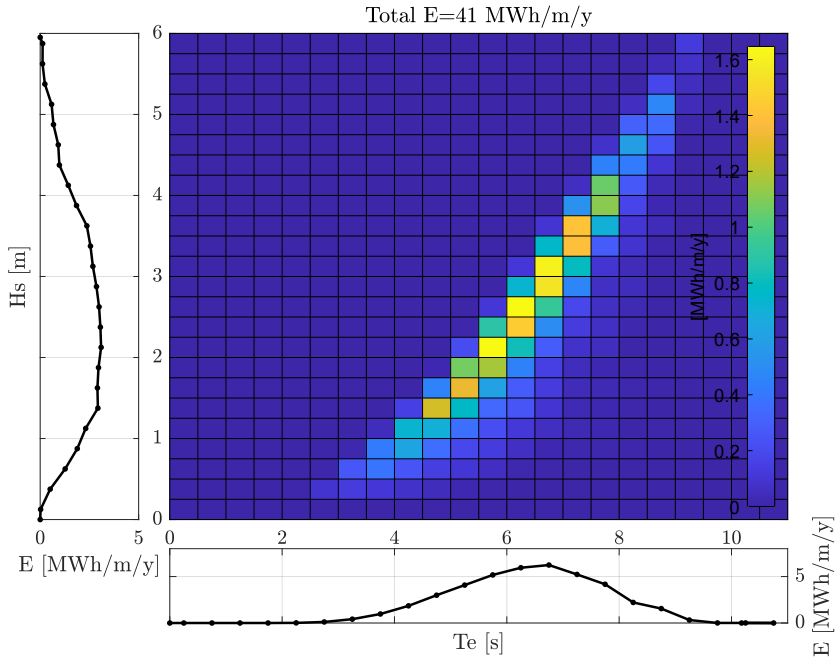

Figure 4.39: Scatter of energy in Pantelleria

prehensive wave resource analysis. Specifically, synthetic parameters derived from the entire spectrum and the partitioned spectra are analyzed to understand the overall characteristics of the waves occurring at Pantelleria, as well as to evaluate the characteristics of wind waves and swell waves.

4.5. CONCLUSION

THE chapter provided a detailed assessment of wave energy resources around the island of Pantelleria using a rigorous methodological approach that combines in-situ data, satellite observations, and numerical models. The analysis highlighted the importance of accurate and reliable data for the calibration and validation of the SWAN model, emphasizing the challenges of obtaining time series of in-situ data and the effectiveness of collocation techniques in mitigating these issues. Specifically, the use of altimetric data, even in geographically unfavorable regions, proved valuable. Although irregular coastlines near the site of interest can reduce the accuracy of satellite observations, the analysis demonstrated that these observations are a valid tool when used as benchmarks for evaluating the accuracy of the numerical model and extending the temporal coverage of the validation dataset.
The calibration and validation of the SWAN model, based on an accurate evaluation of

the parameters H_s and T_e and on the optimization of computational time, demonstrated the effectiveness of the Stage-Gate approach in accelerating the calibration process and focusing on key aspects. This approach enabled the development of a robust and precise numerical model capable of faithfully representing wave conditions in the study area. The analysis of different aspects in setting up the model showed how adjustments correlated with increases or decreases in accuracy relative to the parameters and computational time, ultimately identifying an accurate model with reduced computational time.

Furthermore, the ten-year time series derived from the validated model provided a solid basis for the analysis of wave resources. The examination of synthetic parameters, derived both from the complete spectrum and the spectrum partition, allowed for an understanding of the general characteristics of the waves in Pantelleria, as well as distinguishing between wind waves and swells. This distinction is crucial for the design and optimization of wave energy converters, which can benefit from a detailed understanding of different wave components. The frequency occurrence of bi-modal sea states underscored the importance of using the frequency-directional spectrum as a fundamental tool for comprehensive wave characterization.

III

Literature review: Wave Energy Conveters

5

WAVE ENERGY CONVERTERS DESCRIPTION

5.1. INTRODUCTION

THE Wave Energy Converters (WECs) stand as an emerging frontier in renewable energy technologies, capturing the power of ocean waves to generate electricity. These systems are pivotal for harnessing a vast and largely untapped energy resource, offering a pathway to diversify the renewable energy mix and contribute to global sustainability goals. The development and optimization of WECs involve a multidisciplinary approach, combining marine engineering, fluid dynamics, and renewable energy technology.

Climate change and the mission to sustainably satisfy energy demand are two interconnected and urgent policy challenges for nations worldwide. The exploitation of renewable resources is increasing, and scenarios by the World Energy Outlook and integrated assessment models (IAMs) estimate that, by 2040, renewable energy sources (RESs) may supply 20–30% of the world's primary energy [254]. Currently, most of this energy comes from bioenergy (10%) and hydropower (3%), with the remaining 2% from other renewables such as photovoltaic (PV) and wind energy [255, 256, 257, 258, 259, 260]. As the broad employment of renewable energy is essential, the scientific community is also focusing on wave energy sources, which show great promise [261, 262, 263].

Technologies capable of harnessing wave energy are relatively immature compared to other renewable energy technologies and are currently untapped. However, wave energy has the potential to play a significant role in diversifying the RES portfolio and achieving sustainable growth. In this scenario, there are many types of WECs that can harness energy from waves. These can be classified based on operational principle, absorbing wave direction, location, and power take-off [15, 264]. A basic categorization often used includes terminators, attenuators, and point absorbers [265]. Terminators are characterized by large extensions parallel to the wave direction, while attenuators have a large orthogonal size relative to the wave direction. Both terminators and attenuators are di-

rectional sentitive WECs, as they operate within a narrow range of wave directions. In contrast, point absorbers are smaller than the predominant wavelength and can generate power from waves coming from any direction.

5.2. WAVE ENERGY CONVERTER CLASSIFICATION

DIFFERENT concepts and classifications of WECs exist. First, WECs can be categorized based on their installation location, distance from shore, and bathymetry. Specifically, WECs can be divided into coastal, nearshore, and offshore devices.
Coastal devices are generally fixed structures integrated into port infrastructure. A significant number of these devices are based on the Oscillating Water Column (OWC) technology, which involves a structure where water waves oscillate, causing air trapped in a chamber to flow through a turbine designed to convert wave energy. The advantages of coastal devices include their proximity to the shore and reduced maintenance costs compared to nearshore and offshore devices, which require marine operations for maintenance. However, the high costs of constructing the necessary civil works, along with the significant social and environmental impacts of installing these devices on the shoreline, are notable disadvantages. Additionally, the energy resource in shallow waters is less than that that occur offshore.
Nearshore devices are installed relatively close to the shore, typically about a hundred meters away, in seabed depths between 10 and 25 m. These devices are usually fixed directly to the seabed rather than being anchored with moorings. The advantages include their relative proximity to the shore, which facilitates construction, maintenance, and decommissioning operations and reduces costs due to the shorter distance of the electric cable from the coastline. Furthermore, being installed offshore, they benefit from a greater wave energy resource than coastal devices. The main disadvantage is the environmental and social impact due to the presence of WECs near human activities.
Offshore WECs are installed in locations with bathymetry greater than 40 m and are situated far from shore. These devices are typically floating or submerged and are moored to the seabed. Offshore installations benefit from a greater energy resource and lower environmental and social impacts due to their distance from the coast. However, the harsher marine environments in which they are installed require the devices to be designed to withstand higher loads, leading to increased overall costs.

Another classification is based on the size and orientation of the device with respect to the direction of the incoming wave. Point absorbers are characterized by their relatively small dimensions compared to the incident wavelength. These devices can be either floating (Fig. 5.1) or submerged structures moored to the seabed. They capture wave energy by damping the movement of the structure, typically through the vertical motion known as heave. Due to their compact size, point absorbers are often installed in arrays, which offers significant advantages in terms of economies of scale. This modular approach allows for more efficient energy capture over a larger area and facilitates maintenance and scalability [266, 267].
Examples of point absorbers include the PowerBuoy, a floating device developed by Ocean Power Technologies [268], and the CETO, a fully submerged buoy developed by Carnegie

[269]. Both of these devices exemplify the versatility and effectiveness of point absorbers in harnessing wave energy, showcasing different approaches to optimizing energy capture in various marine environments.

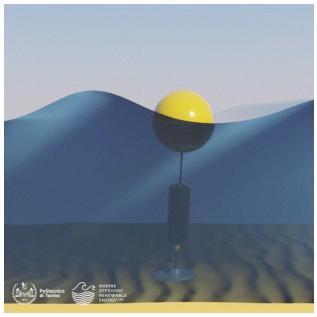

Figure 5.1: Simplified representation of a Notional Heaving Buoy WEC

Attenuator-type WEC (Fig. 5.2) is a device consisting of multiple floating bodies connected to each other, forming a chain. This chain of floating bodies is aligned with the direction of the incoming waves, causing a bending motion as waves pass through the system. This motion drives hydraulic pumps, which ultimately generate electricity. These devices are typically anchored using moorings and are characterized by a total length greater than the incident wavelength. They are floating structures made up of multiple sections connected by hinged joints. The relative movement between these sections is damped by a hydraulic power take-off system, which harnesses the energy of the incident waves. During operation, the multi-body structure aligns with the direction of the dominant wave to maximize energy capture. A well-known example of this type of WEC is the Pelamis [270].

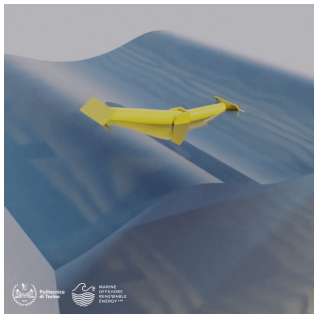

Figure 5.2: Simplified representation of an attenutator-type WEC

WEC devices with a predominant orientation perpendicular to the direction of wave propagation (and consequently parallel to the wave front) are called terminators (Fig. 5.3). These devices are designed to absorb energy from waves as they hit the device head-on.
An example of such a device is the Wave Dragon [271], which utilizes the overtopping

working principle to capture energy from the wave source (Fig. 5.3a). Fixed-structure Oscillating Water Columns (OWCs) are also classified as terminators due to their orientation and energy capture method (Fig. 5.3b).
Additionally, terminators include WECs that exploit wave energy by damping the pitching motion of a device, as Pendulum Wave Energy Converter (PeWEC) [272] (Fig. 5.3c). These devices have their main dimension oriented perpendicular to the direction of the incoming dominant wave, maximizing energy absorption from the wave front.

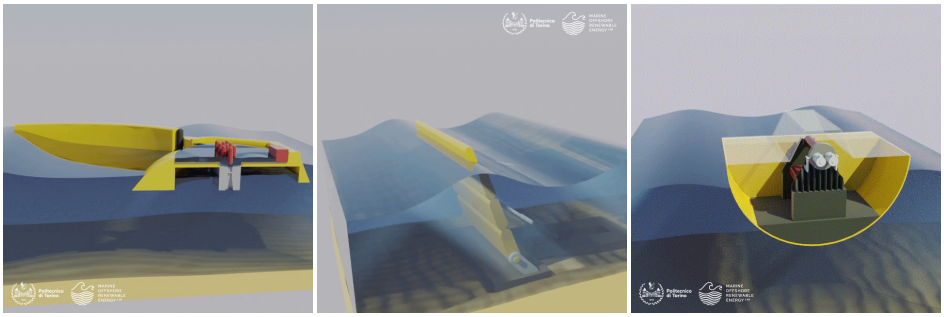

(a) Simplified representation of Overtopping Device (b) Simplified representation of Oscillating Water Columns (c) Simplified representation of Pitching Device

Figure 5.3: Simplified representation of terminators devices

Tab. 5.1 provides an overview of the main characteristics of some of the primary WECs developed. Specifically, the table includes information on the optimal bathymetric depth range and the sensitivity of each device to wave direction. Each WEC operates effectively within a certain depth range, and this operational depth is crucial for maximizing energy capture and efficiency. Additionally, the table distinguishes between directionally sensitive and non-directionally sensitive devices. Direction-sensitive WECs can effectively absorb and convert wave energy from specific directions, while non-directionally sensitive WECs can harness wave energy regardless of its direction.

Table 5.1: WECs' general characteristics

Device	Classification	Depth range [m]	Directional sensitivity
Notional Heaving Buoy	Point-absorber	0-100	No
Attenuator-type	Attenuator	50-70	Yes
Oscillating Surge	Termintor	10-15	Yes
Onshore OWC	Terminator	0-20	Yes
Oscillating Pitch	Termintor	15-40	Yes

5.3. EVOLUTION IN WAVE ENERGY CONVERTER MODELING

WAVE Energy Converters represent a fascinating and evolving field within renewable energy, promising to harness the vast power of ocean waves. The journey towards realizing this potential spans over two centuries, with the first WEC patent filed by Monsieur Girard and his son in 1799. Despite their visionary concept, the lack of numerical tools for power estimation hindered its realization. It wasn't until the oil crisis in 1974 that numerical modelling of WECs gained momentum, marked by significant contributions from pioneers like Salter [273], Evans [274], and Mei [275]. These efforts laid the groundwork for both frequency and time-domain models, revolutionizing the understanding of WEC dynamics.

The late 20th century saw further advancements with the integration of arbitrary shape hydrodynamic coefficients and the introduction of nonlinear potential flow theory models [276]. The turn of the millennium brought computational fluid dynamics (CFD) into the fray, significantly aided by the advent of open-source platforms like OpenFOAM, which provided access to sophisticated modelling tools. The inclusion of WECs in wave propagation models marked another leap forward, enabling the study of far-field effects and array interactions with unprecedented detail.

Despite these advances, the WEC field faces ongoing challenges, primarily around model validation due to scarce full-scale deployment data. Looking ahead, the unceasing increase in computing power and the development of hybrid models promise to push the boundaries further, blending various modeling techniques to achieve higher fidelity and efficiency.

5.4. HYDRODYNAMIC MODELS

THE hydrodynamics of a wave energy system can be analyzed through various techniques, each with different levels of reliability and computational costs. These techniques include different hydrodynamic models, which can be classified as follows:

- **Models based on potential flow theory** that derive hydrodynamic properties through the evaluation of the principles of potential flow theory. These models are mainly used in the first steps of WEC modeling and are based on linearity assumptions.
- **Computational fluid dynamics (CFD) models** address Navier-Stokes equations within discretized domains. These models offer a comprehensive approach taking into account fully nonlinear fluid dynamics, including factors such as viscosity and compressibility of the fluid.

Since the hydrodynamic interaction between WECs and ocean waves presents an extremely complex, higher-order nonlinear process, when certain conditions exists they are simplified. In particular, in cases of oscillatory devices and small-amplitude wave motions, the hydrodynamic problem can be adequately described using a linear approach, which is generally valid throughout the operating regime of the device [277]. This involves the application of the superposition principle [278] which allows harmonic

solutions to be linearly combined to construct more complex solutions. In this context, the representation of reactive forces, as in the case of moorings and PTO, can also be carried out using linear equations. The first significant advance in modeling the dynamics of WECs typically occurs in the frequency domain, where the excitation takes a simple harmonic form. The main challenge in frequency domain analysis is determining the radiation and excitation loads on the device. This is usually based on the application of boundary element methods (BEM), based on potential flow theory, to estimate the hydrodynamic coefficients of added mass, damping and excitation force per unit amplitude of the incident wave. The pioneering numerical methodologies developed by Newman and Lee led to the development of codes WAMIT [279], which is widely used for offshore and naval problems, wave-structure interaction and wave energy conversion. Subsequently, additional BEM codes were developed, such as ANSYS-AQWA [280] and NEMOH [281]. In particular, NEMOH has been developed at the Ecole Centrale de Nantes, and is the first open source potential flow boundary element solver to calculate wave loads on offshore structures.

NEMOH is therefore a solver that allows solving the first-order problem in the frequency domain and provides support in the hydrodynamic design of the floating structure. Since its first release in 2014, the software has been widely used and validated. Many WECs designs have been based on NEMOH [282, 283, 284, 285], as well as floating platforms of offshore wind turbines [286, 287, 288] and hybrid devices for converting energy from wind and waves [289]. Moreover, his performance has been reported in comparative studies with other software such as WAMIT in [283, 284] and HAMS [290] in [291] showing good accuracy in most applications despite limited computational costs. However, the limitations of frequency domain models become evident when trying to validate PTO control strategies [292, 293]. Furthermore, they also show limitations in dealing with nonlinear dynamics introduced by moorings. This requires moving to time domain modeling for a more accurate representation of the performance of a WEC. Time-domain models can capture nonlinearities within the energy conversion chain, including those arising from hydrodynamic forces and damping mechanisms. Furthermore, they are indispensable for simulating transient events that frequency-domain models, suitable only for stationary processes, cannot accurately represent. At the expense of better performance, time domain models require significantly higher computational resources. As a result, their application is generally reserved for the late stages of WEC development, i.e. when, the fundamental design parameters of the device have been consolidated, shifting the focus towards refining the PTO system and refining the control strategy.

5.4.1. POTENTIAL FLOW THEORY

Using potential flow theory to characterize the motion of WECs in response to ocean waves can provide satisfactory accuracy under specific conditions, particularly when the slope of the incident wave and the amplitude of float motion are small. This theory is based on the following hypotheses:

- The floating device is treated as a rigid body.
- The fluid is assumed ideal, meaning it is inviscid, incompressible, and irrotational.

By defining $\boldsymbol{u} = (u_x, u_y, u_z)$ as the velocity field of the fluid and studying an irrotational motion, it is possible to describe this velocity field via the gradient of the scalar potential velocity function:

$$\boldsymbol{u} = \nabla\phi \tag{5.1}$$

The mass balance equation for an incompressible fluid is identically zero since the density remains constant during the motion. It is written:

$$\nabla \cdot \boldsymbol{u} = 0 \tag{5.2}$$

Substituting 5.1 into 5.2, the Laplace's equation for the velocity potential is obtained:

$$\nabla^2\phi = 0 \tag{5.3}$$

To solve the Laplace's equation for the velocity potential, the assignment of boundary conditions is necessary:

- **Dynamic boundary condition on the free surface:** At the undisturbed free surface, the fluid pressure must be equal to atmospheric pressure:

$$\frac{\partial\phi}{\partial t} + g\boldsymbol{\eta} = 0 \quad \text{at } z = 0 \quad \text{for } \frac{H}{L} << 1 \quad \& \frac{H}{h} << 1 \tag{5.4}$$

  where $\boldsymbol{\eta}$ indicates the free surface elevation and g is the gravity acceleration

- **Kinematic boundary condition on the free surface**: Fluid particles on the free surface remain on the free surface for all instants of time; i.e., the normal component of the fluid velocity must be equal to the velocity of the surface:

$$\frac{\partial\phi}{\partial z} - \frac{\partial\boldsymbol{\eta}}{\partial t} = 0 \quad \text{at } z = 0 \quad \text{for } \frac{H}{L} << 1 \quad \& \frac{H}{h} << 1 \tag{5.5}$$

- **Body hull impermeability condition**: The component of fluid velocity normal to the body surface must be equal to the velocity of the body normal $\boldsymbol{u}_n$ to the body surface S_b:

$$\frac{\partial\phi}{\partial n} - \boldsymbol{u}_n = 0 \quad \text{at } S_b \tag{5.6}$$

- **Flat seabed impermeability condition**: Water particles cannot cross through the seabed, so the vertical component of the fluid velocity is zero:

$$\frac{\partial\phi}{\partial z} = 0 \quad \text{at } z = -h \tag{5.7}$$

  where h indicates the depth of the seabed in relation to the mean level of the free surface.

- **Radiation condition**: As the distance from the body (r) increases, the wave potential tends to zero:

$$\lim_{r\to\pm\infty} \nabla\phi = 0 \tag{5.8}$$

Solutions to the Laplace's equation 5.3 have a sinusoidal form and a decomposition of the problem into spatial and temporal dependencies is possible:

$$\begin{cases} \boldsymbol{\eta}(\mathbf{x},t) = \widehat{\boldsymbol{\eta}} e^{i(\mathbf{k}\cdot\mathbf{x}-\omega t)} \\ \phi(\mathbf{x},t) = \frac{g\cosh(|\mathbf{k}|(z+h))}{\omega\cosh(|\mathbf{k}|h)} \widehat{\boldsymbol{\eta}} e^{i(\mathbf{k}\cdot\mathbf{x}-\omega t)} \end{cases} \tag{5.9}$$

where $\mathbf{x} = [x, y]^T$ denotes the coordinates of the wave elevation, $\mathbf{k} = [k_x, k_y]^T$ represents the wave number, $\widehat{\boldsymbol{\eta}}$ is the complex wave amplitude of the wave elevation, ω describes the wave frequency and i is the imaginary unit. The wave number and the wave frequency are related through the dispersion relation, given by:

$$\omega^2 = g\,|\mathbf{k}|\tanh(|\mathbf{k}|\,h) \tag{5.10}$$

WAVE FIELD DECOMPOSTITION

The first-order harmonic fluid potential, according to the potential flow theory described in 5.4.1, may be shortly defined as

$$\phi(\mathbf{x},t) = Re\left\{\phi(\mathbf{x})e^{-iwt}\right\} \tag{5.11}$$

which, according to the linear seakeeping theory [294, 295], may be described as a superimposition of three different wave fields.

$$\phi = \phi_I + \phi_D + \phi_R \tag{5.12}$$

where:

- ϕ_I is the velocity potential of an incident wave field that would exist in the absence of the body, and therefore is the potential velocity of the undisturbed wave. It does not satisfy either the boundary condition on the body or the radiation condition, as it represents wave propagation in the absence of the body. According to the Airy's wave theory [296], and, for a wave elevation η with amplitude A and propagating along the direction θ, the incident potential is written:

$$\phi_I(x,y,z,t) = \frac{g\cosh(|\mathbf{k}|(z+h))}{\omega\cosh(|\mathbf{k}|h)} \widehat{\boldsymbol{\eta}} e^{i[\mathbf{k}(x\cos\theta + ycos\theta)-\omega t]} \tag{5.13}$$

  Only the solution to the incident wave problem can be obtained analytically. The other flow potentials are computed numerically using Green's theorem, which converts a volume integral into a surface integral, making it faster and much easier to manage.

- ϕ_D is the velocity potential of a diffracted wave field caused by the interaction between the body and the incident wave. While analytical solutions exist for certain cases of the diffraction problem, like vertical cylinders [297], the general problem is typically tackled numerically. This is done using BEMs, where the body hull geometry is discretized for computational purposes. Together, the incident and diffracted potentials must satisfy the no-flow condition 5.6 on the hull surface:

$$\frac{\partial\phi_I}{\partial n} + \frac{\partial\phi_D}{\partial n} = 0 \quad \text{at } S_b \tag{5.14}$$

- ϕ_R is the velocity potential of a radiated wave field produced by the oscillation of the body in calm water. Although analytical solutions are available for specific instances of the radiation problem [297], a more widespread approach involves numerical methods. Boundary element methods (BEMs) are commonly employed, requiring the discretization of the body hull geometry to solve the problem computationally. This component must adhere to boundary conditions imposed on the body's surface S_b, accounting for its oscillations in any unconstrained Degree of Freedom (DoF). In terms of boundary conditions, the velocity of the fluid at a point on the wet surface of the hull equals the velocity of the point of the hull itself.

$$\frac{\partial \phi_R}{\partial n} = \boldsymbol{u}_n(x,y,z) \quad \text{at } S_b \tag{5.15}$$

  Where v_n is the normal velocity to the surface of the hull body. Furthermore, for the radiation boundary condition it has to assume that as the distance from the body increases, the potential must decay, ensuring that the wave field converges to the undisturbed state far from the body:

$$\lim_{r\to\pm\infty} \nabla\phi_R = 0 \tag{5.16}$$

According to the described decomposition, Laplace equation becomes:

$$\nabla^2\phi_I + \nabla^2\phi_D + \nabla^2\phi_R = 0 \tag{5.17}$$

Consequently, the linearized fluid equations, satisfied by the three wavefields, are summarized as follows:

$$\begin{cases} \frac{\partial \phi_I}{\partial t} + \frac{\partial \phi_D}{\partial t} + \frac{\partial \phi_R}{\partial t} + g\boldsymbol{\eta} = 0 & \text{at } z = 0 \\ \frac{\partial \phi_I}{\partial z} + \frac{\partial \phi_D}{\partial z} + \frac{\partial \phi_R}{\partial z} - \frac{\partial \boldsymbol{\eta}}{\partial t} = 0 & \text{at } z = 0 \\ \frac{\partial \phi_D}{\partial n} + \frac{\partial \phi_I}{\partial n} = 0 & \& \quad \frac{\partial \phi_R}{\partial n} = \boldsymbol{u}_n(x,y,z) \quad \text{at } S_b \\ \frac{\partial \phi_I}{\partial z} + \frac{\partial \phi_D}{\partial z} + \frac{\partial \phi_R}{\partial z} = 0 & \text{at } z = -h \\ \lim_{r\to\pm\infty} \nabla\phi_D + \nabla\phi_R = 0 \end{cases} \tag{5.18}$$

5.4.2. BODY-WAVE INTERACTION DESCRIPTION

At the basis of WEC modelling is Newton's second law, for which the inertial forces are balanced with those acting on the device. These forces can be classified into external forces, resulting from the hydrodynamic interaction between the device and the waves, and reaction forces, resulting from the coupling between the moving components. Specifically, external forces include:

- **Hydrostatic forces**, resulting from the distribution of hydrostatic pressures on the hull
- **Excitation forces**, generated by incident waves hitting the hull
- **Radiation forces**, exerted on the device due to radiation waves induced by body movement in calm water

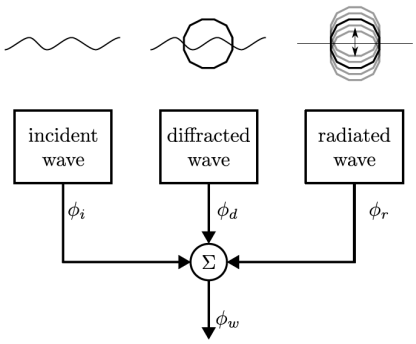

Figure 5.4: Decoupling of the linear potential theory [298]

The reaction forces however vary depending on the type of WEC considered, however generally attributed to:

- **PTO**, i.e. the power extraction subsystem that converts mechanical energy into energy
- **Mooring system**, which is responsible for device station-keeping

The device local frame of reference can be described by a coordinate vector ξ, where x,y,z represent the body translation and α,δ,ψ describe the body rotations:

$$\xi = \begin{bmatrix} x \\ y \\ z \\ \alpha \\ \delta \\ \psi \end{bmatrix} = \begin{bmatrix} surge \\ sway \\ heave \\ roll \\ pitch \\ yaw \end{bmatrix} \tag{5.19}$$

From now on, the origin of the device local frame is assumed located at the mass center of the system. The reference system of a WEC is described in 5.5, where the cartesian global coordinate system is described by (x_0, y_0, z_0). In the time domain, the general motion equation, in accordance with the linear theory and the Newton's second law, is given by:

$$\boldsymbol{M}\ddot{\boldsymbol{\xi}}(t) = \boldsymbol{F}_p(t) + \boldsymbol{F}_{ext}(t) \tag{5.20}$$

where

- $\boldsymbol{M}$ corresponds to the inertia matrix of the device

$$M_s = \begin{bmatrix} m & 0 & 0 & 0 & 0 & 0 \\ 0 & m & 0 & 0 & 0 & 0 \\ 0 & 0 & m & 0 & 0 & 0 \\ 0 & 0 & 0 & I_{xx} & I_{xy} & I_{xz} \\ 0 & 0 & 0 & I_{yx} & I_{yy} & I_{yz} \\ 0 & 0 & 0 & I_{zx} & I_{zx} & I_{zz} \end{bmatrix} \tag{5.21}$$

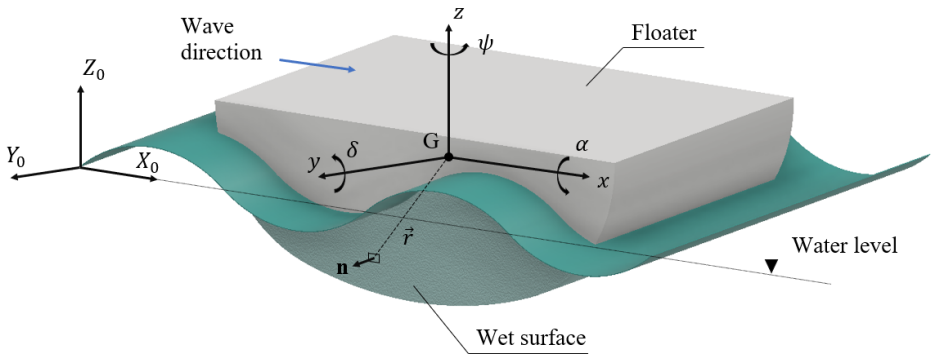

Figure 5.5: WEC's coordinate system

where m is the body mass, and I_{xx}, I_{yy} and I_{zz} are the roll, pitch and yaw moment of inertia, respectively

- $\ddot{\xi}$ is the acceleration of the body
- $\boldsymbol{F}_p$ describes the force caused by external pressure on the hull device, comprising hydrodynamic and hydrostatic forces. This force may be decomposed into the hydrostatic restoring force ($\boldsymbol{F}_{hs}$), caused by the gravity and buoyancy, and the hydrodynamic force ($\boldsymbol{F}_{hd}$).

$$\boldsymbol{F}_p = \boldsymbol{F}_{hs} + \boldsymbol{F}_{hd} \tag{5.22}$$

In turn, the hydrodynamic forces may disjointed in the radiation force ($\boldsymbol{F}_r$) and the wave exitation force ($\boldsymbol{F}_e$). Then:

$$\boldsymbol{F}_{hd} = \boldsymbol{F}_r + \boldsymbol{F}_e \tag{5.23}$$

The **radiation force** represents the reactive force due to the displacement of water induced by the forced motion of the body in the absence of an incident wave field. The exitation force describe the effect of the pressure forces acting on a fixed floating device and can be divided into **Froude-Krylov force** ($\boldsymbol{F}_I$), that takes into account the undisturbed wave velocity potential on the mean wet surface of the body, and the **diffraction force** ($\boldsymbol{F}_D$) that represents the effective disturbance of the wave field due to the body presence.

$$\boldsymbol{F}_e = \boldsymbol{F}_I + \boldsymbol{F}_D \tag{5.24}$$

- $\boldsymbol{F}_{ext}$ represents the external forces. In the present thesis, only the external force of the PTO is considered. To maintain the linear model, the effects of other external forces, such as moorings, are neglected due to their second-order effects.

$$\boldsymbol{F}_{ext} = \boldsymbol{F}_{PTO} + \boldsymbol{F}_m \tag{5.25}$$

FREQUENCY-DOMAIN MODELS

Following the linear theory and the harmonic assumption about the oscillatory device motion, the device displacement vector can be decomposed in its spatial and temporal dependencies through a complex aptitude and a sinusoidal time dependence [299].

$$\xi(t) = Re\left\{\sum_\omega \widehat{\xi}(\omega) e^{-i\omega t}\right\} \tag{5.26}$$

where $\widehat{}$ denotes complex amplitudes. Consequently, the velocity ($\dot{\xi}$) and the acceleration ($\ddot{\xi}$) result

$$\dot{\xi}(t) = Re\left\{i\omega \sum_\omega \widehat{\xi}(\omega) e^{-i\omega t}\right\} \tag{5.27}$$

and

$$\ddot{\xi}(t) = Re\left\{-\omega^2 \sum_\omega \widehat{\xi}(\omega) e^{-i\omega t}\right\} \tag{5.28}$$

Since all forces acting on the floating body can be described by a complex amplitude and a sisusoidal time term, the Newton's low in the frequency domain may be written as

$$-\boldsymbol{M}\omega^2 \widehat{\xi}(\omega) = \widehat{\boldsymbol{F}}_e(\omega) + \widehat{\boldsymbol{F}}_r(\omega) + \widehat{\boldsymbol{F}}_{hs}(\omega) + \widehat{\boldsymbol{F}}_{PTO}(\omega) \tag{5.29}$$

HYDRODYNAMIC FORCES

For all but the simplest geometries, analytically solving the boundary conditions described in 5.4.1 is not feasible. As a result, numerical methods are typically employed to analyze floating structures in the presence of ocean waves [282, 283, 284, 285]. Those numerical methods are based on boundary-integral equation [279, 280, 281], formulated using the Green function [294], that satisfies the linear boundary conditions for harmonic waves.

To evaluate the pressure over the mean wetted surface, distinct solutions are calculated, simultaneously for both the diffraction problem, which accounts for the effects of incident waves on the stationary body, and the radiation problem for each degree of freedom of the body's motion. These solutions are then utilized to derive important hydrodynamic parameters. The potential hydrodynamic forces of the flow are determined by integrating the dynamic pressure on the mean surface of the wetted body (S_b).

The dynamic pressure described by the linearized Bernoulli equation may be written as

$$p_e = -\rho \frac{\partial \phi}{\partial t} \tag{5.30}$$

Therefore, the linear hydrodynamic force on a floating body can be written as

$$\boldsymbol{F}_{hd} = \int_{S_b} p_e \boldsymbol{n} dS_b = -\rho \int_{S_b} \frac{\partial \phi}{\partial t} \boldsymbol{n} dS_b \tag{5.31}$$

Exploiting the decomposition of the velocity potential in the Eq. 5.31, and considering the Eq. 5.24, $\boldsymbol{F}_{hd}$ becomes

$$\boldsymbol{F}_{hd} = \boldsymbol{F}_e + \boldsymbol{F}_r = -\rho \int_{S_b} \left(\frac{\partial \phi_I}{\partial t} + \frac{\partial \phi_D}{\partial t} + \frac{\partial \phi_R}{\partial t}\right) \boldsymbol{n} dS_b \tag{5.32}$$

Integrating the pressure due to the incident and diffracted potentials the wave excitation force, i.e. the Foude-Krylov and Diffraction forces, are obtained

$$\boldsymbol{F}_e = \boldsymbol{F}_I + \boldsymbol{F}_D = -\rho \int_{S_b} \left(\frac{\partial \phi_I}{\partial t} + \frac{\partial \phi_D}{\partial t} \right) \boldsymbol{n} dS_b \tag{5.33}$$

The complex amplitude of the hydrodynamic forces are

$$\widehat{\boldsymbol{F}}_e = \widehat{\boldsymbol{F}}_I + \widehat{\boldsymbol{F}}_D = i\omega\rho \int_{S_b} \left(\widehat{\phi}_I + \widehat{\phi}_D \right) \boldsymbol{n} dS_b \tag{5.34}$$

By exploiting a 3D panel code such as Nemoh [281], it is possible to calculate the complex coefficients of amplitude for the Froude-Krylov and the Diffraction forces for each DoF.

The complex amplitude of the radiation force can be obtained from the third integrated term of the last expression of Eq. 5.32

$$\widehat{\boldsymbol{F}}_r = -\omega^2 \rho \int_{S_b} \widehat{\phi}_R \boldsymbol{n} dS_b \tag{5.35}$$

This hydrodynamic force can be also expand in real and imaginary parts:

$$\widehat{\boldsymbol{F}}_r = -i\omega \boldsymbol{R} \widehat{\xi} + w \boldsymbol{X} \widehat{\xi} \tag{5.36}$$

where $\boldsymbol{R}$ corresponds to the real part and is the so-called hydrodynamic damping coefficient, describing the dissipative effect. Furthermore, the X term describes the imaginary part, representing the radiation reactance, frequently written as $\omega \boldsymbol{A}$, where $\boldsymbol{A}$ is the added mass coefficient corresponding to an inertial increase due to the water displaced caused by the body's motion. Therefore, the hydrodynamic radiation force of a floating device may be given by

$$\widehat{\boldsymbol{F}}_r = -i\omega \boldsymbol{R} \widehat{\xi} + \omega^2 \boldsymbol{A} \widehat{\xi} \tag{5.37}$$

The first term of Eq. 5.37 is the dissipative phenomenon, proportional to the device velocity, and the second one is the inertial term, proportional to the device acceleration.

HYDROSTATIC FORCES

The hydrostatic force results from the balance between gravity and buoyancy and may be calculated integrating the static pressure of the fluid over the wet surface

$$\widehat{\boldsymbol{F}}_{hs} = \rho g \int_{S_b} z \boldsymbol{n} dS_b \tag{5.38}$$

Assuming that the amplitudes of the movements of the floating device are small, linearizing the hydrostatic force yields a reasonably accurate approximation. Here, the hydrostatic force is proportional to the displacement and therefore its complex amplitude is described by

$$\widehat{\boldsymbol{F}}_{hs} = -\boldsymbol{K}_f \widehat{\xi} \tag{5.39}$$

where $\boldsymbol{K}_f$ corresponds to the hydrostatic spring stiffness coefficient.

REACTION FORCES

The reaction forces in the frequency domain for a WEC are essentially represented by components due to the PTO and the mooring system. The dynamic behavior of the PTO is non-linear, due to complex control strategies applied to maximize wave energy capture. However, in the frequency domain, the PTO reaction force must be linearized to keep the superposition principle valid, expressing it as a linear combination of a component proportional to the velocity of the device and a component proportional to the displacement of the device with respect to its equilibrium position.

$$\widehat{\boldsymbol{F}}_{PTO} = -i\omega \boldsymbol{B}_{PTO}\widehat{\xi} - \boldsymbol{K}_{PTO}\widehat{\xi} \tag{5.40}$$

with the $\boldsymbol{B}_{PTO}$ as the damping coefficient, which represents the dissipative effect, and the $\boldsymbol{K}_{PTO}$ as the stiffness coefficient, which simulates the spring effect. The first term of the equation represents the dissipative term of the PTO which converts the mechanical energy of the movement of the device into electrical energy, while the second term is the elastic one that corresponds to a restoring force which tends to bring the device back to its original position.

Under the assumption of harmonic motions and incident sinusoidal waves, Newton's second law can be reformulated in the frequency domain to accurately describe the dynamics of a floating device. This approach simplifies the analysis of WECs by focusing on the relationship between the oscillatory motion of the device and the sinusoidal nature of wave forces.

$$\left[-\omega^2 \left(\boldsymbol{M} + \boldsymbol{A}(\omega)\right) + i\omega \left(\boldsymbol{R}(\omega) + \boldsymbol{B}_{PTO}(\omega)\right) + \boldsymbol{K}_f + \boldsymbol{K}_{PTO}\right] \widehat{\xi}(\omega) = \widehat{\boldsymbol{F}}_e(\omega) \tag{5.41}$$

Accordingly, the complex amplitude of the device motion is

$$\widehat{\xi}(\omega) = \frac{\widehat{\boldsymbol{F}}_e(\omega)}{-\omega^2(\boldsymbol{M}+\boldsymbol{A}(\omega)) + i\omega(\boldsymbol{R}(\omega)+\boldsymbol{B}_{PTO}(\omega)) + \boldsymbol{K}_f + \boldsymbol{K}_{PTO}} \tag{5.42}$$

From the above relationship, the Response Amplitude Operator (RAO) is evaluated in a straightforward way.

$$RAO = \frac{\xi}{\eta} \tag{5.43}$$

where ξ is the motion amplitude and the η is the wave amplitude. The RAO represents the frequency domain transfer function and relates the wave elevation to the floater motion amplitudes at the ω frequency. It provides valuable insights into the dynamic behavior of floating body under wave conditions, aiding in the design and analysis of their performance.

TIME-DOMAIN MODELS

The Cummins equation [300], introduced for the first time in 1962, has become fundamental for understanding and predicting the dynamic behavior of floating bodies under the influence of waves. The equation provides a solid basis for time-domain analysis, based on the assumption that hydrodynamic interactions can be linearized. This

premise facilitates the translation of complex physical phenomena into a simpler form. Within the framework of linear wave theory, assuming small wave steepness and limited motion of the floater, Cummins equation for the time-domain hydrodynamics of the floater can be written

$$(\boldsymbol{M}+\boldsymbol{A}_{\infty})\ddot{\xi}(t)+\int_0^t \boldsymbol{K}_r(t-\tau)\dot{\xi}(\tau)\,d\tau+\boldsymbol{K}_f\xi(t)=\boldsymbol{F}_{\text{wav}}(t)+\boldsymbol{F}_{\text{PTO}}(t) \tag{5.44}$$

where

- $\boldsymbol{M}$ describes the mass of the floating body
- $\boldsymbol{A}_{\infty}$ is the added mass at infinite frequency and reflects the additional inertia imparted to a floating body by the surrounding fluid, assuming the body's motion induces an instantaneous fluid response. It is given by

  $$\boldsymbol{A}_{\infty}=\lim_{\omega\to\infty} A(\omega) \tag{5.45}$$

  where $\boldsymbol{A}(\omega)$ corresponds to the frequency-dependent added mass introduced in 5.4.2
- ξ and $\ddot{\xi}$ represent the position and velocity of the body at time t
- $\boldsymbol{K}_r$ denotes the Radiation Impulse Response Function (RIRF), also know as memory function because its capability for capturing the effect of hydrodynamic memory. This term indicates that the current hydrodynamic forces depend not only on the present but also on the historical motion of the body.
- $\boldsymbol{K}_f$ is the stiffness matrix introduced in 5.39
- $\boldsymbol{F}_{\text{wav}}$ is the wave-induced force at time t
- $\boldsymbol{F}_{\text{PTO}}$ accounts for PTO force

To quantify the radiation forces ($\boldsymbol{F}_r$), it is necessary to evaluate the convolution integral that describes the complex interactions between the motion of the hull and the surrounding fluid [301]. Specifically, the convolution integral for the radiation forces can be expressed as

$$\boldsymbol{F}_r(t)=\int_0^t \boldsymbol{K}_r(t-\tau)\dot{\xi}(\tau)\,d\tau \tag{5.46}$$

Computing the convolution term represents a significant numerical challenge, and replacing this convolution term with an equivalent state space model is a technique to improve computational efficiency. Furthermore, the state space representation is highly advantageous for numerical simulations and facilitates the formulation of control strategies. The state space model for the convolution integral has the following form

$$\begin{cases}\dot{\zeta}(t)=\mathbf{A}_r\zeta(t)+\mathbf{B}_r\xi(t)\\ \boldsymbol{F}_r(t)=\mathbf{C}_r\zeta(t)+\mathbf{D}_r\xi(t)\end{cases} \tag{5.47}$$

Here,

- ζ and $\dot{\zeta}$ represent the state vector and the derivative of the state vector over time t, representing the system's state evolution approximating the radiation force contributions

- $\mathbf{A}_r$, $\mathbf{B}_r$, $\mathbf{C}_r$ and $\mathbf{D}_r$ are the state space matrices that can be identified following the well-known Perez and Fossen and approach [301, 302]. This method exploits a parametric identification of state space matrices in frequency domain.

5.5. WAVE RES PLATFORM

The Wave RES Platform is a web tool designed to aid research and policy-making in assessing wave resources and identifying optimal locations for the installation of renewable energy conversion devices. This platform offers downloadable datasets and diagrams that are valuable for decision-making and providing an initial estimate of wave resources and potential energy extraction. Users can download datasets for their analyses, while the diagrams provide immediate summaries of key wave information.

The developed tool maps wave energy resources and evaluates potential WECs by utilizing key time series available in online public databases, in particular from ERA5 dataset. The Wave RES Platform supports the energy transition and decarbonization efforts, as exploiting wave energy resources is highly desirable due to its vast global potential, minimal environmental impact, and contribution to a diversified energy mix.

The Wave RES Platform is the first of its kind, designed specifically to facilitate the energy transition. The current open-access version offers functionalities for analyzing wave resources at any point in European seas and evaluating the productivity of default technologies provided within the platform. Future commercial versions will include capabilities to study custom devices, perform techno-economic optimization of WEC arrays over large sea areas, account for maritime space planning constraints, and provide productivity analyzes certified by independent third parties. Additionally, a common market feature will match supply and demand.

The current version of the Wave RES Platform is the result of a successful collaboration between two research groups at the Plotecnico di Torino: the MOREnergy Lab (Marine Offshore Renewable Energy Lab) [303] and the EST (Energy Security Transition) Lab [304]. The web implementation was developed in partnership with GDP Analytics [305].

5.5.1. WAVE RES DATASET

WAVE, BATHYMETRY AND HUMAN ACTIVITIES DATASET

The hourly significant wave height, the energy period and the mean direction have been acquired by the ECMWF portal, from the ERA5 dataset [175], while the bathymetric data are obtained from EMODnet [248]. Additionally, information on various human activities is acquired from EMODnet Human Activities [306]. Specifically, the acquired information includes:

- Environment: Nationally designated areas and Natura 2000 sites [307]

- Military Areas

- Oil and Gas: Active licenses, drilled sites, and offshore installations
- Shipping Density: Vessel density data
- Area Management/Designation: Exclusive Economic Zones (EEZs)
- Ocean Energy Facilities: Project locations and test sites
- Wind Farms
- Major Ports

This comprehensive dataset ensures a thorough analysis of the region's marine environment, aiding in various research and policy-making efforts.

WEC PORTFOLIO

The RES platform includes power matrices for existing technologies that are freely available in the literature. They are Oyster [308], Pelamis [270] and Seawave Slot-Cone Generator [309]. Additionally, the MOREnergy Lab team conducted specific analyzes to provide power matrices for two hypothetical wave energy converters: a point absorber and an oscillating wave energy converter. The point absorber employs constrained optimal control, while the oscillating wave energy converter utilizes reactive control with displacement constraints. The productivity assessment for each marine state is carried out using a stochastic approach for irregular waves.

The devices portfolio represent a broad spectrum of WEC types available internationally. Notably, the Notional Heaving Buoy is an omnidirectional device capable of generating energy from wave motion regardless of the direction of the incoming waves. In contrast, the other devices are direction-sensitive WECs, meaning their efficiency varies with the direction of the wave front.
Another significant difference between the WECs included in the platform is the preferred depth ranges for their installation. The Oscillating Surge Wave Energy Converter and the Onshore Oscillating Water Column are both designed for shallow water areas, typically close to the shore. The other devices, however, are intended for greater depths.

This comprehensive platform provides a valuable resource for evaluating and comparing the productivity of different wave energy converters, taking into account various marine states and device-specific characteristics. By offering power matrices and considering the unique attributes of each WEC type, the RES platform supports informed decision-making in the development and optimization of wave energy projects.

5.5.2. TOOL FEATURES

Policymakers, researchers, planners and investors can leverage the Wave RES platform to evaluate wave characteristics at specific sites, compare wave resources at various locations, and identify optimal areas to develop a detailed analysis. Furthermore, the platform helps in the preliminary selection of the most suitable device technology.

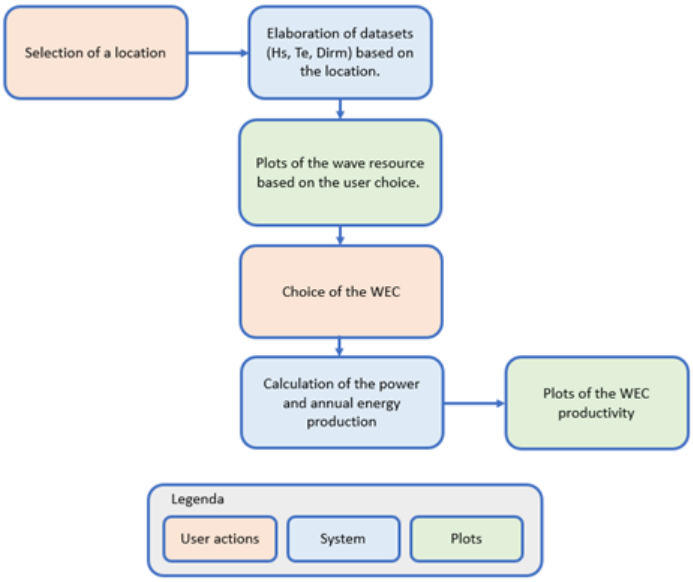

Figure 5.6: Operational diagram for the Wave RES Platform

The Wave RES platform is designed to be versatile and easy to use, effectively supporting user choices. The interactive map, which allows users to visualize marine areas, is characterized by a color scale that provides information on the trend of the depth of the seabed. This feature allows users to select sites based on depth, a critical factor in choosing the appropriate WEC and estimating construction costs. Once a site is selected, users can view representative graphs of wave characteristics and download hourly time series data for each parameter.
For productivity evaluation, users can choose between different WECs, taking into account site or sea area characteristics that optimize WEC performance. This comprehensive approach ensures that the platform supports informed decision-making in the development and implementation of wave energy projects.
The operational diagram is illustrated in Fig. 5.6.

The Wave RES Platform integrates information on waves, bathymetry, and human activities for several regions including the Mediterranean Sea, Black Sea, Sea of Azov, North Atlantic Ocean, Irish Sea, North Sea, Southern Baltic Sea, and Sea of Norway, as illustrated in Fig. 5.7.

The platform allows users to do the following:

1. View support layers for site selection:
    - Bathymetry of marine areas available for analysis
    - Significant average wave height
    - Nationally designated areas

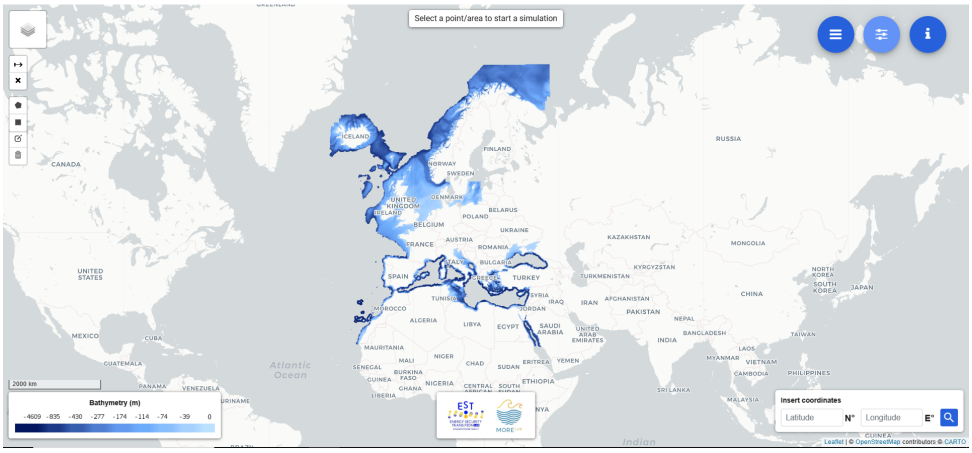

Figure 5.7: Wave RES platform overview [310]

5

- Natura 2000 sites
- Military zones
- Oil and gas facilities, including active licenses, wells and offshore installations
- Shipping density
- Exclusive Economic Zones (EEZs)
- Ocean energy facilities, including project locations and test sites
- Wind farms
- Ports

2. Choose a site of interest and view its seabed depth along with the corresponding latitude and longitude.

3. View wave climate characteristics by obtaining graphical representations of wave climate characteristics at the selected site. Available graphs for synthetic wave parameters and instantaneous average power include:

   - Probability distribution
   - Interannual and intraannual variability
   - Rose diagram of instantaneous average power
   - Scatterplots of wave events
   - Wave energy

   These graphs can be adapted to different time scales such as annual averages, monthly averages, interannual variability and hourly profiles.

4. Carry out the calculation of the productivity of the WECs included in the platform's technological database.

This comprehensive suite of WECs supports detailed site analysis and decision making for wave energy projects, ensuring users have access to actionable data for marine energy infrastructure planning.

5.5.3. WAVE ENERGY RESOURCE

The evaluation of wave energy resources is based on several algorithms that utilize synthetic wave parameters. Each algorithm generates a figure that summarizes the main results. Once the site of interest is selected, the wave resource analysis is conducted using 10 years of wave data.
The graphical interface allows the display of the following graphs:

- **Probability Distribution of Power, Wave Height, and Energy Period:** This graph shows the probability distribution of the selected parameter, highlighting which values occur most frequently and are therefore the most probable.
- **Monthly Variability of Power, Wave Height, and Energy Period:** Users can view the monthly variability of the parameter of interest, including the 5th and 95th percentiles and the average value. The graph also identifies the maximum value for each month.
- **Annual Variability of Power, Wave Height, and Energy Period:** This graph displays the annual variability of the parameter of interest, providing the 5th and 95th percentiles and the average value. It also identifies the maximum value for each year.
- **Monthly Variability of the Wave Energy Resource:** This graph provides information by considering the minimum, average, and maximum values of the wave energy resource for each month over the reference period. The minimum value corresponds to the month with the lowest energy in a given year, the maximum value is calculated similarly, and the average value represents the mean energy for the month across the 10-year analysis period.
- **Annual Variability of the Wave Energy Resource:** This graph allows users to identify the most energetic years and the variability recorded over the 10-year period.
- **Power Rose:** Since some devices are direction-sensitive, the power rose graph shows the direction in which the maximum wave power is concentrated, similar to a wave rose.
- **Occurrence Matrix:** This matrix identifies the most frequent sea states by showing the most common wave height-energy period pairs. It also provides the probability distribution of significant wave height and energy period separately.
- **Power Matrix:** This graph represents the potentially extractable power per meter of wave. It is obtained by multiplying the average power of each marine state by

the occurrence matrix, considering the probability of a specific significant wave height-energy period pair occurring, which determines a certain wave power.

These comprehensive graphical representations help users to thoroughly analyze and understand the wave energy resources at a given site, facilitating informed decision-making for wave energy projects.

5.5.4. WEC'S PRODUCTIVITY

After selecting the site and analyzing the resource, the user can proceed with the productivity estimation analysis. This involves displaying the section for device selection. The portal presents various technologies in a table enriched with helpful information, such as direction sensitivity, the number of parameters describing different possible configurations, minimum and maximum optimal installation depths, as well as descriptions of the devices and relevant literature references.
Once a device is chosen, the user can save the project and view the productivity results through the following graphs:

- **Hourly Variability of Energy Production:** This graph shows the hourly variability of the energy produced by the selected device based on the wave conditions at the identified site.
- **Monthly Variability of Energy Production:** This graph displays the monthly variability of the energy produced by the chosen device, highlighting the minimum, average, and maximum values for each reference month in relation to the wave conditions at the site.
- **Annual Variability of Energy Production:** This graph illustrates the annual variability of the energy produced by the selected device, referencing the wave conditions at the identified site.
- **WEC Power Rose:** The power rose graph indicates the power produced relative to specific wave directions. Depending on the device and its power matrix, there are three cases:
  - *Non-sensitive device:* The device produces energy uniformly regardless of wave direction. The power matrix for such devices does not depend on wave direction and applies to every direction. In the current platform version, only the hypothetical point absorber falls into this category.
  - *Direction-sensitive device with directional efficiency:* The energy conversion efficiency varies with wave direction. A different power matrix is provided for each incidence angle relative to the device's operation direction. The power rose shows power production in all directions, aligning the device with the direction of maximum wave power. In the current platform version, only the hypothetical oscillating wave energy converter fits this category.
  - *Direction-sensitive device without directional efficiency:* The power matrix is provided only for the main operating direction of the device, assuming no

production in other directions. The power rose shows power production only in the direction of maximum wave power. WEC Energy Production: This graph represents the average annual energy produced for each sea state, defined by significant wave height and energy period pairs.

- **WEC Power Device Matrix:** The user can view the device's power matrix for each sea state.

This comprehensive set of tools and visualizations enables users to effectively evaluate the productivity of different wave energy converters based on site-specific wave conditions, facilitating informed decision-making for wave energy projects.

5.6. DICUSSION

THE chapter focuses on the various types of WECs and their main characteristics, providing a comprehensive overview of their classification, evolution, and modeling. The discussion explores how WECs can be classified based on operating principles, wave absorption direction, location, and energy conversion systems. Additionally, it highlights the significant progress made in the field of hydrodynamic modeling, emphasizing the importance of hydrodynamic models, especially those based on flow potential theory, in describing the interaction between waves and the device body.
The chapter also introduces the Wave RES (Resource Evaluation System) platform, designed to support the analysis of wave energy resources and evaluate the productivity of a portfolio of WECs. This platform offers various tools and visualizations that assist users in assessing the energy potential and productivity of different WECs at specific sites. Notably, it helps users evaluate the wave resource and identify the best installation sites for a WEC by providing multiple layers of information on the analyzed sea area. For example, the bathymetric layer allows users to define a site of interest characterized by the depth suitable for the installation of the WEC, while the ship density layer suggests sea areas with lower social and usage conflicts. This unique tool aims to support marine stakeholders in the initial decision-making stages.

5.7. CONCLUSION

THE chapter provided an overview of the various types of WECs, exploring their classification, evolution, and modeling. The discussion highlighted how WECs can be classified based on their operating principles, wave absorption direction, location, and energy conversion systems. A key point of this classification is identifying the sensitivity of WECs to the angle of wave incidence. This not only indicates the category to which a device belongs but also underscores the close correlation between the energy produced and the distribution of wave energy across different directions.

A significant contribution of this chapter is the introduction of the Wave RES (Resource Evaluation System) platform. This platform is designed to support the analysis of wave energy resources and evaluate the productivity of a portfolio of WECs, considering both publicly available power matrix devices and hypothetical devices. By doing so, a profile of WECs has been created, allowing for the calculation of their productiv-

ity at specific sites over time, thus enhancing the planning and implementation of wave energy technologies.

6

PEWEC MODELLING

6.1. INTRODUCTION

THIS thesis aims to evaluate the performance errors of the PeWEC (Pendulum Wave Energy Converter) in relation to the modeling used to describe sea states. Sea waves are frequently characterized by the superposition of wind and wave motion, creating a complex and varied marine environment. Several studies [49, 50] have found that the probability of encountering bimodal spectra in the North Sea varies between 10% and 30%. However, this frequency can be higher depending on specific sea conditions and measurement locations. For example, in the case study of Pantelleria, this probability increases heavily, with an average annual probability of around 93%. The remaining percentage mainly involves waves characterized by three or four simultaneous sea states. In other words, the analysis of the wave resource in Pantelleria reveals that uni-modal sea states are rare. This highlights the complexity and variability of the marine environment in that region, emphasizing the need for performance and design analysis that takes into account the different distribution of energy with respect to the direction of the different wave components. Even in the absence of such superposition, wave energy is not distributed uniformly in a single direction. Instead, around the average direction, there is an energy distribution that can be more or less accentuated, described by the directional spreading parameter. For devices sensitive to the direction of the waves, this distribution of energy leads to a reduction in energy conversion efficiency. Assuming that the average direction of the waves coincides with the operating direction of the device, it is observed that not all wave components impact the device along this direction, thereby influencing the overall efficiency of the system. The PeWEC is particularly sensitive to the direction from which the waves arrive, as its energy conversion relies on the pitching movement induced by the wave impacts on the hull. This sensitivity makes the accurate modeling of wave directionality critical for optimizing performance.
Unfortunately, the extractable wave energy is only a fraction of the wave energy power and depends on the performance of PeWEC. Additionally, both potential wave power and the extractable energy by the device are difficult to evaluate due to the interaction

between wind, sea surface, waves, and devices, which can lead to computational errors. Therefore, accurate sea characterization is critical to reducing uncertainty.

6.2. PEWEC WORKING PRINCILES

THE PeWEC device is a floating wave energy converter that utilizes the rotary motion of a pendulum within its hull [272]. It primarily consists of a floating hull anchored to the seabed through a mooring system and a pendulum connected to the shaft of an electric generator. Crucially, the generator shaft acts as the hinge of the pendulum, and together with the electric generator and all other equipment, is housed within the hull. This design protects the components from the corrosive action of seawater and ensures enhanced durability.
The inception of this project in 2014, funded by the Italian Government through the ENEA-MiSE 2015 Program Agreement, marked a collaborative effort between ENEA (Italian National Agency for new technologies, energy, and sustainable economic development) and the research group at the Polytechnic of Turin [272].

The operational principle of PeWEC relies on the pitch motion induced by wave action. Assuming the hull and pendulum are initially at rest, the arrival of waves prompts the hull to move in surge, heave, and pitch directions. As the hull moves, the integrated pendulum hinge shifts in space, inducing pendulum oscillations. The energy extraction is enabled by the relative rotation of the pendulum with respect to the hull, which drives the shaft of the electric generator. This is accomplished by damping the pendulum's rotations through the electric generator, which is controlled to function as a rotary damper connected to the pendulum [311].

The concept of converting wave energy through the relative rotation of a pendulum was previously explored [312]. Similarly, the SEAREV device, developed by Clément at the LHEEA Laboratory (for the oceanic site of the Isle of Yeu, in France [313, 314], features a sealed floating hull that contains a controlled pendulum to generate electricity. However, a unique aspect of PeWEC lies in its design and optimization specifically for the wave climate of the Mediterranean Sea.
Another distinctive feature of the PeWEC is its capability to extract energy without requiring initial power to start its energy conversion process. This characteristic allows it to be classified as a passive device [315], highlighting its efficiency and sustainability in energy utilization.

6.2.1. PEWEC REFERENCE SYSTEM

Fig. 6.1 provides a simplified two-dimensions representation of the device and the adopted reference system.

- G corresponds to the Center of Gravity (COG) of the system
- A is the position of the hinge of the pendulum
- P describes the center of gravity of the pendulum's mass

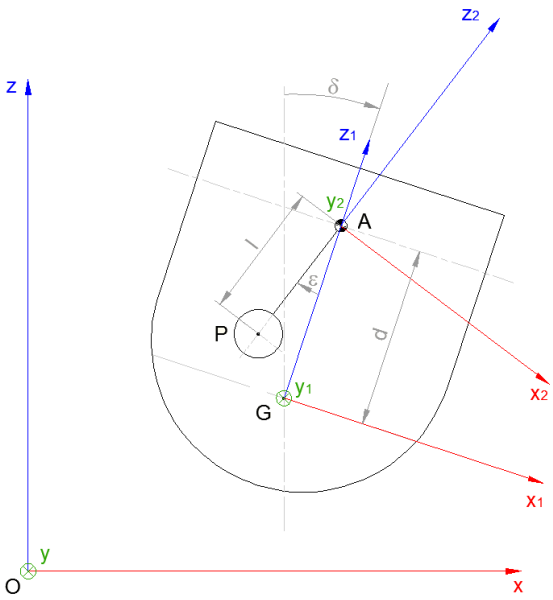

Figure 6.1: The reference frames of PeWEC [311]

- l represents the length of the pendulum
- d is the distance between A and G
- δ is pitch motion around y axis
- ϵ represents the angular coordinate of relative motion between the hull and the inner pendulum
- O-xyz corresponds to the right-handed fixed reference system with origin O
- G-$x_1y_1z_1$ is the right reference system of the device having an origin coinciding with its center of gravity G
- A-$x_2y_2z_2$ represents the right reference system of the mass of the moving pendulum with origin coinciding with its center of rotation A.

Specifically, the x-axis is aligned with the operational orientation of the device. Under these circumstances, the most favorable condition occurs when waves arrive along the x-axis. In this scenario, the positive direction of the x-axis aligns with the wave propagation. The z-axis is defined as vertical, with its positive direction extending from the bottom upwards, while the direction and orientation of the y-axis are defined according to the right-hand rule. The same orientation is assumed for the x_1, y_1, z_1, and x_2, y_2, z_2 axes.

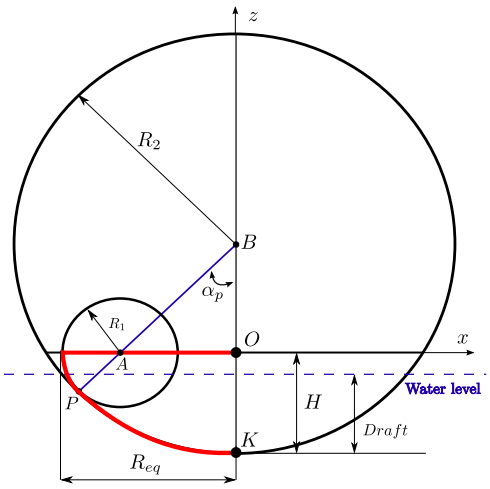

Figure 6.2: PeWEC profile on the x∪z plane [316]

A crucial aspect of PeWEC operation is that the pendulum does not exchange forces along the y-axis. Consequently, only the surge movement (x_1), the heave (z_1), the pitching (δ) of the hull around the y axis are analysed, as well as the relative motion between the hull and the pendulum. (ϵ).
Regarding the possibility of the device to orient itself with respect to the direction of the dominant wave, two cases are brought forward. One concerns the hypothesis that the device is able to orient itself with respect to the direction of the dominant wave. The other analyzes the performance of the device by assuming a fixed orientation, independent of the direction of arrival of the waves. The design of the anchoring system, not discussed in this thesis, can actually allow or prevent rotation. A consequence of the alignment of the device is the possibility of maximizing the power extracted, a particularly significant advantage in sites where the direction of the waves varies throughout the year.

The PeWEC's hull is designed in steel, a standard material in naval carpentry. The walls of the hull can be thought of as thin plates having the profile in the x - y plane given in Fig. 6.2. The profile of the hull is defined using simple parametrized curves. These parameters have undergone a rigorous optimization process. As a result of this optimization, the hull's profile was parametrized using a singular circular arc [317]. The cross-section of the hull, on the other hand, remains constant throughout. Regarding the pendulum, it consists of a cylindrical body with its main axis oriented parallel to the y-axis. The Tab. 6.1 summarizes the main parameters of the PeWEC.

6.3. PEWEC DYNAMIC EQUATION

THE dynamics of the wave-device system depends on several phenomena with the interaction of the waves, the buoyancy, the mooring system and the pendulum. In this

Table 6.1: Floater and pendolum parameters

Parameter	Symbol	Unit	Value
		Floating	
Equivalent radius	R_{eq}	m	7.4
Radius	R_1	m	7.4
Lenght	L	m	14.8
Width	W	m	22.5
Draft	D	m	4.8
Tangency angle	α	deg	90
Mass	m_b	kg	1.12E+06
Pitch moment of inertia	I_{yy}	kg m^2	2.99E+07
		Pendulum	
Mass	m_p	kg	7.17E+04
Lenght	l	m	2.4
Inertia	I_y	kg m^2	5.11E+03
Hinge-hull COG distance	d	m	2.44

study, a linear time domain model is used, which is generally valid within the operating regime of the device [277]. Moreover, the validity of the linearized model was confirmed through an experimental campaign [21], establishing its accuracy and suitability for addressing comprehensive design optimization challenges [283].
However, it is crucial to highlight that this linear assumption is mainly maintained only in the initial stages of device design. As the design progresses to more advanced stages, it becomes critical to account for nonlinear interactions to more accurately predict the device's response to incident waves.

The key premise for linearizing the equations is the assumption that the pitching and swinging motions of the pendulum about their equilibrium position are sufficiently small. Under these idealized conditions, the matrix of the inertial actions of the system (M) and the restoring matrix (K_p) read

$$M_s = \begin{bmatrix} m_p + m_b & 0 & m_p(d-l) & -m_p l \\ 0 & m_p + m_b & 0 & 0 \\ m_p(d-l) & 0 & I_b + I_y + m_p(d-l)^2 & I_y + m_p l^2 - m_p dl \\ -m_p l & 0 & I_y + m_p l^2 - m_p dl & I_y + m_p l^2 \end{bmatrix} \tag{6.1}$$

$$K_p = \begin{bmatrix} 0 & 0 & 0 & 0 \\ 0 & 0 & 0 & 0 \\ 0 & 0 & -m_p g(d-l) & m_p g l \\ 0 & 0 & m_p g l & m_p g l \end{bmatrix} \tag{6.2}$$

$$T_c = c\dot{\epsilon} \tag{6.3}$$

For a stationary floating body, the excitation force can be computed by integrating pressure over its submerged surface. However, for a non-stationary body like a PeWEC, this determination is more complex. Integrating pressure over the submerged hull surface yields a force that encompasses not only the excitation force but also other hydrodynamic forces [318]. The excitation force is determined based on wave elevations and the excitation force coefficient. The procedure to derive these coefficients relies on NEMOH [281], a Boundary Element Method (BEM) code. NEMOH utilizes the device's geometry to create a mesh of the hull and calculates hydrodynamic coefficients such as added mass, radiation damping, and wave excitation force coefficients. Operating in the frequency domain based on linear free surface potential theory, NEMOH assumes conditions of incompressibility, irrotationality, and negligible fluid viscosity, consistent with the assumptions made in this thesis. The time evolution of the wave excitation force is determined by combining the complex wave force coefficients obtained from NEMOH with the amplitudes and phases of the free surface elevation.

6.3.1. WAVE EXCITATION FORCE

This thesis evaluates the performance error of the PeWEC under the assumption of monodirectional wave conditions compared to multidirectional sea states. Although real waves are undeniably directional, monodirectional waves are traditionally modeled and used in literature due to their simplicity. This study quantifies and analyzes the error produced by this overly simplistic representation of sea states.

Initially, the irregular sea conditions are described using both monodirectional and multidirectional spectra. Subsequently, the representation of free surface elevation is detailed, and the numerical model used is introduced. T The device's motions are examined in response to the wave characteristics at Pantelleria Island. The Deterministic Amplitude Scheme (DAS) method is utilized to calculate the components of the directional sea elevation [319].

The free surface elevation can be well approximated by a combination of periodic wave components, each with its own amplitude, phase, angular frequency, and direction[320]. Several methods exist to define the individual wave components, differing primarily in how the spectra are discretized [321]. In this study, the wave spectrum is discretized using the arithmetic progression method for frequencies and the equal energy method for directions. According to this methodology, wave components are characterized by different, equally spaced angular frequencies, and the different directions are defined by considering equal amounts of spectral energy between intervals.

Each frequency is paired with one of the discrete directions, which must be randomly

assigned an equal number of times. To ensure correct energy distribution over different directions, each direction should be repeated equitably. Assuming N_ω as the number of frequency discretizations and N_θ as the number of directional discretizations, each direction is used N_ω / N_θ times. Therefore, the ratio between N_ω and N_θ must be an integer value; in this case, it is taken as 1, with 700 frequencies and 700 directions analyzed. This choice derives from the complex sea states at Pantelleria, characterized by a predominance of bi-modal waves. This ensures that both the frequency and directional spectra are well discretized, providing an accurate determination of wave components.
Figure 6.3 illustrates an example of the discretization of the directional spectrum $D(\omega)$ with respect to the directions ω. In the figure, 31 N_ω discretizations are used, and as observed, $\Delta\omega$ is smaller in the more energetic areas requiring higher resolution.

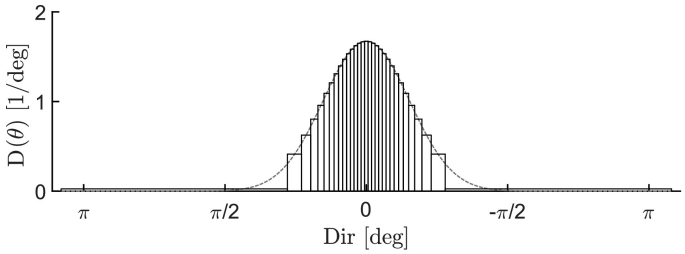

Figure 6.3: Directional distribution discretization using the equal energy method

Finally, the sea surface elevation at a specific point (x, y) and time t is represented as the sum of the N_ω wave components. Using the described method, the summation is performed over frequencies only. Here, A_m denotes the wave component's amplitude, k_m represents the wave number, and x,y,and t indicate the particular location and time. Eq. 6.5 describes the sea surface elevation at a given time t and at a given location (x, y)

$$\eta(x,y,t) = \mathrm{Re}\sum_{m=1}^{N_\omega} a_m\, e^{i[k_m x\cos(\theta_m)+k_m y\sin(\theta_m)-\omega_m t+\varphi_m]} \tag{6.4}$$

where Δ_ω corresponds to the density spectrum frequency resolution.
To statistically represent the interaction between waves and the device, the simulation duration must be adequately long [322]. Alternatively, multiple shorter simulations can be performed, and the final result can be obtained by averaging the outcomes of these different realizations. Based on the results presented in reference to PeWEC in [323], only one realization having T_{sim}=1800 s with a timestep of Δt=0.05 s provide good results.

Considering the complex wave force coefficients along with the amplitudes and phases of a specific free surface elevation, the time history of the irregular wave force acting on the PeWEC has been evaluated.

$$F_{Wi}(t) = \mathrm{Re}\sum_{m=1}^{N_\omega} \left|f_{Wi_m}\right| a_m e^{i[k_m x\cos(\theta_m)+k_m y\sin(\theta_m)-\omega_m t+\varphi_m+\angle f_{Wi_m}]} \tag{6.5}$$

where f_{Wi_j} represents the coefficients of the complex wave force obtained by NEMOH and i is the i^{th} degrees of freedom.

6.3.2. PEWEC RAOS

Response amplitude operators (RAOs) are crucial metrics in the design and analysis of Wave Energy Converters (WECs). Their expression, provided by Eq. 5.43, describes the dynamic response of WECs to incoming waves, offering insights into how the device behaves under various wave conditions. Specifically, RAOs quantify the relationship between the movement of the device and the characteristics of the incoming waves. They depend on the frequency of the incoming waves, which is essential for understanding the WEC's response to different frequency wave spectra, that is, the distribution of wave energy with respect to frequency. Additionally, analyzing the dependence on the wave direction relative to the device's orientation by varying the incidence angle of the incoming waves is fundamental for devices sensitive to wave direction, such as terminators and attenuators.
The RAOs of the device for the degrees of freedom of interest, namely pitch, surge, and heave, are analyzed as a function of frequency and varying the angle of incidence of the forcing relative to the hull. The incidence angle of the forcing varies between 0° and 90°. In particular, due to the symmetry of the device, angles of incidence greater than 90° are equivalent to an angle of incidence of 90° minus the specific angle.

The trend of the different RAOs as a function of the angle of incidence shows that the response of the PeWEC varies significantly with the angle of incidence of the waves. In particular, the RAO for pitch peaks around 1.04 rad/s, similar to the surge RAO, as shown in Fig. 6.4. The RAO for pitch has a very pronounced peak, consistent with the resonant frequency observed in surge. The RAO amplitude in pitch decreases significantly with increasing angle of incidence, indicating that the rotational component is highly sensitive to wave direction. The resonance in both the pitch and surge degrees of freedom at this frequency is due to the excitation of the pendulum's swinging motion by both degrees of freedom.

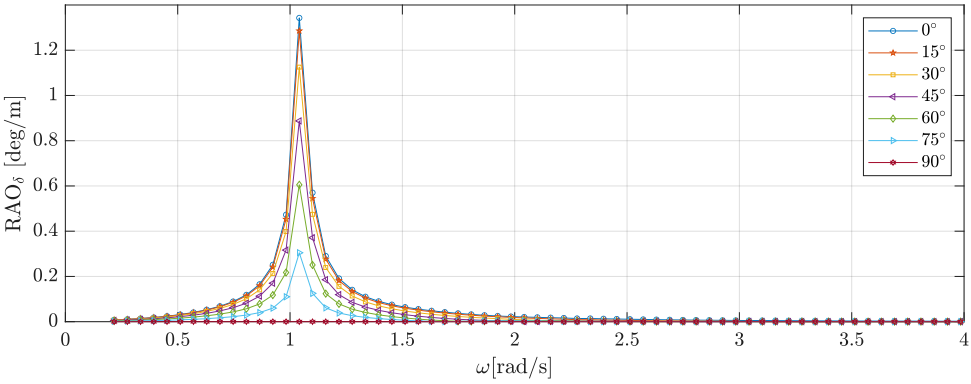

Figure 6.4: RAO$_\delta$ of the pitch angle of the PeWEC

The surge response presents a significant peak around 1.04 rad/s for all incidence angles, indicating a common resonance frequency (Figure 6.5). This peak is critical for optimizing the WEC's energy capture. However, the peak amplitude gradually decreases

with increasing angle of incidence, suggesting that the energy capture efficiency diminishes when the waves do not come directly from the frontal direction (0°), and vanishes at an angle of 90°.

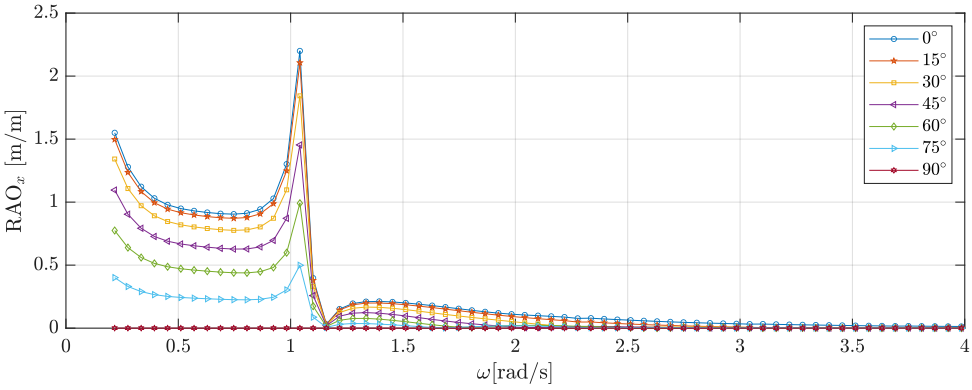

Figure 6.5: RAO$_x$ of the surge of the PeWEC

The RAO for heave, shown in Fig. 6.6, represents the vertical motion of the device. The heave response is also frequency-dependent and varies with the angle of incidence. The graph shows that the heave RAO maintains high values at lower frequencies, gradually decreasing as the frequency increases. This pattern indicates the device's effectiveness in capturing energy from waves of different periods. Similarly, the amplitude of the RAO in heave tends to reduce with increasing angle of incidence, although to a lesser extent than the response in surge and pitch.

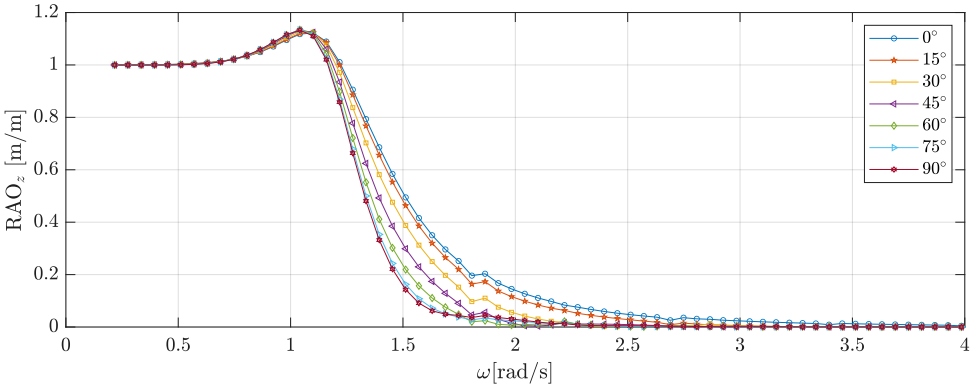

Figure 6.6: RAO$_z$ of the heave of the PeWEC

Overall, the trend of RAOs as a function of angle of incidence indicates that the PeWEC is more efficient at capturing energy when waves come from angles of incidence close to 0°, with efficiency decreasing as the angle of incidence increases.

6.3.3. PEWEC PERFORMANCE

Different wave scenarios are analyzed to evaluate how the PeWEC responds to varying wave incidence angles. Furthermore, the assumptions of monodirectional and multidirectional waves are considered to quantify the error associated with simplified representations of sea conditions.
The analysis is conducted with a significant wave height of 3 m and an energy period of 7 s. The JONSWAP spectrum is used to model the frequency spectrum, while different directional spectra are reconstructed by varying the directional spreading and using the formulation proposed by Mitsuyasu.

Since the JONSWAP spectrum requires significant wave height and peak period, the empirical relationship suggested by the International Towing Tank Conference (ITTC) [324] is applied to calculate the peak period from the energy period.

$$T_p = \frac{Te}{0.8255 + 0.03852\gamma - 0.005537\gamma^2 + 0.0003154\gamma^3} \tag{6.6}$$

with

$$\gamma = \begin{cases} 5 & \text{for} \quad \dfrac{T_p}{\sqrt{H_s}} \leq 3.6 \\ \exp\left(5.75 - 1.15\dfrac{T_p}{\sqrt{H_s}}\right) & \text{for} \quad 3.6 < \dfrac{T_p}{\sqrt{H_s}} < 5 \\ 1 & \text{for} \quad 5 \leq \dfrac{T_p}{\sqrt{H_s}} \end{cases} \tag{6.7}$$

Regarding the directional spreading values, these are chosen to reproduce both wind waves and swell waves. By increasing the directional spreading value, the density spectrum corresponds to swell waves, characterized by a distribution tending towards monodirectionality. Conversely, by reducing directional spreading, the spectrum describes wind waves, which are highly multidirectional. The minimum directional spreading is set at 5°, while the maximum is set at 85°, considering that according to [325], the range for wind waves is around 10°, while for swell waves it is 75°. Intermediate values represent a transition between wind waves and swells.
Fig. 6.7a shows the JONSWAP spectrum based on the established synthetic wave parameters, while Fig. 6.7b compares the different trends of the directional spectrum, highlighting the variation in energy distribution around the average direction. Once the properties of the various density spectra have been defined, the coefficients of the wave components are combined with the coefficients of the excitation forces, and the power of the PeWEC is subsequently determined.

Fig. 6.8 and 6.9 show the PeWEC performance under monodirectional and multidirectional waves, respectively, with respect to different angles of incidence and varying directional spreading.

In Fig. 6.8, it is evident that the PeWEC's performance remains constant across different spreading values under monodirectional wave conditions. This outcome is due to the fact that only the frequency spectrum is used to determine the excitation forces and calculate the power extracted from the PeWEC. The power output is highest when the

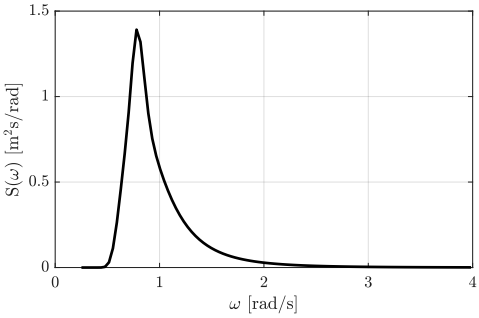

(a) Power computed from 2D wind wave and swell spectra compared with power computed from 1D wind wave and swell spectra

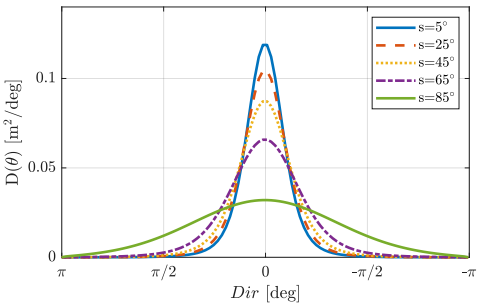

(b) Power computed from 2D wind wave and swell spectra compared with power computed from 2D wind wave and swell spectra obtained from 1D spectra

Figure 6.7: Comparison of the scatter plot of power obtained from wind wave and swell spectra with and without using linear calibration

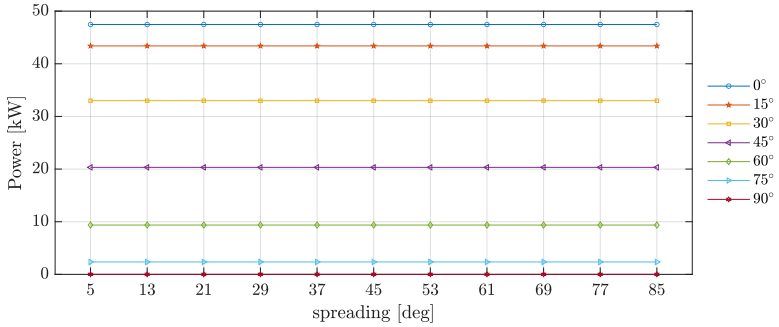

Figure 6.8: PeWEC performance under monodirectional waves with respect to different angles of incidence of the waves with respect to the orientation of the device

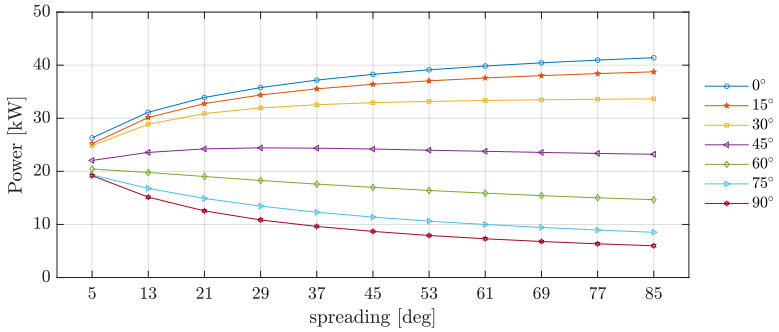

Figure 6.9: PeWEC performance under multidirectional waves with respect to different angles of incidence of the waves with respect to the orientation of the device

waves come from an incidence angle of 0°, and it gradually decreases as the angle of incidence increases. Notably, the power output at 90° is zero. This trend indicates that the

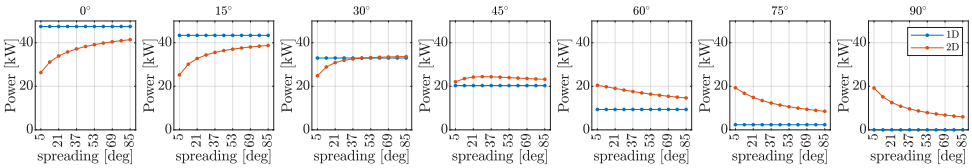

Figure 6.10: PeWEC performance comparison under monodirectional and multidirectional waves with respect to different angles of incidence of the waves with respect to the orientation of the device

device is most efficient when waves approach directly from the front and least efficient when waves come from the side. This result aligns with predictions and provides a clear overview of the reduction in performance as a function of the angle of attack.
In contrast, Fig. 6.9 illustrates the PeWEC's performance under multidirectional wave conditions. Here, the power output shows a different pattern. As the directional spreading increases, the power output also increases for all angles of incidence. This result is due to the fact that, as the directional spreading value increases, the directional spectrum tends to become increasingly narrower. The power output is highest at an incidence angle of 0° and decreases progressively with larger angles, similar to the monodirectional case. However, the multidirectional scenario demonstrates a more pronounced increase in power output with small spreading values, suggesting that the device can capture more energy from waves coming from the same directions. Overall, these results highlight the influence of wave directionality and spreading on the PeWEC's performance. The device performs best with waves approaching directly from the front (0°) and under conditions with smaller directional spreading, which allows it to capture more wave energy. Conversely, the performance diminishes with increasing angles of incidence and higher spreading values.

A comparison between monodirectional and multidirectional cases is conducted to quantify the error induced by assuming waves are monodirectional. Figure 6.10 illustrates the PeWEC performance under monodirectional (1D) and multidirectional (2D) waves, considering different angles of wave incidence relative to the device orientation and varying the directional spreading value.

For an incidence angle of 0°, the power output is highest for both 1D and 2D analyses. However, the power output for 2D waves is generally lower than for 1D waves, suggesting that while the PeWEC performs efficiently with direct wave approach (0°), it captures slightly less energy when wave directionality is considered in the multidirectional analysis.
At an incidence angle of 15°, a similar pattern is observed. The 1D analysis shows a constant power output across all spreading values, while the 2D analysis shows an increasing power output as the spreading value increases. Despite the increase, the 2D power output remains lower than the 1D output, highlighting the impact of directional spreading on energy capture efficiency.
As the incidence angle increases to 30°, 45°, 60°, 75°, and 90°, the differences between 1D and 2D analyses become more pronounced and follow a different trend. At 30° and for directional spreading above 53°, the power of the PeWEC in the 2D spectrum exceeds

that of the 1D spectrum. This result is due to the assumption that energy dispersion in different directions reduces the angle of incidence for some wave components, increasing the excitation force components and moving more effectively on the device.
With an incidence angle of 45°, the power delivered in the 2D analysis shows a slightly accentuated parabolic trend as the directional spreading varies, higher than that in the 1D output. This highlights the impact of directional diffusion on energy capture, as PeWEC is most efficient in multidirectional waves with a peak wave incidence angle of 45°.
For incidence angles of 60° and 75°, the power output in the 1D analysis decreases further while the power output based on the 2D analysis remains gradually higher.
Finally, at a 90° incidence angle, the 1D output power is zero, indicating that no energy is captured from waves coming directly from the side. Conversely, the 2D output power shows a significant decrease as directional spreading increases, with wave components increasingly tending to align in the same direction. For low directional spreading values, the energy distribution across directions is more pronounced, directing a greater number of wave components with a lower angle of incidence.

These results highlight the importance of considering directional spreading to use the directional frequency spectrum effectively and evaluate the impact of energy distribution across different directions.

6.4. DICUSSION

THE chapter focuses on the modeling of the Pendulum Wave Energy Converter (PeWEC), a device specifically developed for the conversion of Mediterranean wave energy. It provides a detailed description of the PeWEC's operating principles, highlighting how its unique design exploits wave-induced pendulum motion to generate power. This innovative approach allows the PeWEC to efficiently absorb wave energy while keeping all mechanical components safely enclosed within the hull.
A crucial aspect of the chapter is the investigation of various scenarios to evaluate the performance of the PeWEC under different wave conditions. The analysis includes both monodirectional and multidirectional assumptions, considering various angles of wave incidence. This section underscores the importance of accounting for multidirectional sea conditions in the design of wave energy converters (WECs). The discussion reveals that monodirectional modeling can yield significantly different results compared to those obtained under multidirectional assumptions, emphasizing the need for comprehensive modeling to ensure accurate performance predictions.

6.5. CONCLUSION

THE chapter analyzes the RAOs of the PeWEC under different wave angles of incidence, which is critical for understanding how the PeWEC responds to incoming wave frequencies and directions. This study examines the RAOs by simulating various wave conditions and observing the resulting response of the PeWEC. The analysis focuses on the three primary degrees of freedom—surge, heave, and pitch—highlighting how each mode of motion is influenced by wave interactions. The results emphasize the importance of accurately modeling these responses to predict the PeWEC's behavior in

real sea conditions and under different wave directions.
Additionally, the performance evaluation of the PeWEC under different wave conditions is conducted. This evaluation involves simulating the PeWEC under both monodirectional and multidirectional waves. The results demonstrate the device's energy absorption efficiency and highlight the differences in performance when considering multidirectional sea states. This section underscores the critical nature of multidirectional modeling, showing that neglecting wave directionality can lead to inaccurate performance predictions. In particular, it can be observed that as the angle of incidence of the wave on the hull increases, the performance of the PeWEC, as determined by monodirectional analysis, decreases rapidly. Conversely, the analysis based on multidirectional waves suggests a less abrupt decline in performance. This result not only highlights the inaccuracies induced by monodirectional analysis but also demonstrates the advantages of using a multidirectional approach when the wave incidence angle relative to the orientation of the PeWEC is not zero. The distribution of wave energy across different directions ensures that some wave components effectively hit the device, thereby enhancing its performance.

IV

NUMERICAL CASE STUDY: PEWEC PERFORMANCE IN PANTELLERIA

7

INTRODUCTION

7.1. INTRODUCTION

VARIOUS analyses are conducted to understand the response of the PeWEC device under different wave conditions and various methodologies used for wave modeling. A common hypothesis across all analyses is that the orientation of the PeWEC varies in accordance with the peak direction of the waves. Specifically, it is assumed that the PeWEC is always oriented parallel to the peak direction of the waves impacting the hull. This property can be achieved through the appropriate design of the hull and mooring line [326].

In general, the response of the PeWEC is evaluated using both monodirectional and multidirectional spectra in order to identify the error induced by the 1D assumption under different conditions. Moreover, some analyzes are based on synthetic parameters, from which the spectrum is reconstructed. In particular, the JONSWAP [126] spectrum is used for the reconstruction of the frequency spectrum, while the directional spectrum is reconstructed using the formulation proposed by Mitsuyasu [60]. Other analyzes are based on the spectrum directly provided by the SWAN model. The main difference between these two cases is inherent in the intrinsic assumption of uni-modal and multi-modal sea states. In particular, the reconstruction of the spectrum from the synthetic parameters induces an assumption of uni-modal wave conditions while the use of the spectrum directly provided by SWAN allows to investigate the PeWEC response even when different sea states are coexisting.

7.2. PEWEC PERFORMANCE INVESTIGATIONS

VARIOUS studies are carried out to highlight the complexity of WEC performance assessments and to undermine some techniques commonly used but characterized by intrinsic assumptions errors. First, the comparison of the PeWEC performance on the sole basis of the data sources used for modeling is carried out. This study aims to

highlight how the use of different datasets can lead to incorrect performance estimates. In particular, the identification of an accurate dataset is fundamental to understand the response of the device and estimate its efficiency.
Among the different studies, one of them is focused on the error induced by the discretization of the syntetic parameters, in order to reproduce the techinique based on the power matrix, which is commonly employed to assess the energy conversion capability of a device based on the scatter of occurrences at a given study site [327, 328, 329, 330, 331]. Three different discretization triplets are used to discretize the significant wave height (H_s), the energy period (T_e), and the directional spreading (s) to understand the impact of bin resolution on the accuracy of the results. This approach helps to determine how varying bin resolution affect the precision and reliability of the performance metrics for the PeWEC device. In particular, the analysis reveals that the size of the chosen bins significantly impacts the accuracy and reliability of the device's performance.
Subsequently, the accuracy of the monodirectional versus multidirectional analysis is evaluated. This investigation utilizes the frequency and frequency-direction spectra obtained from the SWAN model to evaluate the performance error induced by the monodirectional assumption. In particular, a linear correlation between the results resulting from the monodirectional and multidirectional assumptions is identified and simple linear regression is applied to calibrate the data obtained from the 1D assumption and augment the fitting with that obtained from the 2D assumption.
Furthermore, the performance of the PeWEC is analyzed in response to spectra provided by SWAN and frequency and frequency-directional spectra reconstructed based on synthetic parameters obtained by SWAN. This analysis aims to investigate the error induced by spectrum reconstruction based on simplifications of the spectral shape and the assumption of uni-modal waves. The research finds that despite assuming unimodality in a highly multimodal site, estimation errors remain negligible when a multidirectional analysis is carried out.
Finally, an analysis of the energy production potential of the PeWEC is conducted over a ten-year period from 2013 to 2022. This includes a seasonal and inter-annual analysis to identify seasonal trends and annual variability, providing a comprehensive understanding of the PeWEC's performance and its potential impact on energy generation in Pantelleria.

7.2.1. ASSESSING PEWEC PERFORMANCE ESTIMATION ERRORS BASED ON WAVE DATA SOURCES

The design and performance evaluation of WECs is carried out on the basis of the waves characteristics that occur in the sea site of interest. In particular, in the early stages simplifications on WEC models and wave modeling are frequent. These simplifications concern the linearization of the WEC dynamic model and the use of syntetic parameters obtained by coarse spatial resolution wave datasets. Regarding WEC modeling, in the initial phase, different device designs are investigated in order to identify the best performing one. The linearity assumption therefore finds space as it reduces computation times and allows obtaining the first performance estimates [332, 333, 334, 335, 336]. At the same time, the wave data used for evaluate the WECs performance are frequently

numerical data modeled with low spatial resolution [337, 338, 339, 340] with reduced accuracy compared to in-situ instruments and local numerical models data. The use of such wave numerical data derives from the limited availability of in-situ data, both from a temporal and spatial point of view. Furthermore, the implementation of local numerical downscaling models is time consuming and the process is not scalable. In particular, models like SWAN must be calibrated ad hoc in order to identify the best set-up with respect to the location of interest [341, 342, 343].
In this context, the influence of the wave data source on the calculation of WEC performance is investigated to provide a comprehensive overview of the advantages and limitations of different data sources.

WAVE DATA SOURCES FOR PeWEC PERFORMANCE ESTIMATION

The site of interest is Pantelleria, and the device analyzed is PeWEC. Synthetic parameters provided by in-situ instruments are employed to reconstruct time series of frequency spectra and frequency-directional spectra to determine PeWEC's excitation forces. This involves both monodirectional analyses, using the frequency spectrum, and multidirectional analyses, using the frequency-directional spectrum. Similarly, data from the calibrated and validated SWAN model, as well as those provided by ERA5, are utilized, considering the same temporal coverage of the in-situ dataset. The JONSWAP spectrum [126] is employed for reconstructing the frequency spectrum, while the directional spectrum is derived using the formulation proposed by Mitsuyasu [60]. Moreover, this study assumes the PeWEC aligned with the peak direction of incoming waves. In fact, the PeWEC is sensitive to the direction of wave arrival, and the assumption of alignment with the wave front is based on the goal of capturing the maximum possible energy from the waves.
The time windows during which the analysis is conducted are shown in Tab. 7.1, corresponding to the instruments data record and described in Section 4.2.1. It should be emphasized that only the instrumental measurements validated by the quality control process are used in this study. Consequently, only the time instances of these validated measurements are stored and used to identify the wave power from the numerical databases corresponding to the same time instances.

Table 7.1: Time windows coverage for the different instruments installed in Pantelleria

Dataset	Time coverage
Nortek AWAC-AST 600 KHz	26 September 2015 - 4 December 2015
Nortek AWAC-AST 600 KHz	18 July 2019 - 16 September 2019
Datawell Waverider DWR-G buoy	3 September - 2021 28 February 2022
Datawell Waverider DWR-G buoy	1 June 2022 - 1 September 2022

Synthetic parameters derived from in-situ measurements offer a direct representation of local wave conditions. Meanwhile, the SWAN model and ERA5 data provide

broader, model-based perspectives that are calibrated and validated against real-world observations. The primary difference between these two models lies in the spatial resolution of the data. The SWAN model uses an unstructured grid with a minimum spatial resolution of 100 meters near the coast, gradually increasing up to 10 kilometers offshore. This approach reduces computation times compared to a dense structured grid while maintaining high accuracy near the coast. Conversely, ERA5 data have a spatial resolution of 0.5°x0.5° (approximately 50 km x 50km) and do not analyze coastal dynamics in detail, representing wave conditions over a broad sea area. In particular, the comparison is based on SWAN numerical data, referencing the centroid of the triangular cell closest to the instrument installation site (36°49'23"N, 11°55'13"E), with this centroid located at coordinates 36°49'30"N, 11°55'19"E. On the other hand, ERA5 data are provided on a regular grid, with the cell centroid from which the data are extracted positioned at coordinates 37°00'00"N, 12°00'00"E.
The advantage of using ERA5 data compared to in-situ and SWAN data lies in cost-effectiveness, ease, and speed of access. Installing in-situ instruments and implementing the SWAN model are time-consuming and expensive processes. Furthermore, the SWAN model requires in-situ data for calibration and validation, as these data represent the benchmark for estimating the accuracy of all other data sources.

PeWEC PERFORMANCE RESULTS BASED ON DIFFERENT WAVE DATA SOURCES

Fig. 7.1 shows an extract of the time series of the PeWEC power in the monodirectional (1D) and multidirectional (2D) case obtained on the basis of in-situ data and on the basis of SWAN data (Fig. 7.1a) and ERA5 (Fig. 7.1b) respectively.

The temporal resolution of the power time series is hourly. As can be observed, in-situ data exhibit greater variability on a small time scale. These comparisons highlight the influence of different data sources on estimating PeWEC performance. The in-situ data serve as a benchmark for accuracy, demonstrating that the SWAN model, particularly in its 2D analysis, provides a closer approximation to real-world conditions. In contrast, ERA5 data, while useful for broader and more cost-effective evaluations, show more significant deviations, especially in the 1D analysis. This suggests that for precise performance estimation, detailed local measurements and multidirectional analyses are crucial.

To evaluate the fit of the modeled data with the in situ data, scatterplots are used. In particular, the comparison is carried out by evaluating the dispersion of the point cloud in reference to the bisector.

The first set of figures (Fig. 7.2) compares the power obtained by forcing the PeWEC based on in situ data and data provided by SWAN. As observed, around the bisector there is a dispersion which is reduced going from the monodirectional case (1D) to the multidirectional case (2D). This result suggests that increasing the level of detail in the analysis, in particular considering the directional distribution of energy, the correlation between the powers estimated using SWAN data and in-situ data improves.

The second set of figures (Fig. 7.3) shows the correlation between the powers obtained from the in situ data and those obtained by forcing the device using the ERA5 data. In this case there is an overestimation of the power values for the lower ranges and

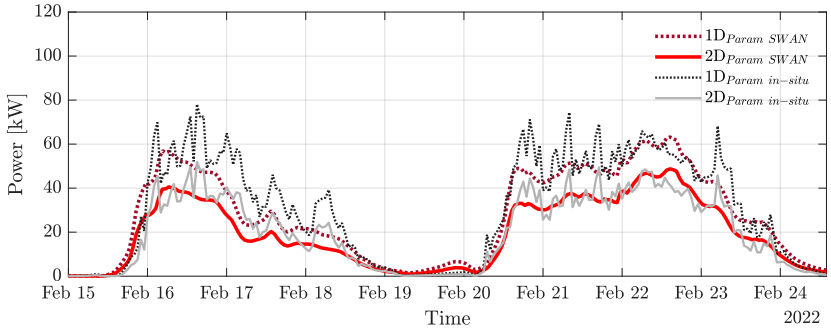

(a) Comparison of the time series of the powers obtained by forcing the PeWEC on the basis of synthetic parameters provided by the in-situ instruments and SWAN numerical model

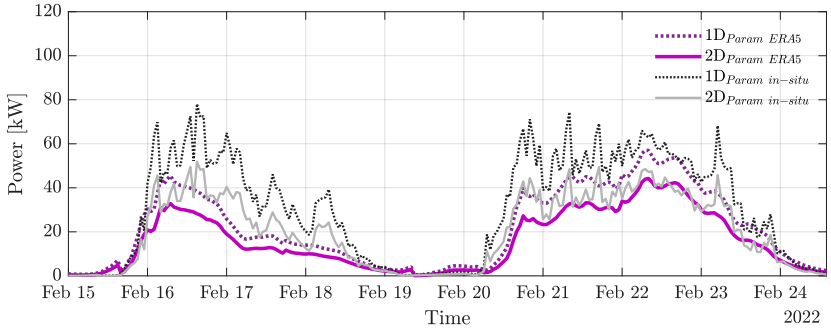

(b) Comparison of the time series of the powers obtained by forcing the PeWEC on the basis of synthetic parameters provided by the in-situ instruments and EAR5 numerical model

7

Figure 7.1: Comparison of the time series of the powers obtained by forcing the PeWEC on the basis of syntetic provided by ERA5 and syntetic parameters provided by the in-situ instruments

an underestimation for the higher ones. Specifically, in both the 1D and 2D cases, the point cloud is positioned above the bisector when focusing on powers calculated using in situ data below 20 kW. For higher power values, however, the point cloud tends to distribute below the bisector, highlighting an average underestimation of power based on ERA5 data.

Tab. 7.2 presents a detailed comparison of PeWEC performance metrics using different data sources. The Root Mean Square Error ($RMSE$) is lower for the SWAN model compared to ERA5 in both 1D and 2D analyses, indicating that the SWAN data offers a closer match to the in-situ data. The $BIAS$ is also lower (closer to zero) for the SWAN model, suggesting smaller systematic error than ERA5. The Correlation Coefficient (CC) is higher for the SWAN model in both cases, demonstrating a better linear relationship with the in-situ data. The dispersion index (S) is lower for the SWAN model, indicating a better overall fit to the in-situ data.

Regarding annual energy conversion and the standard deviation of the power (Tab. 7.3), annual energy conversion is highest for in-situ data, followed by the SWAN model

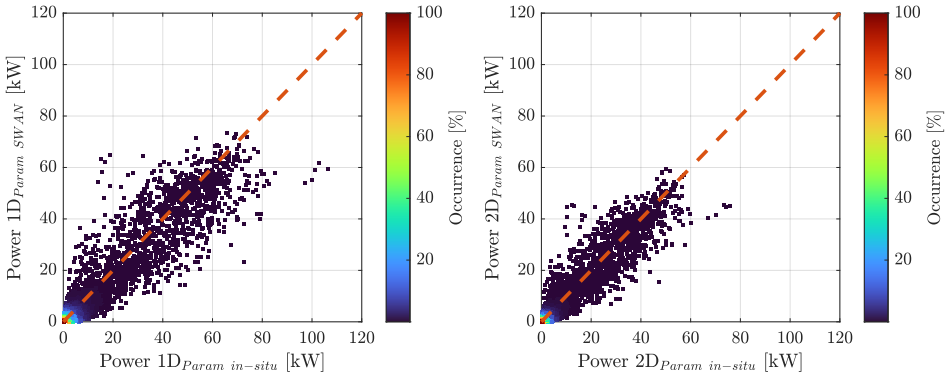

(a) Scatter of the power computed with monodirectional assumption and using in-situ and SWAN wave data

(b) Scatter of the power computed with multidirectional assumption and using in-situ and SWAN wave data

Figure 7.2: Comparison of the scatter plot of power obtained from different wave data souces in 1D and 2D analysis

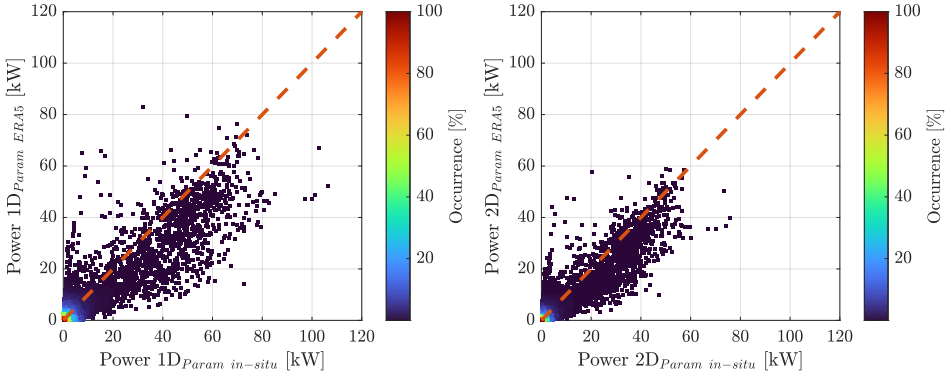

(a) Scatter of the power computed with monodirectional assumption and using in-situ and ERA wave data

(b) Scatter of the power computed with multidirectional assumption and using in-situ and ERA wave data

Figure 7.3: Comparison of the scatter plot of power obtained from different wave data souces in 1D and 2D analysis

and lowest for ERA5 in both 1D and 2D analyses. This confirms that ERA5 data tends to underestimate the energy potential compared to in-situ measurements. The standard deviation of power follows a similar trend, being highest for in-situ data and lowest for ERA5. This indicates that ERA5 data can smooth out some of the variability present in real measurements. In particular, the results show that in the monodirectional case, the underestimation of the energy produced by the PeWEC based on SWAN data, in regard to the in-situ data, is 9.1%, which increases to 17.4% when using ERA5 data. Conversely, the underestimation is reduced when moving to multidirectional analysis. Specifically, the energy produced by the PeWEC calculated using SWAN data underestimates that calculated with in-situ data by 6.3%, while the underestimation is 12.9% when using ERA5

Table 7.2: Performance indicators for PeWEC power production using using different wave data sources for monodirectional (1D) and multidirectional (2D) analyses

Dataset	*RMSE* **[kW]**	*BIAS* **[kW]**	*CC*	*S*
$1D_{Param\ in-situ}$-$1D_{Param\ SWAN}$	5.411	-0.826	0.946	1.091
$1D_{Param\ in-situ}$-$1D_{Param\ ERA5}$	7.456	-1.581	0.907	1.278
$2D_{Param\ in-situ}$-$2D_{Param\ SWAN}$	3.533	-0.390	0.952	1.044
$2D_{Param\ in-situ}$-$2D_{Param\ ERA5}$	4.762	-0.799	0.918	1.202

data.
When comparing the error induced by the monodirectional analysis to the multidirectional one, a similar overestimation is observed across different datasets. Specifically, this overestimation is 31.9% for the in-situ observations, 29.8% for the SWAN data, and 28.1% for the ERA5 data. In conclusion, it appears that, on average, in Pantelleria, there is an overestimation of energy of around 30% if the monodirectional assumption is made. This result stems from the distribution of energy across different directions.

Table 7.3: Annual PeWEC energy conversion and standard deviation of the power using different wave data sources for monodirectional (1D) and multidirectional (2D) analyses

Dataset	E **[kWh]**	σ_{Power} **[kW]**
$1D_{Param\ in-situ}$	72.72	16.428
$1D_{Param\ SWAN}$	66.07	15.102
$1D_{Param\ ERA5}$	60.06	12.631
$2D_{Param\ in-situ}$	49.52	11.532
$2D_{Param\ SWAN}$	46.38	11.110
$2D_{Param\ ERA5}$	43.14	9.471

PEWEC PERFORMANCE RESULTS DISCUSSION BASED ON DIFFERENT WAVE DATA SOURCES

Identifying the appropriate wave dataset to characterize the site of interest is crucial for conducting an accurate wave resource estimate.
Databases such as INSITU_GLO_WAV_DISCRETE_MY_013_045 [147] and the National Data Buoy Center [150] provide valuable resources for finding free in situ measurements near the area of interest. These datasets offer time series of wave measurements time-series validated through quality control processes. However, the global distribution of such instruments is uneven, with regions like South America, Africa, and Australia being poorly covered. The scarcity of in-situ measurements and their limited temporal coverage necessitate the search for alternatives.

Marine stakeholders and WEC developers sometimes install in situ instruments directly at the site of interest. However, this approach faces bureaucratic challenges, high costs, and extended timescales, making it particularly difficult. As a result, alternatives such as global or local numerical models become essential.
From the analysis conducted, it is evident that the SWAN model, especially in its 2D analysis, provides a more accurate approximation to in-situ data than ERA5, both in terms of error metrics and energy estimation. While ERA5 data are useful for broader, cost-effective evaluations, they exhibit more significant deviations and lower variability, making them less accurate for detailed estimates of PeWEC performance. This underscores the importance of using high-resolution, locally calibrated models like SWAN for precise energy predictions in wave energy applications.

7.2.2. ASSESSING PEWEC PERFORMANCE ESTIMATION ERRORS BASED ON DISCRETIZED SYNTETIC PARAMETERS

THE evaluation of the error induced by the use of the power matrix and the scatter of occurrences for determining the energy conversion of the PeWEC, with reference to the sea states occurred in Pantelleria in 2022, is investigated. This common methodology involves determining the device's power matrix relative to different pairs of values of H_s and T_e. By multiplying this matrix by another matrix with the same bin resolution, which describes the average annual occurrence of the $H_s - T_e$ pairs, one can determine the energy produced for each pair. This approach is commonly used to estimate a device's capacity to extract energy at a specific site [327, 328, 329, 330, 331].

In this section, the errors resulting from this methodology are investigated by using three different bin resolutions for the $H_s - T_e$ value pairs in the monodirectional analysis, and three different resolution triplets for $H_s - T_e - s$ in the multidirectional analysis. It should be noted that common practice usually employs only the $H_s - T_e$ pairs, and the analysis is typically based on the assumption of monodirectional waves. In this case, the standard methodology is enhanced by incorporating the s parameter. Through directional spreading, we can account for the dispersion of energy around the average wave direction, providing a more accurate representation of the wave energy spectrum.
In detail, the methodology followed is based on the identification of three different discretization scenarios of the synthetic parameters. Once the resolution of the different bins is defined, both the frequency spectrum and the frequency-directional spectrum are reconstructed for each sea state, approximating the values of the synthetic parameters obtained from the SWAN model with respect to the closest value of the discretized parameters. For the reconstruction of the frequency spectrum the JONSWAN [126] spectrum is used, while for the directional spectrum the formulation proposed by Mitsuyasu [60] is used.

PEWEC PERFORMANCE RESULTS BASED ON DISCRETIZED SYNTETIC PARAMETERS

The Fig. 7.4 present an extract of the hourly time series of the PeWEC power calculated using different discretizations compared with the power time series based on synthetic parameters directly provided by SWAN. The comparison of the spectra obtained by the syntetic parameters computed via SWAN with the spectra reconstructed using the discretized synthetic parameters, both in the monodirectional (1D) and multidirectional (2D) cases, is provided. These synthetic parameters are also obtained from the SWAN model and subsequently discretized based on the chosen bin cell. The resolutions of the synthetic parameters vary between the three analysis, offering a comparison of the performance of PeWEC under different discretization conditions.

In the Fig. 7.4a, the power converted by PeWEC is calculated using a synthetic parameters resolutions of $\Delta H_s = 0.25m$ $\Delta T_e = 0.5s$ and $\Delta s = 2.5°$. The red lines represent the reference data, with the dotted line indicating the monodirectional spectrum and the solid line the multidirectional spectrum. The green lines show the results obtained using the discretized synthetic parameters, respectively in the monodirectional (dashed line) and multidirectional (solid line) cases. It is observed that the power calculated with discretized synthetic parameters follows the reference lines quite closely, indicating a good match with the original SWAN data. However, there are some discrepancies, especially in power peaks, suggesting that the chosen resolution may not be sufficient to capture all variations.
The Fig. 7.4b uses a coarser resolution of the synthetic parameters: $\Delta H_s = 0.5m$ $\Delta T_e = 1s$ and $\Delta s = 5°$. Here too, the red lines represent reference power data and the green lines the results obtained with the discretization of the synthetic parameters. We note that the correspondence between the synthetic and reference data is slightly less precise than in Fig. 7.4a, with larger discrepancies in the power peaks. This indicates that coarser resolution may lead to a decrease in the accuracy of power estimates.
In the Fig. 7.4c, the resolution of the synthetic parameters is further decreased to $\Delta H_s = 1m$ $\Delta T_e = 2s$ and $\Delta s = 10°$. The discrepancies between the red and green lines are even more noticeable, especially during periods of high power. This suggests that too low resolution of synthetic parameters is unable to adequately capture wave variability and complexity, leading to less accurate power estimates.
Overall, the graphs highlight the importance of using adequate resolution of synthetic parameters to obtain accurate estimates of power produced by PeWEC. Multi-directional (2D) analysis tends to provide more precise results than mono-directional (1D) analysis, as it is better able to capture the complexity of sea waves. These results suggest that greater attention to the choice of parameter resolution is crucial for improving WEC energy conversion predictions.

For a more detailed comparison of the different cases, the scatterplot is used. This graph shows a comparison of the PeWEC powers obtained by forcing the device with the spectra obtained by the syntetic parameters directly provided by SWAN and with those reconstructed using discretized synthetic parameters, both in the monodirectional (1D) and multidirectional (2D) cases. The different resolutions of the synthetic parameters used in the graphs allow analyzing and comparing the performance of the PeWEC under

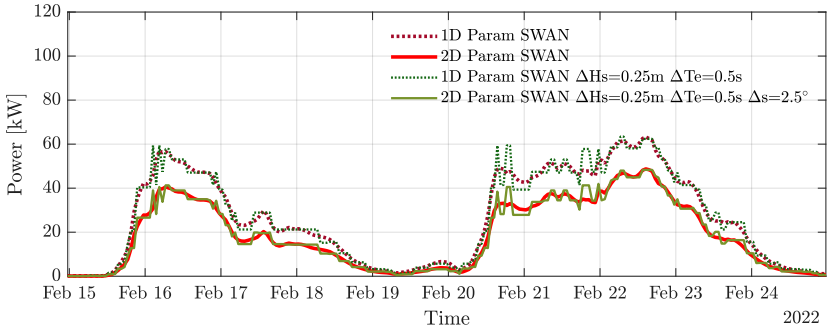

(a) Comparison of the time series of the powers obtained by forcing the PeWEC on the basis of spectra computed by synthetic parameters provided by SWAN and spectra reconstructed using discretized synthetic parameters provided by SWAN, using $\Delta H_s = 0.25m$ $\Delta T_e = 0.5s$ and $\Delta s = 2.5°$ as bin resolution

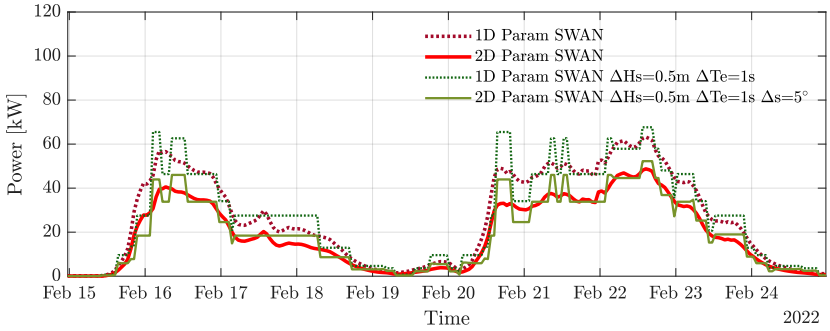

(b) Comparison of the time series of the powers obtained by forcing the PeWEC on the basis of spectra computed by synthetic parameters provided by SWAN and spectra reconstructed using discretized synthetic parameters provided by SWAN, using $\Delta H_s = 0.5m$ $\Delta T_e = 1s$ and $\Delta s = 5°$ as bin resolution

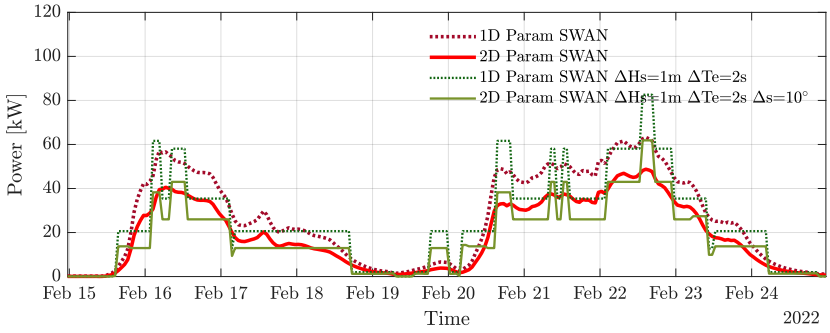

(c) Comparison of the time series of the powers obtained by forcing the PeWEC on the basis of spectra computed by synthetic parameters provided by SWAN and spectra reconstructed using discretized synthetic parameters provided by SWAN, using $\Delta H_s = 1m$ $\Delta T_e = 2s$ and $\Delta s = 10°$ as bin resolution

Figure 7.4: Extract of the hourly time series of the power extracted from PeWEC as a function of the discretization of the synthetic parameters provided by SWAN, both in the monodirectional (1D) and multidirectional (2D) case

various discretization conditions, providing a more complete view of the accuracy and variability of the power estimates as a function of the different methodologies adopted. In Fig. 7.5a, the power produced by PeWEC is calculated using a synthetic parameter resolution of $\Delta H_s = 0.25m$ and $\Delta T_e = 0.5s$. Most of the points align well with the dashed diagonal line, which represents a perfect match between the powers calculated with the discretized synthetic parameters and the reference ones. However, some discrepancies are present, especially in the higher power values, suggesting that this resolution may not fully capture all variations in the sea states. In Fig. 7.5b, the PeWEC power is calculated using a similar resolution but in the context of a multidirectional analysis, with the addition of the parameter s with resolution $\Delta s = 2.5°$. Here too, most points follow the diagonal line, indicating a good match, but discrepancies in the highest power values persist.

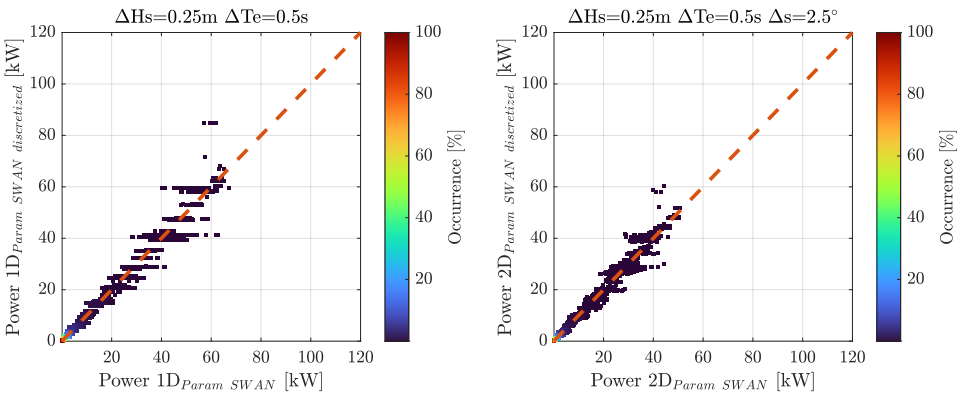

(a) Comparison of the powers obtained by forcing the PeWEC on the basis of 1D spectra obtained by original synthetic parameters provided by SWAN and 1D spectra reconstructed using discretized synthetic parameters provided by SWAN, using $\Delta H_s = 0.25m$ and $\Delta T_e = 0.5s$ as bin resolution

(b) Comparison of the powers obtained by forcing the PeWEC on the basis of 2D spectra obtained by original synthetic parameters provided by SWAN and 2D spectra reconstructed using discretized synthetic parameters provided by SWAN, using $\Delta H_s = 0.25m$ $\Delta T_e = 0.5s$ and $\Delta s = 2.5°$ as bin resolution

Figure 7.5: Comparison of the scatter plot of power obtained from wind wave and swell spectra with and without using linear calibration for different cases

Fig. 7.6a shows the results obtained with a resolution of the synthetic parameters of $\Delta H_s = 0.5m$ and $\Delta T_e = 1s$. in a monodirectional context. The dots show greater scatter around the diagonal line compared to previous plots, indicating that coarser resolution leads to a decrease in the accuracy of power estimates. Fig.7.6b uses the same parameter resolution as the 7.6a graph but in a multidirectional context, with the addition of the s parameter with $\Delta s = 5°$. Although there is a slight reduction in discrepancies compared to Fig. 7.6a, the scatter of points still suggests that this resolution is not optimal for accurately capturing wave variability.

Finally, Fig. 7.7a and 7.7b use an even coarser resolution of $\Delta H_s = 1m$ and $\Delta T_e = 2s$, respectively in monodirectional analysis, and multidirectional, with the parameter s discretized according to the bin $\Delta s = 10°$. These plots show the greater dispersion of the points around the diagonal line, highlighting how too low a resolution is unable to adequately capture the complexity of the waves, leading to less accurate power estimates.

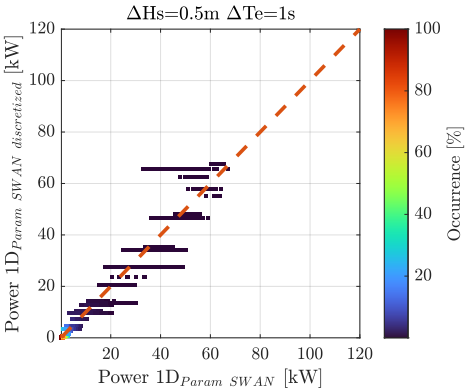

(a) Comparison of the powers obtained by forcing the PeWEC on the basis of 1D spectra obtained by original synthetic parameters provided by SWAN and 1D spectra reconstructed using discretized synthetic parameters provided by SWAN, using $\Delta H_s = 0.5m$ and $\Delta T_e = 1s$ as bin resolution

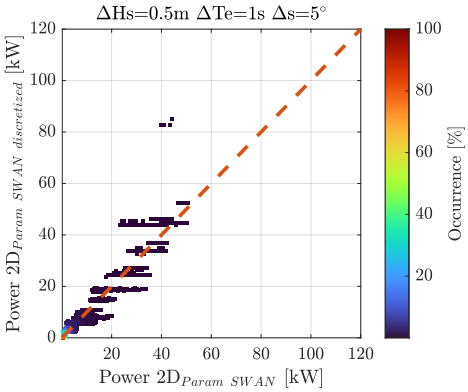

(b) Comparison of the powers obtained by forcing the PeWEC on the basis of 2D spectra obtained by original synthetic parameters provided by SWAN and 2D spectra reconstructed using discretized synthetic parameters provided by SWAN,using $\Delta H_s = 0.5m$ $\Delta T_e = 1s$ and $\Delta s = 5°$ as bin resolution

Figure 7.6: Comparison of the scatter plot of power obtained from the original synthetic parameters provided by SWAN and using discretized synthetic parameters provided by SWAN

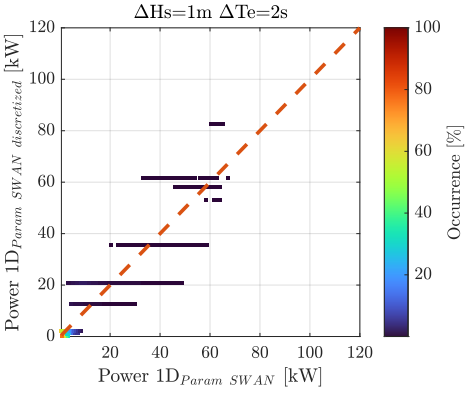

(a) Comparison of the powers obtained by forcing the PeWEC on the basis of 1D spectra obtained by original synthetic parameters provided by SWAN and 1D spectra reconstructed using discretized synthetic parameters provided by SWAN, using $\Delta H_s = 1m$ and $\Delta T_e = 2s$ as bin resolution

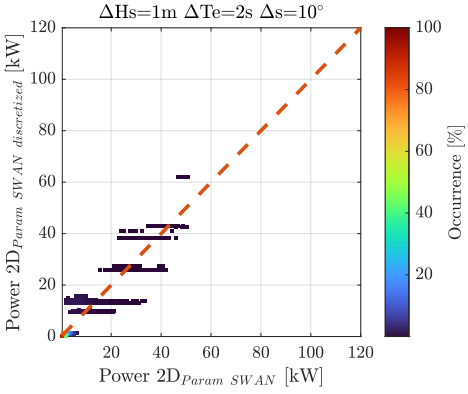

(b) Comparison of the powers obtained by forcing the PeWEC on the basis of 2D spectra obtained by original synthetic parameters provided by SWAN and 2D spectra reconstructed using discretized synthetic parameters provided by SWAN, using $\Delta H_s = 1m$ $\Delta T_e = 2s$ and $\Delta s = 10°$ as bin resolution

Figure 7.7: Comparison of the scatter plot of power obtained from the original synthetic parameters provided by SWAN and using discretized synthetic parameters provided by SWAN

Overall, these plots highlight the importance of using adequate resolution of synthetic parameters to obtain accurate estimates of power extracted from WEC. Multidirectional analysis tends to provide more precise results than monodirectional analysis, as it better captures the complexity of sea waves.

Tab. 7.4 provides a comparison of the performance indicator based on the power generated by PeWEC and using different resolutions of the synthetic parameters for monodi-

rectional (1D) and multidirectional (2D) analyses.

Table 7.4: Performance indicators for PeWEC power production using the original synthetic parameters provided by SWAN and using discretized synthetic parameters provided by SWAN, for unidirectional (1D) and multidirectional (2D) analyses

Dataset	*RMSE* **[kW]**	*BIAS* **[kW]**	*CC*	*S*
$1D_{Param}$-$1D_{Param\ \Delta H_s=0.25m\ \Delta T_e=0.5s}$	1.883	0.013	0.990	0.991
$1D_{Param}$-$1D_{Param\ \Delta H_s=0.5m\ \Delta T_e=1s}$	3.924	-0.031	0.959	0.964
$1D_{Param}$-$1D_{Param\ \Delta H_s=1m\ \Delta T_e=2s}$	5.747	0.562	0.911	0.952
$2D_{Param}$-$2D_{Param\ \Delta H_s=0.25m\ \Delta T_e=0.5s\ \Delta s=2.5°}$	1.245	0.006	0.991	0.993
$2D_{Param}$-$2D_{Param\ \Delta H_s=0.5m\ \Delta T_e=1s\ \Delta s=5°}$	2.591	-0.016	0.965	0.966
$2D_{Param}$-$2D_{Param\ \Delta H_s=1m\ \Delta T_e=2s\ \Delta s=10°}$	3.856	0.326	0.918	0.978

Regarding the monodirectional (1D) analysis, the configuration with $\Delta H_s = 0.25m$ and $\Delta T_e = 0.5s$ shows an $RMSE$ of 1.883 kW and a $BIAS$ of 0.013 kW, with a correlation coefficient (CC) of 99.0% and a scatter index (S) of 0.991. These values indicate a good correspondence between the data obtained from the reconstruction of the spectrum from discretized synthetic parameters and the reference ones, with a low error and a high correlation. However, by increasing the resolution to $\Delta H_s = 0.5m$ and $\Delta T_e = 1s$, the $RMSE$ increases to 3.924 kW and the $BIAS$ moves to -0.031 kW, while the CC decreases to 95.9% and the scatter index becomes 0.964. This indicates a decrease in the accuracy of power estimates with increasing parameter resolution. The configuration with $\Delta H_s = 1m$ and $\Delta T_e = 2s$ shows a further deterioration in performance, with a $RMSE$ of 5.747 kW, a $BIAS$ of 0.562 kW, a CC of 91.1% and a scatter index of 0.952, highlighting how too low a resolution reduces the accuracy of the results.

For multidirectional (2D) analysis, the configuration with $\Delta H_s = 0.25m$, $\Delta T_e = 0.5s$ and $\Delta s = 2.5°$ presents much better values, with a $RMSE$ of 1.245 kW, a $BIAS$ of 0.006 kW, a CC of 99.1% and a scatter index of 0.993. These results suggest that adding the directional dispersion parameter improves the accuracy of the estimates. The configuration with $\Delta H_s = 0.5m$, $\Delta T_e = 1s$ and $\Delta s = 5°$ shows an $RMSE$ of 2.591 kW, a $BIAS$ of -0.016 kW, a CC of 96.5% and a scatter index of 0.966, indicating a slight degradation in performance compared to the finer resolution configuration. Finally, the configuration with $\Delta H_s = 1m$, $\Delta T_e = 2s$ and $\Delta s = 10°$ shows a $RMSE$ of 3.856 kW, a $BIAS$ of 0.326 kW, a CC of 91.8 % and a scatter index of 0.978, confirming that too low a resolution of the synthetic parameters not completely capture the complexity of the waves.

In general, the results show that the $RMSE$ increases with the bin size, while the CC and S decrease. Regarding the $BIAS$, there is no clear trend, as the rounding of the synthetic parameter values to a higher or lower value is unpredictable and depends on the specific data distribution. This variability in rounding making it difficult to establish a definitive pattern.

The Tab. 7.5 provides a comparison of the total energy produced (E) in the year 2022 and the standard deviation of the power (σ_{power}) also based on the hourly historical series of the power in the year 2022, in reference to the different case studies.

Table 7.5: Annual PeWEC energy conversion and standard deviation of the power using the original synthetic parameters provided by SWAN and using discretized synthetic parameters provided by SWAN, for monodirectional (1D) and multidirectional (2D) analyses

Dataset	E **[kWh]**	σ_{Power} **[kW]**
$1D_{Param}$	59.54	13.207
$1D_{Param\ \Delta H_s=0.25m\ \Delta T_e=0.5s}$	59.64	13.353
$1D_{Param\ \Delta H_s=0.5m\ \Delta T_e=1s}$	59.29	13.870
$1D_{Param\ \Delta H_s=1m\ \Delta T_e=2s}$	64.06	13.772
$2D_{Param}$	40.79	9.462
$2D_{Param\ \Delta H_s=0.25m\ \Delta T_e=0.5s\ \Delta s=2.5°}$	40.84	9.546
$2D_{Param\ \Delta H_s=0.5m\ \Delta T_e=1s\ \Delta s=5°}$	40.66	9.897
$2D_{Param\ \Delta H_s=1m\ \Delta T_e=2s\ \Delta s=10°}$	43.41	9.561

For both monodirectional and multidirectional analyses, the results indicate that there is no universally applicable trend based on bin size, regardless of whether it is more whether it is finer or larger. Specifically, it is not possible to identify a constant trend of underestimation or overestimation of the power and, consequently, of the energy produced by the devices. This result is directly related to the rounding effects on the synthetic parameters as described above. Rounding can lead to unpredictable variations in results, preventing the creation of a clear pattern.

However, if we analyze the absolute error between the energy obtained using the synthetic parameters provided directly by SWAN to reconstruct the spectra and those obtained with discretized synthetic parameters, some conclusions can be drawn. In the monodirectional case, the absolute error is 0.16% for the dataset with the densest discretization, 0.42% for the medium discretization, and 7.59% for the sparsest discretization. For the multidirectional case, the absolute error is 0.12% for the densest discretization, 0.32% for the average one, and 6.42% for the sparsest discretization.

Comparing the energy obtained from the monodirectional analysis using a discretization of $\Delta H_s = 1m$ and $\Delta T_e = 2s$ with the energy obtained from the multidirectional analysis based on the synthetic parameters provided directly from SWAN, a significant error of 57.1% occurs. This substantial discrepancy underlines the importance of considering the directional distribution of energy and highlights the impact of discretization choices on the accuracy of the energy estimate for the PeWEC. As expected, the multidirectional methodology tends to provide lower estimates of converted energy, since not all wave components hit the device hull perpendicularly.

Furthermore, with coarser resolutions of the synthetic parameters, the energy estimation error and power standard deviation increase significantly, confirming that higher

resolution is necessary to adequately capture the complexity of sea waves.

PeWEC PERFORMANCE RESULTS DISCUSSION BASED ON DISCRETIZED SYNTETIC PARAMETERS

The use of power matrix, based on significant wave height (H_s) and energy period (T_e), is the simplest methodology for calculating the total energy extractable from waves using a WEC. This matrix is pre-processed independently of the time series of sea states. Once the H_s-T_e pairs are defined, the power calculation is carried out, and the matrix is built based on the H_s and T_e bins. By multiplying the power matrix with the scatter of occurrences for the site of interest, the total energy produced is directly determined without generating a time series of the power extracted from the WEC.
This methodology is straightforward and offers significant computational benefits. Additionally, the power matrix can be determined even without specific wave information from a site, allowing for the evaluation of the best site for WEC installation by multiplying the power matrix by the scatters of occurrences at different locations. However, the assumption of monodirectionality, combined with a coarse choice of matrix bins, can lead to high absolute errors. Specifically, for PeWEC at the locality of Pantelleria per the 2022 year, this error exceeds 50%.
The results indicate that the main source of error is the assumption of monodirectionality. When comparing spectra reconstructed using the original synthetic parameters provided by SWAN under monodirectional and multidirectional assumptions, there is an overestimation of 31.5% for the year 2022. Using bins of $\Delta H_s = 0.25m$ and $\Delta T_e = 0.5s$ in the monodirectional assumption and $\Delta H_s = 0.25m$ $\Delta T_e = 0.5s$ and $\Delta s = 2.5°$ in the multidirectional case, the overestimation remains 31.5%. For intermediate discretization, the overestimation is 31.2%, reaching 32.2% for bins with lower resolution. These results suggest that regardless of bin resolution, the overestimation error is approximately 30% for this specific case.
To mitigate this error, it is recommended to use a three-dimensional scatter that also accounts for the directional distribution of energy through the s parameter. This approach eliminates the error associated with the assumption of monodirectionality, leaving bin choice as the primary error factor. It is advised to set the bins accurately, avoiding site-specific configurations. Identifying the resolution of the cells based on specific sea site conditions may be optimal for the studied case, but applying this method to another site could lead to excessive approximations. The analysis shows that there is no linear trend in overestimation or underestimation of energy as a function of bin resolution, due to the unpredictable and uncontrollable allocation of synthetic parameters within specific cells.
In conclusion, these comparisons highlight the trade-offs between computational simplicity and the precision of energy conversion estimates. The analysis underscores the potential improvements that can be made to the standard methodology by incorporating the s parameter. This additional parameter allows for the consideration of the directional spreading of wave energy, which is often overlooked in traditional monodirectional analyses.

7.2.3. ASSESSING THE PEWEC PERFORMANCE CORRELATION BASED ON 1D AND 2D ASSUMPTION

As previously described, monodirectional analysis is commonly employed to determine the power extracted from WECs based on the sea states at a specific site. This common methodology typically involves using the significant wave height and the energy period to reconstruct the frequency spectrum and calculate the excitation forces acting on the device, and finally deduce the power extracted by the device. The analysis conducted in this study aims to explore the correlation between the results obtained from monodirectional analysis and those from multidirectional analysis. Moreover, in these analysis the PeWEC is assumed to always be aligned with the peak direction of the spectra.
The study aims to investigate whether there is a correlation between the power results obtained from the monodirectional assumption and those derived from multidirectional analysis. This analysis is important because standard practice often involves identifying the power extractable from WECs based on their interaction with frequency wave spectra. The objective is to develop an innovative methodology that accurately and simply determines the power extractable from WECs, thereby avoiding the need for comprehensive studies on multidirectional interactions. Instead, the focus is on identifying the correlation between monodirectional and multidirectional analyses.
Such a comparison is crucial for understanding the accuracy and reliability of power predictions made using different analytical methods. By doing so, the study aims to optimize the performance and implementation of WECs in various marine environments. This approach could significantly streamline the process of evaluating WEC performance, making it more efficient and less resource-intensive while maintaining accuracy.
By evaluating the correlation between monodirectional and multidirectional power estimations, the study seeks to provide a practical and effective tool for marine energy stakeholders. This tool would allow for the rapid assessment of potential WEC sites and configurations without the need for detailed directional analysis, thus facilitating better decision-making and faster deployment of wave energy technologies.
The wave dataset used is from the SWAN model for the year 2022. In this case, the spectrum directly provided by SWAN is utilized to calculate the excitation forces. The directional frequency spectrum is directly obtained from the model output, while the frequency spectrum is determined by integrating the 2D spectrum over all directions.

PEWEC PERFORMANCE CORRELATION RESULTS BASED ON 1D AND 2D ASSUMPTION

A correlation emerges from the comparison of the results between 1D analysis and 2D analysis (Fig. 7.8). In particular, despite a deviations from the bisector of the scatter plot, which represents perfect correlation between the data, the clouds of points follow a smooth trend, indicating a significant linear correlation.

The simple linear regression [344] is uned in this analysis and is one of several Bias Correction Techniques that can be used to adjust raw data values to better approximate the statistical properties to more reliable reference data [345]. These techniques are purely statistical tools and are widely used in climate and meteorological studies [346,

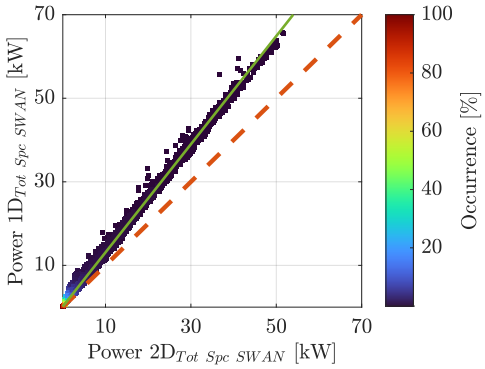

Figure 7.8: Scatter of the power computed from 1D and 2D assumptions

347]. Notably, the application of these techniques does not necessitate a fundamental understanding of the underlying physical processes or data assimilation methods [348], making them versatile for a variety of variables. However, the accuracy and reliability of the calibrated dataset are highly dependent on the quality of the reference dataset, which is considered the ground truth.

This technique consists in fitting a simple linear regression model to the data. In this process the power are calculated using both the 1D assumption (monodirectional analysis) and the 2D assumption (multidirectional analysis) for the dataset, that is split in a calibration and a validation dataset. Specifically, the first 10 days of each month of 2022 are extracted and used to create the calibration dataset, while the remaining days of the year are used as validation one. The 1D power values of the calibrated dataset serve as the independent variable (X), while the 2D power values of the calibration dataset serve as the dependent variable (Y). In this scenario, the regression model can be expressed as

$$Y_{calib} = a + bX_{calib} \tag{7.1}$$

where the regression coefficients a and b are the intercept and the slope pf the straight line, respectively. These coefficients are calculated using the least squares method [349], which minimizes the sum of the squared differences between the dependent and independent variable.

$$b = \frac{COV(X_{calib}, Y_{calib})}{VAR(X_{calib})} \tag{7.2}$$

$$a = Y_{calib} - bX_{calib} \tag{7.3}$$

Once the regression coefficients a and b are determined, the regression equation can be used to adjust the 1D power values, resulting in bias-corrected power values:

$$Y_{valid_{linearcalib.}} = a + bX_{valid} \tag{7.4}$$

This method directly applies linear regression to model the relationship between the 1D and 2D power values, providing a straightforward approach to linear correction. By adjusting the 1D power values of the validation dataset using the regression model, the

accuracy of the power estimates is enhanced.

The Fig. 7.9 provides an extract of the time series of the power obtained by PeWEC with respect to the 1D and 2D assumption. As can be seen, the power obtained from the 2D spectra is lower than that based on the frequency spectrum, following however the same trend.

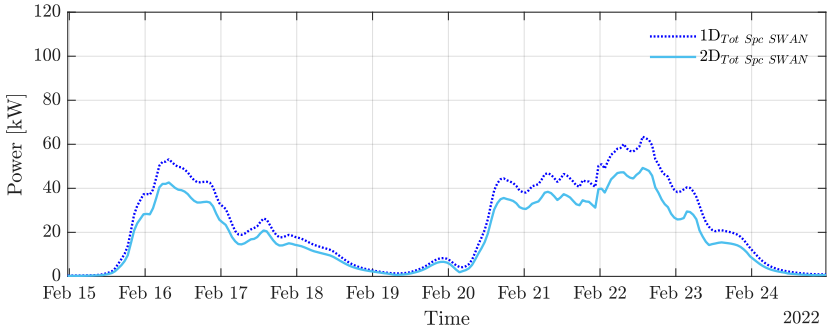

Figure 7.9: Extract of the hourly time series of the power extracted from PeWEC as a function of the monodirectional (1D) and multidirectional (2D) analysis

Based on the evident linear correlation between the 1D and 2D hypotheses (emerged from Fig. 7.8), a calibration dataset and a validation dataset is identified, and the coefficients for the linear calibration are determined based on the calibration dataset and the effectiveness evaluated on the validation dataset.
Figure 7.10a shows the comparison between the power obtained from the monodirectional and multidirectional assumption with reference to the calibration dataset, where the dashed red line represents the bisector and the solid green line represents the linear regression line of the data points. The scatter plot shows a linear trend, suggesting that the power calculated from the 1D and 2D spectra follows a consistent relationship, which can be described by linear regression.
Figure 7.10b corresponds to the calibration dataset after applying linear calibration using the equation derived from linear regression. This figure shows that the calibrated data points align more closely with the bisector, highlighting the effectiveness of linear calibration in improving the correlation between 1D and 2D assumptions.
In the validation dataset (Fig. 7.10c and 7.10d), the performance of the linear calibration is further evaluated. The scatter plots reveal that the linear calibration derived from the calibration dataset successfully maintains a strong linear relationship between the 1D and 2D analysis throughout the entire year. The dashed red line still represents the bisector, and the alignment of the data points along this line after calibration indicates that the simple linear regression effectively reduces the discrepancies observed in the raw data.

Overall, the analysis confirms that linear calibration significantly improves the correlation between 1D and 2D hypotheses, leading to more accurate predictions of PeWEC output power. The use of performance indicators is carried out in order to quantify the improvement obtained from linear calibration. Tab. 7.6 presents a comparison of the

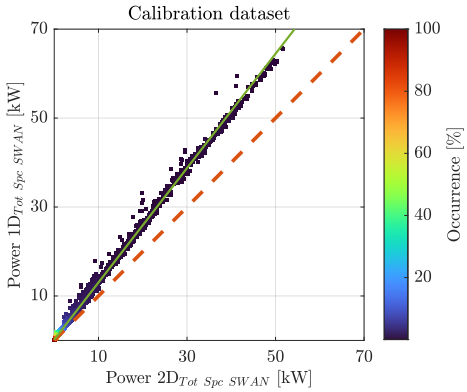

(a) Scatter of the power computed from 2D analysis with power computed from 1D analysis, for the calibration dataset

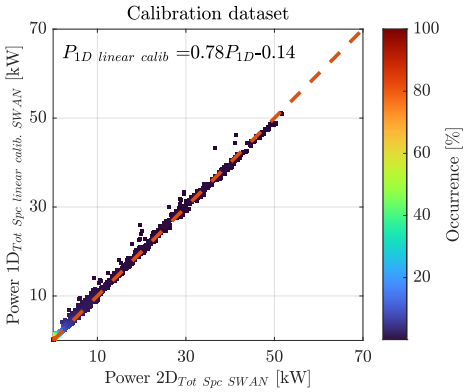

(b) Scatter of the power computed from 2D analysis with power computed from 1D analysis linear calibrated, for the calibration dataset

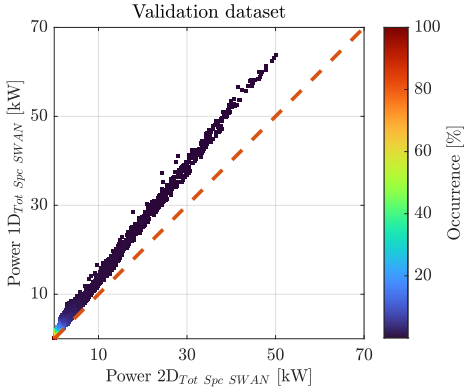

(c) Scatter of the power computed from 2D analysis with power computed from 1D analysis, for the validation dataset

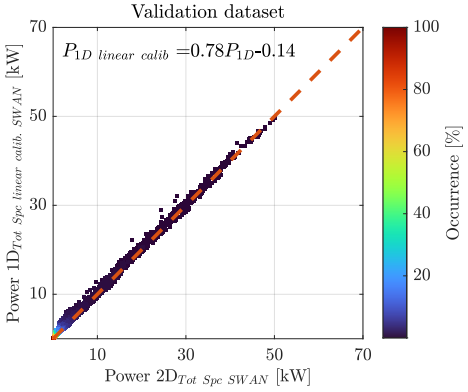

(d) Scatter of the power computed from 2D analysis with power computed from 1D analysis linear calibrated, for the validation dataset

Figure 7.10: Comparison of the scatter plot of power obtained from 1D and 2D spectra with and without using linear calibration

performance indicators based on the calibration and validation datasets described previously. These performance indicators are calculated both before and after applying linear calibration.

In the calibration dataset, the Root Mean Square Error ($RMSE$) without calibration is 3.886 kW, while after applying linear calibration, the $RMSE$ drops to 0.534 kW. This represents a significant reduction in error, demonstrating the effectiveness of linear calibration. The $BIAS$ goes from 2.152 kW to a value close to zero (1E-15 kW), indicating that the calibration almost completely eliminates any systematic error. The correlation coefficient (CC) remains very high (99.8%) in both cases, showing a strong linear correlation between 1D and 2D data. The scatter index (S) improves from 0.774 to 1.00, suggesting that the linear calibration brings the data almost perfectly in line with the bisector.
In the validation dataset, the $RMSE$ drops from 2.947 kW to 0.468 kW after linear cali-

Table 7.6: Performance indicators for PeWEC power production using SWAN spectra in monodirectional (1D) and multidirectional (2D) analyses based on calibration and validation datasets

Dataset	$RMSE$ [kW]	$BIAS$ [kW]	CC	S
Calibration				
$2D_{Tot\ Spc}$-$1D_{Tot\ Spc}$	3.886	2.152	0.998	0.774
$2D_{Tot\ Spc}$-$1D_{Tot\ Spc\ linear\ calib.}$	0.534	1E-15	0.998	1.00
Validation				
$2D_{Tot\ Spc}$-$1D_{Tot\ Spc}$	2.947	1.493	0.998	0.764
$2D_{Tot\ Spc}$-$1D_{Tot\ Spc\ linear\ calib.}$	0.468	0.028	0.998	0.990

bration, confirming that the calibration remains effective even on data not used for the initial calibration. The $BIAS$ is reduced from 1.493 kW to 0.028 kW, almost completely eliminating the systematic error. Again, the CC remains constant at 99.8%, indicating a strong linear correlation between the data. The S improves from 0.764 to 0.990, demonstrating that linear calibration significantly improves the match between 1D and 2D data.

The Tab. 7.7 shows a comparison of the total energy produced (E) and standard deviation of the power (σ_{Power}) for the calibration and validation datasets. Three different analysis methods are considered: using 2D spectra, using 1D spectra, and applying a linear calibration on the 1D results.

Table 7.7: Comparison of PeWEC yearly energy production and standard deviation of the power using SWAN spectra with 1D assumption, 2D assumption, and linearly calibrated 1D assumption for calibration and validation datasets

Dataset	E [kWh]	σ_{Power} [kW]
Calibration		
$2D_{Tot\ Spc}$	18.18	11.184
$1D_{Tot\ Spc}$	23.86	14.363
$1D_{Tot\ Spc\ linear\ calib.}$	18.18	11.171
Validation		
$2D_{Tot\ Spc}$	24.64	8.286
$1D_{Tot\ Spc}$	32.91	10.773
$1D_{Tot\ Spc\ linear\ calib.}$	24.79	8.379

In the calibration dataset, the total energy produced using 2D spectra is 18.18 kWh with a power standard deviation of 11.184 kW. When using 1D spectra, the total energy produced increases to 23.86 kWh, but the standard deviation of power also increases to 14,363 kW, indicating greater variability in power production. After applying linear cali-

bration, the total energy produced returns to 18.18 kWh, with a power standard deviation of 11.171 kW, very similar to the values obtained with the 2D spectra. This suggests that linear calibration is effective in correcting discrepancies between power estimates based on 1D and 2D assumptions.
In the validation dataset, the total energy produced using 2D spectra is 24.64 kWh with a power standard deviation of 8.286 kW. Using 1D spectra, the total energy produced increases to 32.91 kWh, while the standard deviation of the power increases to 10.773 kW. After applying linear calibration, the total energy produced is reduced to 24.79 kWh, with a power standard deviation of 8.379 kW. This demonstrates that linear calibration manages to reduce the differences between the results obtained with the 1D spectra and those obtained with the 2D spectra, improving the accuracy of the power estimates.
It should be emphasized that the differences between the energy obtained from the calibration dataset and the validation dataset are due to the fact that, in the first case, the energy corresponds to the total energy produced during the first 10 days of each month in 2022. In contrast, the energy obtained from the validation dataset refers to the remaining days of the year. Consequently, the annual energy production is derived from the sum of the energy obtained from both the calibration and validation datasets.

PeWEC performance correlation results discussion based on 1D and 2D assumption

The use of simple linear regression to estimate wave power based on 1D analyses, aligned with the results of 2D analyses, demonstrates its validity for multimodal sea states, such as those occurring in Pantelleria in 2022. This finding represents a significant advance in the field of renewable energy derived from sea waves. The commonly used technique assumes unidirectionality, which, as indicated by the results, leads to an overestimation of performance.
The advantages of simple linear regression include increased accuracy, simplicity, and practical application. The linear regression model corrects biases in the 1D power estimates, aligning them more closely with the more accurate 2D power values. Linear regression is easy to implement and computationally efficient, making it accessible for various applications. This method is especially useful when 2D data is more accurate but also more computationally demanding to obtain.
Greater precision in power estimates not only improves the reliability of energy forecasts but also contributes to more efficient and optimal planning of the installation and operation of wave energy conversion devices. Consequently, this approach can promote the wider adoption of marine renewable energy technologies, significantly contributing to sustainability and carbon emission reduction goals.

7.2.4. Assessing the PeWEC performance error based on multipeak and monopeak spectra

A detailed analysis of sea states is critically important when designing a WEC and testing its performance. As highlighted in previous analyses, the inclusion of directionality plays a key role in accurately identifying the excitation forces that impact the device. However, in earlier analyses, synthetic parameters representing the entire spectrum are

used to construct the frequency and frequency-directional spectra. This methodology finds full theoretical support when the analyzed sea state is uni-modal. To evaluate the error induced by this assumption, the power extracted by PeWEC under different wave analysis techniques is examined. Specifically, the device performances obtained from spectra reconstructed using synthetic parameters from the SWAN model are compared with those obtained by calculating the excitation forces based on 1D and 2D spectra directly provided by SWAN. In particular, the 1D spectrum provided directly by SWAN should be understood as the integral of the frequency-directional spectrum supplied by the model. This analysis evaluates the error caused by assumptions of uni-modal versus multi-modal sea states.
The analyses conducted on the Pantelleria wave resource (Section 4.3.1) reveal the persistence of bi-modal sea states, that occur more than 90% of the time. The remaining waves are primarily characterized by the coexistence of three or four different sea states. However, 75% of the total annual wave energy is attributed to wind waves and the remaining percentage is attributed to swell. This characterization of sea waves is particularly relevant for the analysis conducted. In fact, the objective of this study is precisely the evaluation of the error induced by the assumption of uni-modality in multi-modality conditions.

PeWEC PERFORMANCE ERROR RESULS BASED ON MULTIPEAK AND MONOPEAK SPECTRA

Fig. 7.11 shows an extract of the power output of the PeWEC time series obtained from the monodirectional and multidirectional analyzes based on the spectra reconstructed from the synthetic parameters and directly provided by SWAN.

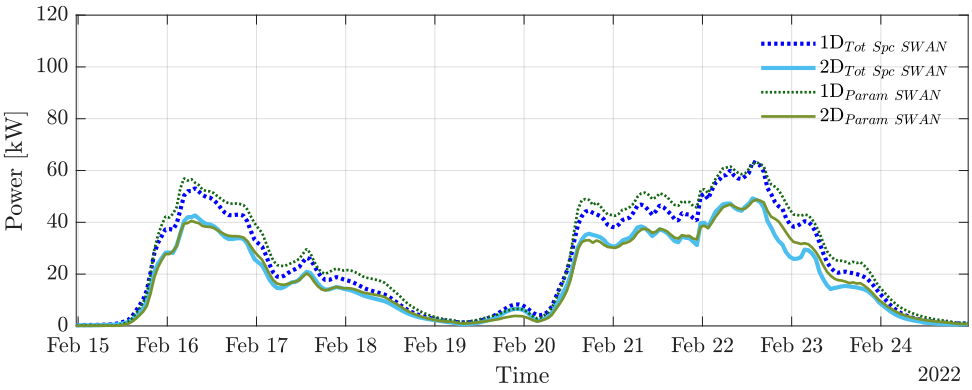

Figure 7.11: Power time series computed from 1D and 2D swell spectra with alignment of the hull orientation with the peak direction

As can be seen in the time series comparison, the power values obtained by monodirectional analysis and based on the reconstruction of the spectra using synthetic parameters are generally haigher the monodirectional analysis based directly on SWAN spectra. This result is consistent throughout the rest of the time series and is attributed to the fact that the energy is assumed concentrated around a single frequency peak despite

being distributed across at least two peaks: one attributed to wind waves and the other to swells. Regarding the comparison between the power obtained from the frequency-directional spectra reconstructed from synthetic parameters and the spectra directly supplied by SWAN, a closer match is observed. This improved agreement is due to the inclusion of energy distribution on different directions, which enhances the analysis by accounting for the multidirectional nature of the sea states. However, even in this case there are discrepancies and the reason is attributed to the different distribution of energy on frequencies and directions.
Fig. 7.12 presents two scatter plots comparing the power calculated from the spectra provided directly by SWAN with the power obtained from the spectra reconstructed using synthetic parameters from SWAN for the year 2022.

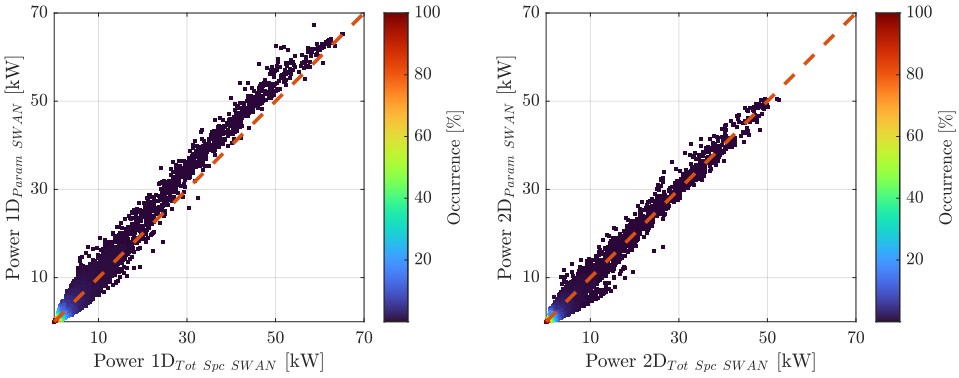

(a) Power computed from 1D SWAN spectra compared with power computed from 1D spectra reconstructed from SWAN synthetic parameters

(b) Power computed from 2D SWAN spectra compared with power computed from 2D spectra reconstructed from SWAN synthetic parameters

Figure 7.12: Comparison of the scatter plot of power obtained from SWAN spectra

The scatter plot of Fig. 7.12a compares the power calculated from the 1D SWAN frequency spectra with the power calculated from the 1D frequency spectra reconstructed from SWAN synthetic parameters. The graph shows a strong correlation between the two sets of power values, indicated by the clustering of data points around the bisector (orange dotted line). However, there is a tendency to overestimate the power when using reconstructed spectra compared to using the spectra directly provided by SWAN. This slight dispersion is linked to the distribution of energy around a single frequency peak, while the sea states at Pantelleria were found to be predominantly multimodal.
Fig. 7.12b shows the power calculated from the 2D spectra obtained directly from SWAN compared with the power calculated from the 2D spectra reconstructed from SWAN synthetic parameters. Similar to the first plot, there is a strong correlation between the two datasets, with the point cloud closely following the bisector. This correlation confirms that the 2D spectra reconstructed using SWAN synthetic parameters effectively represent the 2D spectra obtained directly from SWAN. The results indicate that incorporating multidirectional analysis significantly refines and enhances the accuracy of the power estimations.

Overall, the figures demonstrate that power estimates derived from spectra reconstructed using SWAN synthetic parameters are in good agreement with those obtained directly from SWAN spectra. To further detail the analysis and numerically evaluate the congruence between the two datasets, correlation indicators are used.
The Tab. 7.8 presents the correlation results of the PeWEC performance of the two datasets, using a monodirectional and a multidirectional assumption. The performance metrics included are $RMSE$, $BIAS$, CC and S.

Table 7.8: Performance indicators for PeWEC power production using SWAN spectra and spectra recustructed from SWAN synthetic parameters, in monodirectional (1D) and multidirectional (2D) analyses

Dataset	$RMSE$ **[kW]**	$BIAS$ **[kW]**	CC	S
Calibration				
$1D_{Tot\ Spc}$-$1D_{Param}$	2.008	0.664	0.994	0.902
$2D_{Tot\ Spc}$-$2D_{Param}$	1.212	-0.094	0.992	0.990

For the monodirectional comparison the $RMSE$ is 2.008 kW, indicating a significant error margin in the power estimates when using 1D spectra compared to reconstructed 1D parameters. The $BIAS$ value of 0.664 kW suggests an overall overestimation of power. However, the correlation coefficient (CC) is very high at 99.4%, indicating a strong linear relationship between the datasets. The S value of 0.902 further supports the similarity between the datasets despite the observed errors.
In contrast, the multidirectional analysis shows a lower $RMSE$ of 1.212 kW, which indicates a more accurate power estimation. The near-zero $BIAS$ value of -0.094 kW suggests that the 2D analysis does not systematically overestimate or underestimate the power. The CC for the 2D dataset is 99.2%, reflecting a strong linear relationship between the direct and reconstructed 2D SWAN spectra. The S value of 0.990 indicates a high degree of similarity between the direct and reconstructed 2D spectra.
Overall, the table demonstrates that the 2D analysis provides a more accurate and unbiased power estimation compared to the 1D analysis. The lower $RMSE$ and near-zero $BIAS$ in the 2D case indicate fewer errors and better alignment with the two dataset. Although both methods show high correlation and similarity, the 2D analysis significantly refines and enhances the accuracy of the power estimates. This underscores the importance of considering multidirectional wave characteristics for reliable wave energy resource assessments.

The Tab. 7.9 compares the yearly energy production and the standard deviation of the power for PeWEC using SWAN spectra and spectra reconstructed from SWAN synthetic parameters, considering both monodirectional (1D) and multidirectional (2D) analyses. For the power obtained by monodirectional assumption based on 1D SWAN spectra, the yearly energy production is 48.45 kWh with a standard deviation of 11.935 kW. When using the 1D recustructed spectra from SWAN synthetic parameters, the energy production increases to 53.30 kWh with a higher standard deviation of 13.255 kW.

Table 7.9: Comparison of PeWEC yearly energy production and standard deviation of the power using SWAN spectra and spectra recustructed from SWAN synthetic parameters, in monodirectional (1D) and multidirectional (2D) analyses

Dataset	E **[kWh]**	σ_{Power} **[kW]**
$1D_{Tot\ Spc}$	48.45	11.935
$1D_{Param}$	53.30	13.255
$2D_{Tot\ Spc}$	37.28	9.3502
$2D_{Param}$	36.59	9.5247

This suggests that the use of synthetic parameters in the 1D analysis results in a higher estimate of energy production and also introduces greater variability.
In the case of the 2D analysis, the power obtained by SWAN spectra shows a yearly energy production of 37.28 kWh with a standard deviation of 9.3502 kW. The power computed from the 2D recustructed spectra using synthetic parameters, on the other hand, indicates a slightly lower energy production of 36.59 kWh and a standard deviation of 9.5247 kW. This indicates that the multidirectional analysis yields lower and more consistent energy estimates compared to the monodirectional analysis.
Overall, the comparison highlights that the 1D analysis based on the synthetic parameters tends to overestimate energy production and exhibits higher variability, whereas the 2D analysis provides more consistent estimates. This underscores the importance of using multidirectional analysis for more accurate and reliable wave energy assessments.

PeWEC PERFORMANCE ERROR RESULS DISCUSSION BASED ON MULTIPEAK AND MONOPEAK SPECTRA

Detailed knowledge of the sea states at the WEC installation site is essential for detailed design and correct identification of the forcing agents on the device. This includes evaluating the persistence of single-modal or multi-modal sea states and incorporating directional information through the directional spreading parameter.
Several studies have indicated that the probability of encountering bimodal spectra in the North Sea varies between 10% and 30%. However, this frequency may increase depending on specific sea conditions and measurement locations. For instance, in the case of Pantelleria, the occurrence of multimodal sea states is higher than 90%, with the remaining sea states characterized by the existence of three or four different sea states. This result emphasizes the importance of in-depth analysis of wave conditions at the site of interest, as the coexistence of different sea states redistributes wave energy across two or more peaks.
Based on the evidence described, a comparative analysis was conducted between the performance evaluation of the PeWEC in Pantelleria in 2022 using spectra directly provided by SWAN and spectra reconstructed from the synthetic parameters provided by SWAN. The spectra directly provided by SWAN are frequency-directional and account for the coexistence of different sea states. In contrast, the reconstruction of the spectra from SWAN's synthetic parameters is based on the assumption of mono-modal sea

states, characterized by a single peak. The JONSWAN spectrum is used to identify the distribution of wave energy along the frequencies, and the directional spectrum is reconstructed based on the formulation proposed by Mitsuyasu. This approach replicates common practice to identify its limitations and quantify the induced error in the specific case.
The comparison between the powers obtained under the monodirectional assumption shows that the use of synthetic parameters for the reconstruction of the spectrum induces an overestimation of the energy by 10%. This result is attributed to the assumption of uni-modal sea states, where the energy is distributed around a single peak frequency. In the case of multi-modal sea states, however, two or more peaks coexist, and the energy is distributed in a more complex and less narrow manner.
The results based on the multidirectional analyzes show greater congruence between the data, with a minimal underestimation of 1.8% between the use of the reconstructed spectra and the ones directly provided by SWAN. This result is attributed to the complex energy distribution on 2D spectra characterized by two or more peaks. In particular, the directional spreading parameter calculated on the basis of the entire directional spectrum provides a representative value of the wave energy distribution around the average direction. Consequently, the presence of two or more directional peaks increases this parameter, as it represents the standard deviation of the distribution. Assuming the coexistence of only two sea states, as the directional difference between the peak directions of these sea states increases, the directional spreading parameter calculated on the entire directional spectrum also increases.
These findings highlight the critical importance of considering directional spreading and the use of synthetic parameters for the reconstruction of single-modal spectra demonstrates its reliability, with a reduced error rate. This result is encouraging, as the obtaining and processing of synthetic parameters appears to be simpler and better known.

7.3. PEWEC ENERGY CONVERSION IN PANTELLERIA

THE analysis of the performance of the PeWEC in Pantelleria is based on 10 years of 2D and 1D hourly spectra obtained from the SWAN model. This analysis aims to evaluate the manufacturability of the device at the identified site and to quantify the errors arising from the assumption of monodirectionality.
Fig. 7.13 illustrates the seasonal variability of the power output of the PeWEC based on the monodirectional and multidirectional assumptions.
The Fig. 7.13a shows the monthly minimum, maximum, average, 5^{th} percentile, and 95^{th} percentile of power output throughout the year. From the graph, it is clear that energy production fluctuates significantly over the year. Maximum power output is consistently higher in the winter months, with peaks observed in March and November. These results indicate that wave energy, assumed to be monodirectional, is most potent during the winter months, which is typical due to increased wave activity during this season. The 5^{th} percentile line remains close to zero, indicating the presence of sea states with very low wave energy. The 95^{th} percentile line, representing the highest energy events, shows substantial variability, particularly in the winter months, suggesting more frequent high-energy wave events during this period.

Figure 7.13b presents the seasonal variability of the power output of the PeWEC based on the multidirectional assumption. Similar to the monodirectional assumption, the graph shows the monthly minimum, maximum, average, 5^{th} percentile, and 95^{th} percentile of power output. The graph reveals that power production under the multidirectional assumption also fluctuates throughout the year, but with some differences compared to the monodirectional assumption. The maximum power output in the winter months is still higher than in the summer months, but the peaks are less pronounced. This indicates a more coherent distribution of wave energy across different directions, reducing the impact of high-energy events. The 5^{th} percentile line remains close to zero, indicating periods of low wave energy. The 95^{th} percentile line shows less variability than under the monodirectional assumption, reflecting wave energy that is more evenly distributed across multiple directions.

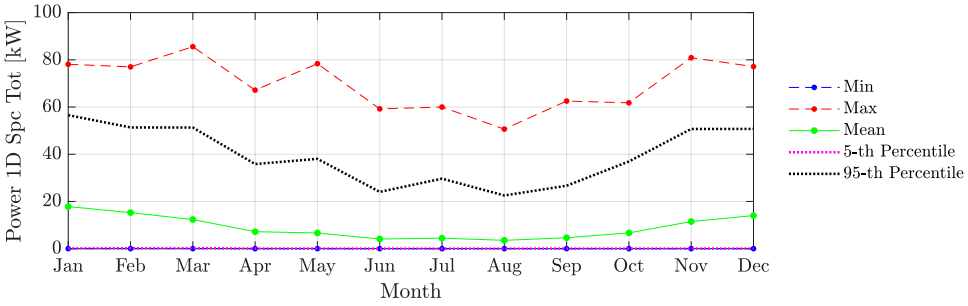

(a) Seasonal variability of PeWEC power output based on monodirectional assumption

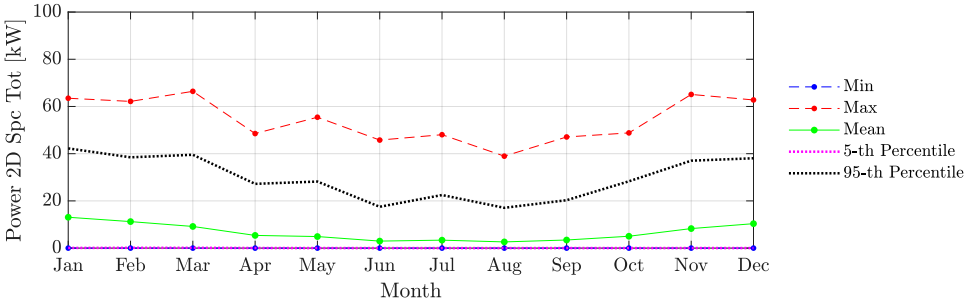

(b) Seasonal variability of PeWEC power output based on monodirectional and multidirectional assumption

Figure 7.13: Season variability of PeWEC power output based on monodirectional and multidirectional assumption

The analysis of the seasonal variability of PeWEC power production under both monodirectional and multidirectional assumptions highlights the importance of considering directional spreading in wave energy resource assessments. The monodirectional assumption tends to overestimate energy production during high-energy events, particularly in the winter months. In contrast, the multidirectional assumption provides a more balanced and accurate representation of the wave energy resource, leading to more reliable estimates of device performance.

Fig. 7.14 illustrates the inter-annual variability of PeWEC power output based on the

monodirectional and multidirectional assumption from 2013 to 2022. The graphs show the yearly minimum, maximum, mean, 5^{th} percentile, and 95^{th} percentile of the power output. The data based on the monodirectional assumption (Fig. 7.14a) indicate that the maximum power output remains relatively consistent across the years, with slight fluctuations. Peaks are observed in the years 2013 and 2021, suggesting that these years experienced higher wave energy events. The mean power output remains stable across the decade, indicating consistent wave energy availability. The 5^{th} percentile line remains close to zero, reflecting periods with very low wave energy, while the 95^{th} percentile shows slight variability, particularly, highlighting the occurrence of high-energy wave events.

Fig. 7.14b presents the inter-annual variability of PeWEC power output based on the multidirectional assumption over the same period. Similar to the monodirectional assumption, the graph shows the yearly minimum, maximum, mean, 5^{th} percentile, and 95^{th} percentile of power output. The maximum power output in the multidirectional analysis also shows slight fluctuations, with peaks in 2013 and 2021, but the peaks are less pronounced compared to the monodirectional assumption. The mean power output remains stable, and the 5^{th} percentile line stays close to zero, indicating low-energy periods. The 95^{th} percentile shows less variability than the monodirectional assumption.

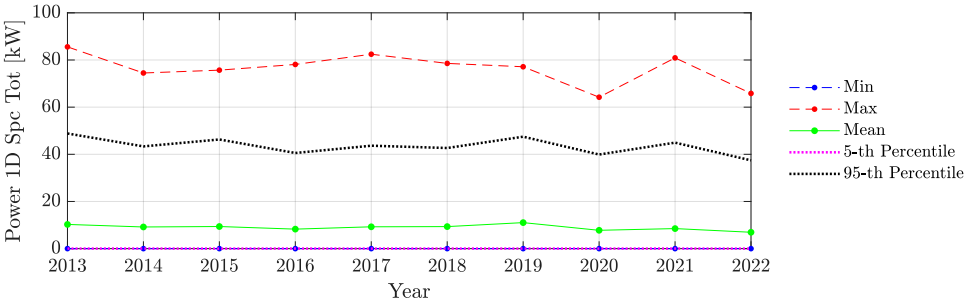

(a) Inter-annual variability of PeWEC power output based on monodirectional assumption

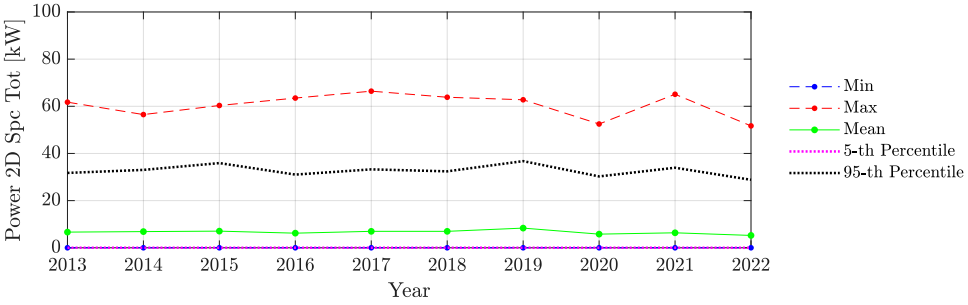

(b) Inter-annual variability of PeWEC power output based on multidirectional assumption

Figure 7.14: Inter-annual variability of PeWEC power output based on monodirectional and multidirectional assumption

The comparison between the two figures underscores the importance of considering

multidirectional wave energy analysis for accurate performance evaluation of wave energy converters. The monodirectional assumption tends to overestimate power output during high-energy events, as evidenced by the more pronounced peaks in the maximum power output. In contrast, the multidirectional assumption provides a more balanced and accurate representation of wave energy, with less pronounced peaks and reduced variability in the 95^{th} percentile. Overall, the multidirectional analysis results in more reliable and consistent estimates of PeWEC power output, minimizing the risk of overestimating energy production. This comprehensive approach to evaluating wave energy resources ensures better-informed decisions regarding the design, placement, and operation of wave energy converters, ultimately enhancing the efficiency and reliability of marine renewable energy systems.

7.4. DISCUSSION

THE chapter focuses on evaluating the performance of the PeWEC using various data sources and spectral approximations.
The primary objective of this chapter is to analyze the errors in performance estimation that arise from utilizing different wave data sources and assumptions about wave spectra. The study evaluates PeWEC's performance using both monodirectional and multidirectional spectral approximations. By comparing these approaches, it becomes evident that monodirectional assumptions tend to overestimate power output, leading to inaccuracies. In contrast, multidirectional analysis provides a more balanced and realistic representation of wave energy, resulting in more reliable estimates of PeWEC's performance. This discrepancy underscores the necessity of considering wave directionality in performance evaluations to avoid significant errors in energy production predictions.

The chapter begins with a detailed examination of the impact of different data sources, including in-situ measurements, global numerical models, and local numerical models, on PeWEC performance evaluation, highlighting their respective advantages and limitations in providing accurate wave data.

Furthermore, the chapter investigates the errors in performance estimation based on discretized synthetic parameters, reproducing the commonly used technique based on the power matrix to estimate the producibility of WECs. This involves analyzing PeWEC's power output relative to different pairs of significant wave height and energy period values under the monodirectional assumption, and the triplet of significant wave height, energy period, and directional spreading under the multidirectional assumption. The findings demonstrate that simplifying the study using discrete parameters can lead to substantial estimation errors.

The correlation between performance estimates derived from 1D (monodirectional) and 2D (multidirectional) assumptions is also explored. The results highlight that multidirectional wave interactions must be considered for a more realistic assessment of PeWEC's performance. The study shows that neglecting these interactions can result in overestimations of up to 30% in energy production, significantly impacting the feasibil-

ity and design of wave energy projects. To overcome this discrepancy, the use of Bias Correction techniques, such as simple linear regression, shows promising results.

Moreover, the chapter examines the impact of multi-peak versus single-peak spectra on performance estimation. The analysis reveals that complex wave spectra characterized by multiple energy peaks, typical of the Pantelleria site, require detailed spectral representations to obtain accurate performance predictions. In particular, comparing the results of these two cases under the assumption of monodirectionality, clear estimation errors are identified. However, the inclusion of directional energy spreading leads to more accurate estimates and reduces errors.

Lastly, the chapter evaluates the performance of PeWEC in reference to the sea conditions at Pantelleria from 2013 to 2022, providing insights into stationary and inter-annual variability.

7.5. CONCLUSION

THIS chapter concludes that accurate performance evaluation of the PeWEC requires the use of multidirectional spectral data. The findings highlight that monodirectional assumptions and simplified spectral representations introduce significant errors in energy production estimates. By employing multidirectional wave data and detailed spectral models, the study demonstrates a more accurate and reliable prediction of PeWEC's performance.

The comparison of various data sources reveals that high-resolution, locally calibrated models, such as SWAN, offer better approximations to in-situ data than global models like ERA5. Although ERA5 is useful for initial evaluations, its lower accuracy underscores the importance of using precise local models for detailed assessments. The study reveals that the 1D analysis based on ERA5 data induces an error of 21.3% compared to the 2D assumption based on in-situ data.

Moreover, the investigation into discretized synthetic parameters and their impact on performance estimation underscores the necessity of detailed spectral analysis. Research shows that simplified parameters may fail to capture the complexity of wave conditions, leading to estimation errors. The analysis indicates that, under the multidirectional assumption, the absolute error between parameters provided by SWAN and those discretized according to different bins varies between 0.12% for the densest discretization and 6.42% for the sparsest discretization.

The chapter also addresses the error induced by the assumption of monodirectionality and suggests using a simple linear regression technique to calibrate data obtained from the 1D assumption with respect to the 2D one. The results show that the overestimation of the energy converted by PeWEC exceeds 30% when directional information is neglected. However, by applying data calibration, this overestimation decreases to 0.6% for the specific case.

In conclusion, the chapter compares the power estimates obtained using spectra directly provided by SWAN with those reconstructed from synthetic parameters provided by SWAN. This comparison aims to highlight how the assumption of unimodal sea states can negatively impact the performance estimate of a device installed at a site characterized by multimodal sea states. The analysis shows a clear difference in performance under the monodirectional assumption, which is drastically reduced when using multidirectional data. Specifically, the overestimation in the 1D case is 10%, while in the 2D case, it is reduced to 1.8%.

8

CONCLUSIONS AND FUTURE WORKS

8.1. CONCLUSIONS AND FUTURE WORKS DESCRIPTION

THIS thesis has explored in depth the energy potential of sea waves fot the Pantelleria case and the effectiveness of PeWEC under this wave conditions. Through a combination of in-situ measurement recors, satellite observations and numerical models, it is possible to obtain a detailed picture of the wave conditions and energy potential of the site. The main results and conclusions reached are summarized below.

Satellite collocation analysis: The use of satellite data for the validation of numerical models has become increasingly popular. In particular, since in-situ instruments are difficult to access and find, as well as having frequent gaps in the records, the expansion of the validation datasets with the inclusion of satellite data is a useful strategy.
The reliability analysis of satellite data is conducted using a 30-minute time criterion for data collocation and varying spatial distances from the buoy installation site, ranging from 10 km to 90 km. This approach aims to determine the optimal spatial range for integrating satellite data with in-situ buoy data, ensuring a comprehensive understanding of how spatial factors influence data congruence. Proximity to Tunisia limited the maximum distance to 90 km, and a sensitivity analysis assessed the impact of including or excluding satellite measurements from the southeast quadrant relative to the buoy.
Two methodologies are used to identify the satellites significant wave height value for each collocation: the nearest measurement to the installation site and the mean value of the measurements at each collocation. In particular, four case studies are analyzed: MDQ (Mean-Distance-Quadrant), NDQ (Near-Distance-Quadrant), MD (Mean-Distance), and ND (Near-Distance), with MDQ and NDQ excluding the southeast quadrant.
Cases with a radius of 10 and 20 km are excluded from the performance analysis due to small datasets and poor adherence to in-situ data. The analysis indicates that increasing the radius of the spatial collocation criterion improves the adherence of satellite data to

in-situ measurements, likely due to the larger dataset allowing for more comprehensive sea condition comparisons. Unexpectedly, excluding data from the southeast quadrant reduced overall performance, suggesting that including this quadrant enhances the robustness of the analysis. This finding warrants further investigation with higher temporal coverage and similar geographical configurations.
The best performance is observed in the MD case with an 80 km radius, achieving a correlation coefficient (CC) of 87.8% and an $RMSD$ of 0.316 m, demonstrating good adherence of satellite data to in-situ data despite the challenging geographical conditions.
In conclusion, the results underscore the potential of satellite data even in less favorable locations and highlight the importance of analyzing spatial criteria to identify optimal performance conditions. To validate these findings further, similar analyses in different locations are recommended. For this thesis, satellite data from AODN are used as a benchmark for validating the SWAN numerical model, extending the temporal coverage of the validation beyond what in-situ data alone can offer.

SWAN model calibration through the Stage-Gate approach: Calibrating numerical model such as SWAN is essential for ensuring accurate predictions of sea wave conditions. The Stage-Gate approach adopted in this thesis provides a systematic and efficient method to calibrate SWAN by reducing the number of configurations to analyze and optimizing both accuracy and computational times. This approach divides the calibration process into distinct phases (Stages), each representing a specific set of parameters to be calibrated. Each phase is followed by a checkpoint (Gate) where the model's performance is evaluated, and decisions are made on how to proceed. This method allows a progressive focus on the most relevant aspects, enhancing the efficiency of the calibration process.
In particular, the calibration of the SWAN model using the Stage-Gate approach led to notable improvements in terms of accuracy and compuatational times, especially in the calibration phase of the bathymetric source and mesh resolution. The use of EMODnet bathymetry, compared to GEBCO, showed a more accurate representation of the parameters H_s and T_e thanks to the greater spatial resolution provided by EMODnet (approximately 115 m compared to 460 m of GEBCO). In the time-step calibration phase, the configuration with a 30-minute interval proved to be the most efficient, reducing calculation time by 87% compared to the configuration with a 5-minute interval, while maintaining the same level of accuracy.
Configurations for wind and wave boundary conditions, based on two-dimensional frequency-directional spectra, improved the accuracy of H_s and T_e with a 22.5% increase in calculation time compared to conventional descriptions based on synthetic parameters. The frequency range analysis phase shows that aligning the frequency range with that of the in-situ instruments for spectral density propagation and output calculations led to the highest accuracy, especially for the T_e parameter.
The analysis of whitecapping and exponential wind growth patterns led to selecting configurations based on Rogers' formulations, improving the accuracy of both H_s and T_e, albeit with a 24% increase in computation time compared to the default configurations. The wind drag analysis phase identified the default configuration as the most accurate, maintaining similar compuatational times compared to other formulations.

Further analysis of additional physical components, such as linear wind growth, bottom friction, and triad-triad wave interaction, highlights that their inclusion does not improve the model's accuracy, despite a slight increase in computation time. This underscores the need to carefully evaluate the inclusion of such physical phenomena.
The results indicate that significant improvements in the accuracy of H_s are not achieved, with $RMSD$ consistently around 0.241 m and CC stable at approximately 96.7%. However, the accuracy of T_e predictions saw notable improvements, with $RMSD$ decreasing from 0.726 s in the initial configuration to 0.432 s in the final configuration. CC_{T_e} increased from 87.8% to 93.4% from the first to the last configuration obtained via the Stage-Gate approach.
In summary, the choice of bathymetric source and mesh resolution significantly impacts model accuracy. Balancing the time interval and the maximum number of iterations is crucial for optimal model performance, as is the careful selection of the physical model for whitecapping and exponential wind growth. The Stage-Gate approach, by breaking the problem into manageable subproblems, has proven to be an effective method for optimizing SWAN model configurations, providing a reliable and efficient tool for obtaining accurate data in reasonable computation times.

Prevalence of multi-modal sea states: Wave energy assessment analysis is of fundamental importance when operating in the marine sector. In particular, in the field of Wave Energy Converter (WEC) design, conducting analyses in compliance with IEC/TS 62600-101:2015 standards allows for a coherent and detailed investigation of the sea states at the study site.
A particularly relevant result emerges from the analysis conducted for the Pantelleria site. A predominance of bi-modal maritime states is revealed, characterized by the combination of wind waves and swell, occurring with a frequency greater than 80%. The remaining sea states consist of a superposition of wind waves and at least two swell components. Furthermore, the energy contribution of wind waves is significant but not totalitarian, constituting approximately 75% of the total wave energy.
These findings highlight how the assumption of uni-modal sea states, described through synthetic parameters obtained from the overall spectrum, does not accurately characterize the site of interest. This result underscores the importance of investigating the directional and multi-modal nature of sea states to obtain a comprehensive understanding of the wave energy resource. It is crucial to partition the wave spectrum and analyze the individual components to accurately capture the complexity of the sea conditions.

Performance evaluation for wave direction sensitive WECs: PeWEC proves to be a promising device for wave energy conversion in the Mediterranean Sea. Performance evaluations under various wave conditions highlight the importance of considering multidirectional waves to obtain accurate estimates of energy production. The analysis reveals that monodirectional assumptions tend to overestimate energy production, leading to significant energy conversion errors. Comparison of data from different sources shows that high-resolution local models, such as SWAN, provide better approximations than global data sources like ERA5. This underscores the importance of using accurate local models for detailed assessments. Specifically, the study reveals that monodirec-

tional analysis based on ERA5 data induces an error of 21.2% compared to the multidirectional hypothesis based on in-situ data. When using SWAN data, this error is 33.4%. The reason lies in the underestimation of ERA5 data compared to the wave resource in Pantelleria and the overestimation due to the assumption of monodirectionality. Comparing the errors of the powers extracted by PeWEC based on ERA5 and SWAN data in the multidirectional case shows an underestimation of 12.8% in the first case and 6.3% in the second if compared with the power conversion obtained using in-situ data.
Additionally, the analysis concludes that an accurate evaluation of PeWEC's performance requires the use of multidirectional spectral data. However, in the absence of such information, synthetic parameters can reconstruct frequency-directional spectra, provided the analysis is carried out under the hypothesis of multidirectionality.
Further investigation of discretized synthetic parameters and their impact on performance estimation highlights the need for detailed spectral analysis, avoiding the use of coarse bins as much as possible. Research indicates that simplified parameters may fail to capture the complexity of wave conditions, leading to estimation errors. The analysis shows that, under the multidirectional hypothesis, the absolute error between the parameters provided by SWAN and those discretized according to different bins varies between 0.12% for the densest discretization (i.e. $\Delta H_s = 0.25m$ $\Delta T_e = 0.5s$ and $\Delta s = 2.5°$) and 6.42% for the most scattered (i.e. $\Delta H_s = 1m$ $\Delta T_e = 2s$ and $\Delta s = 10°$).
The study also addresses the error induced by the monodirectionality hypothesis and suggests using a simple linear regression technique to calibrate the data obtained from the monodirectional hypothesis versus the multidirectional one. However, this approach requires conducting both monodirectional and multidirectional analyses to identify the correlation coefficients necessary for the calibration. Results show that the overestimation of the energy converted by PeWEC exceeds 30% when neglecting directional information. However, by applying data calibration, this overestimation decreases to 0.6% in the case of Pantelleria.
These analyses aim to highlight how the hypothesis of uni-modal, monodirectional, and simplified sea states can negatively impact the performance estimate of a device installed in a site characterized by complex sea states. The analysis shows a clear difference in performance under the monodirectional assumption, which is dramatically reduced when using multidirectional data. Evaluation of the PeWEC model demonstrates that exploiting high-resolution local models and considering the multidirectional nature of waves is essential for precise estimates of energy production. The results also emphasize the importance of comprehensive wave characterization for the effective design and optimization of wave energy converters.
This results demonstrates that combining advanced measurement methods with numerical models can provide accurate estimates of wave energy resources and the performance of conversion devices. The results underscore the importance of considering wave multidirectionality and utilizing high-resolution local models for precise assessments. This integrated approach not only enhances the understanding of marine energy resources but also offers valuable insights for the design and optimization of wave energy converters, significantly contributing to sustainable development and efficient utilization of marine resources.
The work conducted represents a significant advancement in evaluating wave energy

resources and designing efficient devices for their conversion. The methodologies developed and the results obtained can be applied to other sites, contributing to a broader and more informed dissemination of wave energy technologies and supporting the transition towards a more sustainable and diversified energy mix. This thesis, therefore, provides a solid foundation for future studies and applications in the field of wave energy, highlighting the importance of data accuracy and the integration of various measurement and modeling techniques to address challenges related to the assessment and utilization of marine resources.
Future works will include the application of non-linear modeling for the analysis of wave-device interactions. In reality, these interactions are complex and non-linear, and linearity can only be assumed under simplifying hypotheses, such as the assumption of small motions of the WEC. Addressing these complexities will further enhance the accuracy and reliability of wave energy assessments and the design of wave energy converters.

BIBLIOGRAPHY

[1] T Kober et al. “Global energy perspectives to 2060–WEC’s World Energy Scenarios 2019”. In: *Energy Strategy Reviews* 31 (2020), p. 100523.

[2] Stéphanie Bouckaert et al. “Net zero by 2050: A roadmap for the global energy sector”. In: (2021).

[3] Sunny Kumar Poguluri and Yoon Hyeok Bae. “A study on performance assessment of WEC rotor in the Jeju western waters”. In: *Ocean systems engineering* 8.4 (2018), pp. 361–380.

[4] YaJun Fan, AnLe Mu, and Tao Ma. “Design and control of a point absorber wave energy converter with an open loop hydraulic transmission”. In: *Energy conversion and management* 121 (2016), pp. 13–21.

[5] Gordon Reikard, Bryson Robertson, and Jean-Raymond Bidlot. “Combining wave energy with wind and solar: Short-term forecasting”. In: *Renewable Energy* 81 (2015), pp. 442–456.

[6] Davide Magagna and Andreas Uihlein. “Ocean energy development in Europe: Current status and future perspectives”. In: *International Journal of Marine Energy* 11 (2015), pp. 84–104.

[7] Aurélien Babarit. *Ocean wave energy conversion: resource, technologies and performance*. Elsevier, 2017.

[8] John V Ringwood. “Wave energy control: status and perspectives 2020”. In: *IFAC-PapersOnLine* 53.2 (2020), pp. 12271–12282.

[9] Chenglong Guo et al. “A review of the levelized cost of wave energy based on a techno-economic model”. In: *Energies* 16.5 (2023), p. 2144.

[10] Seyed Abolfazl Mortazavizadeh et al. “Fault Diagnosis and Condition Monitoring in Wave Energy Converters: A Review”. In: *Energies* 16.19 (2023).

[11] Carlos V.C. Weiss et al. “Marine renewable energy potential: A global perspective for offshore wind and wave exploitation”. In: *Energy Convers. Manag.* 177.September (2018), pp. 43–54.

[12] Nicolas Guillou. “Estimating wave energy flux from significant wave height and peak period”. In: *Renew. Energy* 155 (2020), pp. 1383–1393. ISSN: 18790682. DOI: 10.1016/j.renene.2020.03.124.

[13] World Meteoroligcal Organization. *Guide to Wave Analysis and Forecasting*. Vol. 1998. 702. 1998, pp. 1–109. ISBN: 9263127026.

[14] Leo H. Holthuijsen and Leo H. Holthuijsen. “Linear wave theory”. In: *Waves Ocean. Coast. Waters* February (2010), pp. 318–323. DOI: 10.1017/cbo9780511618536.012.

[15] B. Drew, A. R. Plummer, and M. N. Sahinkaya. “A review of wave energy converter technology”. In: *Proceedings of the Institution of Mechanical Engineers, Part A: Journal of Power and Energy*. Vol. 223. 2009, pp. 887–902. DOI: 10.1243/09576509JPE782.

[16] Arthur Pecher and Jens Peter Kofoed. *Handbook of ocean wave energy*. Springer Nature, 2017.

[17] João Cruz. *Ocean wave energy. Current status and future perspectives*. Springer-Verlag, 2008.

[18] Tiago Duarte et al. “Computation of wave loads under multidirectional sea states for floating offshore wind turbines”. In: *Proc. Int. Conf. Offshore Mech. Arct. Eng. - OMAE* 9B.March (2014). DOI: 10.1115/OMAE2014-24148.

[19] M. J. Tucker, P. G. Challenor, and D. J.T. Carter. “Numerical simulation of a random sea: a common error and its effect upon wave group statistics”. In: *Appl. Ocean Res.* 6.2 (1984), pp. 118–122. ISSN: 01411187. DOI: 10.1016/0141-1187(84)90050-6.

[20] Alberto Meucci et al. “Comparison of wind speed and wave height trends from twentieth-century models and satellite altimeters”. In: *J. Clim.* 33.2 (2020), pp. 611–624. ISSN: 08948755. DOI: 10.1175/JCLI-D-19-0540.1.

[21] Nicola Pozzi et al. “PeWEC: Experimental validation of wave to PTO numerical model”. In: *Ocean Engineering* 167 (2018), pp. 114–129. ISSN: 0029-8018.

[22] “PeWEC: Preliminary design of a full-scale plant for the mediterranean sea”. In: *NAV International Conference on Ship and Shipping Research*. 221499. 2018, pp. 504–514. DOI: 10.3233/978-1-61499-870-9-504.

[23] Walter Heinrich Munk. *Origin and generation of waves*. Scripps Institution of Oceanography La Jolla, California, 1951.

[24] Leo H. Holthuijsen. *Waves in Oceanic and Coastal Waters*. Cambridge University Press, 2007.

[25] Robert L Wiegel. “Wind waves and swell”. In: *Coastal Engineering Proceedings* 7 (1960), pp. 1–1.

[26] Norman Frederick Barber and Fritz Ursell. “The generation and propagation of ocean waves and swell. I. Wave periods and velocities”. In: *Philosophical Transactions of the Royal Society of London. Series A, Mathematical and Physical Sciences* 240.824 (1948), pp. 527–560.

[27] Mercè Casas-Prat and Leo H Holthuijsen. “Short-term statistics of waves observed in deep water”. In: *Journal of Geophysical Research: Oceans* 115.C9 (2010).

[28] Yi-Chih Chow et al. “Parametric design methodology for maximizing energy capture of a bottom-hinged flap-type WEC with medium wave resources”. In: *Renewable energy* 126 (2018), pp. 605–616.

[29] Ryan G Coe, Yi-Hsiang Yu, and Jennifer Van Rij. “A survey of WEC reliability, survival and design practices”. In: *Energies* 11.1 (2017), p. 4.

[30] Øistein Hagen et al. “Analysis of Short-Term and Long-Term wave statistics by time domain simulations statistics”. In: *International Conference on Offshore Mechanics and Arctic Engineering*. Vol. 57656. American Society of Mechanical Engineers. 2017, V03AT02A045.

[31] Hong-Yeon Cho et al. “Relationship between wave height and sampling interval: revisiting individual wave analysis method”. In: *Journal of Coastal Research* 85 (2018), pp. 1136–1140.

[32] J Lawrence et al. “D2. 1 Wave Instrumentation Database. Work Package 2: Standards and Best Practice-Revision: 05”. In: (2012).

[33] Kiyoshi Horikawa. “Coastal engineering: an introduction to ocean engineering”. In: *Publ. by: University of Tokyo Press* (1978).

[34] United States. Army. Corps of Engineers. *Coastal engineering manual*. US Army Corps of Engineers, 2002.

[35] G Giorgi et al. “Wave energy converters technology database for a web-based platform for evaluating wave energy resource and productivity potential”. In: *Trends in Renewable Energies Offshore* (2022), pp. 33–41.

[36] Giulia Cervelli et al. “On the errors in annual energy yield estimation due to monodirectional wave spectra assumption”. In: *Proceedings of the European Wave and Tidal Energy Conference* 15 (2023).

[37] Igor Rychlik, Pär Johannesson, and Malcolm R Leadbetter. “Modelling and statistical analysis of ocean-wave data using transformed Gaussian processes”. In: *Marine Structures* 10.1 (1997), pp. 13–47.

[38] World Meteorological Organization. *Guide to wave analysis and forecasting*. Secretariat of the World Meteorological Organization, 1998.

[39] James W Cooley and John W Tukey. “An algorithm for the machine calculation of complex Fourier series”. In: *Mathematics of computation* 19.90 (1965), pp. 297–301.

[40] Young Jun Yang and Sun Hong Kwon. “Prediction for irregular ocean wave and floating body motion by regularization: Part 1. Irregular wave prediction”. In: *Transactions of FAMENA* 40.4 (2016), pp. 41–54.

[41] Ole Gunnar Houmb and E Due. “On the occurrence of wave spectra with more than one peak”. In: *(No Title)* (1978).

[42] Michael S Longuet-Higgins. “Observation of the directional spectrum of sea waves using the motions of a floating buoy”. In: *Oc. Wave Spectra* (1963).

[43] Michael Selwyn Longuet-Higgins. “Statistical properties of wave groups in a random sea state”. In: *Philosophical Transactions of the Royal Society of London. Series A, Mathematical and Physical Sciences* 312.1521 (1984), pp. 219–250.

[44] Robert G Dean and Robert A Dalrymple. *Water wave mechanics for engineers and scientists*. Vol. 2. world scientific publishing company, 1991.

[45] AJ Kuik, G Ph Van Vledder, and LH Holthuijsen. “A method for the routine analysis of pitch-and-roll buoy wave data”. In: *Journal of physical oceanography* 18.7 (1988), pp. 1020–1034.

[46] Denis Mollison. “Wave climate and the wave power resource”. In: *Hydrodynamics of Ocean Wave-Energy Utilization: IUTAM Symposium Lisbon/Portugal 1985*. Springer. 1986, pp. 133–156.

[47] P Hawkes, T Coates, and RJ Jones. “Impact of bi-model seas on beaches and control structures”. In: (1998).

[48] MD Earle. “Development of algorithms for separation of sea and swell”. In: *National Data Buoy Center Tech Rep MEC-87-1, Hancock County* 53 (1984), pp. 1–53.

[49] S Aranuvachapun. “Parameters of Jonswap spectral model for surface gravity waves—II. Predictability from real data”. In: *Ocean engineering* 14.2 (1987), pp. 101–115.

[50] C Guedes Soares. “On the occurence of double peaked wave spectra”. In: *Ocean Engineering* 18.1-2 (1991), pp. 167–171.

[51] Daniel A Thompson, Harshinie Karunarathna, and Dominic E Reeve. “An Analysis of Swell and Bimodality around the South and South-west coastline of England”. In: *Natural Hazards and Earth System Sciences Discussions* 2018 (2018), pp. 1–28.

[52] Willard J Pierson Jr and Lionel Moskowitz. “A proposed spectral form for fully developed wind seas based on the similarity theory of SA Kitaigorodskii”. In: *Journal of geophysical research* 69.24 (1964), pp. 5181–5190.

[53] Malcolm John Tucker and Edward G Pitt. *Waves in ocean engineering*. Volume 5. 2001.

[54] T Fossen. “Guidance and Control of Ocean Vehicles. John Willey & Sons”. In: *Inc., New York* (1994).

[55] TP Barnett and AJ Sutherland. “A note on an overshoot effect in wind-generated waves”. In: *Journal of Geophysical Research* 73.22 (1968), pp. 6879–6885.

[56] Klaus Hasselmann et al. “Measurements of wind-wave growth and swell decay during the Joint North Sea Wave Project (JONSWAP).” In: *Ergaenzungsheft zur Deutschen Hydrographischen Zeitschrift, Reihe A* (1973).

[57] Michel K Ochi and E Nadine Hubble. “Six-parameter wave spectra”. In: *Coastal Engineering 1976*. 1976, pp. 301–328.

[58] Knut Torsethaugen. “A two peak wave spectrum model”. In: (1993).

[59] Kantilal Varichand Mardia. “Statistics of directional data”. In: *Journal of the Royal Statistical Society Series B: Statistical Methodology* 37.3 (1975), pp. 349–371.

[60] Hisashi Mitsuyasu et al. “Observations of the directional spectrum of ocean WavesUsing a cloverleaf buoy”. In: *Journal of Physical Oceanography* 5.4 (1975), pp. 750–760.

[61] Dieter E Hasselmann, M Dunckel, and JA Ewing. “Directional wave spectra observed during JONSWAP 1973”. In: *Journal of physical oceanography* 10.8 (1980), pp. 1264–1280.

[62] Mark A. Donelan, J. E. M. Hamilton, and W. H. Hui. “Directional spectra of wind-generated ocean waves”. In: *Philosophical Transactions of the Royal Society of London. Series A, Mathematical and Physical Sciences* 315 (1985), pp. 509–562.

[63] Michael L Banner. “Equilibrium spectra of wind waves”. In: *Journal of Physical Oceanography* 20.7 (1990), pp. 966–984.

[64] David W Wang and Paul A Hwang. “An operational method for separating wind sea and swell from ocean wave spectra”. In: *Journal of Atmospheric and Oceanic Technology* 18.12 (2001), pp. 2052–2062.

[65] García-Nava Hwang Ocampo-Torres. “Wind sea and swell separation of 1D wave spectrum by a spectrum integration method”. In: *Journal of Atmospheric and Oceanic Technology* (2012).

[66] Jesús Portilla, Francisco J Ocampo-Torres, and Jaak Monbaliu. “Spectral partitioning and identification of wind sea and swell”. In: *Journal of atmospheric and oceanic technology* 26.1 (2009), pp. 107–122.

[67] Thomas W Gerling. “Partitioning sequences and arrays of directional ocean wave spectra into component wave systems”. In: *Journal of atmospheric and Oceanic Technology* 9.4 (1992), pp. 444–458.

[68] GJ Komen, Susanne Hasselmann, and Klaus Hasselmann. “On the existence of a fully developed wind-sea spectrum”. In: *Journal of physical oceanography* 14.8 (1984), pp. 1271–1285.

[69] Barbara Tracy et al. “Wind sea and swell delineation for numerical wave modeling”. In: *10th international workshop on wave hindcasting and forecasting & coastal hazards symposium, JCOMM Tech. Rep.* Vol. 41. 2007, p. 1442.

[70] Luc Vincent and Pierre Soille. “Watersheds in digital spaces: an efficient algorithm based on immersion simulations”. In: *IEEE Transactions on Pattern Analysis & Machine Intelligence* 13.06 (1991), pp. 583–598.

[71] Jeffrey L Hanson and Robert E Jensen. “Wave system diagnostics for numerical wave models”. In: *8th International Workshop on Wave Hindcasting and Forecasting, Oahu, Hawaii*. 2004, pp. 231–238.

[72] Hendrik L Tolman et al. “User manual and system documentation of WAVEWATCH III R version 4.07”. In: *Tech. Rept. NOAA/NWS/NCEP/MMAB Tech. Note 222* (2014).

[73] C Douglas and G Voulgaris. “WavePART: MATLAB (r) software for the partition of directional ocean wave spectra”. In: *Zenodo* (2019).

[74] Ana Nobre Silva et al. “Wave directional spreading importance on sheltered embayed beaches”. In: *Journal of Coastal Research* 95.SI (2020), pp. 1536–1541.

[75] BG Reguero, IJ Losada, and FJ Méndez. “A global wave power resource and its seasonal, interannual and long-term variability”. In: *Applied Energy* 148 (2015), pp. 366–380.

[76] Miraj Ahmed Bhuiyan et al. “Economic feasibility of marine renewable energy”. In: *Frontiers in Marine Science* 9 (2022), p. 988513.

[77] Marcela Santana Guzmán. “Caracterización de la energía del oleaje en Yucatán”. MA thesis. Tesis (MC)–Centro de Investigación y de Estudios Avanzados del IPN Unidad …, 2021.

[78] Xiao-Ming Li, Susanne Lehner, and Ming-Xia He. “Ocean wave measurements based on satellite synthetic aperture radar (SAR) and numerical wave model (WAM) data–extreme sea state and cross sea analysis”. In: *International Journal of Remote Sensing* 29.21 (2008), pp. 6403–6416.

[79] Agustinus Ribal and Ian R Young. “33 years of globally calibrated wave height and wind speed data based on altimeter observations”. In: *Scientific data* 6.1 (2019), p. 77.

[80] Justin E Stopa et al. “Comparison and validation of physical wave parameterizations in spectral wave models”. In: *Ocean Modelling* 103 (2016), pp. 2–17.

[81] BW Timmermans et al. “Global wave height trends and variability from new multimission satellite altimeter products, reanalyses, and wave buoys”. In: *Geophysical Research Letters* 47.9 (2020), e2019GL086880.

[82] E Medina-Lopez et al. “Satellite data for the offshore renewable energy sector: synergies and innovation opportunities”. In: *Remote Sensing of Environment* 264 (2021), p. 112588.

[83] BV Datawell. “Datawell waverider reference manual”. In: *Datawell BV, Zumerlustraat* 4 (2006), p. 2012.

[84] DE Cartwright. “Buoy techniques for obtaining directional wave spectra”. In: *Buoy Technology Symposium*. 1964, pp. 173–162.

[85] Stephen Barstow et al. “WorldWaves wave energy resource assessments from the deep ocean to the coast”. In: *Journal of Energy and Power Engineering* 5.8 (2011), pp. 730–742.

[86] Luigi Cavaleri and Paola Malanotte Rizzoli. “Wind wave prediction in shallow water: Theory and applications”. In: *Journal of Geophysical Research: Oceans* 86.C11 (1981), pp. 10961–10973.

[87] K Rorbaek and H Andersen. “Evaluation of wave measurements with an acoustic Doppler current profiler”. In: *OCEANS 2000 MTS/IEEE Conference and Exhibition. Conference Proceedings (Cat. No. 00CH37158)*. Vol. 2. IEEE. 2000, pp. 1181–1187.

[88] Arnold Schumacher. *Stereophotogrammetrische Wellenaufnahmen*. Vol. 7. W. de Gruyter, 1939.

[89] Joseph Chase et al. “The directional spectrum of a wind generated sea as determined from data obtained by the Stereo Wave Observation Project”. In: *New York University, College of Engineering, Research Division, Department of Meteorology and Oceanography and Engineering Statistics Group: New York, NY, USA* (1957).

[90] Peter Sutherland and W Kendall Melville. “Field measurements and scaling of ocean surface wave-breaking statistics”. In: *Geophysical Research Letters* 40.12 (2013), pp. 3074–3079.

[91] Ian R Young and Agustinus Ribal. “Multiplatform evaluation of global trends in wind speed and wave height”. In: *Science* 364.6440 (2019), pp. 548–552.

[92] VD Kuznetsov, VM Sinelnikov, and SN Alpert. “Yakov Alpert: Sputnik-1 and the first satellite ionospheric experiment”. In: *Advances in Space Research* 55.12 (2015), pp. 2833–2839.

[93] NA Space. “National Aeronautics and Space Administration”. In: *Retrieved from National Aeronautics and Space Administration: www. nasa. gov* (1977).

[94] Ricardo Eito-Brun and Maria Ledesma Rodriguez. “50 years of space research in Europe: a bibliometric profile of the European Space Agency (ESA)”. In: *Scientometrics* 109.1 (2016), pp. 551–576.

[95] Dr Yuri Karash. “Russian Space Program: financial state, current plans, ambitions and cooperation with the United States”. In: (2016).

[96] Gu Xingfa and Tong Xudong. “Overview of China earth observation satellite programs [space agencies]”. In: *IEEE Geoscience and remote sensing magazine* 3.3 (2015), pp. 113–129.

[97] Felipe M Santos et al. “A simulator of Synthetic Aperture Radar (SAR) image spectra: the applications on oceanswell waves”. In: *International journal of remote sensing* 42.8 (2021), pp. 2981–3001.

[98] Geir Engen et al. “Directional wave spectra by inversion of ERS-1 synthetic aperture radar ocean imagery”. In: *IEEE transactions on geoscience and remote sensing* 32.2 (1994), pp. 340–352.

[99] C. A. Wiley. “Synthetic Aperture Radars”. In: *IEEE Transactions on Aerospace and Electronic Systems* AES-21 (1985), pp. 440–443.

[100] G. S. Brown. “The average impulse response of a rough surface and its applications”. In: *IEEE Transactions on Antennas and Propagation* 25 (1977), pp. 67–74.

[101] CK Shum, JC Ries, and BD Tapley. “The accuracy and applications of satellite altimetry”. In: *Geophysical Journal International* 121.2 (1995), pp. 321–336.

[102] Anita C Brenner, John P DiMarzio, and H Jay Zwally. “Precision and accuracy of satellite radar and laser altimeter data over the continental ice sheets”. In: *IEEE Transactions on Geoscience and Remote Sensing* 45.2 (2007), pp. 321–331.

[103] Xi Zhang et al. “Assessment of arctic sea ice classification ability of Chinese HY-2B dual-band radar altimeter during winter to early spring conditions”. In: *IEEE Journal of Selected Topics in Applied Earth Observations and Remote Sensing* 14 (2021), pp. 9855–9872.

[104] Stefano Vignudelli and Nurul Hazrina Idris. *Coastal Altimetry: Selected Case Studies from Asian Shelf Seas*. Elsevier, 2023.

[105] Dudley B Chelton et al. “Satellite altimetry”. In: *International geophysics*. Vol. 69. Elsevier, 2001, pp. 1–ii.

[106] Xiaoli Deng et al. “Estimation of contamination of ERS-2 and POSEIDON satellite radar altimetry close to the coasts of Australia”. In: *Marine Geodesy* 25.4 (2002), pp. 249–271.

[107] Alejandro Egido and Walter HF Smith. “Fully focused SAR altimetry: Theory and applications”. In: *IEEE Transactions on Geoscience and Remote Sensing* 55.1 (2016), pp. 392–406.

[108] Liguang Jiang et al. “CryoSat-2 altimetry applications over rivers and lakes”. In: *Water* 9.3 (2017), p. 211.

[109] SKM Ali. “Meteorological observations”. In: (1998).

[110] Harald Ulrik Sverdrup and Walter Heinrich Munk. “Empirical and theoretical relations between wind, sea, and swell”. In: *Eos, Transactions American Geophysical Union* 27.6 (1946), pp. 823–827.

[111] Willard J Pierson and Wilbur Marks. “The power spectrum analysis of ocean-wave records”. In: *Eos, Transactions American Geophysical Union* 33.6 (1952), pp. 834–844.

[112] John W Miles. “On the generation of surface waves by shear flows”. In: *Journal of Fluid Mechanics* 3.2 (1957), pp. 185–204.

[113] Klaus Hasselmann et al. “The WAM model-a third generation ocean wave prediction model”. In: *Journal of Physical Oceanography* 18 (1988), pp. 1775–1810.

[114] TS IEC. “62600-101: 2015; Marine Energy–Wave, Tidal and Other Water Current Converters–Part 101: Wave Energy Resource Assessment and Characterization”. In: *International Electrotechnical Commission: Geneva, Switzerland* (2015).

[115] Gerald Beresford Whitham. *Linear and nonlinear waves*. John Wiley & Sons, 2011.

[116] SWAN Team. “SWAN, Scientific and Technical Documentation, SWAN Cycle III version 41.45”. In: (2023).

[117] Hendrik L Tolman. “User manual and system documentation of WAVEWATCH-III version 2.22”. In: *Technical Note, US Department of Commerce, NOAA, NWS, NCEP, Washington, DC* (2002).

[118] Gerbrand J Komen et al. *Dynamics and modelling of ocean waves*. 1996.

[119] IR Warren and H_K_ Bach. “MIKE 21: a modelling system for estuaries, coastal waters and seas”. In: *Environmental Software* 7.4 (1992), pp. 229–240.

[120] George Lavidas and Vengatesan Venugopal. “Application of numerical wave models at European coastlines: A review”. In: *Renewable and Sustainable Energy Reviews* 92 (2018), pp. 489–500.

[121] Jean-Raymond Bidlot et al. “A revised formulation of ocean wave dissipation and its model impact”. In: (2007).

[122] NRRC Booij, Roeland C Ris, and Leo H Holthuijsen. “A third-generation wave model for coastal regions: 1. Model description and validation”. In: *Journal of geophysical research: Oceans* 104.C4 (1999), pp. 7649–7666.

8

[123] SWAN Team et al. “User Manual SWAN—Cycle III version 41.31 AB”. In: *Delft University of Technology: Delft, The Netherlands* 152 (2021).

[124] S Mostafa Siadatmousavi, F Jose, and GW Stone. “On the importance of high frequency tail in third generation wave models”. In: *Coastal Engineering* 60 (2012), pp. 248–260.

[125] Susanne Hasselmann and Klaus Hasselmann. “Computations and parameterizations of the nonlinear energy transfer in a gravity-wave spectrum. Part I: A new method for efficient computations of the exact nonlinear transfer integral”. In: *Journal of Physical Oceanography* 15.11 (1985), pp. 1369–1377.

[126] Klaus Hasselmann et al. “Measurements of wind-wave growth and swell decay during the Joint North Sea Wave Project (JONSWAP).” In: *Ergaenzungsheft zur Deutschen Hydrographischen Zeitschrift, Reihe A* (1973).

[127] Peter AEM Janssen. “Quasi-linear theory of wind-wave generation applied to wave forecasting”. In: *Journal of physical oceanography* 21.11 (1991), pp. 1631–1642.

[128] W Erick Rogers, Alexander V Babanin, and David W Wang. “Observation-consistent input and whitecapping dissipation in a model for wind-generated surface waves: Description and simple calculations”. In: *Journal of Atmospheric and Oceanic Technology* 29.9 (2012), pp. 1329–1346.

[129] André J van der Westhuysen, Marcel Zijlema, and Jurjen A Battjes. “Nonlinear saturation-based whitecapping dissipation in SWAN for deep and shallow water”. In: *Coastal Engineering* 54.2 (2007), pp. 151–170.

[130] RL Snyder et al. “Array measurements of atmospheric pressure fluctuations above surface gravity waves”. In: *Journal of Fluid mechanics* 102 (1981), pp. 1–59.

[131] L Yan. “An improved wind input source term for third generation ocean wave modelling”. In: *Wetenschappelijk rapport= Scientific report. Koninklijk Nederlands Meteorologisch Instituut* (1987).

[132] William J Plant. “A relationship between wind stress and wave slope”. In: *Journal of Geophysical Research: Oceans* 87.C3 (1982), pp. 1961–1967.

[133] Paul A Hwang. “A note on the ocean surface roughness spectrum”. In: *Journal of Atmospheric and Oceanic Technology* 28.3 (2011), pp. 436–443.

[134] Yalin Fan et al. “Global ocean surface wave simulation using a coupled atmosphere–wave model”. In: *Journal of Climate* 25.18 (2012), pp. 6233–6252.

[135] Owen M Phillips. “On the generation of waves by turbulent wind”. In: *Journal of fluid mechanics* 2.5 (1957), pp. 417–445.

[136] Hendrik L Tolman. “Effects of numerics on the physics in a third-generation wind-wave model”. In: *Journal of physical Oceanography* 22.10 (1992), pp. 1095–1111.

[137] Yasser Eldeberky. “Nonlinear transformation of wave spectra in the nearshore zone”. In: *Oceanographic Literature Review* 4.44 (1997), p. 297.

[138] PA Madsen and OR Sørensen. “Bound waves and triad interactions in shallow water”. In: *Ocean Engineering* 20.4 (1993), pp. 359–388.

[139] KL Phan et al. “The effects of wave non-linearity on wave attenuation by vegetation”. In: *Coastal Engineering* 147 (2019), pp. 63–74.

[140] Randal D Koster et al. *Technical Report Series on Global Modeling and Data Assimilation, Volume 43*. Tech. rep. 2015.

[141] Hans Hersbach et al. “The ERA5 global reanalysis”. In: *Quarterly Journal of the Royal Meteorological Society* 146.730 (2020), pp. 1999–2049.

[142] Giulia Cervelli et al. “Comparison of the era5 wave forecasting dataset against buoy record”. In: *Instrumentation, Mesure, Metrologie* 21.3 (2022), p. 87.

[143] Junliang Liu et al. “Evaluation of ERA5 wave parameters with in situ data in the South China Sea”. In: *Atmosphere* 13.6 (2022), p. 935.

[144] Justin E Stopa and Alexis Mouche. “Significant wave heights from S entinel-1 SAR: Validation and applications”. In: *Journal of Geophysical Research: Oceans* 122.3 (2017), pp. 1827–1848.

[145] Parag Vaze et al. “The Jason-3 Mission: Completing the transition of ocean altimetry from research to operations”. In: *Sensors, systems, and next-generation satellites XIV*. Vol. 7826. SPIE. 2010, pp. 264–268.

[146] Jacques Verron et al. “The SARAL/AltiKa altimetry satellite mission”. In: *Marine Geodesy* 38.sup1 (2015), pp. 2–21.

[147] Marta de Alfonso, Fernando Manzano, and Alejandro Gallardo. “IN SITU TAC INSITU_GLO_WAV_DISCRETE_MY_013_045”. In: (2023).

[148] L Pecci, Michele Fichaut, and D Schaap. “SeaDataNet, an enhanced ocean data infrastructure giving services to scientists and society”. In: *IOP Conference Series: Earth and Environmental Science*. Vol. 509. 1. IOP Publishing. 2020, p. 012042.

[149] Space Weather Prediction Center. “National oceanic and atmospheric administration”. In: *National Weather Service (NOAA/NWS), cited* (2012), pp. 1950–2011.

[150] William Burnett and Richard Crout. “The NDBC IOOS® Data Assembly Center”. In: *OCEANS 2009*. IEEE. 2009, pp. 1–8.

[151] Candice Hall and Robert E Jensen. “Utilizing data from the noaa national data buoy center”. In: (2021).

[152] PD Cotton and DJT Carter. “Cross calibration of TOPEX, ERS-I, and Geosat wave heights”. In: *Journal of Geophysical Research: Oceans* 99.C12 (1994), pp. 25025–25033.

[153] S Zieger, J Vinoth, and IR Young. “Joint calibration of multiplatform altimeter measurements of wind speed and wave height over the past 20 years”. In: *Journal of Atmospheric and Oceanic Technology* 26.12 (2009), pp. 2549–2564.

[154] George H Born et al. “Calibration of the TOPEX altimeter using a GPS buoy”. In: *Journal of Geophysical Research: Oceans* 99.C12 (1994), pp. 24517–24526.

[155] Christopher Stephen Watson. “Satellite altimeter calibration and validation using GPS buoy technology”. In: (2005).

[156] Ronald Kolenkiewicz and Chreston F Martin. “SEASAT altimeter height calibration”. In: *Journal of Geophysical Research: Oceans* 87.C5 (1982), pp. 3189–3197.

[157] Ricardo M Campos. “Analysis of Spatial and Temporal Criteria for Altimeter Collocation of Significant Wave Height and Wind Speed Data in Deep Waters”. In: *Remote Sensing* 15.8 (2023), p. 2203.

[158] E Charles and A Ollivier. “WAVE Thematic Assembly Centre: WAVE_GLO_PHY_SWH_L3_MY_014_00 In: ().

[159] SB Luthcke et al. “The 1-centimeter orbit: Jason-1 precision orbit determination using GPS, SLR, DORIS, and altimeter data special issue: Jason-1 calibration/validation”. In: *Marine Geodesy* 26.3-4 (2003), pp. 399–421.

[160] Juliette Lambin et al. “The OSTM/jason-2 mission”. In: *Marine Geodesy* 33.S1 (2010), pp. 4–25.

[161] Jacques Louet and Stefano Bruzzi. “ENVISAT mission and system”. In: *IEEE 1999 International Geoscience and Remote Sensing Symposium. IGARSS’99 (Cat. No. 99CH36293)*. Vol. 3. IEEE. 1999, pp. 1680–1682.

[162] S Labroue et al. “First quality assessment of the Cryosat-2 altimetric system over ocean”. In: *Advances in Space Research* 50.8 (2012), pp. 1030–1045.

[163] Danièle Hauser et al. “Overview of the CFOSAT mission”. In: *2016 IEEE International Geoscience and Remote Sensing Symposium (IGARSS)*. IEEE. 2016, pp. 5789–5792.

[164] Mingzhi Sun et al. “Detecting lake level change from 1992 to 2019 of Zhari Namco in Tibet using altimetry data of TOPEX/Poseidon and Jason-1/2/3 missions”. In: *Frontiers in Earth Science* 9 (2021), p. 640553.

[165] Jacques Verron et al. “The SARAL/AltiKa mission: A step forward to the future of altimetry”. In: *Advances in Space Research* 68.2 (2021), pp. 808–828.

[166] P Queffeulou. “Validation of Jason-3 altimeter wave height measurements (poster)”. In: *OSTST meeting, November*. 2016, pp. 1–4.

[167] Bruce C Douglas and Robert E Cheney. “Geosat: Beginning a new era in satellite oceanography”. In: *Journal of Geophysical Research: Oceans* 95.C3 (1990), pp. 2833–2836.

[168] William F Townsend and Jean-Louis Fellous. “TOPEX/POSEIDON: An international satellite oceanography mission”. In: *Acta Astronautica* 16 (1987), pp. 213–220.

[169] CR Francis et al. “The ERS-2 spacecraft and its payload”. In: *Esa Bulletin* 83 (1995), pp. 13–31.

[170] Robert Barry. “The Geosat follow-on (GFO) program spacecraft”. In: *Space Programs and Technologies Conference and Exhibit*. 1993, p. 4106.

[171] Ian R Young and Agustinus Ribal. “Can multi-mission altimeter datasets accurately measure long-term trends in wave height?” In: *Remote Sensing* 14.4 (2022), p. 974.

[172] Li Erikson et al. “Global ocean wave fields show consistent regional trends between 1980 and 2014 in a multi-product ensemble”. In: *Communications Earth & Environment* 3.1 (2022), p. 320.

[173] Ricardo M Campos et al. “Assessment and calibration of ERA5 severe winds in the Atlantic Ocean using satellite data”. In: *Remote Sensing* 14.19 (2022), p. 4918.

[174] IR Young and MA Donelan. “On the determination of global ocean wind and wave climate from satellite observations”. In: *Remote Sensing of Environment* 215 (2018), pp. 228–241.

[175] Hans Hersbach. “The ERA5 Atmospheric Reanalysis.” In: *AGU fall meeting abstracts*. Vol. 2016. 2016, NG33D–01.

[176] Ronald Gelaro et al. “The modern-era retrospective analysis for research and applications, version 2 (MERRA-2)”. In: *Journal of climate* 30.14 (2017), pp. 5419–5454.

[177] Dick P Dee et al. “The ERA-Interim reanalysis: Configuration and performance of the data assimilation system”. In: *Quarterly Journal of the royal meteorological society* 137.656 (2011), pp. 553–597.

[178] Suranjana Saha et al. “The NCEP climate forecast system version 2”. In: *Journal of climate* 27.6 (2014), pp. 2185–2208.

[179] V Sharmar and M Markina. “Validation of global wind wave hindcasts using ERA5, MERRA2, ERA-Interim and CFSRv2 reanalyzes”. In: *IOP Conference Series: Earth and Environmental Science*. Vol. 606. 1. IOP Publishing. 2020, p. 012056.

[180] Mateusz Taszarek et al. “Comparison of convective parameters derived from ERA5 and MERRA-2 with rawinsonde data over Europe and North America”. In: *Journal of Climate* 34.8 (2021), pp. 3211–3237.

[181] AJ Simmons et al. “The ECMWF medium-range prediction models development of the numerical formulations and the impact of increased resolution”. In: *Meteorology and atmospheric physics* 40 (1989), pp. 28–60.

[182] Jean-Raymond Bidlot et al. “Inter-comparison of operational wave forecasting systems”. In: *10th international workshop on wave hindcasting and forecasting and coastal hazard symposium, North Shore, Oahu, Hawaii*. 2007, pp. 11–16.

[183] DS Richardson et al. *Verification statistics and evaluations of ECMWF forecasts in 2008-2009*. ECMWF Reading, UK, 2009.

[184] Jichao Wang and Yue Wang. “Evaluation of the ERA5 significant wave height against NDBC buoy data from 1979 to 2019”. In: *Marine Geodesy* 45.2 (2022), pp. 151–165.

[185] Peter AEM Janssen, Björn Hansen, and Jean-Raymond Bidlot. “Verification of the ECMWF wave forecasting system against buoy and altimeter data”. In: *Weather and forecasting* 12.4 (1997), pp. 763–784.

[186] Liliana Rusu and Eugen Rusu. “Evaluation of the worldwide wave energy distribution based on ERA5 data and altimeter measurements”. In: *Energies* 14.2 (2021), p. 394.

[187] Maria Francesca Bruno et al. “Performance assessment of ERA5 wave data in a swell dominated region”. In: *Journal of Marine Science and Engineering* 8.3 (2020), p. 214.

[188] Victor Ramos and John V Ringwood. “Exploring the utility and effectiveness of the IEC (International Electrotechnical Commission) wave energy resource assessment and characterisation standard: A case study”. In: *Energy* 107 (2016), pp. 668–682.

[189] Det Norske Veritas. “Certification of tidal and wave energy converters”. In: *Offshore ServiceSpecification DNV-OSS-312* (2008).

[190] Dick MA Schaap and Roy K Lowry. “SeaDataNet–Pan-European infrastructure for marine and ocean data management: unified access to distributed data sets”. In: *International Journal of Digital Earth* 3.S1 (2010), pp. 50–69.

[191] Adam M Leadbetter. “Linked ocean data”. In: *The Semantic Web in Earth and Space Science. Current Status and Future Directions*. IOS Press, 2015, pp. 11–31.

[192] Silvia Bozzi et al. “Modeling of a Point Absorber for Energy Conversion in Italian Seas”. In: *Energies* 6.6 (2013), pp. 3033–3051. ISSN: 1996-1073.

[193] Huakun Hu et al. “Bibliometric analysis for ocean renewable energy: An comprehensive review for hotspots, frontiers, and emerging trends”. In: *Renewable and Sustainable Energy Reviews* 167 (2022), p. 112739.

[194] R Carballo et al. “Wave farm planning through high-resolution resource and performance characterization”. In: *Renewable Energy* 135 (2019), pp. 1097–1107.

[195] N Arean, R Carballo, and G Iglesias. “An integrated approach for the installation of a wave farm”. In: *Energy* 138 (2017), pp. 910–919.

[196] Giuliana Mattiazzo. “State of the art and perspectives of wave energy in the Mediterranean sea: Backstage of ISWEC”. In: *Frontiers in Energy Research* 7 (2019), p. 114.

[197] Vincenzo Franzitta and Domenico Curto. “Sustainability of the renewable energy extraction close to the Mediterranean Islands”. In: *Energies* 10.3 (2017), p. 283.

[198] Alberto Ghigo et al. “Design and Optimization of a Point Absorber for the Mediterranean Sea”. In: *International Conference on Offshore Mechanics and Arctic Engineering*. Vol. 85932. American Society of Mechanical Engineers. 2022, V008T09A088.

[199] Nicola Pozzi et al. “PeWEC: Preliminary design of a full-scale plant for the mediterranean sea”. In: *Technology and Science for the Ships of the Future*. IOS Press, 2018, pp. 504–514.

[200] Marine Offshore Renewable Energy Lab. “Marine Offshore Renewable Energy Lab website”. In: http://www.morenergylab.polito.it/ (Date accessed: 11/12/2023) (2021).

[201] Torstein Pedersen, Eric Siegel, and Jon Wood. “Directional wave measurements from a subsurface buoy with an acoustic wave and current profiler (AWAC)”. In: *OCEANS 2007*. IEEE. 2007, pp. 1–10.

[202] IR Young, Stefan Zieger, and Alexander V Babanin. “Global trends in wind speed and wave height”. In: *Science* 332.6028 (2011), pp. 451–455.

[203] Andrew T Cox and Val R Swail. “A global wave hindcast over the period 1958–1997: Validation and climate assessment”. In: *Journal of Geophysical Research: Oceans* 106.C2 (2001), pp. 2313–2329.

[204] Justin E Stopa, Kwok Fai Cheung, and Yi-Leng Chen. “Assessment of wave energy resources in Hawaii”. In: *Renewable Energy* 36.2 (2011), pp. 554–567.

[205] Xavier Bertin, Elizabeth Prouteau, and Camille Letetrel. “A significant increase in wave height in the North Atlantic Ocean over the 20th century”. In: *Global and Planetary Change* 106 (2013), pp. 77–83.

[206] Jianjun Kang et al. “Comparative analysis of significant wave height between a new Southern Ocean buoy and satellite altimeter”. In: *Atmospheric and Oceanic Science Letters* 14.5 (2021), p. 100044.

[207] EPW Attema, G Duchossois, and G Kohlhammer. “ERS-1/2 SAR land applications: overview and main results”. In: *IGARSS'98. Sensing and Managing the Environment. 1998 IEEE International Geoscience and Remote Sensing. Symposium Proceedings.(Cat. No. 98CH36174)*. Vol. 4. IEEE. 1998, pp. 1796–1798.

[208] Xiaoxi Guo. “Chinese Satellite Program”. In: *Handbook of Space Security: Policies, Applications and Programs*. Springer, 2020, pp. 1381–1399.

[209] Saleh Abdalla, Peter AEM Janssen, and Jean-Raymond Bidlot. “Jason-2 OGDR wind and wave products: Monitoring, validation and assimilation”. In: *Marine Geodesy* 33.S1 (2010), pp. 239–255.

[210] GD Quartly et al. “Sentinel-3 Mission Performance Centre: Ensuring a high-quality altimetric dataset”. In: *Proceedings of Sentinel-3 for Science Workshop (2-5 June 2015, Venice, Italy)*. ESA. 2015.

[211] O Andersen and H Ranndal. “Global and Regional Evaluation of the First Two Years of Sentinel-3A and Very First Sentinel-3B and the Impact of Mean Sea Surfaces and Ocean Tide Corrections.” In: *25 years of progress in radar altimetry symposium*. 2018.

[212] RW Welch and C Gay. “TOPEX/POSEIDON (T/P)”. In: *Automatic Control in Aerospace 1992: Selected Papers from the 12th IFAC Symposium, Ottobrunn, Germany, 7-11 September 1992*. Elsevier. 2017, p. 151.

[213] Gerbrant Ph Van Vledder and Adem Akpınar. “Wave model predictions in the Black Sea: Sensitivity to wind fields”. In: *Applied Ocean Research* 53 (2015), pp. 161–178.

[214] Adem Akpinar and S Ponce De León. “An assessment of the wind re-analyses in the modelling of an extreme sea state in the Black Sea”. In: *Dynamics of Atmospheres and Oceans* 73 (2016), pp. 61–75.

[215] Burak Aydoğan and Berna Ayat. “Performance evaluation of SWAN ST6 physics forced by ERA5 wind fields for wave prediction in an enclosed basin”. In: *Ocean Engineering* 240 (2021), p. 109936.

[216] Taiping Wang et al. “A sensitivity analysis of the wind forcing effect on the accuracy of large-wave hindcasting”. In: *Journal of Marine Science and Engineering* 6.4 (2018), p. 139.

[217] George Lavidas, Vengatesan Venugopal, and Daniel Friedrich. "Sensitivity of a numerical wave model on wind re-analysis datasets". In: *Dynamics of Atmospheres and Oceans* 77 (2017), pp. 1–16.

[218] Mostafa Beyramzade, Seyed Mostafa Siadatmousavi, and Mahyar Majidy Nik. "Skill assessment of SWAN model in the red sea using different wind data". In: *Regional Studies in Marine Science* 30 (2019), p. 100714.

[219] Wenfan Wu et al. "Evaluation of different wind resources in simulating wave height for the Bohai, Yellow, and East China Seas (BYES) with SWAN model". In: *Continental Shelf Research* 207 (2020), p. 104217.

[220] Asmaa A Abu Zed et al. "Wind and wave climate southeastern of the Mediterranean Sea based on a high-resolution SWAN model". In: *Dynamics of Atmospheres and Oceans* 99 (2022), p. 101311.

[221] María O Molina, Claudia Gutiérrez, and Enrique Sánchez. "Comparison of ERA5 surface wind speed climatologies over Europe with observations from the HadISD dataset". In: *International Journal of Climatology* 41.10 (2021), pp. 4864–4878.

[222] Sakari M Uppala et al. "The ERA-40 re-analysis". In: *Quarterly Journal of the Royal Meteorological Society: A journal of the atmospheric sciences, applied meteorology and physical oceanography* 131.612 (2005), pp. 2961–3012.

[223] Shinya Kobayashi et al. "The JRA-55 reanalysis: General specifications and basic characteristics". In: *Journal of the Meteorological Society of Japan. Ser. II* 93.1 (2015), pp. 5–48.

[224] Kazutoshi Onogi et al. "The JRA-25 reanalysis". In: *Journal of the Meteorological Society of Japan. Ser. II* 85.3 (2007), pp. 369–432.

[225] Suranjana Saha et al. "The NCEP climate forecast system reanalysis". In: *Bulletin of the American Meteorological Society* 91.8 (2010), pp. 1015–1058.

[226] Dick P Dee et al. "The ERA-Interim reanalysis: Configuration and performance of the data assimilation system". In: *Quarterly Journal of the royal meteorological society* 137.656 (2011), pp. 553–597.

[227] Michele M Rienecker et al. "MERRA: NASA's modern-era retrospective analysis for research and applications". In: *Journal of climate* 24.14 (2011), pp. 3624–3648.

[228] Masao Kanamitsu et al. "Ncep–doe amip-ii reanalysis (r-2)". In: *Bulletin of the American Meteorological Society* 83.11 (2002), pp. 1631–1644.

[229] Ronald Gelaro et al. "The modern-era retrospective analysis for research and applications, version 2 (MERRA-2)". In: *Journal of climate* 30.14 (2017), pp. 5419–5454.

[230] Suranjana Saha et al. "The NCEP climate forecast system version 2". In: *Journal of climate* 27.6 (2014), pp. 2185–2208.

[231] FJ Wentz et al. "Remote Sensing Systems Cross-Calibrated Multi-Platform (CCMP) 6-hourly ocean vector wind analysis product on 0.25 deg grid, Version 2.0". In: *Remote Sensing Systems, Santa Rosa, CA* 126 (2015).

[232] Carl A Mears et al. “A near-real-time version of the cross-calibrated multiplatform (CCMP) ocean surface wind velocity data set”. In: *Journal of Geophysical Research: Oceans* 124.10 (2019), pp. 6997–7010.

[233] National Centers for Environmental Prediction/National Weather Service/NOAA/US Department of Commerce. “NCEP FNL operational model global tropospheric analyses, continuing from July 1999”. In: *Research Data Archive at the National Center for Atmospheric Research, Computational and Information Systems Laboratory* (2000).

[234] Konstantinos Christakos et al. “Modelling wave growth in narrow fetch geometries: The white-capping and wind input formulations”. In: *Ocean Modelling* 157 (2021), p. 101730.

[235] Khalid Amarouche et al. “Evaluation of a high-resolution wave hindcast model SWAN for the West Mediterranean basin”. In: *Applied Ocean Research* 84 (2019), pp. 225–241.

[236] MM Amrutha et al. “Wave hindcast studies using SWAN nested in WAVEWATCH III-comparison with measured nearshore buoy data off Karwar, eastern Arabian Sea”. In: *Ocean Engineering* 119 (2016), pp. 114–124.

[237] W Erick Rogers, Paul A Hwang, and David W Wang. “Investigation of wave growth and decay in the SWAN model: three regional-scale applications”. In: *Journal of Physical Oceanography* 33.2 (2003), pp. 366–389.

[238] Konstantinos Christakos et al. “The importance of wind forcing in fjord wave modelling”. In: *Ocean Dynamics* 70 (2020), pp. 57–75.

[239] Liliana Rusu. “Assessment of the wave energy in the Black Sea based on a 15-year hindcast with data assimilation”. In: *Energies* 8.9 (2015), pp. 10370–10388.

[240] Wei-Cheng Wu et al. “Development and validation of a high-resolution regional wave hindcast model for US West Coast wave resource characterization”. In: *Renewable Energy* 152 (2020), pp. 736–753.

[241] Øyvind Breivik et al. “Nearshore wave forecasting and hindcasting by dynamical and statistical downscaling”. In: *Journal of Marine Systems* 78 (2009), S235–S243.

[242] George Lavidas and Henk Polinder. “*North Sea Wave Database (NSWD) and the Need for Reliable Resource Data: A 38 Year Database for Metocean and Wave Energy Assessments*”. In: *Atmosphere* 10 (2019), pp. 1–27.

[243] Qingxiang Liu et al. “Global Wave Hindcasts Using the Observation-Based Source Terms: Description and Validation”. In: *Journal of Advances in Modeling Earth Systems* 13.8 (2021).

[244] Jean-Raymond Bidlot, Gil Lemos, and Alvaro Semedo. “ERA5 reanalysis and ERA5-based ocean wave hindcast”. In: *2nd International Workshop on Waves, Storm Surges, and Coastal Hazards. VIC, Australia, University of Melbourne*. Vol. 1. 2019, pp. 1–28.

[245] Tom H Durrant, Diana JM Greenslade, and Ian Simmonds. “Validation of Jason-1 and Envisat remotely sensed wave heights”. In: *Journal of Atmospheric and Oceanic Technology* 26.1 (2009), pp. 123–134.

[246] Saleh Abdalla et al. “Assessment of CryoSat-2 SAR mode wind and wave data”. In: *Advances in Space Research* 62.6 (2018), pp. 1421–1433.

[247] Pauline Weatherall et al. “A new digital bathymetric model of the world’s oceans”. In: *Earth and space Science* 2.8 (2015), pp. 331–345.

[248] C Palmiotto and MF Loreto. “Regional scale morphological pattern of the Tyrrhenian Sea: New insights from EMODnet bathymetry”. In: *Geomorphology* 332 (2019), pp. 88–99.

[249] Karl E Taylor. “Summarizing multiple aspects of model performance in a single diagram”. In: *Journal of geophysical research: atmospheres* 106.D7 (2001), pp. 7183–7192.

[250] Richard Courant, Kurt Friedrichs, and Hans Lewy. “On the partial difference equations of mathematical physics”. In: *IBM journal of Research and Development* 11.2 (1967), pp. 215–234.

[251] J.A. Battjes and J.P.F.M. Janssen. “Energy loss and set-up due to breaking of random waves”. In: *Coastal Engineering Proceedings* 1.16 (1978), p. 32.

[252] Leandro Fernández, Clément Calvino, and Frédéric Dias. “Sensitivity analysis of wind input parametrizations in the WAVEWATCH III spectral wave model using the ST6 source term package for Ireland”. In: *Applied Ocean Research* 115 (2021), p. 102826.

[253] Sara Oliveira-Pinto, Paulo Rosa-Santos, and Francisco Taveira-Pinto. “Assessment of the potential of combining wave and solar energy resources to power supply worldwide offshore oil and gas platforms”. In: *Energy Conversion and Management* 223 (2020), p. 113299.

[254] Hans-Wilhelm Schiffer, Tom Kober, and Evangelos Panos. “World energy council’s global energy scenarios to 2060”. In: *Zeitschrift für Energiewirtschaft* 2.42 (2018), pp. 91–102.

[255] Manish Ram, Arman Aghahosseini, and Christian Breyer. “Job creation during the global energy transition towards 100% renewable power system by 2050”. In: *Technological Forecasting and Social Change* 151 (2020), p. 119682.

[256] Mark Z Jacobson et al. “Matching demand with supply at low cost in 139 countries among 20 world regions with 100% intermittent wind, water, and sunlight (WWS) for all purposes”. In: *Renewable Energy* 123 (2018), pp. 236–248.

[257] Sven Teske. *Achieving the Paris climate agreement goals: Global and regional 100% renewable energy scenarios with non-energy GHG pathways for+ 1.5 C and+ 2 C*. Springer Nature, 2019.

[258] Dmitrii Bogdanov et al. “Radical transformation pathway towards sustainable electricity via evolutionary steps”. In: *Nature communications* 10.1 (2019), pp. 1–16.

[259] Kenneth Hansen, Christian Breyer, and Henrik Lund. “Status and perspectives on 100% renewable energy systems”. In: *Energy* 175 (2019), pp. 471–480.

[260] Carlos VC Weiss et al. “Marine renewable energy potential: A global perspective for offshore wind and wave exploitation”. In: *Energy conversion and management* 177 (2018), pp. 43–54.

[261] Andrew M Cornett. “A global wave energy resource assessment”. In: *ISOPE International Ocean and Polar Engineering Conference*. ISOPE. 2008, ISOPE–I.

[262] Bryson Robertson et al. “Holistic marine energy resource assessments: A wave and offshore wind perspective of metocean conditions”. In: *Renewable Energy* 170 (2021), pp. 286–301.

[263] Kester Gunn and Clym Stock-Williams. “Quantifying the global wave power resource”. In: *Renewable energy* 44 (2012), pp. 296–304.

[264] Arthur Pecher and Jens Peter Kofoed. *Handbook of ocean wave energy*. Springer Nature, 2017.

[265] Joao Cruz. *Ocean wave energy: current status and future prespectives*. Springer Science & Business Media, 2007.

[266] Ke Sun et al. “Experimental investigation of semi-submersible platform combined with point-absorber array”. In: *Energy Conversion and Management* 245 (2021), p. 114623.

[267] Tim Stallard, Peter K Stansby, and Alan J Williamson. “An experimental study of closely spaced point absorber arrays”. In: *ISOPE International Ocean and Polar Engineering Conference*. ISOPE. 2008, ISOPE–I.

[268] Kathleen Edwards, Mike Mekhiche, et al. “Ocean power technologies powerbuoy®: system-level design, development and validation methodology”. In: (2014).

[269] Laurence D Mann. “Application of ocean observations & analysis: The CETO wave energy project”. In: *Operational Oceanography in the 21st Century* (2011), pp. 721–729.

[270] DJ Pizer, CH Retzler, and RW Yemm. “The OPD Pelamis: experimental and numerical results from the hydrodynamic work program”. In: *Proceedings of the EWTEC 2000 European Wave Energy Conference, Aalborg, Denmark*. 2000, pp. 227–234.

[271] LARS Christensen, E Friis-Madsen, and Jens Peter Kofoed. “The wave energy challenge: the wave dragon case”. In: *Proceedings of the POWER-GEN 2005 Europe Conference: Milan, Italy, June 2005*. 2005.

[272] Nicola Pozzi et al. “Numerical modeling and experimental testing of a pendulum wave energy converter (PeWEC)”. In: *Politecnico di Torino, Torino, Italy* (2018).

[273] Stephen H Salter. “Wave power”. In: *Nature* 249.5459 (1974), pp. 720–724.

[274] DV Evans. “A theory for wave-power absorption by oscillating bodies”. In: *Journal of Fluid Mechanics* 77.1 (1976), pp. 1–25.

[275] Chiang C Mei. “Power extraction from water waves”. In: *Journal of Ship Research* 20.02 (1976), pp. 63–66.

[276] Alain H Clément. “Dynamic nonlinear response of OWC wave energy devices”. In: *International Journal of Offshore and Polar Engineering* 7.02 (1997).

[277] Johannes Falnes and Adi Kurniawan. *Ocean waves and oscillating systems: linear interactions including wave-energy extraction*. Vol. 8. Cambridge university press, 2020.

[278] Manley St. Denis. "Some cautions on the employment of the spectral technique to describe the waves of the sea and the response thereto of oceanic systems". In: *Offshore Technology Conference*. OTC. 1973, OTC–1819.

[279] C Lee and JN Newman. "WAMIT user manual, version 7.0". In: *WAMIT Inc, Chestnut Hill, Massachusetts* (2013).

[280] AQWA Ansys. "AQWA theory manual". In: *AQWA: Canonsburg, PA, USA* (2013).

[281] Aurélien Babarit and Gérard Delhommeau. "Theoretical and numerical aspects of the open source BEM solver NEMOH". In: *11th European wave and tidal energy conference (EWTEC2015)*. 2015.

[282] Pál Schmitt et al. "Development and validation of a procedure for numerical vibration analysis of an oscillating wave surge converter". In: *European Journal of Mechanics-B/Fluids* 58 (2016), pp. 9–19.

[283] Markel Penalba, Thomas Kelly, and John Ringwood. "Using NEMOH for modelling wave energy converters: A comparative study with WAMIT". In: (2017).

[284] W Sheng et al. "Hydrodynamic studies of floating structures: Comparison of wave-structure interaction modelling". In: *Ocean Engineering* 249 (2022), p. 110878.

[285] Alireza Shadmani, Mohammad Reza Nikoo, and Amir H Gandomi. "Adaptive systematic optimization of a multi-axis ocean wave energy converter". In: *Renewable and Sustainable Energy Reviews* 189 (2024), p. 113920.

[286] Jiayao Meng, Ross A McAdam, and Manolis N Chatzis. "A Simulink Model for the Dynamic Analysis of Floating Wind Turbines". In: *Society for Experimental Mechanics Annual Conference and Exposition*. Springer. 2023, pp. 229–239.

[287] Ristiyanto Adiputra et al. "Roundness and slenderness effects on the dynamic characteristics of spar-type floating offshore wind turbine". In: *Curved and Layered Structures* 10.1 (2023), p. 20220213.

[288] Nurman Firdaus et al. "The dynamic parameters of a spar-type floating offshore wind turbine: A benchmarking assessment". In: *Procedia Structural Integrity* 48 (2023), pp. 58–64.

[289] LSPa da Silva et al. "Dynamics of hybrid offshore renewable energy platforms: Heaving point absorbers connected to a semi-submersible floating offshore wind turbine". In: *Renewable Energy* 199 (2022), pp. 1424–1439.

[290] Yingyi Liu. "Introduction of the open-source boundary element method solver hams to the ocean renewable energy community". In: *Proceedings of the European wave and tidal energy conference: EWTEC 2021*. Technical Committee of the European Wave and Tidal Energy Conference (EWTEC). 2021.

[291] Yingyi Liu et al. "2022A-GS18-3 Review of the Open-Source Boundary Element Method Framework for Ocean Renewable Energy". In: *Conference Proceedings The Japan Society of Naval Architects and Ocean Engineers 35*. The Japan Society of Naval Architects and Ocean Engineers. 2022, pp. 637–638.

[292] RE Hoskin and Nancy Nichols. “Optimal strategies for phase control of wave energy devices”. In: (1987).

[293] Aurélien Babarit, Michel Guglielmi, and Alain H Clément. “Declutching control of a wave energy converter”. In: *Ocean engineering* 36.12-13 (2009), pp. 1015–1024.

[294] Odd Faltinsen. *Sea loads on ships and offshore structures*. Vol. 1. Cambridge university press, 1993.

[295] Subrata Kumar Chakrabarti. *Hydrodynamics of offshore structures*. WIT press, 1987.

[296] G.B. Airy. *Tides and Waves*. B. Fellowes, 1845.

[297] Bernard Molin. *Hydrodynamique des structures offshore*. Editions Technip, 2002.

[298] Bruno Paduano et al. “Modelling, survivability, assessment, and control of moored wave energy conversion systems”. In: (2023).

[299] M Alves. “Frequency-domain models”. In: *Numerical Modelling of Wave Energy Converters*. Elsevier, 2016, pp. 11–30.

[300] WE Cummins et al. “The impulse response function and ship motions”. In: (1962).

[301] Tristan Perez and Thor I Fossen. “Joint identification of infinite-frequency added mass and fluid-memory models of marine structures”. In: (2008).

[302] Tristan Pérez and Thor Fossen. “Time-vs. frequency-domain identification of parametric radiation force models for marine structures at zero speed”. In: *Modeling, Identification and Control* 29.1 (2008), pp. 1–19.

[303] MOREnergy Lab. *MOREnergy Lab*. http://www.morenergylab.polito.it/. Accessed: 2024-02-28.

[304] ESTLab Energy Center. *ESTLab Energy Center LinkedIn*. https://www.linkedin.com/company/estlab-energycenter/?originalSubdomain=it. Accessed: 2024-05-28.

[305] GDP Analytics. *GDP Analytics*. https://www.gdpanalytics.com/. Accessed: 2024-05-08.

[306] Oihana Solaun et al. “Spatial overlap between human activities and seabed habitats in European seas: Insights into EMODnet’s data for management purposes”. In: *Marine Policy* 130 (2021), p. 104551.

[307] Audrey Trochet and Dirk Schmeller. “Effectiveness of the Natura 2000 network to cover threatened species”. In: *Nature Conservation* 4 (2013), pp. 35–53.

[308] Santanu Koley and Kshma Trivedi. “Mathematical modeling of Oyster wave energy converter device”. In: *AIP Conference Proceedings*. Vol. 2277. AIP Publishing LLC. 2020, p. 130014.

[309] Diego Vicinanza et al. “The SSG wave energy converter: Performance, status and recent developments”. In: *Energies* 5.2 (2012), pp. 193–226.

[310] Wave RES Platform. *Wave RES Platform Bathymetry Map*. https://wave.est.polito.it/dashboard/map/bathymetry. Accessed: 2024-06-02.

[311] Pozzi Nicola et al. “Wave tank testing of a pendulum wave energy converter 1: 12 scale model”. In: *International Journal of Applied Mechanics* 9.02 (2017), p. 1750024.

[312] Chang Hyuck Lim et al. “The study on design of the floating pendulum wave energy converter (FPWEC) operation system”. In: *ISOPE International Ocean and Polar Engineering Conference*. ISOPE. 2015, ISOPE–I.

[313] Aurélien Babarit et al. “Stakeholder requirements for commercially successful wave energy converter farms”. In: *Renewable energy* 113 (2017), pp. 742–755.

[314] Alain Clément et al. “The SEAREV wave energy converter”. In: *Proceedings of the 6th Wave and Tidal Energy Conference, Glasgow, UK*. Vol. 29. 2005.

[315] G Rinaldi et al. “Development of a simplified analytical model for a passive inertial system solicited by wave motion”. In: *International Journal of Marine Energy* 13 (2016), pp. 45–61.

[316] Fabio Carapellese et al. “Intuitive LTI energy-maximising control for multi-degree of freedom wave energy converters: The PeWEC case”. In: *Ocean Engineering* 256 (2022), p. 111444.

[317] Sergej Antonello Sirigu et al. “Techno-Economic optimisation for a wave energy converter via genetic algorithm”. In: *Journal of Marine Science and Engineering* 8.7 (2020), p. 482.

[318] Mauro Bonfanti et al. “Real-time wave excitation forces estimation: An application on the ISWEC device”. In: *Journal of Marine Science and Engineering* 8.10 (2020), p. 825.

[319] Alexis Mérigaud and John V Ringwood. “Free-surface time-series generation for wave energy applications”. In: *IEEE Journal of Oceanic Engineering* 43.1 (2017), pp. 19–35.

[320] Michel K Ochi. *Ocean waves: the stochastic approach*. Vol. 6. Cambridge University Press, 2005.

[321] Tiago Duarte et al. “Computation of wave loads under multidirectional sea states for floating offshore wind turbines”. In: *International Conference on Offshore Mechanics and Arctic Engineering*. Vol. 45547. American Society of Mechanical Engineers. 2014, V09BT09A023.

[322] Pierpaolo Ricci. “Time-domain models”. In: *Numerical Modelling of Wave Energy Converters*. Elsevier, 2016, pp. 31–66.

[323] Giulia Cervelli, Beatrice Battisti, and Giuliana Mattiazzo. “On the influence of multidirectional irregular waves on the PeWEC device”. In: *Frontiers in Energy Research* 10 (2022).

[324] The Specialist Committee on Stationary Floating Systems. “Final Report and Recommendations to the 23rd ITTC”. In: *Proceedings of the 23rd ITTC (International Towing Tank Conference)*. Vol. 2. 2002, pp. 553–738.

[325] Yoshimi Goda. “A comparative review on the functional forms of directional wave spectrum”. In: *Coastal Engineering Journal* 41.1 (1999), pp. 1–20.

[326] Iraide López et al. “Review of wave energy technologies and the necessary power-equipment”. In: *Renewable and sustainable energy reviews* 27 (2013), pp. 413–434.

[327] Liliana Rusu and C Guedes Soares. “Wave energy assessments in the Azores islands”. In: *Renewable Energy* 45 (2012), pp. 183–196.

[328] Dina Silva, Eugen Rusu, and Carlos Guedes Soares. “Evaluation of various technologies for wave energy conversion in the Portuguese nearshore”. In: *Energies* 6.3 (2013), pp. 1344–1364.

[329] Yue Hong et al. “Damping studies on PMLG-based wave energy converter under oceanic wave climates”. In: *Energies* 14.4 (2021), p. 920.

[330] Hamid Reza Ghafari, Hassan Ghassemi, and Atefeh Neisi. “Power matrix and dynamic response of the hybrid Wavestar-DeepCwind platform under different diameters and regular wave conditions”. In: *Ocean Engineering* 247 (2022), p. 110734.

[331] Raphael Stuhlmeier and Dali Xu. “WEC design based on refined mean annual energy production for the Israeli Mediterranean coast”. In: *Journal of Waterway, Port, Coastal, and Ocean Engineering* 144.4 (2018), p. 06018002.

[332] Yuping Gao et al. “A fully floating system for a wave energy converter with direct-driven linear generator”. In: *Energy* 95 (2016), pp. 99–109.

[333] Ossama Abdelkhalik et al. “WEC geometry optimization with advanced control”. In: *International conference on offshore mechanics and arctic engineering*. Vol. 57786. American Society of Mechanical Engineers. 2017, V010T09A031.

[334] Ao Gang et al. “Performance analysis of a coast–OWC wave energy converter integrated system”. In: *Applied Energy* 311 (2022), p. 118605.

[335] Oskar Danielsson et al. “Simulated response of a linear generator wave energy converter”. In: *ISOPE International Ocean and Polar Engineering Conference*. ISOPE. 2004, ISOPE–I.

[336] Raju Ahamed, Kristoffer McKee, and Ian Howard. “A review of the linear generator type of wave energy converters’ power take-off systems”. In: *Sustainability* 14.16 (2022), p. 9936.

[337] Florin Onea and Eugen Rusu. “Expected Performances of WEC Systems Operating Near the European Offshore Wind Sites”. In: *Advances in Clean Energy Systems and Technologies*. Springer, 2024, pp. 85–92.

[338] Yong Wan et al. “Performance Evaluation of Advanced Wave Energy Converters in the Nearshore Areas of the North Indian Ocean”. In: *China Ocean Engineering* 36.6 (2022), pp. 980–993.

[339] Kimon Kardakaris, Ifigeneia Boufidi, and Takvor Soukissian. “Offshore wind and wave energy complementarity in the Greek seas based on ERA5 data”. In: *Atmosphere* 12.10 (2021), p. 1360.

[340] Alain Ulazia et al. “On the impact of long-term wave trends on the geometry optimisation of oscillating water column wave energy converters”. In: *Energy* 206 (2020), p. 118146.

[341] Rodrigo Alonso, Sebastián Solari, and Luis Teixeira. “Wave energy resource assessment in Uruguay”. In: *Energy* 93 (2015), pp. 683–696.

[342] R Carballo et al. “A high resolution geospatial database for wave energy exploitation”. In: *Energy* 68 (2014), pp. 572–583.

[343] G Iglesias and R Carballo. “Wave power for la isla bonita”. In: *Energy* 35.12 (2010), pp. 5013–5021.

[344] Jongwoo Song. “Bias corrections for Random Forest in regression using residual rotation”. In: *Journal of the Korean Statistical Society* 44.2 (2015), pp. 321–326.

[345] Markel Penalba et al. “Bias correction techniques for uncertainty reduction of long-term metocean data for ocean renewable energy systems”. In: *Renewable Energy* 219 (2023), p. 119404.

[346] Claudia Teutschbein and Jan Seibert. “Bias correction of regional climate model simulations for hydrological climate-change impact studies: Review and evaluation of different methods”. In: *Journal of hydrology* 456 (2012), pp. 12–29.

[347] Douglas Maraun. “Bias correcting climate change simulations-a critical review”. In: *Current Climate Change Reports* 2.4 (2016), pp. 211–220.

[348] Uwe Ehret et al. “HESS Opinions" Should we apply bias correction to global and regional climate model data?"”. In: *Hydrology and Earth System Sciences* 16.9 (2012), pp. 3391–3404.

[349] Åke Björck. “Least squares methods”. In: *Handbook of numerical analysis* 1 (1990), pp. 465–652.

LIST OF PUBLICATIONS

1. **B. Fenu, V. Attanasio, P. Casalone, R. Novo, G. Cervelli, M. Bonfanti, S.A. Sirigu, G. Bracco, G. Mattiazzo**, *Analysis of a gyroscopic-stabilized floating offshore hybrid wind-wave platform*, Journal of Marine Science and Engineering **8**, 439 (2020).

2. **S.A. Sirigu, L. Foglietta, G. Giorgi, M. Bonfanti, G. Cervelli, G. Bracco, G. Mattiazzo**, *Techno-Economic optimisation for a wave energy converter via genetic algorithm*, Journal of Marine Science and Engineering **8**, 482 (2020).

3. **G. Cervelli, F. Carapellese, G. Bracco, G. Mattiazzo**, *Variability of wecs' performance according to the wave directional spreading variation*, Proceedings of the European Wave and Tidal Energy Conference, **2288–1** (2021).

4. **G. Cervelli, L. Parrinello, C. Moscoloni, G. Giorgi**, *Comparison of the ERA5 Wave Forecasting Dataset Against Buoy Record*, Instrumentation, Mesures, Métrologies, **21**, 3 (2022).

5. **G. Cervelli, B. Battisti, G. Mattiazzo**, *On the influence of multidirectional irregular waves on the PeWEC device*, Frontiers in Energy Research **10**, 908529 (2022).

6. **G. Giorgi, R. Novo, G. Cervelli, G. Bracco**, *Wave energy converters technology database for a web-based platform for evaluating wave energy resource and productivity potential*, Trends in Renewable Energies Offshore, **33–41** (2022).

7. **M. Penalba, C. Guo, A. Zarketa-Astigarraga, G. Cervelli, G. Giorgi, B. Robertson**, *Bias correction techniques for uncertainty reduction of long-term metocean data for ocean renewable energy systems*,Renewable Energy **219**, 119404 (2023).

8. **R. Novo, G. Giorgi, G. Cervelli, N. Faedo, G. Mattiazzo**, *Identification of optimal sites for the deployment of wave energy converters: the importance of a technology-centred approach*, Proceedings of the European Wave and Tidal Energy Conference, **15**, 1–9 (2023).

9. **G. Cervelli,G. Giorgi, G. Mattiazzo**, *On the errors in annual energy yield estimation due to monodirectional wave spectra assumption*, Proceedings of the European Wave and Tidal Energy Conference, **15** (2023).

10. **G. Cervelli, C. Moscoloni, G. Giorgi, G. Mattiazzo**, *Optimal Site Selection for Wave Energy Converter Installation on Pantelleria*, Proceedings of the ISOPE International Ocean and Polar Engineering Conference, **ISOPE–I** (2024).